A Geodetic Study of Crustal Deformation in the Ventura Basin Region, Southern California

Thesis by

Andrea Donnellan

In Partial Fulfillment of the Requirements

for the Degree of

Doctor of Philosophy

California Institute of Technology

Pasadena, California

1992

(Submitted July 19, 1991)

Acknowledgements

I must start by thanking Brad Hager for his time as my thesis advisor. I appreciate his dedication to the Ventura basin project and his enthusiasm for scientific discussion and discovery. I also thank Brad for his encouragement and for his willingness to listen and provide advice. I have enjoyed working with him.

Many thanks also to Patty Hager for her endless hospitality, and to Emily and Anna for the friendship and many smiles they gave me during my stays in Boston. I thank Axel for his companionship and long walks through the woods.

I appreciate the many people at MIT who were involved in this project in one way or another. Bob King was a constant source of help, information and encouragement, with apparently endless patience. I thank all of those who worked on the GAMIT software, including Bob King, Mark Murray, Kurt Feigl, and Da-nan Dong and Yehuda Bock. Thanks also to Tom Herring for his assistance with the program GLOBK. I know that my interaction with these people resulted in a great improvement of this thesis.

Lynda Bell and Chopo Ma, from NASA/GSFC, provided much help and information pertaining to the VLBI sites Santa Paula and Palos Verdes. I appreciate the speed with which Yehuda Bock made the 1991 Caltrans GPS data available to me,

and also thank him for his friendship and encouragement.

I express my gratitude to my High School science teacher, Mr. Saulius Ploplys, for his excellent teaching and enthusiasm for the sciences. Without his interest and support I would never have pursued a scientific career.

I thank the members of my thesis defense committee, Don Anderson, Rob Clayton, Hiroo Kanamori, Lee Silver and of course Brad Hager, for the time and effort they invested toward the improvement of this thesis. I found the exam to be very interesting and appreciate the insights that were shared with me through the course of the exam.

I also thank my advisor from Ohio State University, Dr. Ian Whillans, for his continued interest in my work. He was an exceptional advisor and I thank him for the background he gave me. In addition, Ian and the Ohio State University provided GPS receivers during 1987 and 1989, which enabled me to broaden the scope of this project. UNAVCO, MIT, and Scripps Institute of Oceanography provided additional receivers for the experiments.

I especially thank all of those who so graciously assisted with the field work. These people include: Duncan Agnew, Ericka Anderson, Michael Baumer, Robert Clayton, Rich Dixon, Da-nan Dong, Doug Dreger, Peng Fang, Kurt Feigl, ShangXing Gao, X. Bob Ge, William Greer, Brad Hager, Jeffrey Hammond, Manabu Hashimoto, George Hathaway, Greg Holk, Lorraine Hwang, Dave Jackson, David Johnson, Hadley Johnson, Laura Jones, Sharon Kedar, Tom Kelecy, Louise Kellogg, Bob King, Nancy King, Scott King, Shawn Larsen, Kristine Larson, Linda Maepa, Jim Martin, Scott Mitchell, Doug Neuhauser, Svetlana Panasyuk, Helen Qian, Jeanne Sauber, Zheng-

Kang Shen, Leslie Sonder, D. L. Sprangers, Joanne Stock, L. Sung, Paul Tackley, Hong-Kie Thio, Dave Tralli, Victor Vasquez, Dave Wald, Lisa Wald, Shingo Watada, Kathy Watts, Frank Webb, C. Bruce Worden, and Yan Zhang. This list is not necessarily inclusive, and I thank any others who may have helped. I also thank the many land owners, oil companies, and government agencies for their willingness to allow access to private or restricted lands.

Egill Hauksson was always available for discussion which I appreciated greatly. I also extend thanks to Steve Bryant for his help and patience and to Lucy Jones for her insights into the seismicity of the basin. Robert Clayton took over as my Caltech advisor after Brad left for MIT. I appreciate his doing so, and thank him for time he spent advising me and for his support.

I thank the many people who made my stay at Caltech more enjoyable. Scott King and Tom Duffy were pleasant officemates and are good friends. Louise Kellogg was especially supportive and insightful. I always enjoyed the group meetings and lunches, which included Scott King, Brad Hager, Louise Kellogg and Walter Kiefer. I never would have survived the computers without Doug Neuhauser's extensive knowledge and boundless energy. Doug also provided steady friendship throughout my graduate career. I enjoyed the time I spent with Dave and Lisa Wald, Hong-Kie Thio, Sharon Kedar, Bradley Woods, Doug Dreger, and Craig Schrivner. I especially enjoyed our trips to the Red Door Café. The members of the staff were always helpful, and I especially thank Janet Fernandez for her willingness to assist and for her friendship.

Scott Ross, and Claudia Barner were wonderful neighbors and friends and were

always helpful. I feel as if they are part of my extended family and I know that Jeremy thinks that they *are* family. I also appreciate the help and friendship of Remo and Hanni. I thank both my parents and my sisters and brother for their encouragement and interest in my work.

Many thanks to Jeremy, Sarah, Tim and Blue for their love and furriness. I appreciated their ability to reduce my stress level – at least when they weren't adding to it. They provided much needed laughter and diversions from my work.

Most of all I want to thank Bruce Worden for his love and support. Bruce is always willing to listen to my crazy scientific ideas as well as my joys and complaints. I probably never would have survived Caltech without his friendship and understanding.

This work was supported by NASA grant numbers **NAG5-1132** and **NAG5-842**.

To *Helen Abernathy*

Abstract

Andrea Donnellan, Ph.D.

California Institute of Technology 1992

The Ventura basin lies within the north-south compressive western Transverse Ranges in southern California. The basin is characterized by rapid north-south convergence on geologic time-scales, with Quaternary rates of convergence across the basin estimated to be approximately 20 mm/yr. Global Positioning System (GPS) observations carried out over a period of 2.7 years suggest rapid rates of convergence of 7 ± 2 mm/yr on geodetic time scales. The deformation corresponds to a maximum shear strain rate of 0.6 ± 0.1 μrad/yr with the azimuth of maximum compression oriented N $16° \pm 8°$ W. The dilatation rate of $0.3 \pm .1 \times 10^{-6}\mathrm{yr}^{-1}$ indicates that a significant amount of compression is occurring. The strain rates of 0.1 ± 0.1 μrad/yr south of the basin are much lower. Strain rates calculated from the GPS measurements are consistent with those calculated from comparisons between GPS and historical triangulation data. The deformation in the basin region cannot be modeled as a megashear zone, which best describes much of California.

The observed deformation can be modeled by creep on detachment faults both north and south of the basin. Faults near the surface are most likely locked. Rupture

of the San Cayetano fault within the next 200 years is possible, resulting in an earthquake of moment magnitude 6.0–6.8. Based on the fault models, the south side of the basin is capable of producing a magnitude 5.5–6.0 earthquake. The models of the short-term deformation suggest that the observed rate is consistent with the geologic record, but that the observations have taken place over a small fraction of the earthquake cycle.

Table of Contents

1 Geology, seismology and other notable characteristics of the Ventura basin **1**
1.1 Background 2
1.2 Geologic History of the Basin 8
1.3 Quaternary Geology of the Basin 8
1.4 Seismicity of the Basin 16
1.5 Heat flow and gravity 20
1.6 Geodetic Studies in Areas Surrounding the Ventura Basin 21
1.7 Geodesy in the Basin 29
1.7.1 Measurement of Current Deformation in the Ventura Basin . . 30
1.7.2 Seismic Hazard Assessment 32
1.7.3 Tectonic Footprint of the Santa Paula VLBI site 33

2 Network and data analysis **35**
2.1 Historical Triangulation 35
2.2 Evolution of the Current Network 38
2.3 Description of Monuments and Sites 43
2.4 GPS Data Collection and Analysis 45
2.5 GPS Results 49
2.5.1 October 5-8, 1987 49
2.5.2 April 4-7, 1989 50
2.5.3 June 11-21, 1990 54
2.5.4 May 23-25, 1991 54
2.6 Error Analysis 68

3 Results and Deformation **72**
3.1 GPS results 72
3.1.1 Velocities 73
3.1.2 Strain Calculations 92
3.2 Comparison of Triangulation and GPS 100
3.2.1 Reference Ellipsoids 101

3.2.2 Deflection of the Vertical 102
3.2.3 Lateral Refraction 110
3.2.4 Ties between GPS and Triangulation Sites 113
3.2.5 Results 115

4 Modeling and interpretations **126**
4.1 Consideration of non-tectonic causes 126
4.1.1 Site stability 127
4.1.2 Oil withdrawal 128
4.1.3 The effect of recent large earthquakes 133
4.2 Current Tectonics of the Ventura Basin 138
4.2.1 Fault models 139
4.3 Implications 158
4.3.1 Seismic hazard assessment 158
4.3.2 Santa Paula VLBI Footprint 161
4.3.3 Relation to other observations 166
4.4 Regional setting of the Ventura basin 168

Bibliography **178**

A Method of Processing the GPS Data **185**
A.1 TREX9: October 5-7, 1987 187
A.2 TREX16: April 4-7, 1989 188
A.3 TREX19: June 11-21, 1990 190
A.3.1 Orbits 192
A.4 Caltrans Survey: April 23-25, 1991 196
A.5 GLOBK solution 196

B Results from Data Collected Only in 1990 **200**

C Triangulation Data Used for Strain Calculations **207**

List of Tables

2.1 Station names and four-character identification codes 41
2.2 History of GPS site occupations for the Ventura basin 47

3.1 Velocities of sites relative to HOPP 76
3.2 Velocities of sites relative to SAFE 77
3.3 Strain calculations for the basin and subnetworks both north and south of the basin 96
3.4 Strain calculations for the east and central basin subnetworks 97
3.5 Deflections of the vertical provided by the National Geodetic Survey for the Ventura basin sites and calculated from astronomic observations 109
3.6 Corrections greater than 0.3″ to angles within the Ventura basin triangulation network 111
3.7 Strain calculations from triangulation and GPS measurements for central and eastern regions of the basin and for the region south of the basin 115

4.1 Comparison of results from VLBI and GPS 162

A.1 GPS site occupation history for the Ventura Basin 186
A.2 Coordinates used for the Trex9 orbit improvement 187
A.3 Fiducial data used for orbit determination during Trex16 189
A.4 Coordinates used for the Trex16 orbit determination 189
A.5 Summary of which stations were sampled under compact format and which were sampled under Trimble standard format 191
A.6 Days of the fiducial data used for calculating the orbits for Trex19 . 194
A.7 Geocentric (spherical) coordinates used to constrain the orbits of the satellites during Trex19 197
A.8 Sites used in the 1991 solution 197
A.9 Coordinates used for the Caltrans orbit improvement 197
A.10 Constraints applied to the stations 198
A.11 Stochastic orbit specifications 199

C.1 History of triangulation for the east-central part of the Ventura basin, near Fillmore, and the observed directions 208
C.2 History of triangulation for the eastern Ventura basin and the observed directions 209
C.3 History of triangulation directly south of the Ventura basin and the observed directions 212
C.4 Directions calculated from the GPS observations 216
C.5 Deflection of the vertical applied to each direction for the strain calculations 218

List of Figures

1.1 Map showing the location of the Ventura basin relative to southern California 5
1.2 Subdivisions of the Ventura Basin and regional faults 6
1.3 North-south cross-section near Fillmore showing faults dipping north and south, away from the basin 7
1.4 Cross-section showing the Oak Ridge as a fault-propagation fold . . . 11
1.5 Cross-section through the central Ventura basin showing the Sisar decollement 14
1.6 Contour map showing the maximum depth of seismicity in the Ventura basin region 18
1.7 Seismicity map of southern California showing the lower number of earthquakes occurring in the eastern Ventura basin 19
1.8 Summary of principal strains calculated from geodetic results near the Ventura basin 22
1.9 Leveling lines showing differential uplift in the western part of the Ventura Basin 27

2.1 Ventura basin network. 40
2.2 Repeatability plots for the 1987 experiment 51
2.3 Repeatability plots for the 1989 experiment 55
2.4 Repeatability plots for the 1990 experiment 61
2.5 Component of repeatability by baseline length 69
2.6 Component of repeatability by component offset 70

3.1 Velocities of sites relative to HOPP 74
3.2 Velocities of sites relative to SAFE 75
3.3 Baseline component versus time plots for all data with at least two epochs of measurements 80
3.4 Shaded zones mark the various regions for the strain calculations . . 94
3.5 Arrows showing the principal compression and extension strain axes 98
3.6 Arrows showing the principal compression and extension strain axes for the region near the Ventura basin 99

3.7 Correction, A_{ij}, for various values of the elevation angle between stations, β, and the deflection of the vertical normal to the line, ζ . . 105
3.8 Model used to calculated the deflection of the vertical north and south of the basin 107
3.9 Bouguer anomalies resulting from the presence of the Ventura basin and the depression of the Moho by the Western Transverse Ranges . 108
3.10 Residual plots for the region south of the Ventura basin 117
3.11 Residual plots for the east-central region of the Ventura basin 118
3.12 Residual plots for the eastern region of the Ventura basin 119
3.13 Residual plots for the total Ventura basin 122

4.1 Cross-section through the south mountain oil field 131
4.2 Predicted displacements of the Kern County earthquake 135
4.3 Predicted displacements of the San Fernando earthquake 137
4.4 Velocities of the stations minus the predicted motion from the San Andreas, Garlock, and Big Pine faults. 140
4.5 Map showing cross-section A–A' used for the dislocation calculations 142
4.6 a) Fault model used for the dislocation calculations. b) Observed and modeled horizontal displacements relative to HOPP 144
4.7 a) Fault model used for the dislocation calculations. b) Observed and modeled horizontal displacements relative to HOPP 147
4.8 Effect on the velocity profile from varying dips on a fault that extends to 1 km from the surface 149
4.9 Effect on the velocity profile from varying dips on a fault that extends to 5 km from the surface 150
4.10 Effect on the velocity profile from varying depths 151
4.11 Focal mechanisms for events from 15-20 km near the Ventura basin . 155
4.12 Focal mechanisms for events from 20-25 km near the Ventura basin . 156
4.13 Focal mechanisms for events from 25-30 km near the Ventura basin . 157
4.14 Plots showing baseline component changes with time of Palos Verdes relative to Mojave 163
4.15 Plots showing baseline component changes with time of Palos Verdes relative to Mojave 164
4.16 Velocities of sites in the western Transverse Ranges 170
4.17 Velocities of sites in the western Transverse Ranges calculated from the *Eberhart-Phillips et al.* [1990] model of creep at depth on the San Andreas, Garlock and Big Pine faults 171
4.18 Residual velocities in the western Transverse Ranges of the difference between the observed velocities and the *Eberhart-Phillips et al.* [1990] model 172

4.19 Cartoon of block motions relative to Palos Verdes (PVER) south of the San Andreas fault 174

A.1 Sky plot of the satellite tracks during June 11-12, 1990 from 19:18 to 3:02 UTC 193

B.1 Repeatability plots of stations not shown in Chapter 2 for the 1990 experiment 201

Generations come and generations go,

but the earth remains forever.

—OLD TESTAMENT, NIV, *Ecclesiastes 1:4*

Chapter 1

Geology, seismology and other notable characteristics of the Ventura basin

California is marked by the boundary between the Pacific and North American plates. Motion between these plates has formed a complex tectonic environment in southern California. The development of precise space-based and ground-based geodetic techniques has made it possible to measure crustal deformation over the order of a few years to several decades. Measurement of crustal deformation can be integrated with other geological and geophysical observations to improve understanding of a tectonic regime.

Many geodetic networks exist in southern California. As resources have become more available, many of these networks have been refined or expanded, thus improving the tectonic understanding of the region. The Ventura basin, located about 60 km northwest of Los Angeles, is a region inferred to be actively deforming. Because of the apparent rapid deformation and the lack of any geodetic studies of the Ventura

basin, we chose to implement a network to measure the deformation of the basin and surrounding region. To carry out the study, we used the Global Positioning System (GPS), a precise relative positioning space-geodetic technique

1.1 Background

Southern California lies within a complex tectonic environment. Two major tectonic features run through the region: the San Andreas fault and the east-west trending Transverse Ranges. The San Andreas fault is a major continental transform fault that originates at the Gulf of California spreading center. It strikes in a northwesterly direction towards the Transverse Ranges, where it changes strike at the southern bend [*Hill*, 1982] to a more westerly direction. It then returns to its typical strike of N35°W north of the western Transverse Ranges at what is termed the "big bend" of the San Andreas [*Hill and Dibblee*, 1953]. South of the Transverse Ranges, several strike-slip faults parallel the San Andreas. The major faults west of the San Andreas are the San Jacinto, Elsinore, and Newport-Inglewood faults. These faults are fairly evenly spaced at a distance of about 50 km between faults. Slip rates become progressively less on each fault westward from the San Andreas. A summation of slip rates across this region [*Weldon and Humphreys*, 1986] does not account for the full Pacific-North American plate motion of 48 mm/yr, oriented N 35° ± 2° W [*DeMets et al.*, 1987]. Because of the discrepancy between the plate motion rate and summation of known slip rates across faults in southern California, *Weldon and Humphreys* [1986] suggest that a significant amount of deformation must be occurring offshore in the continental borderland of southern California. Recent geodetic measurements of the continental

borderland suggest an offshore strike-slip rate of 8 ± 3 mm/yr relative to the coast, accounting for most of the missing plate motion [*Larson* 1990].

Where the San Andreas strikes more westerly, the Transverse Ranges are a prominent tectonic feature. They comprise a north-south compressive regime, and are characterized primarily by east-west trending thrust faults and folds. It is near the two bends of the San Andreas fault that compression seems to be currently taking place. A considerable amount of northwest convergence, on the order of 25 mm/yr [*Weldon and Humphreys*, 1986], is occurring in the eastern Transverse Ranges, near the southern bend of the San Andreas fault [*Allen*, 1957; *Bird and Rosenstock*, 1984]. Geologic evidence indicates that very little convergence is currently taking place throughout the central Transverse Ranges [*Weldon and Humphreys*, 1986] where most of the active deformation is strike-slip, parallel to the San Andreas fault [*Weldon*, 1985]. The western Transverse Ranges are undergoing convergence at a rate of approximately 23 mm/yr, similar to the rate in the eastern Transverse Ranges [*Namson and Davis*, 1988; *Yeats*, 1983]. We note here that, just to the east of the big bend, the northeast trending, left-lateral, strike-slip Garlock fault is truncated by the San Andreas fault. In the Ventura basin, just south of the big bend of the San Andreas, convergence rates of approximately 23 mm/yr of north-south shortening are inferred from the geology [*Yeats*, 1983]. Only through the western Transverse Ranges are *Weldon and Humphreys* [1986] able to fit the plate motion by integrating slip rates on faults. Their transect includes the Ventura basin.

The Ventura basin is an east-west trending trough located in the western Transverse Ranges (figure 1.1). The basin is situated approximately 60 km south of the

big bend of the San Andreas fault, and about 50 km south of the confluence of the Garlock and San Andreas faults. Between these faults and the Ventura basin, the mountains, which exceed elevations of 2500 m (8000 feet), are among the highest in the Transverse Ranges, aside from San Jacinto and San Gorgonio peaks near the southern bend of the San Andreas fault. The Ventura basin is very low, narrow, and flat, and elevations reach only about to 80 m (300 feet).

While the surface elevation of the basin is not very high, the thickness of the basin is extraordinary. This was recognized as early as 1936 when *Reed and Hollister* [1936] estimated a thickness of 12–21 km (40,000–68,000 feet) of the "sedimentary blanket" of the Ventura basin, by measuring the mean thicknesses of beds exposed both north and south of the basin. Even the minimum thickness that *Reed and Hollister* [1936] assign to the section is still quite thick for a basin that is only about 10 km wide. A more recent estimate of the thickness of the sedimentary section within the basin is 17.7 km (58,000 feet), with 15 km of the 17.7 km being deposited during the Cenozoic era [*Norris and Webb*, 1990].

The center trough of the Ventura basin is a synclinal structure. It is is bounded on the north by the east-west striking San Cayetano thrust fault and on the south by the Oak Ridge, an anticlinal structure overlying the Oak Ridge fault. The western portion of the basin opens up into the Oxnard Plain and is bounded on the north by the Red Mountain thrust fault (figure 1.2). The bounding thrust faults dip away from the basin (figure 1.3).

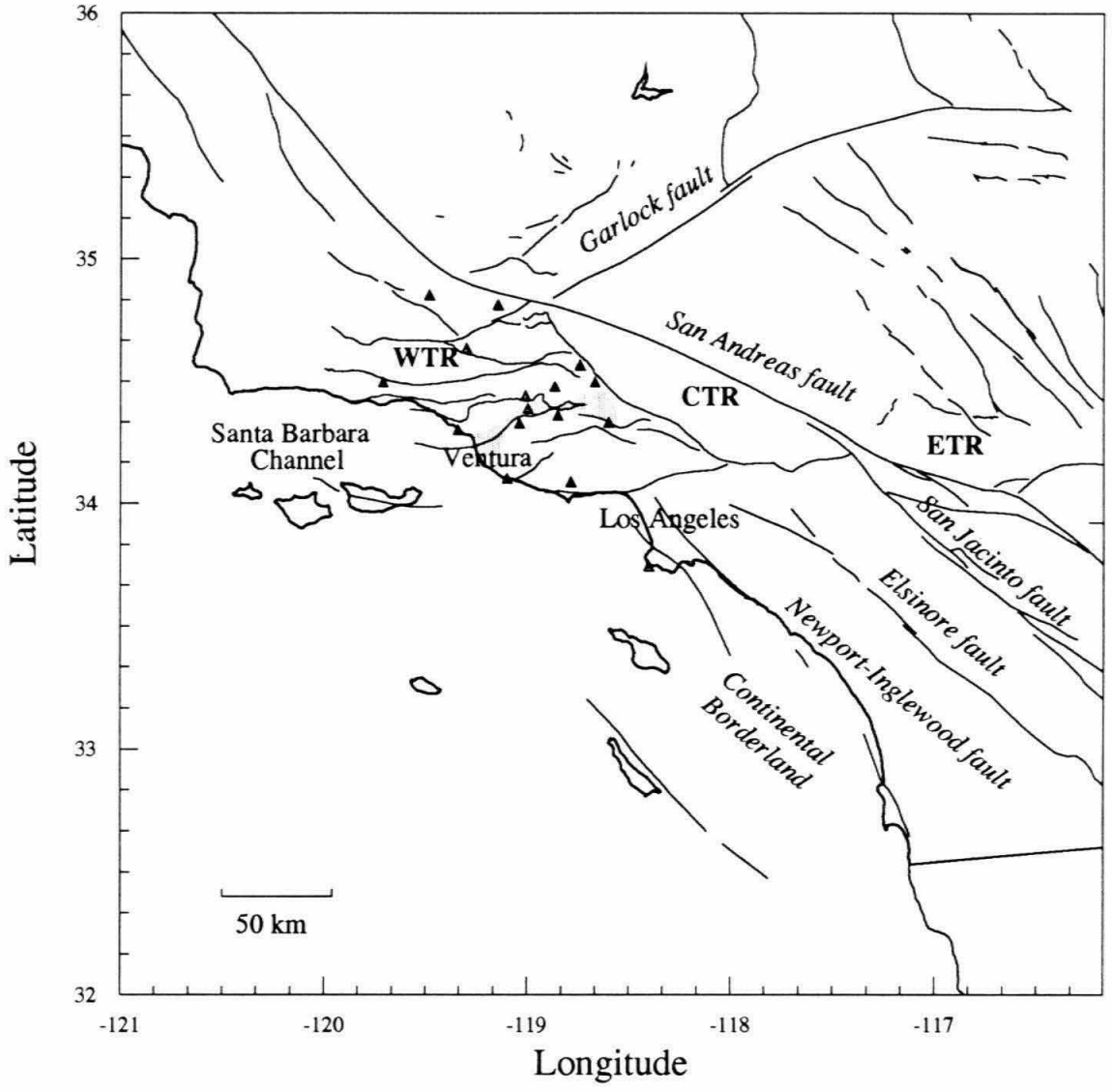

Figure 1.1: Map showing the location of the Ventura basin relative to southern California. The basin is within the gray area north and east of the town of Ventura. WTR–western Transverse Ranges, CTR–central Transverse Ranges, ETR–eastern Transverse Ranges.

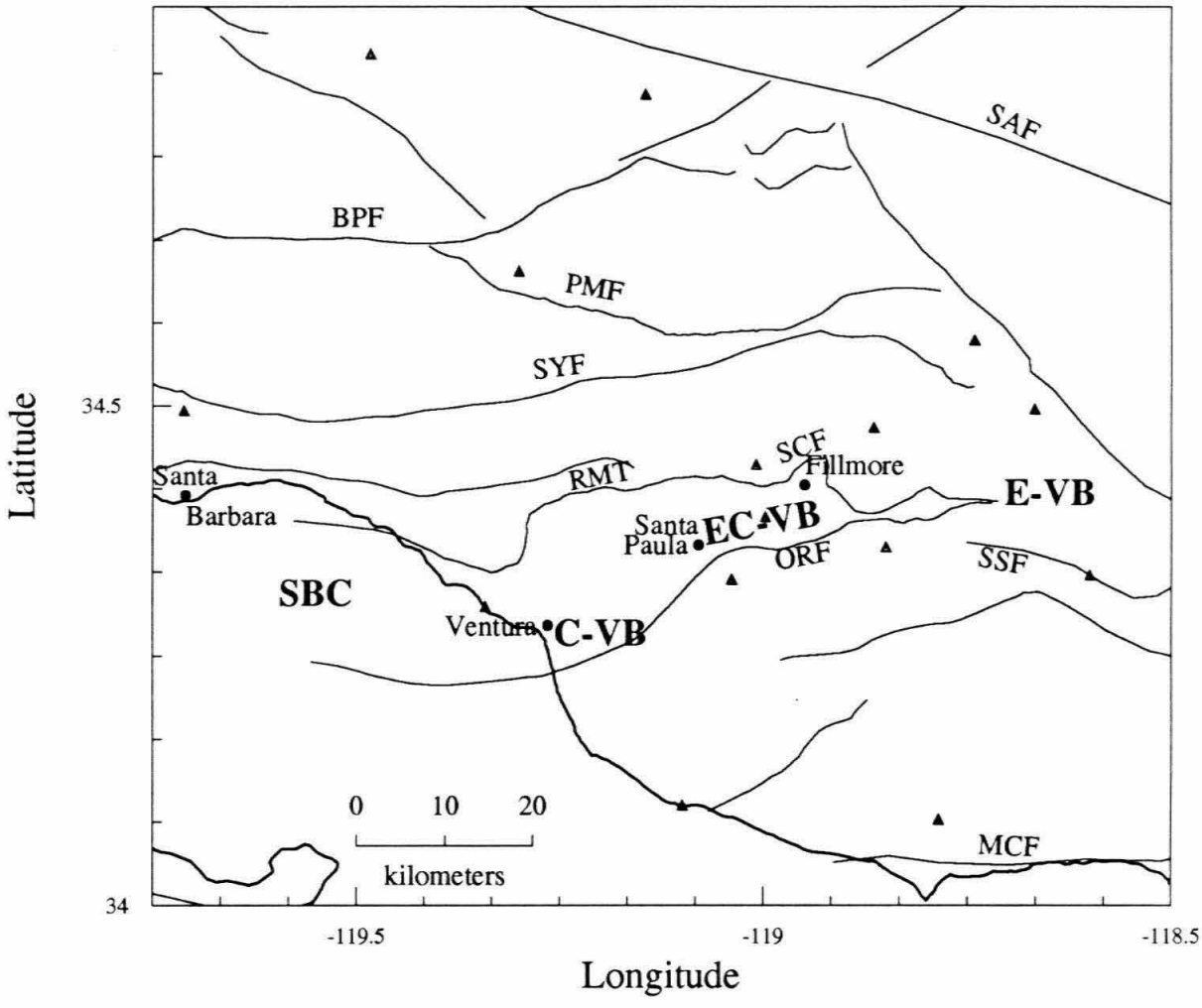

Figure 1.2: Subdivisions of the Ventura Basin and regional faults. SAF–San Andreas fault, BPF–Big Pine fault, PMF–Pine Mountain fault, SYF–Santa Ynez Fault, RMT–Red Mountain Thrust fault, SCF–San Cayetano fault, ORF–Oak Ridge fault, SSF–Santa Susana fault, MCF–Malibu Coast fault. **SBC**–Santa Barbara Channel, **C-VB**–central Ventura basin, **EC-VB**–east-central Ventura basin, **E-VB**–east Ventura basin. Triangles mark the geodetic network of this study.

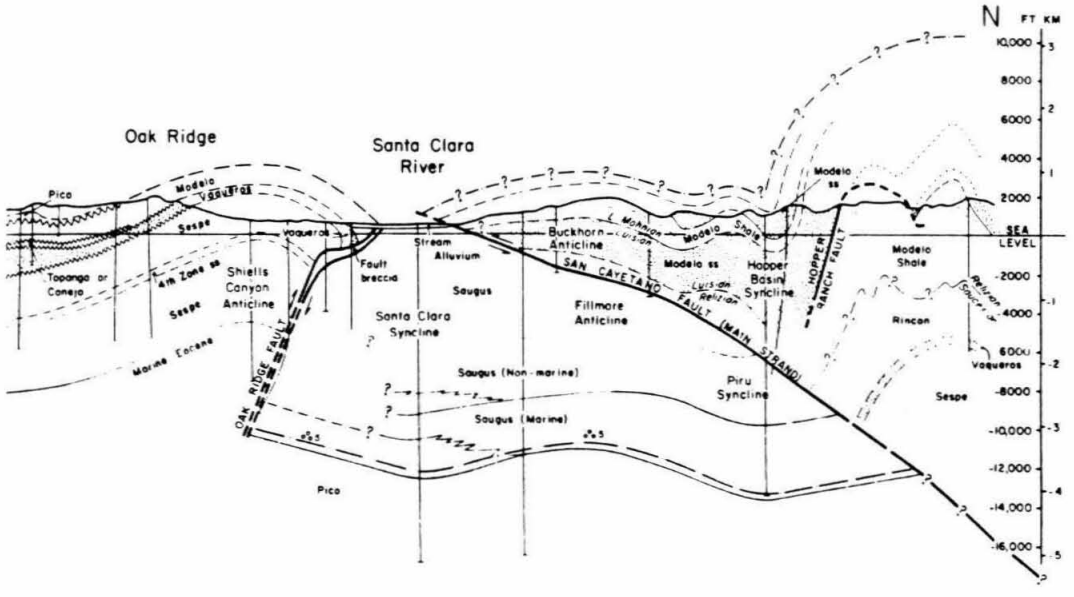

Figure 1.3: North-south cross-section near Fillmore showing faults dipping north and south, away from the basin. North is to the right in the figure. [From *Yeats*, 1983].

1.2 Geologic History of the Basin

The Ventura basin originated as a foredeep some 400 km south of its present location [*Crowell*, 1987]. Subduction of the East Pacific Rise during the late Cretaceous and early Tertiary created a foredeep basin in which the first sediments were deposited into what are now the San Joaquin, Los Angeles, and Ventura basins. In the early Miocene (22 m.y.), crustal stretching and breaking replaced subduction, forming the individual basins. At around 6 m.y. rapid subsidence was renewed and the surface of the Ventura basin may have reached 1.5 km (5,000 feet) below sea level. This provided a deep basin, in which great thicknesses of Pliocene sediments could be deposited. The current compressive regime began to form during the middle Pleistocene as the area experienced uplift, folding and faulting [*Norris and Webb*, 1990].

1.3 Quaternary Geology of the Basin

Yeats [1983] and *Çemen* [1989] divide the Ventura basin into three parts: offshore, central and eastern (figure 1.2). Although we maintain their divisions, we further subdivide the basin in terms of the observed deformation rates. The central Ventura basin encompasses the area surrounding the town of Ventura. The east-central Ventura basin lies in the Fillmore/Santa Paula area. Unlike the central portion of the basin, the east-central basin is very narrow. The San Cayetano fault, on the north, and the Oak Ridge fault, to the south, pinch the basin and are less than 3 km apart at their closest point, which is just east of the town of Fillmore (figure 1.2). The basin opens out in the eastern Ventura basin. The San Cayetano fault is not exposed on

the north side of the basin, and the Santa Susana fault marks the southern boundary of the eastern Ventura basin. The mountains bounding the basin reach elevations of 1650 m on the north side and 1100 m on the south side. The basin itself, being filled with sediments, is quite flat. We will sometimes refer to the offshore Ventura Basin as the Santa Barbara Channel.

Large displacements on faults in the Ventura basin have been inferred by several geologists, and high rates of north-south convergence across the basin have been determined [*Yeats*, 1983, *Rockwell*, 1988, *Çemen*, 1989]. *Yeats* [1983] discusses large-scale Quaternary detachments in the basin. Quaternary rates of convergence across the central Ventura basin, near the town of Ventura, are estimated at 23 mm/yr for the last 200,000 years [*Yeats*, 1983]. In the central part of the basin, between Fillmore and Piru (about 13 kilometers east of SNPA), *Yeats* [1983] calculates the minimum rate of convergence to be 12 mm/yr and the maximum rate of 58 mm/yr. *Yeats* [1983] arrives at the 23 mm/yr estimate of convergence by comparison to the rates determined elsewhere in the basin, and by the Pacific-North American plate motion.

The pinching of the east-central Ventura basin can be explained by differential motion along the north-dipping San Cayetano fault. *Rockwell* [1988] presents a detailed study of displacements on this fault and shows that dip-slip motions on the fault increase towards the east. Dip-slip motions are 1.1 $\pm$ 0.2 mm/yr, near the western end of the fault, and increase to the east *Rockwell* [1988]. The maximum displacement rate is measured at Timber Canyon about 8 km west of Fillmore, where the displacement rate is 8.8 $\pm$ 2.0 mm/yr. Displacement rates are not determined

east of this area, but dip-slip separations become progressively less eastward along the San Cayetano fault until it dies out about 7 km east of Fillmore [*Çemen*, 1989].

The Oak Ridge fault on the south side of the basin also dies out near the east end of the San Cayetano fault, and both faults end in a synclinal structure [*Çemen*, 1989]. *Çemen* [1989] interprets this change in environment from faulting to folding as due to the two faults becoming younger to the east.

Dips of beds at the surface, and well data, show that the Oak Ridge on the south side of the basin is an anticlinal structure [*Yeats*, 1983]. The structure of the fold matches the structure of a fault-propagation fold [*Suppe and Medwedeff*, 1990]. By using theory for both fixed-axis and constant-thickness fault-propagation folding, *Suppe and Medwedeff* [1990] infer that a low angle decollement ramps to about 5 km underneath the southern margin of the Oak Ridge. The extension of the fault dips more steeply underneath the Oak Ridge and terminates at a depth of 3 kilometers (figure 1.4). (Constant-thickness theory requires conservation of bed thickness and length. Fixed-axis theory allows for change in thickness of the beds in the steeply dipping limb while the axial surface of the fold remains constant [*Suppe and Medwedeff*, 1990].)

The Saugus formation can be found directly under alluvium in the Santa Clara River valley (east-central Ventura basin) and just south of the Oak Ridge. Near Santa Paula, *Yeats* [1988] projected the Saugus formation above the Oak Ridge by following the dips of beds within the ridge. He measured a vertical offset of 2240–2345 m between the projection of the Saugus formation, at the top of the Oak Ridge, and beds within the Santa Clara River valley (within the Ventura basin). The age of

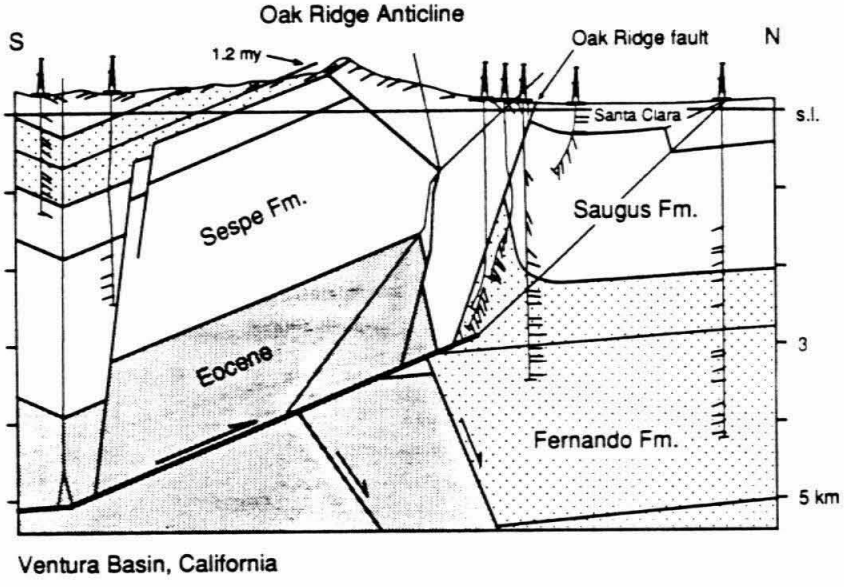

Figure 1.4: Cross-section showing the Oak Ridge as a fault-propagation fold. The heavy line marks the propagating fault. Slip goes to zero at the fault tip and deformation is accommodated by folding above the tip. [From *Suppe and Medwedeff*, 1990].

the top of the Saugus is between 0.2 and 0.4 m.y. Based on the measured offset and the age of the Saugus formation, the average rate of uplift of the Oak Ridge would be 5.75–11.5 mm/yr. *Yeats* [1988] places all of the long-term deformation on the Oak Ridge fault at a displacement rate of 5.9–12.5 mm/yr. *Suppe and Medwedeff* [1990] claim that the Oak Ridge fault is a pre-existing normal fault, because unfolding of the Oak Ridge leaves the fault with an original dip of 65° north, but they allow that the fault may have undergone minor reactivation.

The offset of the projected beds at the fault, from *Yeats'* [1988] section, is only 855 m. In this case, the average rate of displacement on the Oak Ridge fault during the last 0.2–0.4 m.y. is 2.3–4.6 mm/yr. *Yeats* [1988] extends the Oak Ridge fault to 5 km depth, while *Suppe and Medwedeff* [1990] truncate the south dipping section at 3 km by the active decollement. *Yeats* [1988] justifies using the separation between the top of the Saugus formation at the crest of the Oak Ridge and the basin because he interprets folding of beds near the faults as drag folds and shallow features. With this interpretation the beds would not be folded at depths of 5 km. If the fault, in its present form, only extends to 3 km, reactivated displacement on the fault is likely to be low.

The possibility of the Oak Ridge fault being an active fault should not be overlooked, however. The rate of 2.3–4.6 mm/yr is only an average rate for the last 0.2–0.4 m.y. Rates are higher if the fault has been recently activated. In *Suppe and Medwedeff's* [1990] cross-section the tip of the propagating decollement is very near the Oak Ridge fault, indicating that it has only recently cut through the fault (figure 1.4). In western Taiwan normal faults play a major role in causing inter-

ruptions of fault-propagation folding in the form of folding and thrust ramps [*Suppe*, 1986]. The Oak Ridge fault might also play an important part in altering decollement tectonics of the Ventura basin region.

The west end of the Oak Ridge terminates at the Oxnard Plain, about 15 km east of the town of Ventura. A boundary extends from this point northward in which decollement tectonics are transferred from the Oak Ridge to the Sisar decollement, which runs under the basin west of the Oak Ridge [*Yeats et al.*, 1988]. The Sisar decollement is present in a ductile Miocene shale and mudstone layer [*Yeats et al.*, 1988]. Below the decollement are flat-lying layers, while rootless folds, such as the Ventura Avenue anticline, are present above [*Yeats et al.*, 1988; *Namson and Davis*, 1988; *Rockwell et al.*, 1988]. The decollement ramps up to the surface at Sulfur Mountain (figure 1.5). It is possible that the presence of the Oak Ridge fault as an old normal fault might cause the change in the nature of the decollement further east in the Ventura basin. It also may be that a change in facies of the decollement layer, from shale and mudstone, to interbedded sandstone and shale, further east, causes the change. The interbedded sandstone and shale layers may increase the strength of the strata and force the deformation elsewhere [*Yeats et al.*, 1988]. Perhaps both possibilities are controlling factors.

Shortening of the Ventura Avenue anticline above the Sisar decollement has been taking place at an average rate of 9 mm/yr, during the past 0.2 m.y. [*Rockwell et al.*, 1988]. The rise and fall of sea level during this time period has made it possible to locate and date Pleistocene river terraces on the anticline. The rate of uplift of the fold may have slowed from a rate of 14 mm/yr to 2 mm/yr during the past 0.2 m.y.

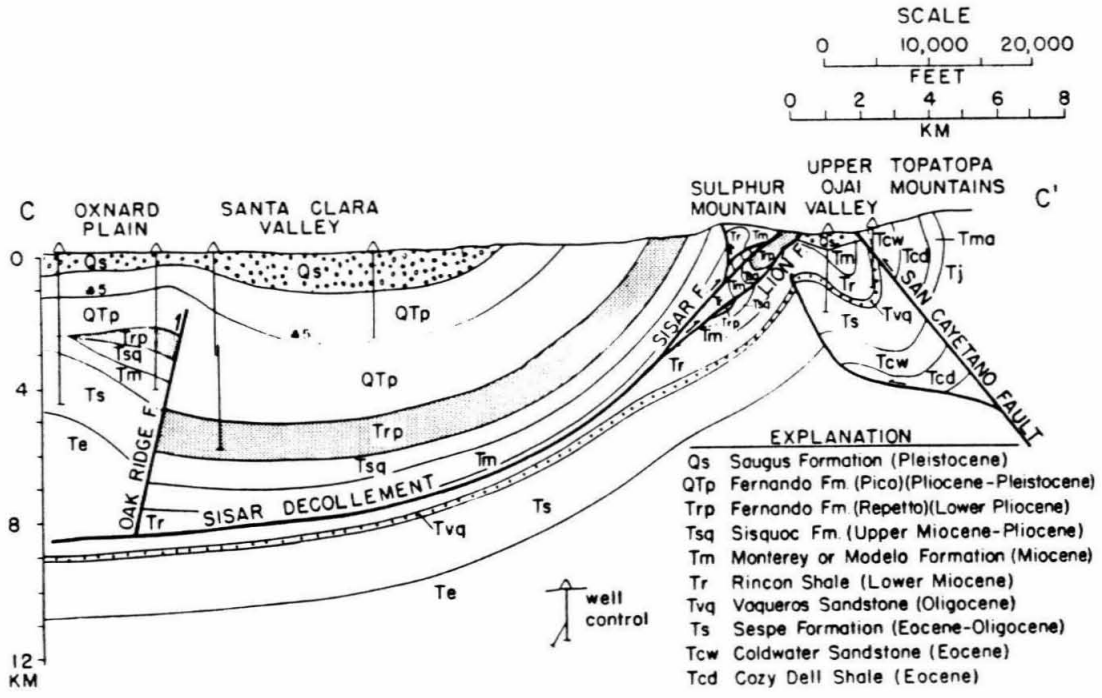

Figure 1.5: Cross-section through the central Ventura basin showing the Sisar decollement. [From *Yeats et al.*, 1988].

Rockwell et al. [1988]. The rate of horizontal shortening has also decreased from 20 mm/yr, during the period of 200–80 k.y., to 5 mm/yr for the past 30 k.y. For a constant rate of tectonic shortening the uplift rate should decrease through time, as shown in a mathematical formulation of the mechanics of flexural folding [*Rockwell et al.*, 1988]. The decrease in the rate of horizontal shortening suggests that the tectonic deformation across the fold is not uniform in time. Vertical displacement of the steeply north-dipping Ventura fault, at the south limb of the anticline, compensates for the decrease in deformation of the fold itself [*Yerkes et al.*, 1987]. *Rockwell et al.* [1988] agree with other workers that a decollement under the Ventura Avenue anticline is likely, and, from their model, calculate an average rate of slip on the decollement of 7.7–10.1 mm/yr.

Dates on offset marine terraces that cross the Red Mountain thrust fault near the northwest limb of the Ventura Avenue anticline indicate that average rates of slip during the last 0.5 m.y. were 0.5–1.6 mm/yr [*Sarna-Wojcicki et al.*, 1979]. Closer to the axis, and the center of the anticline, interpretation of subsurface data implies 13 mm/yr vertical uplift along the fault [*Sarna-Wojcicki et al.*, 1979]. The subsurface well data imply 5.5 km of stratigraphic separation on this part of the fault [*Yeats et al*, 1987]. *Rockwell et al.* [1984] dated river terraces approximately 10 km north of the Ventura Avenue anticline and north of the Red Mountain fault. The terraces do not show evidence for tilting, and rates of uplift vary from 0.3–1.1 mm/yr, which are lower than for the Ventura Avenue anticline. Interpretation of these results implies that, on geologic time-scales of tens of thousands of years, the tectonic deformation has been confined to a fairly narrow zone across the central Ventura basin.

At the east end of the basin the Santa Susana fault bounds the southern margin of the eastern Oak Ridge [*Reed and Hollister*, 1936]. The Santa Susana fault is a north-dipping thrust fault that begins its exposure where the San Cayetano and Oak Ridge faults die out. Measurement of displacement rates on the fault is difficult because the fault is largely a bedding plane fault. Even so, a stratigraphic separation of 4 km is measured at one point on the fault [*Yeats*, 1987]. There is no evidence of Holocene rupture of the fault, but the far eastern zone ruptured in association with the 1971 San Fernando earthquake [*Yeats*, 1987]. *Yeats* [1987] estimates that the Santa Susana fault is characterized by brittle failure at depth, which is propagated to the surface on the order of thousands of years. Trenching studies indicate that, in at least one place, the most likely age of displacement on the fault is greater than 10,000 years [*Lung and Weick*, 1987].

1.4 Seismicity of the Basin

Current crustal deformation, as indicated by the geologic record, is occurring across the Ventura basin and across the westward extension of the basin. A map of focal mechanisms of earthquakes from 1970–1975 provides similar evidence for such deformation [*Yerkes and Lee*, 1979]. Ninety percent of the events occurred south of the Santa Ynez fault [*Yerkes and Lee*, 1987]. The depths of the earthquakes north of the San Cayetano and Red Mountain faults are generally greater than 10 km. Cross-sections of seismicity indicate that these events occur on north-dipping thrust faults. Two of those events are interpreted to have occurred on the San Cayetano fault, while four events occurred on the Red Mountain fault [*Yerkes and Lee*, 1987].

P axes from earthquakes in and around the Ventura basin region trend north [*Yerkes and Lee*, 1987], although they are somewhat variable (figures 4.11–4.13). Of the 50 most reliably located earthquakes, in the period from 1970–1975, nearly all indicate thrust events [*Yerkes and Lee*, 1979]. In some cases slip, with a left-lateral sense, accompanies the reverse slip. The north-south orientation of *P* axes is consistent with north-south compression found in the central Transverse Ranges [*Webb and Kanamori*, 1985].

One remarkable feature of the Ventura Basin is that earthquakes occur there to depths greater than 28 km, much deeper than elsewhere in southern California. Contours of maximum depths of earthquakes form ellipses with the major axes following the trend of the Ventura basin (figure 1.6). They form a bull's eye about the center of the Ventura Basin near Santa Paula. *Yerkes and Lee* [1987] observed that the deepest earthquakes, in their study, occurred along this same trend in the Santa Barbara Channel and Oxnard plain. Earthquakes in the Channel were reliably located to 19 km, and to 17 km in the Oxnard plain.

Although many earthquakes have been located near the Ventura basin, the seismicity is much lower near the eastern basin than elsewhere in southern California (figure 1.7). In 200 years of record keeping, no major earthquake has been recorded in the Ventura basin [*Yeats*, 1988].

One interesting feature of the deepest earthquakes in the basin and Santa Barbara Channel is that the focal mechanisms show normal faulting [*Bryant and Jones*, Caltech, USGS, personal communication]. The nodal planes of the normal events strike north-south, indicating east-west extension. These events have been recorded

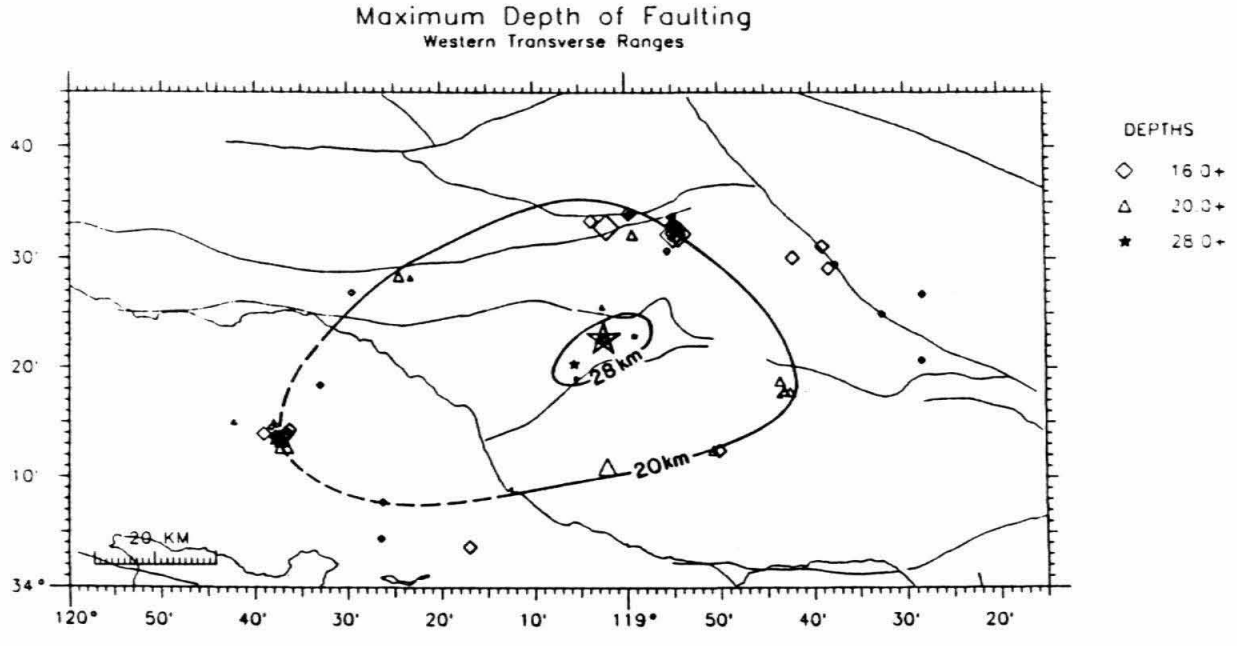

Figure 1.6: Contour map showing the maximum depth of seismicity in the Ventura basin region. [From *Bryant and Jones*, 1991].

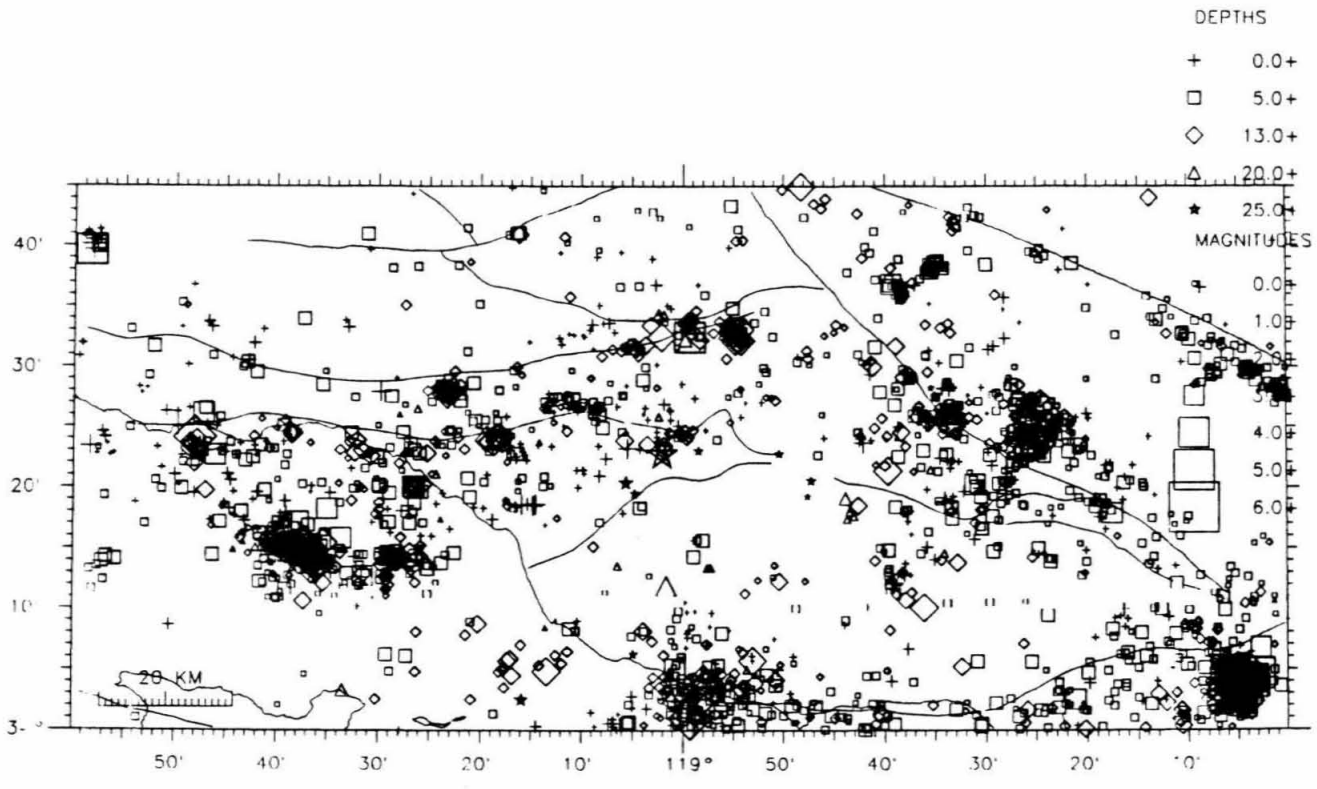

Figure 1.7: Seismicity map of southern California showing the lower number of earthquakes occurring in the eastern Ventura basin. [Courtesy *Steven A. Bryant*, Southern California Seismographic Network, operated by the USGS and Caltech, personal communication.]

near Santa Paula (large star, figure 1.6) and in the Channel between the town of Santa Barbara and Santa Cruz Island. Mechanisms offshore are less reliable, however, due to a poor velocity model there [*Bryant and Jones*, Caltech, USGS, personal communication].

Many of the deeper events may identify a mid-crustal decollement that originates at the brittle-ductile transition [*Anderson*, 1971]. *Hadley and Kanamori* [1978] observed that low-angle reverse mechanisms occurred at the depth of the seismogenic zone, near the epicenter of the 1971 San Fernando earthquake, in the west-central Transverse Ranges. Several deep mechanisms provide evidence of a regional decollement in the western Transverse Ranges [*Webb and Kanamori*, 1985]. The depths of the subhorizontal mechanisms range from 8–15 km. Outside the Ventura basin the depth of the seismogenic zone is approximately 15 km [*Webb and Kanamori*, 1985]. In general, slip vectors for the earthquakes are northward near the coast, and southward north of the coast, of the hanging wall relative to the footwall.

1.5 Heat flow and gravity

Both geologic and seismological studies provide evidence for a very deep Ventura basin. The sedimentary section is extremely thick (15–20 km) and the basin is brittle to depths as great as 28 km, suggesting that the basin is low-density and cold relative to the surrounding region. Evidence of these characteristics is also present in both heat flow and gravity data.

An isostatic gravity map of southern California [*Roberts et al.*, 1981] shows gravity anomalies for all of the Miocene basins in southern California [*Luyendyk and*

Hornafius, 1987]. The Ventura basin shows an anomaly of −60 mgal, the most pronounced anomaly in southern California. Other large anomalies range from −25 to −35 mgal for locations such as the Santa Maria and Los Angeles basins. The anomaly may correspond to a sediment thickness of 3600–14,300 m for sedimentary/crystalline density contrasts of 0.4 g/cm^3 or contrasts between sediments of 0.1 g/cm^3 [*Luyendyk and Hornafius*, 1987].

Heat flow in the Ventura basin (48 mW/m^2) is lower than determined elsewhere in southern California (70 mW/m^2) [*DeRito et al.*, 1989]. The heat flow in the Fillmore-Santa Paula area is particularly anomalous and the temperature gradient to 750 m is depressed. The unusual gradient near Fillmore is still enigmatic, but the overall low heat flow of the basin can be explained by rapid deposition of cold sediments during the Cenozoic [*DeRito et al.*, 1988].

1.6 Geodetic Studies in Areas Surrounding the Ventura Basin

Several geodetic networks of varying types surround the Ventura basin. The observed patterns of crustal deformation in these networks provide insight toward understanding deformation of the basin region (figure 1.8).

The Los Padres and Tehachapi trilateration networks lie to the north of the Ventura basin. Data from these networks, established by the USGS, span the period 1973–1987 [*Eberhart-Phillips et al.*, 1990]. The southern margin of the Los Padres network lies along the northern boundary of the central Ventura basin. The network extends north to the big bend region of the San Andreas fault. The Tehachapi network spans both the San Andreas fault, east of the big bend, and the Garlock fault.

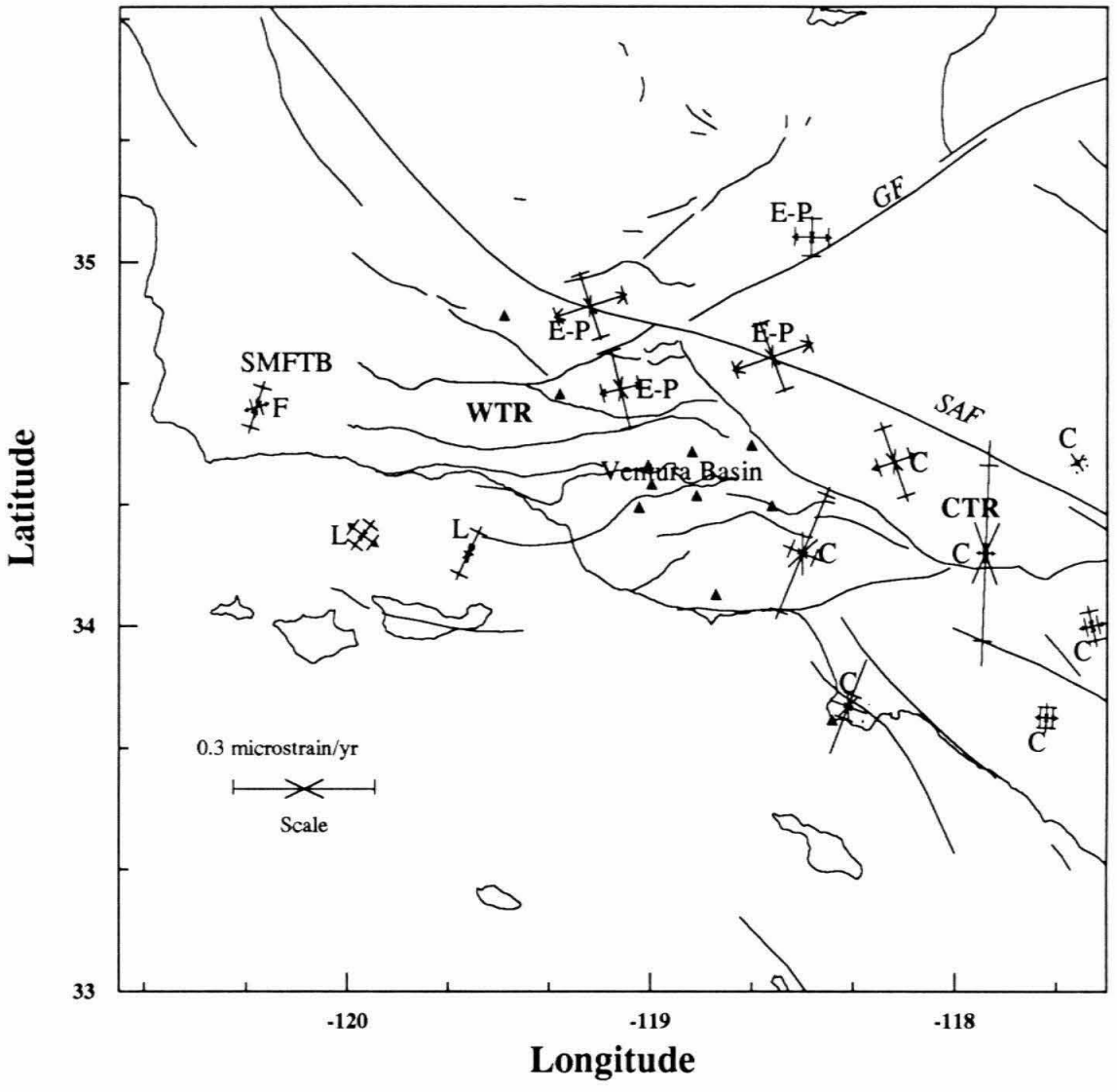

Figure 1.8: Summary of principal strains calculated from geodetic results near the Ventura basin. The cross marks on the axes represent the standard error of the strain component. *GF*–Garlock fault, *SAF*–San Andreas fault, **WTR**–western Transverse Ranges, **CTR**–central Transverse Ranges, SMFTB–Santa Maria fold and thrust belt, F–*Feigl et al.*, [1990], L–*Larsen* [1991], E-P–*Eberhart-Phillips et al.*, [1990], C–*Cline et al*, [1984].

The axis of maximum shear strain (0.38 ± 0.02 μrad/yr oriented N 63° W) is subparallel to the San Andreas within 10 km of the fault. 15 to 70 km away from the San Andreas fault the maximum shear strain (0.19 ± 0.01 μrad/yr) is oriented N 44° W, similar to the plate motion direction [*Eberhart-Phillips et al.*, 1990]. This change in shear orientation implies a component of compression normal to the San Andreas fault, but *Eberhart-Phillips et al.* [1990] find negligible dilatation within the two networks. The Los Padres network, with sites west of the big bend excluded, shows the most compressive dilatation of -0.10 ± 0.02 μstrain/yr. All other subnetworks have dilatation ranging from -0.02 ± 0.01 to 0.02 ± 0.01 μstrain/yr. The network spans a zone of about 40 km across the western Transverse Ranges, resulting in about 7 mm/yr of north-south contraction. This is 10 mm/yr less than the most conservative geologic estimate of convergence across the western Transverse Ranges [*Namson and Davis*, 1988]. The additional component of compression must lie somewhere outside the Los Padres and Tehachapi networks. In order to fit the plate motion, *Weldon and Humphreys* [1986] require 15 mm/yr of convergence through the western Transverse Ranges south of the Big Pine fault. The additional compression must be occurring to the north or to the south of the Los Padres network.

The eastern Santa Barbara Channel may accommodate some of the short-term north-south compression that is not observed in the Los-Padres network. By comparing Global Positioning System (GPS) data and trilateration data, *Larsen* [1991] estimated that 6.4 mm/yr of almost pure compression, oriented N 25° E, must be occurring across the eastern Santa Barbara Channel. Dilatation is significant at 0.12 ± 0.04 μstrain/yr. The maximum shear strain rate is 0.16 ± 0.03 μstrain/yr.

The central Santa Barbara Channel shows a marked difference from the eastern Channel in that the strain is accommodated by shear rather than compression. The dilatation is near zero and the maximum shear strain rate is $0.19 \pm .03$ μstrain/yr [*Larsen*, 1991]. The strain pattern is consistent with both earthquake focal mechanisms and bathymetry of the Santa Barbara Channel [*Larsen*, 1991]. There must be some transfer of compressive strain away from the Channel elsewhere or a change to a strike-slip environment.

It is possible that the zone of compression migrates north towards the mountains in the far western region of the Transverse Ranges. Two years between GPS measurements show that a site just north of the town of Santa Barbara (La Cumbre Peak) is moving 6.9 ± 2 mm/yr in a direction S $17° \pm 10°$ W relative to a station near Point Arguello (VNDN), at the far western end of the Santa Barbara Channel. This is supported by sixteen years between GPS and trilateration [*Larson*, 1990]. More recent GPS measurements indicate that La Cumbre Peak is moving at rate of $7.7 \pm 0.6 mm/yr$ S $25° \pm 7°$ W relative to Vandenberg [*Murray*, 1991]. Vandenberg (VNDN) shows little motion relative to Santa Cruz Island at the southern margin of the channel. Continuation of the compressive strain would require that the zone of compression be situated north of Pt. Arguello, most likely in the Santa Maria fold and thrust belt.

Further west, in the Santa Maria fold and thrust belt, *Feigl et al.* [1990] calculated a maximum shear strain of 0.19 ± 0.01 μrad/yr, from triangulation, trilateration and GPS data. This is similar to measurements of maximum shear strain found elsewhere in southern California. The maximum compression calculated from the data is $0.13 \pm$

0.03 μstrain/yr oriented N 17° E. The dilatation (-0.07 ± 0.05 μstrain/yr) shows that some compression oriented N-NE may be occurring in the Santa Maria fold and thrust belt. *Feigl et al.* [1990] infer 6 ± 2 mm/yr of crustal shortening along an axis oriented N 30° E, and 3 ± 1 mm/yr of right-lateral shear across that axis.

Interpretation of the above results suggests that a zone of compression steps down from the Santa Maria fold and thrust belt, near the town of Santa Barbara, into the eastern Santa Barbara Channel. Along this entire zone the crustal shortening occurs at a rate of 6–7 mm/yr. Projection of this zone of convergence eastward would place it in the region of the Ventura basin. The Ventura basin lies just south of the Los Padres trilateration network, which shows little evidence of compression. There is also no resolvable deformation of the Oxnard plain, directly south of the Ventura basin [*Webb*, 1991]. It is possible, then, that the Ventura basin is accommodating a significant amount of compression in the short term.

Just west of the Ventura Basin, uplift seems to be occurring most rapidly along the coast rather than inland towards the mountains [*Buchanan-Banks et al.*, 1975]. Figure 1.9 shows two leveling profiles reduced by *Buchanan-Banks et al.* [1975]. The first profile runs northwest up the coast from the Ventura Basin and the second runs north from Ventura, through Ojai to the Munson Creek fault. For data spanning 1920–1968, the average tilt across the first profile is 13 μrad. This is derived from an uplift of 244 mm of the northwest end of the line relative to I 30 (figure 1.9). Assuming no variations temporally, this difference corresponds to an uplift rate of 4 mm/yr along the coast west of Ventura. Along the north-south line the uplift rate is 2 mm/yr. These results suggest that much of the current deformation occurs near

the coast. The workers have inferred from the data that the Red Mountain fault is currently the most active fault in the area of study. Extrapolating the observed uplift eastward into the Ventura Basin suggests that the northern part of the basin should also be active and show deformation detectable by geodetic techniques.

Over a period of 120 years considerable triangulation, trilateration and astronomic azimuth data were collected in the vicinity of the Los Angeles basin. The National Geodetic Survey (NGS) launched a program, termed REDEAM (REgional Deformation of the EArth Models), to produce a model of crustal deformation for the Los Angeles region that accounts for both spatial and temporal variations in strain [*Cline et al.*, 1984]. The region of this study includes the area between the San Gabriel segment of the San Andreas fault and the coast, and was divided into eight subregions. Strain parameters were calculated for these regions [*Cline et al.*, 1984]. Compressional areas trend along the southern margin of the Transverse Ranges, while the rest of the region can be described by shear. The authors caution that scale biases, from combining different trilateration surveys, may affect the dilatational components of the strain tensor. The shear components of the strain tensor and orientation of shear are not affected by scale biases and are therefore more reliable [*Cline et al.*, 1984]. As in the Los Padres trilateration network, the direction of maximum shear strain parallels the San Andreas fault close to the fault (N 64° $\pm$ 3° W), and is closer to the plate motion away from the fault (N 24°–42° W). The highest shear strain rates are measured along the southern margin of the Transverse Ranges (0.58 ± 0.12 μrad/yr) and along the San Andreas fault (0.30 ± 0.03 μstrain/yr). The rate of shear near the San Andreas fault is similar to that obtained further northwest

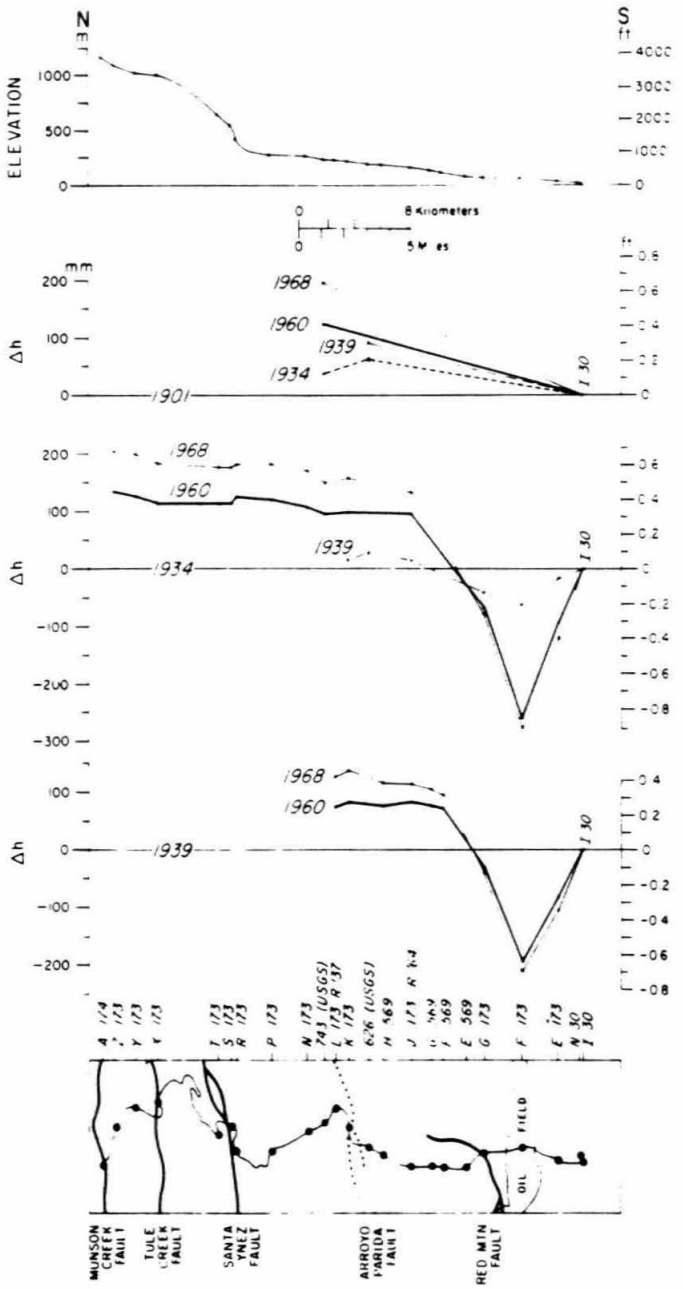

Figure 1.9: Leveling lines showing differential uplift in the western part of the Ventura Basin. [From *Buchanan-Banks et al.*, 1975].

in the Los Padres-Tehachapi networks.

Because north-south compression is indicated at the southern margin of the Transverse Ranges, both east and west of the Ventura basin area, it is probable that convergence is also taking place in or near the Ventura basin. The lack of significant dilatation in the Los Padres trilateration network implies that a convergent zone must exist south of the network if the present-day strain rate matches the geologic record.

Since 1985, mobile Very Long Baseline Interferometry (VLBI) data have been collected for a sparse distribution of sites in and near the western Transverse Ranges. One of the sites, SANP (SANta Paula), is situated within the east-central Ventura basin just north of the centerline of the basin. Unfortunately, the site was observed fairly infrequently during the period 1985–1990, and rate determinations for this site differ depending upon the analysis. For example, *Ward* [1990] discusses a preliminary analysis, by NASA/GSFC, of VLBI data collected through February 1989. In this analysis, the site SANP is moving at a rate of 6 ± 2 mm/yr south and 4 ± 2 mm/yr west with respect to the site on the Palos Verdes peninsula. On the other hand, *Herring* [MIT, personal communication, 1991] analyzed the VLBI data through 1990 and obtained a velocity of SANP relative to PVER of 2 ± 1 mm/yr and 0 ± 1 mm/yr, south and east respectively. Evaluation of the same data by the Goddard Space Flight Center shows a rate of 5.0 ± 1.5 mm/yr south and -0.3 ± 1.1 mm/yr west of SANP relative to PVER (*Chopo Ma*, NASA/GSFC, written communication).

The VLBI data in their present state appear to be inadequate for determining whether any compressive strain is accumulating north or south of the SANP mark or

across the entire Ventura basin at all. A more detailed geodetic network is necessary to understand the deformation pattern in the region of the Ventura basin.

1.7 Geodesy in the Basin

As previously discussed, the present Ventura Basin is characterized by high rates of convergence taken up by both thrust faults and folds, but the rates are not well constrained. Such high rates can be detected with geodetic techniques. First order triangulation provides an accuracy of 0.7″ [*Gossett*, 1959] or about 50 mm on baselines of 15 km. Thus, only a decade of time is required to observe rates of 10–20 mm/yr across the central part of the Ventura basin, assuming such rates exist and that they are fairly uniform in time. The Global Positioning System (GPS) provides much higher accuracies of 5–10 mm over 100 km [e.g., *Dong and Bock*, 1987]. One to two years of repeated GPS measurements should be sufficient to resolve the 10–20 mm/yr of convergence in the basin if the short-term strain rate is similar to the long-term strain rate. Space geodetic techniques can address several problems, since all components of the displacement field are solved for in a reference frame external to the network. In this thesis we address three tectonic problems of the Ventura Basin area. The first is to measure and interpret the present-day deformation of the basin. Second, we will address the seismic hazard of the basin. The third goal is to measure the deformation around the Santa Paula (SANP) VLBI site, referred to as a footprint, to place the site within its tectonic setting.

1.7.1 Measurement of Current Deformation in the Ventura Basin

The rates mentioned above that have been geologically determined are long-term averages. The rate that *Yeats* [1983] estimates for convergence in the Ventura Basin is an average rate over the last 200,000 years. The rate given by *Namson and Davis* [1988] is the average rate over the last 2–3 m.y. We compare the geology and the geodesy to test whether the rates measured over the last several years with geodetic techniques are representative of the geologic rates. If the geology and the geodesy do not match, any of three factors might account for the discrepancy. It is possible that the current average rate is simply not the same as the previous rate. Perhaps the interpretation of the geology over- or underestimates the rate of convergence across the basin or western Transverse Ranges. It is more likely, however, that the two types of measurements do not agree because the displacements are not temporally uniform. A large earthquake could make up any deficiencies in the convergence rate. Of course, site instabilities can also contribute to differences between geologic and apparent geodetic rates. We will examine the possibility of site instabilities in the Ventura basin network.

Estimating the spatial distribution of the deformation is also important in the comparison between the geology and geodesy. *Namson and Davis* [1988] have estimated a geologic rate of convergence of 17–26 mm/yr across a north-south cross-section of the Transverse Ranges, and *Yeats* [1983] has inferred that over the last 200,000 years the convergence across the Ventura basin is of a similar rate. It is possible, then, that most or all of the north-south convergence is accommodated at the southern edge of the western Transverse Ranges. Geodetic and other geologic

studies provide evidence for a zone of crustal shortening at the southern edge of the western Transverse Ranges. We will examine whether the spatial distribution of the deformation within the Ventura basin is similar to the deformation west of the basin, and if the current pattern of deformation matches that inferred from the geologic record.

GPS provides a direct measurement of relative site velocities in a global reference frame. Because of this, we can directly measure rotations of the crust. Paleomagnetic observations have been used to show that clockwise rotations on the order of 5°/m.y. have occurred on geologic time-scales in the western Transverse Ranges [*Hornafius*, 1985; *Kamerling and Luyendyk*, 1985]. *Jackson and Molnar* [1990] propose that clockwise block rotations must still be occurring within the western Transverse Ranges. They base their idea on slip vectors from major earthquakes and observations from VLBI measurements spanning a period of five years. *Jackson and Molnar* [1990] go on to propose, as a mechanism for the rotations, that the blocks of crust are moving as if carried passively by a continuously deforming substratum. *Jackson and Molnar* [1990] detail several mechanisms that could cause rotations about vertical axes and assess the likelihood of each mechanism accounting for the observed rotations. The observations that these workers use to choose the most appropriate mechanism are fairly limited. Their hypothesis is based on focal mechanisms of four large earthquakes in the area and on two VLBI vectors, one measured at the western margin of their area of study and one on the eastern side of the western Transverse Ranges. The geodetic network that we occupied is a far more detailed network in *Jackson and Molnar's* [1990] area of study, so we will be better able to constrain

kinematic models of the area based on velocity vectors obtained from GPS over a period of 2.7 years.

1.7.2 Seismic Hazard Assessment

Geology and geodesy can be compared to estimate the seismic hazard in the Ventura basin. According to *Wesnousky* [1986], the Ventura basin, along with the San Andreas and San Jacinto faults, should have the most frequent occurrence of potentially destructive strong ground motions in southern California. In 200 years of record keeping, however, there have been no large earthquakes in the Ventura basin [*Yeats*, 1988]. Although there have been no large earthquakes within the Ventura basin historically, the basin has been surrounded by large earthquakes very recently. The magnitude 6.5 1971 San Fernando earthquake occurred along the eastern extension of the basin [*e.g., Heaton*, 1982]. The magnitude 7.2 Kern County earthquake occurred in 1952 about 40 kilometers due north of the Ventura Basin [e.g., *Stein and Thatcher*, 1981]. In 1926 and 1978 earthquakes occurred west of Santa Barbara [e.g., *Corbett and Johnson*, 1982]. Both the Kern County and the San Fernando earthquakes were thrust events with left-lateral components. A similar event might occur within the Ventura Basin. We assess the possibility of such an event by comparing the geodesy and geology and by modeling the observed displacements.

Understanding the spatial distribution of the deformation is important to assessing the seismic hazard of the Ventura basin. If all of the deformation is occurring in a narrow zone it is possible that creep is occurring on a fault, or faults, near the surface. This could lower the hazard, because elastic strain might not be accumulating. Rather, aseismic flexural slip between beds during folding might accommodate the

strain. A broad zone of deformation, on the other hand, might indicate that strain is accumulating and that faults are locked near the surface.

1.7.3 Tectonic Footprint of the Santa Paula VLBI site

Tectonic interpretations from VLBI results are based on data collected at widely separated sites. In southern California, VLBI baseline lengths are on the order of 100–200 km. Understanding the deformation between those sites is essential to developing accurate tectonic models. This deformation can occur on any scale, ranging from a few centimeters to tens of kilometers. Small-scale deformation can arise from site instabilities and larger scale deformation patterns may result from the tectonic environment. Understanding the velocity of a site in terms of its environment is referred to as *footprinting.* Two types of footprints apply to geodesy. The first is a site stability footprint and the second is a tectonic footprint. Our goal is to footprint the Santa Paula VLBI site, located in the east-central Ventura basin.

Site stability footprints are important to assure the geodetic integrity of observations at a given site [*Bell et al.*, 1991]. If a site is locally unstable, rates obtained between that site and others are inadequate for determining tectonic motion. NASA has set forth guidelines for this type of footprint. Footprint sites must not cross any faults, so that tectonic motion is not confused with motion due to an unstable site [*Bell*, NASA/GSFC, personal communication]. Baselines should be short. NASA will implement a site stability footprint around the Santa Paula VLBI mark.

We will focus on the tectonic footprint of the Santa Paula VLBI mark. A tectonic footprint measures the local strain field so that motion of a monument can be understood on regional scales [*Bell et al.*, 1991]. (When we refer to footprint without

a modifier we are referring to a tectonic footprint.)

Throughout most of this chapter we have been discussing evidence for compression along the southern margin of the western Transverse Ranges. Velocities from 5.5 years of VLBI data fit a model in which California is a shear zone between the North American and Pacific plates [*Ward*, 1988]. The Santa Paula VLBI mark (SANP) was not used in the above model, but the rate of motion of Santa Paula (SANP) relative to the Palos Verdes peninsula (PVER), obtained by *Herring* [MIT, personal communication, 1991], is consistent with the model. *Ward's* [1990] rate, however, indicates convergence and left-lateral shear between the two sites. In terms of modeling the plate boundary as a megashear zone, SANP could be viewed as an outlier if *Ward's* [1990] results are used in the analysis. On the other hand, Herring's rate may fit the model well, but a compressional zone across the Ventura basin may be completely missed. Understanding the local deformation around the site is important for interpreting the larger-scale results. While VLBI data collected from sites separated by 100–200 km may be adequate for modeling the gross structure between the Pacific and North American plates, more detail is required to understand the finer scale pattern of deformation.

Chapter 2

Network and data analysis

Because the Ventura basin is inferred to be so tectonically active, geodetic studies, carried out over of a few years, could provide useful insight into the current characteristics of the basin. As mentioned in Chapter 1, the Global Positioning System (GPS) provides accuracy of horizontal baseline measurements on the order of 5–10 mm [e.g., *Dong and Bock*, 1989; Dixon et al, 1990]. This should be sufficient to estimate the velocity distribution and patterns of strain in and near the Ventura basin. Over a period of 2.7 years we collected three epochs of GPS measurements from a network that spans the Ventura basin. In addition, we used historical triangulation measurements to obtain an estimate of the strain field over a 28–100 year period of time.

2.1 Historical Triangulation

Prior to the development of electronic distance measurement (EDM), station coordinates were calculated from a technique called *triangulation.* *Gosset* [1959] described

triangulation as follows:

> Geodetic triangulation is a very efficient method of controlling surveys over extensive areas of the earth's surface and is utilized in the basic horizontal control networks of the major countries of the world. Triangulation is a method of surveying in which the stations are points on the ground at vertices of triangles forming chains or networks. In these triangles, the angles are observed instrumentally, and the sides are determined by successive computations through the chains of triangles from selected triangle sides called base lines, the lengths of which are obtained from direct measurements on the ground. Triangulation in which the figure and size of the earth are taken into account is called geodetic triangulation. The highest form of survey engineering is involved in geodetic triangulation, necessitating extremely precise instrumental equipment and observational techniques, capable and conscientious personnel, and detailed computations [*Gosset*, 1959].

Triangulation was widely used to establish a horizontal control network for the United States. The value of using triangulation to measure earth movements was recognized after the 1906 San Francisco earthquake [*Hayford and Baldwin*, 1907]. During the first half of this century, triangulation monuments were reoccupied approximately once a decade in an attempt to measure crustal deformation throughout California [*Hager et al.*, 1991]. Two of these stations are on the southern margin of the Ventura basin and a third near the coast south of the basin. The National Geodetic Survey (NGS) added other marks near the basin to the horizontal control

network in the 1930's and 1950's.

First order triangulation was subject to strict controls by the U. S. Coast and Geodetic Survey (now the National Geodetic Survey (NGS)). Because triangulation is a line-of-sight method, interstation visibility is required. In mountainous southern California this necessitated that most sites be established on peaks. Line lengths between monuments were to be 4–10 miles (6.5–16.1 km). Workers observed at night by positioning the theodolite at one station and sighting on lamps at other stations. Night observations were made in order to avoid horizontal refraction from differential temperature effects [*Gossett*, 1959]. According to *Bomford* [1971], in mountainous terrain, horizontal refraction is smallest at sunrise and sunset, and of opposite sign during the day and night. We will explore the problems of lateral refraction later. Twelve sets of directions to each station were measured. Any direction that deviated from the mean by more than $4''$ was thrown out and reobserved. A direction is a measurement from the theodolite to a single station; an angle is the difference of directions between two stations. Rounds of angles that best closed to 360° plus the spherical eccentricity were retained. Occasionally a light was not visible and the work was completed at a later time. For first order triangulation a direction generally carries an error of $0.7''$ [*Gossett*, 1959] or $0.85''$ for an angle.

Beginning in 1932, a series of first-order triangulation measurements were carried out across the Ventura basin as part of the National Geodetic Survey's (NGS) first-order adjustment of California (tables C.1–C.2). Directly south of the basin angles between stations were observed five times from 1898–1968 (table C.3). Although triangulation maintains an accuracy of 4 parts in 10^6 ($0.85''$) the long time history

makes it possible to recover information about crustal deformation of the region. Unfortunately, triangulation across the west-central Ventura basin is woefully sparse and monuments have been destroyed. We were able to recover triangulation in the east-central and eastern Ventura basin, however, which is the region of the basin inferred to be the most actively deforming. We added a longer time history to our GPS study by occupying historical triangulation stations. By comparing angles calculated from GPS with historical triangulation data we could improve our understanding of strain across the basin by verifying the GPS results. We will discuss the problems we encountered in a later section. Triangulation data exist somewhat sparsely to the north of the Ventura basin, so we will rely primarily on trilateration results of others to examine the crustal deformation in that region.

2.2 Evolution of the Current Network

Geologic and other studies indicate that the Ventura basin is a rapidly deforming region. Previous geodetic studies did not focus on the Ventura basin, and the current distribution of strain across the basin was not well understood. If the deformation in the basin is as rapid as suggested, only a short period of time should be required to constrain the rate and nature of deformation. During 1986–1991 a consortium of Caltech, MIT, Scripps and UCLA was collecting GPS data as part of a study to measure crustal deformation in Southern California. In 1987 we piggybacked, onto the larger one, an experiment that focused on the Ventura basin. Our goal was to compare historical triangulation with results from GPS to measure the strain across the basin. Although funds, time and personnel were limited we were able to obtain

interesting results from the experiment and also establish an adequate network for future studies.

In order to test for deformation across the Ventura basin after the first epoch of GPS measurements, we chose sites where data from triangulation surveys existed. This placed limits on our choice of stations because many of the original horizontal control marks were destroyed. In some cases our stations occupy marks near the original mark and we have chosen to rely on geodetic ties to recover the historical triangulation. Our original network spanned the geologically most active part of the basin and was comprised of 6 sites (figure 2.1, table 2.1). During all of our GPS occupations we collected data at the Very Long Baseline Interferometry (VLBI) station Palos Verdes (PVER) in order to have a common reference for the observations. Coincident with our 1987 measurements, a mark on Castro Peak (CATO) was also occupied. This proved to be fortuitous and we have occupied that site in subsequent observations.

After comparing the 1987 GPS results to the historical triangulation data we detected considerable strain across the basin. We discuss details of this comparison in future sections, but will note it here because of the role these results played in planning future experiments. Although our results showed high rates of convergence across the Ventura basin, we were unable to determine whether these results were due to tectonic or other effects. Better spatial control around the basin would enable us to assess whether we were observing local effects. We therefore added two stations north of the basin in 1989 and continued to observe at the station CATO (figure 2.1). The additional stations are Yam 2 (YAM2), in the Cuyama Valley, and Munson (MUNS)

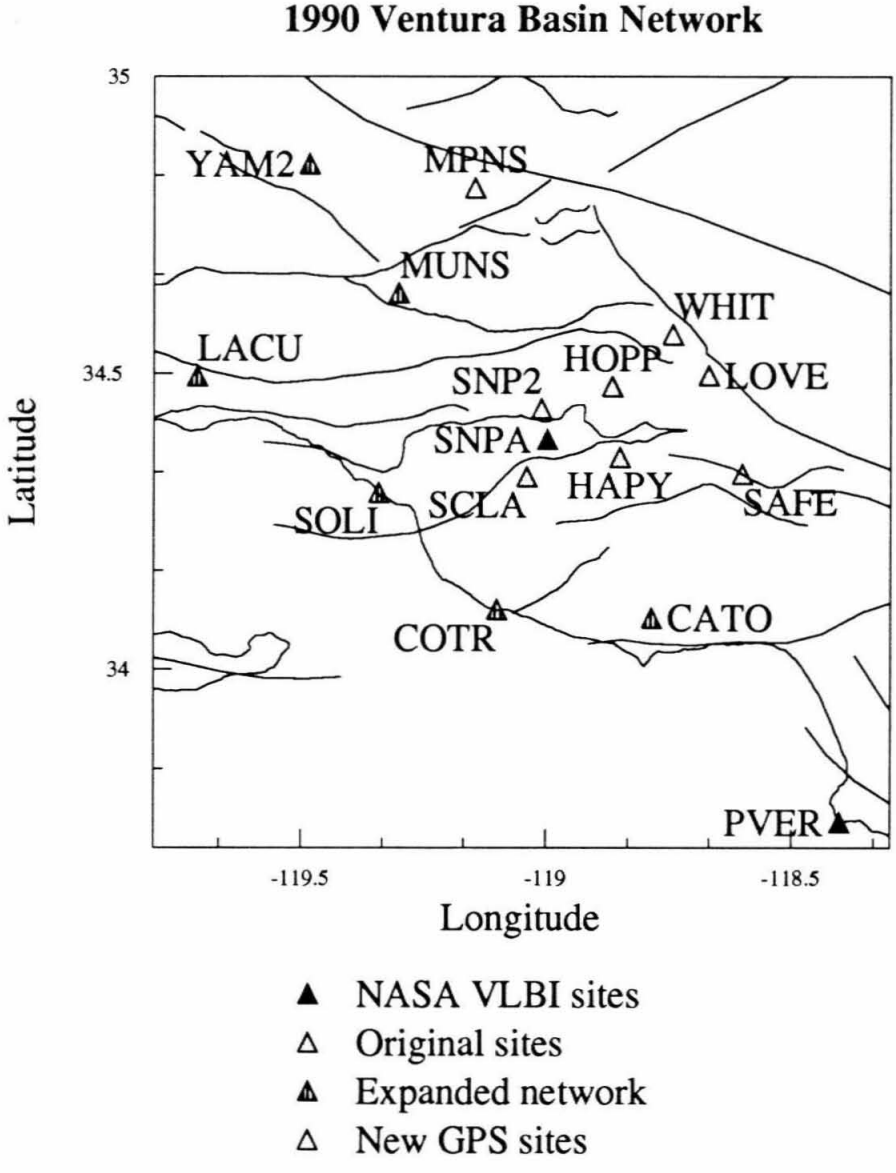

Figure 2.1: Ventura basin network.

site ID	Stamping	Location	Latitude	Longitude
CATO	Solstice B2 aux 66	Castro Peak	34.086	-118.786
COTR	None	Pac. Miss. Test Cen.	34.1	-119.1
HAPY	Happy	Happy Peak	34.358	-118.850
HOPP	Hopper 1941	Hopper Mountain	34.478	-118.866
LACU	none	La Cumbre Peak	34.495	-119.712
LOVE	Loma Verde Reset 1963	Loma Verde Peak	34.496	- 118.669
MUNS	Munson TPC 1971	Pine Ridge	34.636	-119.301
MPNS	Mount Pinos 1941	Mount Piños	34.812	-119.145
PVER	Palos Verdes aries 1976	Rancho Palos Verdes	33.743	- 118.403
SAFE	Pico L9C (LAC)	Oat Mountain	34.330	-118.601
SCLA	Santa Clara 1898	Santa Clara Peak	34.326	-119.039
SNPA	Santa Paula NCMN 1981	Toland Road	34.388	-118.998
SNP2	Santa Paula 1941	Santa Paula Peak	34.440	-119.010
SOLI	Solimar 1974	Ventura	34.298	-119.342
WHIT	Whitaker 1964 A-7A	Whitaker Peak	34.566	-118.742
YAM2	USGS 2749 ft.	Cuyama Ranger St.	34.853	-119.483

Table 2.1: Station names and four-character identification codes. Approximate location is given. Tables of the fiducial stations used are in Appendix A.

located on the ridge of Pine Mountain. Neither of the northern sites are historical triangulation sites.

During the 1990 experiment we expanded our network considerably. We reobserved all previous Ventura basin sites and added new sites, in order to tie the basin network into surrounding geodetic networks and add better spatial control. We occupied the stations La Cumbre Peak (LACU), Cotar (COTR) and Solimar (SOLI), which are part of the southern California GPS network. These stations were previously occupied with GPS, making it possible to assess deformation across the western margin of the Ventura basin. The two additional sites, which were not measured previously with GPS, are Mount Piños (MPNS) and Whitaker Peak (WHIT). These stations are part of the USGS Los Padres and Tehachapi trilateration networks [*Eberhart-Phillips et al.*, 1990], which tie the Ventura basin network into the USGS networks north of the basin. Subsequent measurements at these sites will provide rates of deformation north of the eastern Ventura basin.

The Santa Paula VLBI site (SANP/SNPA) is situated in the center of the Ventura basin. We occupied the site in 1989 and 1990. (When referring to GPS observations from the mark we will refer to the site as SNPA. We will refer to this mark as SANP when discussing VLBI observations.) We also designed the Ventura basin network as a tectonic footprint around the Santa Paula VLBI (SANP) mark. Santa Paula (SNPA) lies within possibly the most active part of the Ventura basin and is just south of the surface expression of the San Cayetano Fault. We designed the 1990 network to provide complete coverage around the Santa Paula VLBI mark. Because Santa Paula (SNPA) is the only mark occupied within the basin, it is also important

for determining the partitioning of strain across the basin.

2.3 Description of Monuments and Sites

Because we are looking for baseline length changes of millimeters to centimeters, site stability is of the utmost importance. A variety of organizations monumented the sites that we used so different sites meet different specifications.

All of the sites used for historical triangulation are first order monuments. As mentioned before, these sites are all located on peaks. Each of the monuments is placed in sedimentary bedrock. The first order triangulation monuments are brass disks, 90 mm in diameter. The shank of the mark is 25 mm in diameter and 80 mm long. A wedge is inserted into a slit in the lower edge of the shank so that it bulges at the bottom when driven into a drill hole [*Mitchell*, 1936]. Other marks consist of a brass rod two feet long and four inches in diameter, set in a tile pipe and encased in concrete. The mountains in this network are rapidly eroding; some of the sites have been eroded to the point of being unstable and thus unusable. Before occupying any of the monuments, we examined them closely to assure ourselves that the bedrock was stable.

Three of the sites in the network are not located in outcropping bedrock but are driven to the point of refusal. These are Cotar, located at the Pacific Missile Test Center, the Santa Paula VLBI (SNPA) monument and the site Yam 2 (YAM2). Cotar (COTR) is situated a few hundred meters from the ocean, in a sandy swampy area on the Oxnard Plain. Pumping of groundwater out of the Oxnard Plain has caused subsidence of the site (*Richard Dixon*, PMTC, personal communication). The

unstable ground around the site, may cause horizontal fluctuations of the site position which should be taken into consideration when interpreting results from that site. The site Santa Paula (SNPA) is located on the northern side of the Ventura basin, on an alluvial fan but the shaft of the monument is driven into bedrock. NASA will be resurveying the monument and the reference marks late in 1991 to test for local site stability. Because the monuments are situated on an alluvial fan, it is possible that the level of the water table might cause fluctuations of the site position. The station Yam 2 (YAM2) located in the Cuyama Valley is a U. S. Geological Survey benchmark. (Benchmarks are vertical control points, rather than horizontal control points.) This mark may also be subject to fluctuations of the water table.

Most of the sites are clear of any obstructions of the sky and are not in close proximity to any objects on the ground. Trees north of Hopper (HOPP) slightly obstruct the site. Santa Clara (SCLA) was situated next to oil tanks during the 1987 experiment and for part of the 1990 experiment. These tanks did not cause multipath problems, however, because a 15 foot tall steel survey tower was still set up over the mark. To occupy this site we set up the antenna on top of the survey tower. This required careful plumbing to the monument 5 meters below. It appears that the presence of the tower did not hamper the GPS observations. The site Castro (CATO) is a less than ideal site in terms of multipath effects. The site is surrounded by a chain link fence about 3 m away from the monument and is also near several sheds. In addition to this, the site shares a hilltop with several radio transmitting antennas. Radio frequency interference, at Castro (CATO), caused us to lose all but one day of data at the site during 1990. Another questionable site in terms of

multipath is Palos Verdes (PVER). During the 1990 experiment heavy equipment was parked near the site. The data at the site appear not to be noticeably affected by signal multipathing, however.

2.4 GPS Data Collection and Analysis

The Global Positioning System (GPS) can be used for high-accuracy relative (vector) positioning at a fairly low cost. GPS is a space-based geodetic technique. Radio signals from orbiting GPS satellites are tracked simultaneously at ground stations and are analyzed to obtain relative positions between the stations. Overviews of GPS applied to crustal deformation studies are presented in *Hager et al.* [1991] and *Dixon* [1991]. Details of the Global Positioning System and methods of analyzing the radio signals are described in *King et al.* [1985] and *Wells* [1987]. *Dong and Bock* [1989], *Feigl* [1991], and *Murray* [1991] discuss the methods we used to process the Ventura basin data. We will briefly discuss the data and methods we used to process the data here, although details of the data processing are presented in Appendix A.

We collected data over a period of days, for eight hour sessions, during each experiment. Several days of data provide checks of repeatability between sites and also allow for improved orbits [*Dong and Bock*, 1989]. The number of days that sites were occupied varied for each experiment (table 2.2). During the first experiment in 1987 we were able to occupy each station for only two days due to limited resources but four days comprised the experiment. During the 1989 experiment we occupied each site for a longer period of time (four days) but limited the number of sites. Our most ambitious experiment was in June of 1990. We occupied each site for a period

of three days, during one of three sub-experiments. In order to tie the network together, we occupied two sites, Santa Paula (SNPA) and Palos Verdes (PVER), during all nine days. In the spring of 1991, Caltrans surveyed Santa Paula (SNPA) and Palos Verdes (PVER) during a readjustment of California. We obtained and processed these data to add strength to the displacement rate between the two sites. Palos Verdes (PVER) was occupied for six hours on days 113 and 114 of 1991 and Santa Paula (SNPA) was occupied for six hours on days 114 and 115.

The data were interactively cleaned to remove cycle slips and "bad" data as described in Appendix A. To improve the orbits we used data from well-located global fiducial sites. We tightly constrained the positions of the global sites to best estimate the six Keplerian orbital elements. We also improved the orbits by using multi-day orbital arcs. We used the improved orbits and the global sites to resolve the integer ambiguities between the satellites and the stations. Properly estimating the number of integer cycles between the stations and satellites significantly improves the east component error [*Dong and Bock*, 1989]. We used a Kalman filter to estimate the site velocities, after solving for the biases (integer ambiguities). The Kalman filter stochastically models the satellite orbits and simultaneously solves for station positions as a function of time using data from all experiments, with the technique described in *Herring et al* [1990].

For the first two experiments (October 1987 and April 1989) we collected data at 30 second intervals. After cleaning the data, we decimated the data by a factor of four, to two minute intervals. For the 1990 experiment we collected data at 15 second intervals and decimated the data by a factor of two, to 30 second intervals,

Site	Oct 87				Apr89				Jun 90A			Jun 90B			Jun 90C		
d	2	2	2	2	0	0	0	0	1	1	1	1	1	1	1	1	1
a	7	7	8	8	9	9	9	9	6	6	6	6	6	6	7	7	7
y	8	9	0	1	4	5	6	7	2	3	4	6	7	8	0	1	2
CATO	X	X			X	X	X	X							X	X	X
HAPY			X	X									X	X			
HOPP			X	X	X	X	X	X				X	X	X			
LOVE	X	X													X	X	X
MUNS					X	X	X	X				X	X	X			
PVER	X	X	X	X	X	X	X	X	X	O	X	X	X	X	X	X	X
SAFE	X	X			X	X	X	X							X	X	X
SCLA			X	X											X	X	X
SNP2				X								X	X	X			
SNPA					X	X	X	X	X	O	X	X	X	X	X	X	X
YAM2						X	X	X	X	O	X						

Table 2.2: History of GPS site occupations for the Ventura basin. O's indicate that the data were not used in the final solution.

after removing cycle slips. For all experiments we performed single-day solutions with the global data included. The orbits we used for these single-day solutions were integrated from the multi-day solutions. We estimated the biases for each day's solution by loosely constraining the orbital elements and by tightly constraining the global tracking stations (see Appendix A). The Kalman filter uses the site estimates and covariances with biases fixed or free to solve for site velocities. We used the bias-fixed solutions for the 1987–1990 experiments.

The constellation that we tracked during the first two experiments was a test constellation made up of seven satellites. The satellites of the test constellation are called Block I satellites. By 1990 the military had launched several Block II satellites in the operational constellation. The clocks of the Block II satellites are subject to dithering, called Selective Availability (S/A). In order to cancel out the effects of the dithered clocks, the GPS signals must be recorded at precisely the same time at each station. Until very recently, the global tracking stations recorded data at varying times. To further complicate matters, the receivers in the Ventura basin network also asyncronously sampled the data for the first seven days of the nine day experiment. We have collected the data from the Block II satellites, but do not include these data in the solutions presented here. As algorithms are developed to avoid adverse effects of S/A we will reprocess the data with all of the satellites included. By 1990 one of the seven Block I satellites was no longer operational, so our experiment may be somewhat weakened by the fewer data. Baseline repeatabilities are discussed in the next section.

All of the data that we used from the 1991 observations were synchronously

sampled. We included both Block I and Block II satellites in the analysis of the data. For this experiment we also used data sampled at 30 seconds. The data from the local sites PVER and SNPA covered 6 hours and we used 13 hours per day of the global data. Because data from so few regional sites were included in the solution we could not reliably fix biases. For this experiment we used the bias free solutions in the simultaneous estimation of site velocities.

2.5 GPS Results

We will first examine the results from each experiment before discussing the velocities obtained from the GPS surveys. Two issues are involved in assessing the quality of the results; these are accuracy and repeatability. We cannot directly assess the accuracy of our surveys, but comparison of VLBI and GPS shows agreement to under 5 mm for bias-fixed solutions [*Dong and Bock*, 1989; *Dixon et al*, 1990]. We are unable to make such a comparison at the VLBI monuments that we occupied because the two sites, Santa Paula (SNPA) and Palos Verdes (PVER), were not occupied simultaneously with VLBI. In chapter 4 we do compare the rates between the sites estimated from both VLBI and GPS. Proper velocity estimates depend on long-term repeatability, and accuracy is the most reliable way of assessing long-term repeatability. We can examine the short-term repeatability by comparing solutions from individual days for each experiment.

2.5.1 October 5-8, 1987

We occupied each site for two days, during the four days of the 1987 experiment. We divided the network so that half of the sites were occupied during the first two

days, and half were occupied the third and fourth days. Palos Verdes (PVER) was occupied during the entire experiment to provide a common reference. As shown in figure 2.2, the day-to-day repeatability for this is experiment is remarkably good. For the north, east and up components, the weighted root mean square scatter (σ) is on the order of a few millimeters. For the longer baselines the north component is about a factor of two better than the east component. For the short lines (page 53) the north component error is similar to the east component error. Two of the sites, Hopper (HOPP) and Santa Paula Peak (SNP2), have only one day of usable data, so it is encouraging that for short lines the repeatability is on the order of a few millimeters. The vertical component has both larger errors and a larger scatter. Because of the larger errors for the vertical component we do not make any assessment of differential vertical motion between the experiments. The error bars represent one formal standard deviation of the solution, weighted by a 10 mm scatter of the GPS data.

2.5.2 April 4-7, 1989

We occupied six sites simultaneously during the 1989 experiment, which continued for four days, although figure 2.3 shows that many of the sites do not have four days of usable data. For many of the baselines the wrms scatter (σ) of the east component is as large as 10 mm, while the north component scatter is under 3 mm, again suggesting that the north component is more reliable than the east component. This implies that the north component of velocity between sites will be better determined than the east component of velocity. The 1989 experiment occurred near a solar maximum, and sunspot activity was fairly high during this time. The effect of the

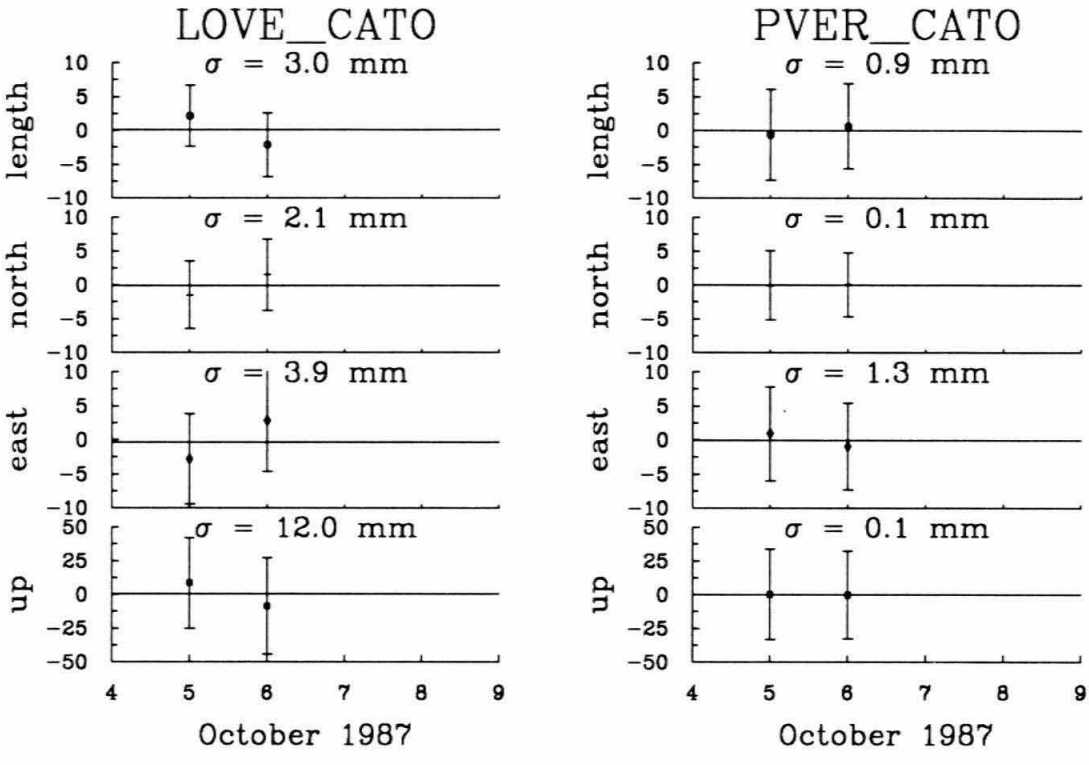

Figure 2.2: Repeatability plots for the 1987 experiment. Zero is the average value of the points. The horizontal line near zero is the weighted mean of the points. The components are the coordinate of the second site minus the first site, with the average subtracted out. The components are in millimeters. σ is the wrms scatter of the baseline component. The figure continues for three pages.

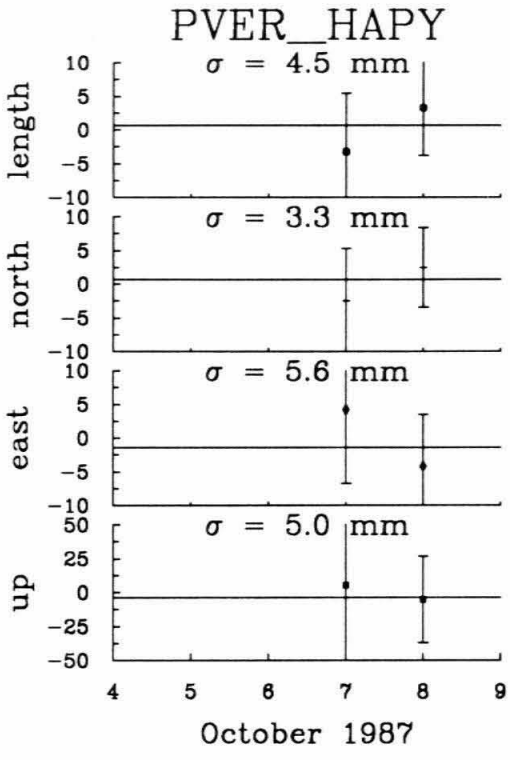
PVER_HAPY
σ = 4.5 mm
σ = 3.3 mm
σ = 5.6 mm
σ = 5.0 mm
length
north
east
up
October 1987

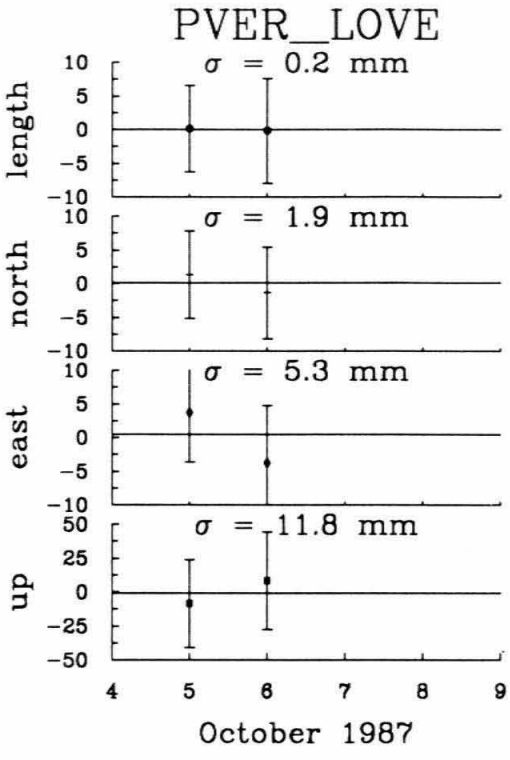
PVER_LOVE
σ = 0.2 mm
σ = 1.9 mm
σ = 5.3 mm
σ = 11.8 mm
length
north
east
up
October 1987

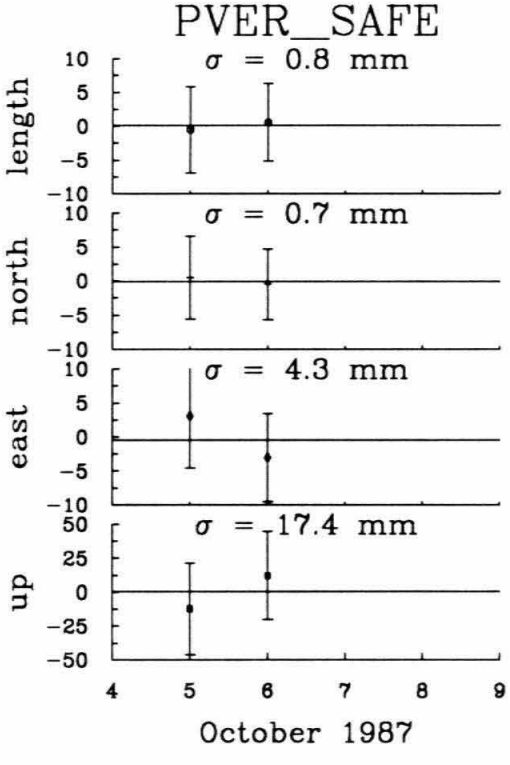
PVER_SAFE
σ = 0.8 mm
σ = 0.7 mm
σ = 4.3 mm
σ = 17.4 mm
length
north
east
up
October 1987

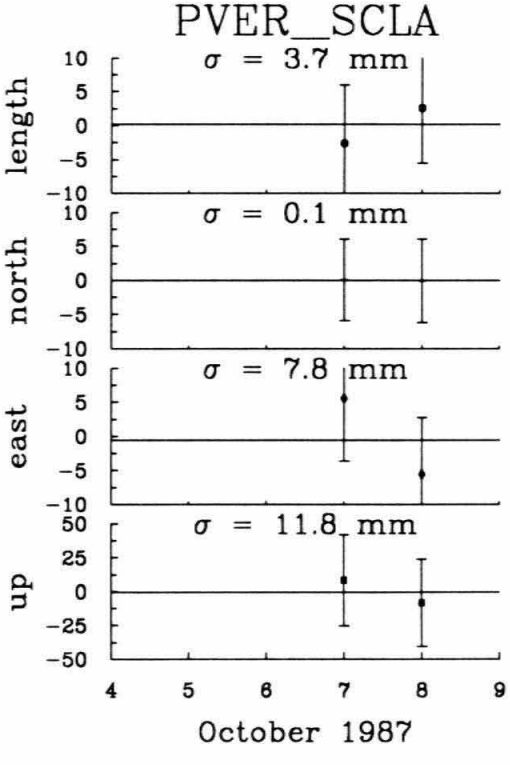
PVER_SCLA
σ = 3.7 mm
σ = 0.1 mm
σ = 7.8 mm
σ = 11.8 mm
length
north
east
up
October 1987

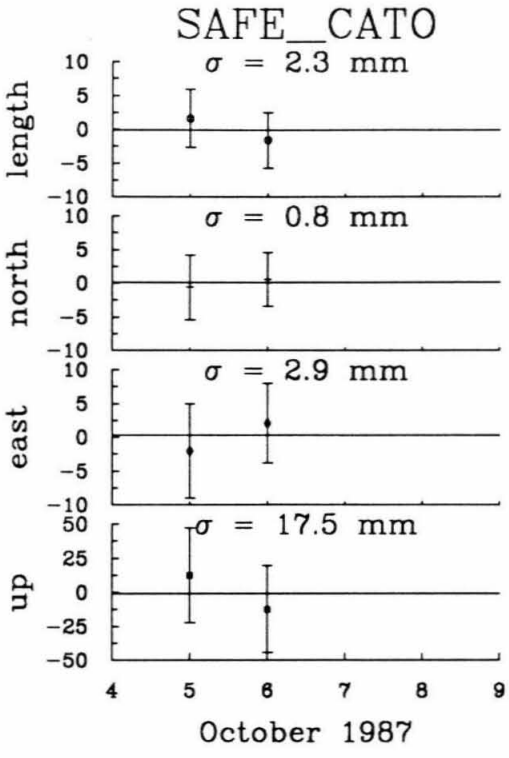
SAFE__CATO
σ = 2.3 mm
σ = 0.8 mm
σ = 2.9 mm
σ = 17.5 mm
length
north
east
up
October 1987

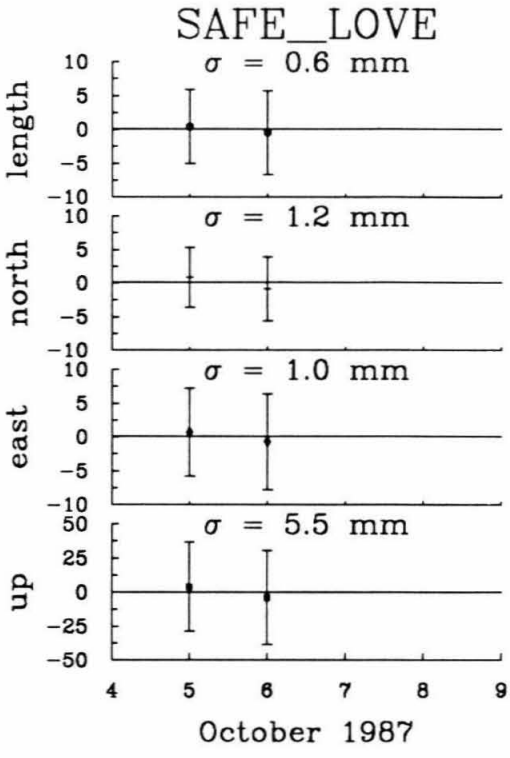
SAFE__LOVE
σ = 0.6 mm
σ = 1.2 mm
σ = 1.0 mm
σ = 5.5 mm
length
north
east
up
October 1987

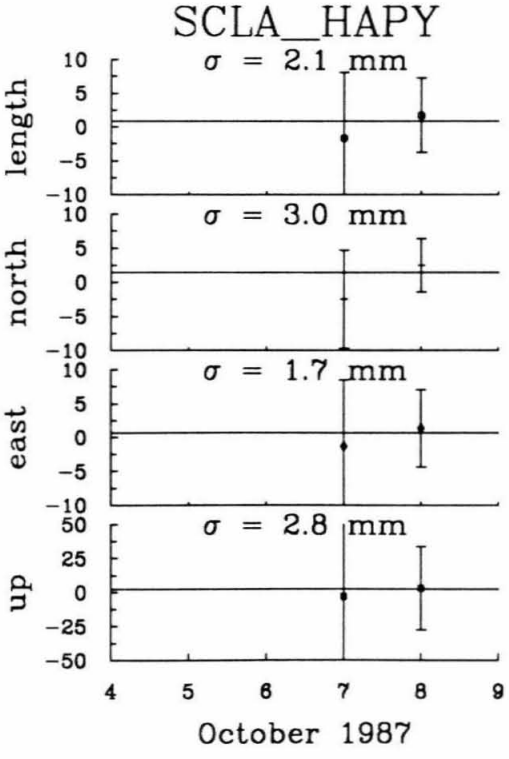
SCLA__HAPY
σ = 2.1 mm
σ = 3.0 mm
σ = 1.7 mm
σ = 2.8 mm
length
north
east
up
October 1987

solar activity on the ionosphere may have degraded the solutions if any of the biases were incorrectly fixed.

2.5.3 June 11-21, 1990

The June 1990 experiment was the most ambitious experiment, with sixteen sites being occupied over a period of nine days. We divided the experiment into three sub-experiments, and occupied Santa Paula (SNPA) and Palos Verdes (PVER) for the entire nine days. The day-to-day baseline components for the Santa Paula (SNPA) to Palos Verdes (PVER) baseline provide the most information about the experiment (figure 2.4, page 66). The north component shows the best repeatability for this baseline. The east component is much weaker with one outlier whose value is 24.7 $\pm$ 9.5 mm, off scale, on June 20, 1990. As in the other experiments the shorter lines show the best repeatability on the order of 5 mm or better. Baselines that include Palos Verdes (PVER) show the worst scatter. Palos Verdes (PVER) is farthest from the other sites in the network, so the baselines are the longest. Length dependent errors, perhaps from a poor position estimate at one of the fiducials might be the cause of the degradation. A noisy ionosphere, due to the experiment taking place during a solar maximum, may also account for the degradation of repeatability for the longer lines if biases were missed.

2.5.4 May 23-25, 1991

We were forced to use bias free estimations of the 1991 solution since so few stations were used. We are unable to compare repeatabilities because Santa Paula (SNPA) and Palos Verdes (PVER) were only occupied simultaneously during one of the three

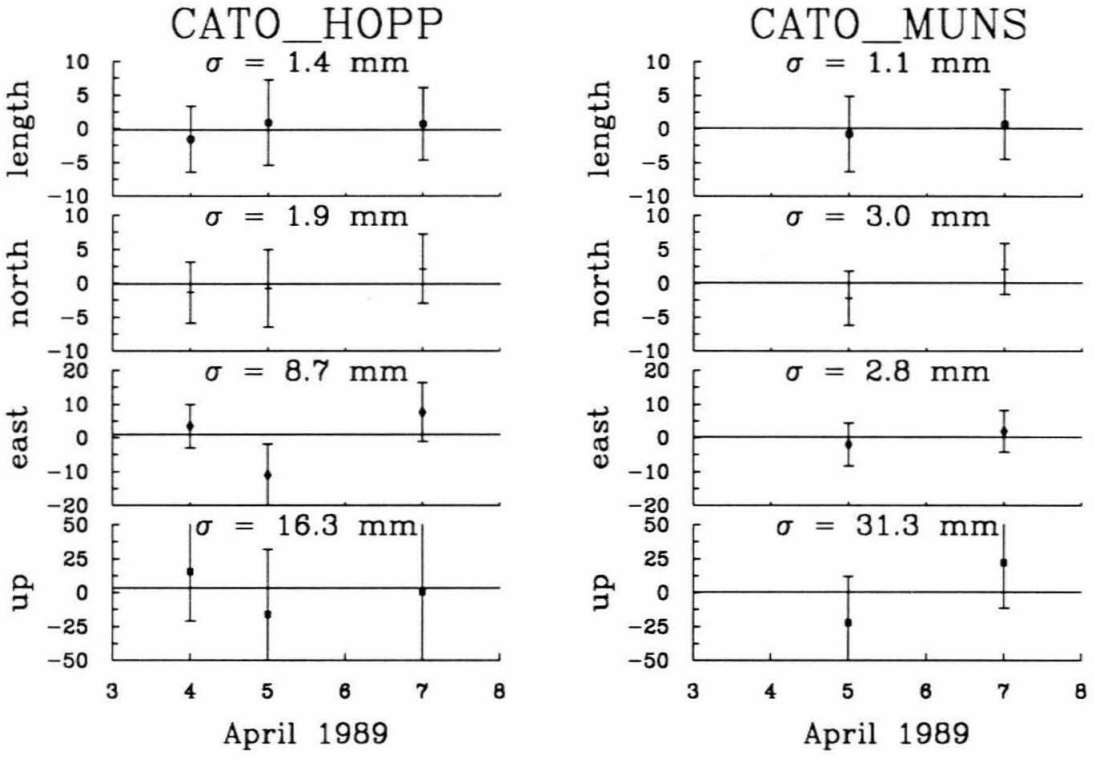

Figure 2.3: Repeatability plots for the 1989 experiment. Zero is the average value of the points. The horizontal line near zero is the weighted mean of the points. The components are the coordinate of the second site minus the first site, with the average subtracted out. σ is the wrms scatter of the baseline component. The figure continues for six pages.

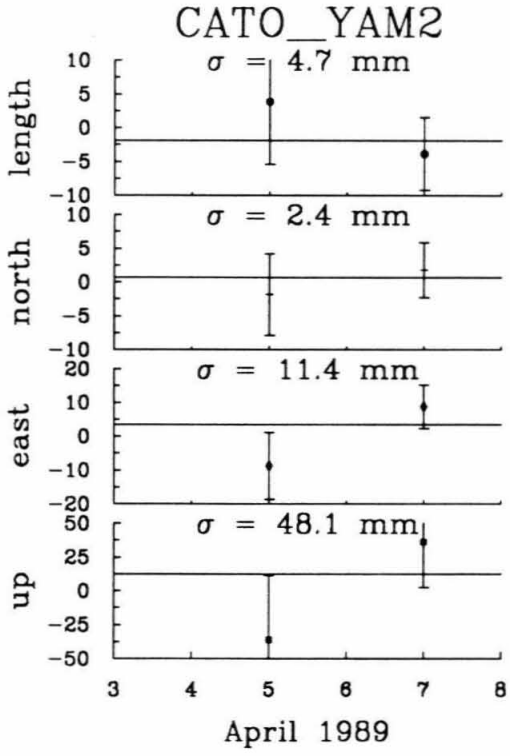
CATO_YAM2
σ = 4.7 mm
σ = 2.4 mm
σ = 11.4 mm
σ = 48.1 mm
length
north
east
up
April 1989

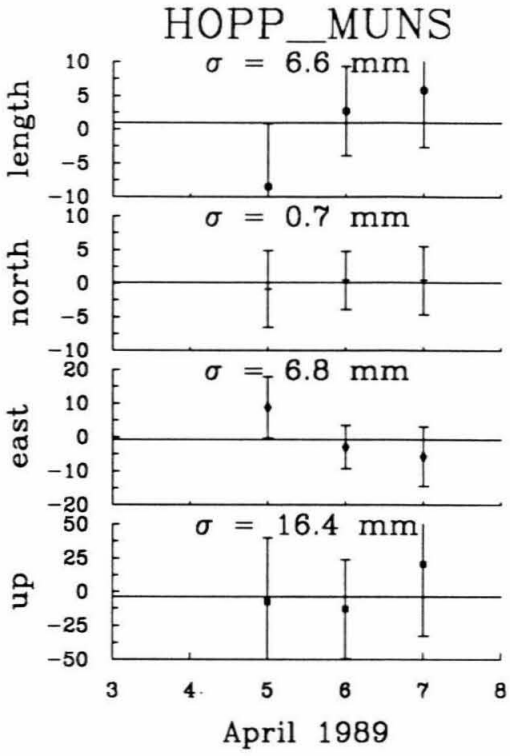
HOPP_MUNS
σ = 6.6 mm
σ = 0.7 mm
σ = 6.8 mm
σ = 16.4 mm
length
north
east
up
April 1989

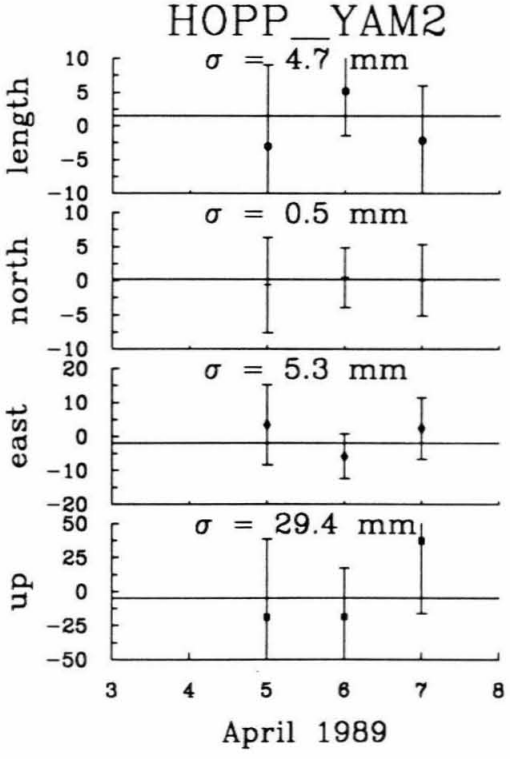
HOPP_YAM2
σ = 4.7 mm
σ = 0.5 mm
σ = 5.3 mm
σ = 29.4 mm
length
north
east
up
April 1989

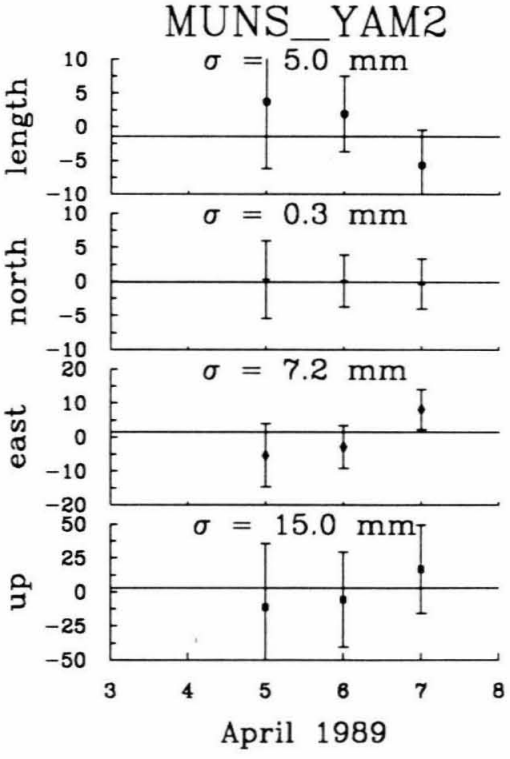
MUNS_YAM2
σ = 5.0 mm
σ = 0.3 mm
σ = 7.2 mm
σ = 15.0 mm
length
north
east
up
April 1989

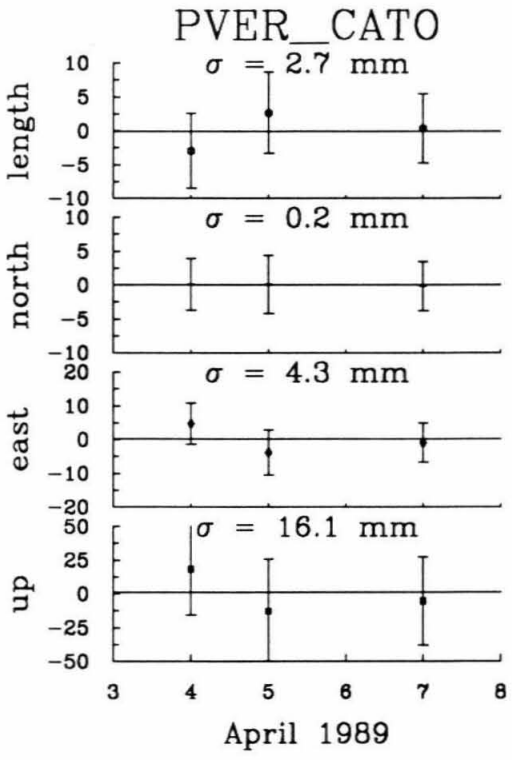
PVER_CATO
σ = 2.7 mm
σ = 0.2 mm
σ = 4.3 mm
σ = 16.1 mm
length
north
east
up
April 1989

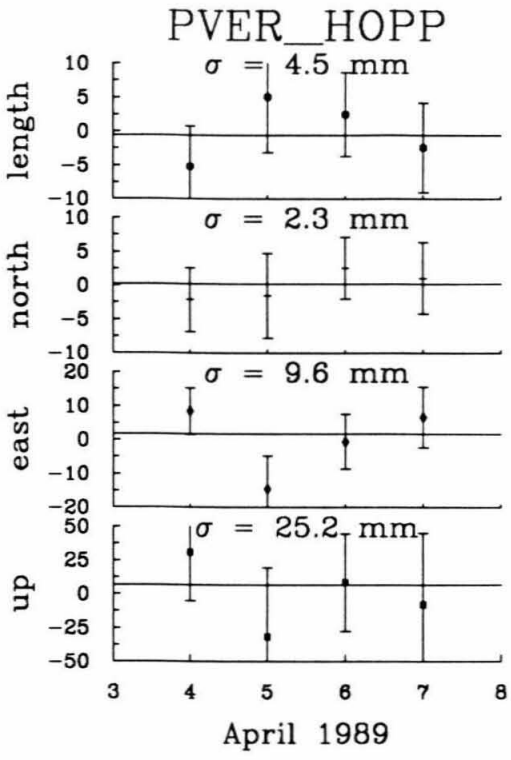
PVER_HOPP
σ = 4.5 mm
σ = 2.3 mm
σ = 9.6 mm
σ = 25.2 mm
length
north
east
up
April 1989

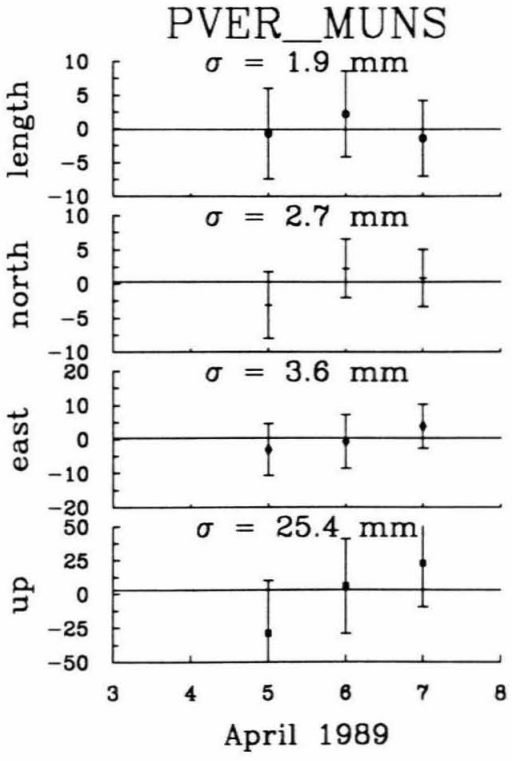
PVER_MUNS
σ = 1.9 mm
σ = 2.7 mm
σ = 3.6 mm
σ = 25.4 mm
length
north
east
up
April 1989

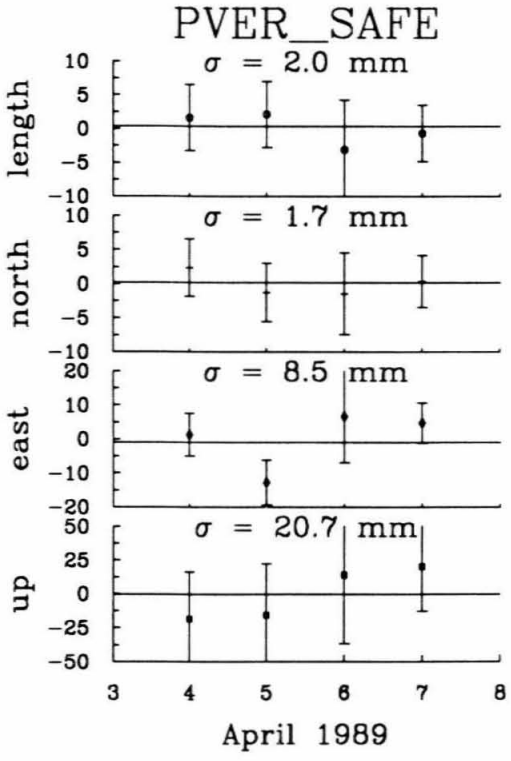
PVER_SAFE
σ = 2.0 mm
σ = 1.7 mm
σ = 8.5 mm
σ = 20.7 mm
length
north
east
up
April 1989

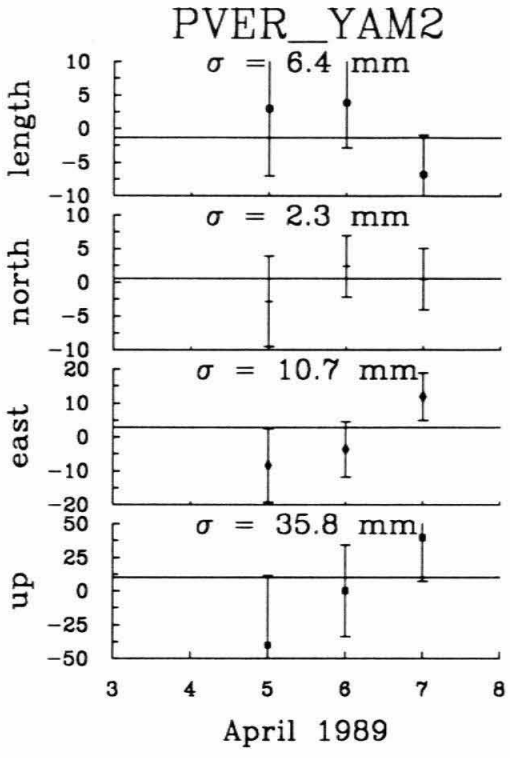
PVER__YAM2
σ = 6.4 mm
σ = 2.3 mm
σ = 10.7 mm
σ = 35.8 mm
length
north
east
up
April 1989

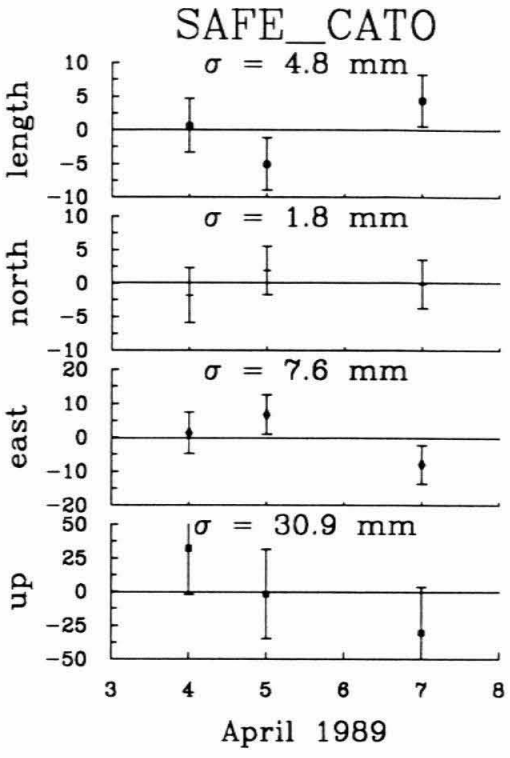
SAFE__CATO
σ = 4.8 mm
σ = 1.8 mm
σ = 7.6 mm
σ = 30.9 mm
length
north
east
up
April 1989

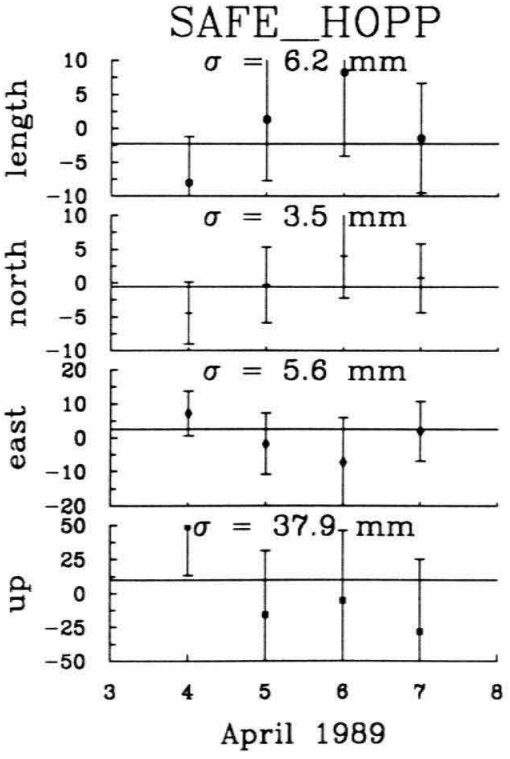
SAFE__HOPP
σ = 6.2 mm
σ = 3.5 mm
σ = 5.6 mm
σ = 37.9 mm
length
north
east
up
April 1989

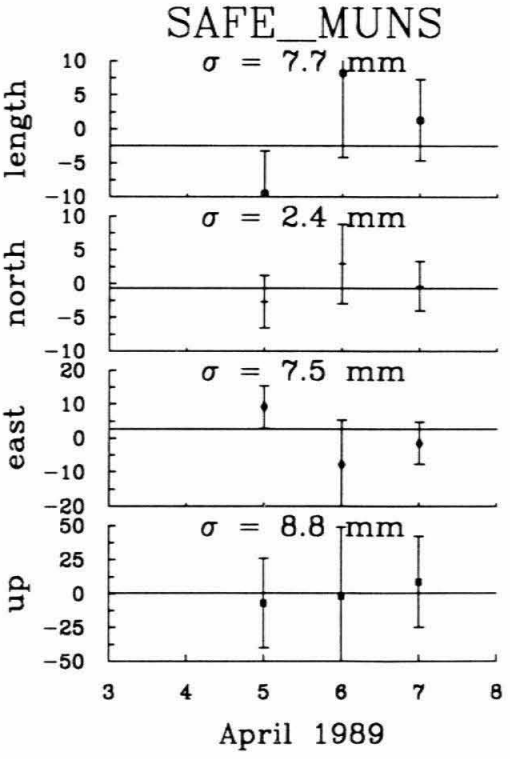
SAFE__MUNS
σ = 7.7 mm
σ = 2.4 mm
σ = 7.5 mm
σ = 8.8 mm
length
north
east
up
April 1989

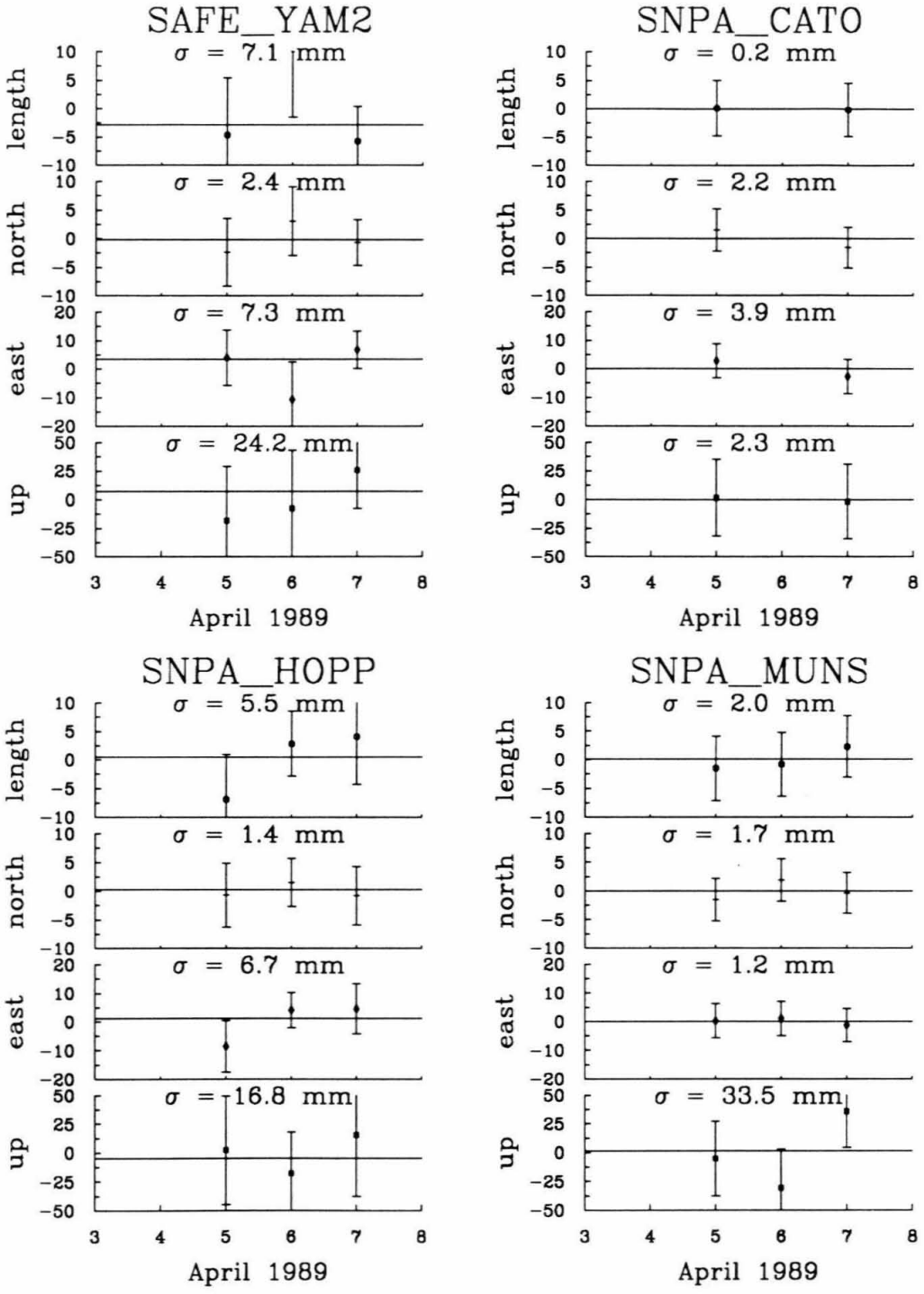
SAFE_YAM2
σ = 7.1 mm
σ = 2.4 mm
σ = 7.3 mm
σ = 24.2 mm
length
north
east
up
April 1989
SNPA_CATO
σ = 0.2 mm
σ = 2.2 mm
σ = 3.9 mm
σ = 2.3 mm
length
north
east
up
April 1989
SNPA_HOPP
σ = 5.5 mm
σ = 1.4 mm
σ = 6.7 mm
σ = 16.8 mm
length
north
east
up
April 1989
SNPA_MUNS
σ = 2.0 mm
σ = 1.7 mm
σ = 1.2 mm
σ = 33.5 mm
length
north
east
up
April 1989

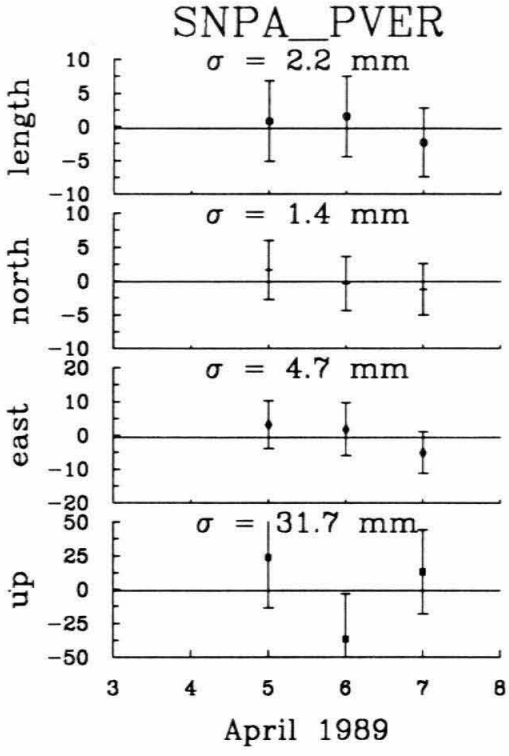
SNPA_PVER
σ = 2.2 mm
σ = 1.4 mm
σ = 4.7 mm
σ = 31.7 mm
length
north
east
up
April 1989

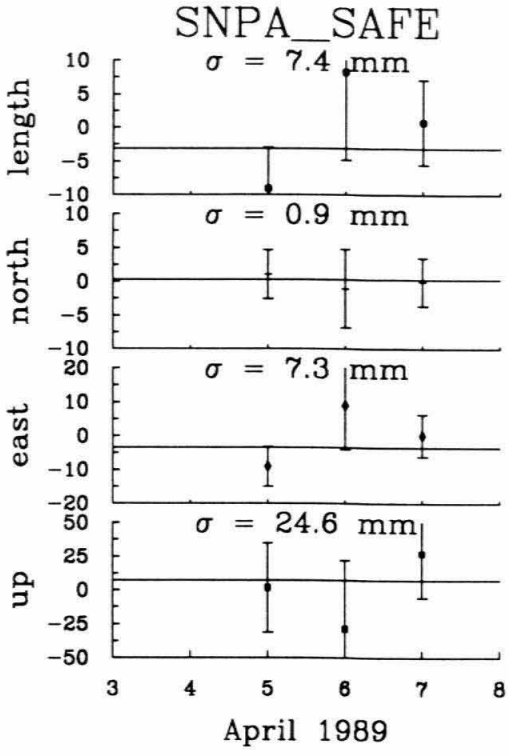
SNPA_SAFE
σ = 7.4 mm
σ = 0.9 mm
σ = 7.3 mm
σ = 24.6 mm
length
north
east
up
April 1989

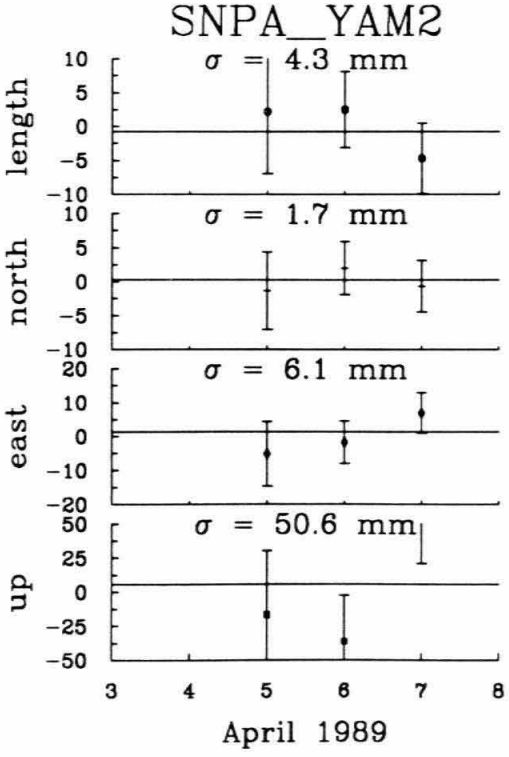
SNPA_YAM2
σ = 4.3 mm
σ = 1.7 mm
σ = 6.1 mm
σ = 50.6 mm
length
north
east
up
April 1989

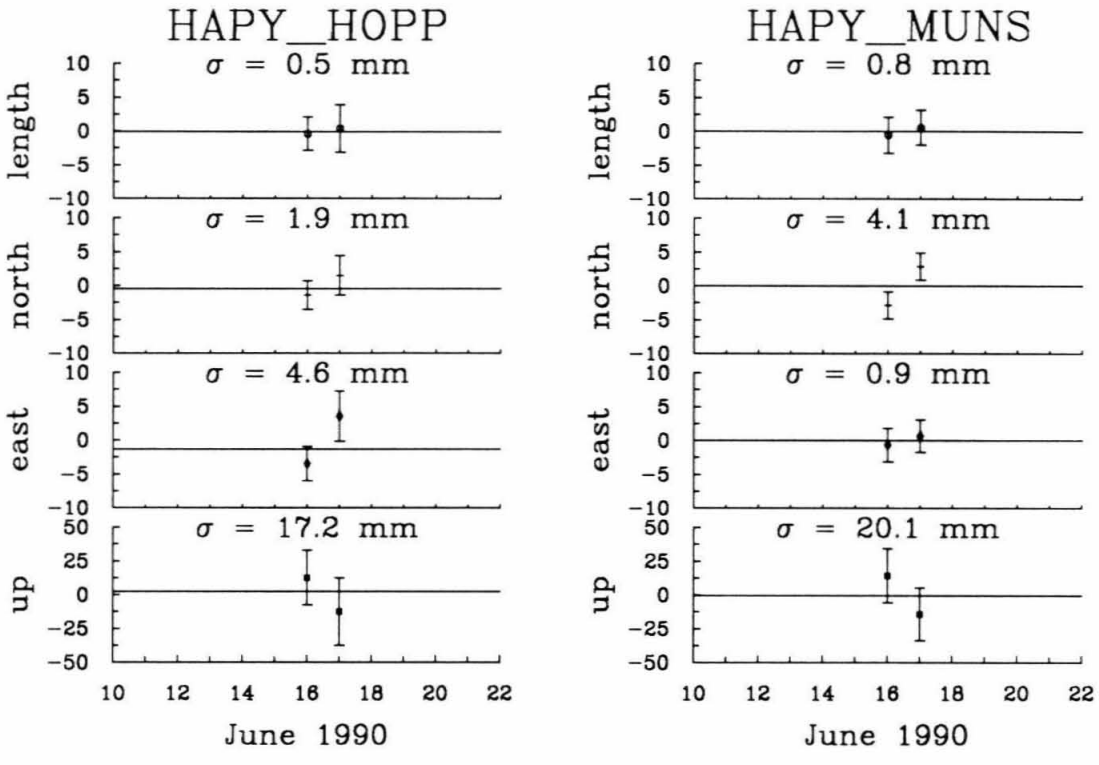

Figure 2.4: Repeatability plots for the 1990 experiment. Zero is the average value of the points. The horizontal line near zero is the weighted mean of the points. The components are the coordinate of the second site minus the first site, with the average subtracted out. σ is the wrms scatter of the baseline component. The figure continues for seven pages.

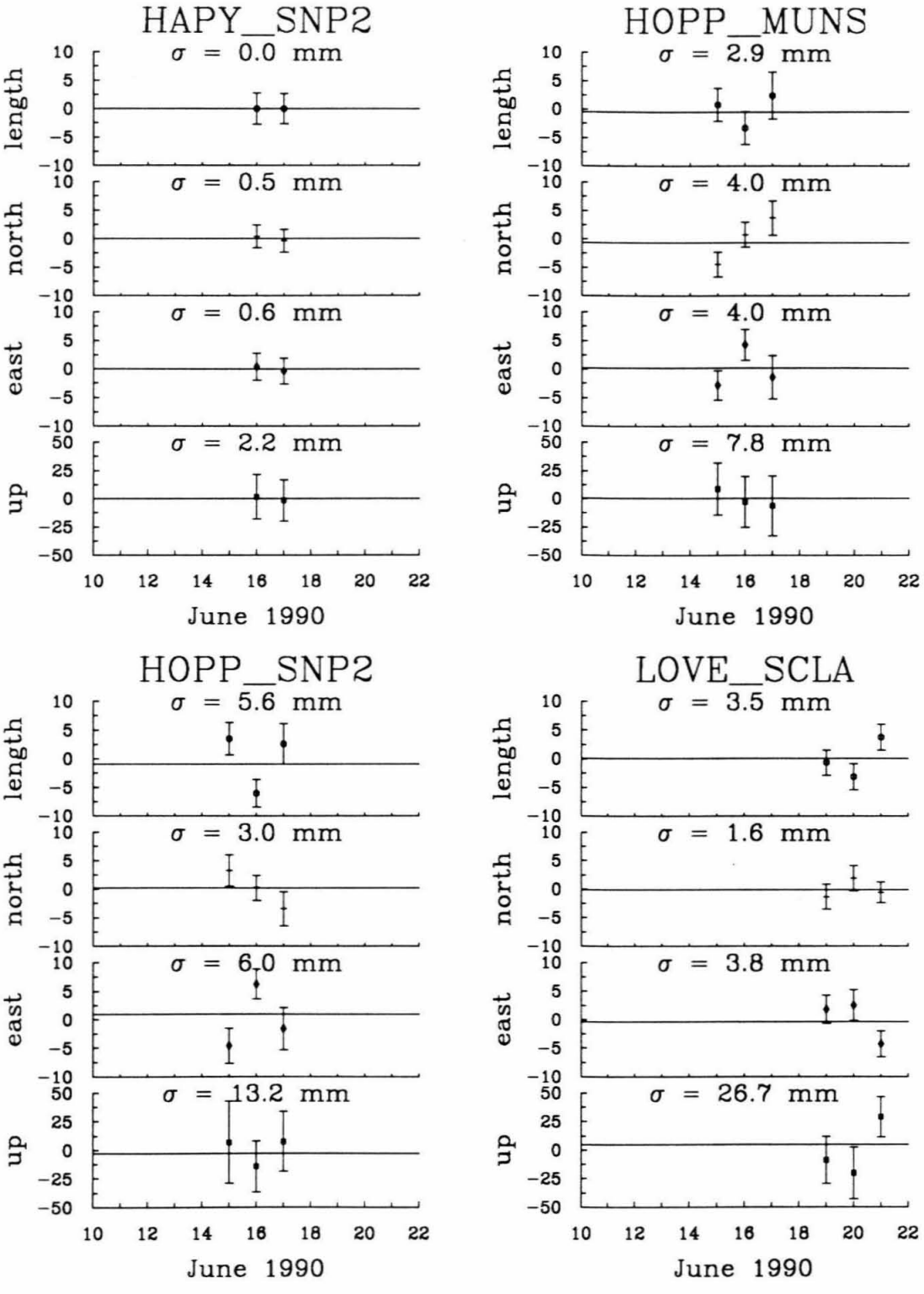
HAPY_SNP2
σ = 0.0 mm
σ = 0.5 mm
σ = 0.6 mm
σ = 2.2 mm
HOPP_MUNS
σ = 2.9 mm
σ = 4.0 mm
σ = 4.0 mm
σ = 7.8 mm
HOPP_SNP2
σ = 5.6 mm
σ = 3.0 mm
σ = 6.0 mm
σ = 13.2 mm
LOVE_SCLA
σ = 3.5 mm
σ = 1.6 mm
σ = 3.8 mm
σ = 26.7 mm
length
north
east
up
June 1990

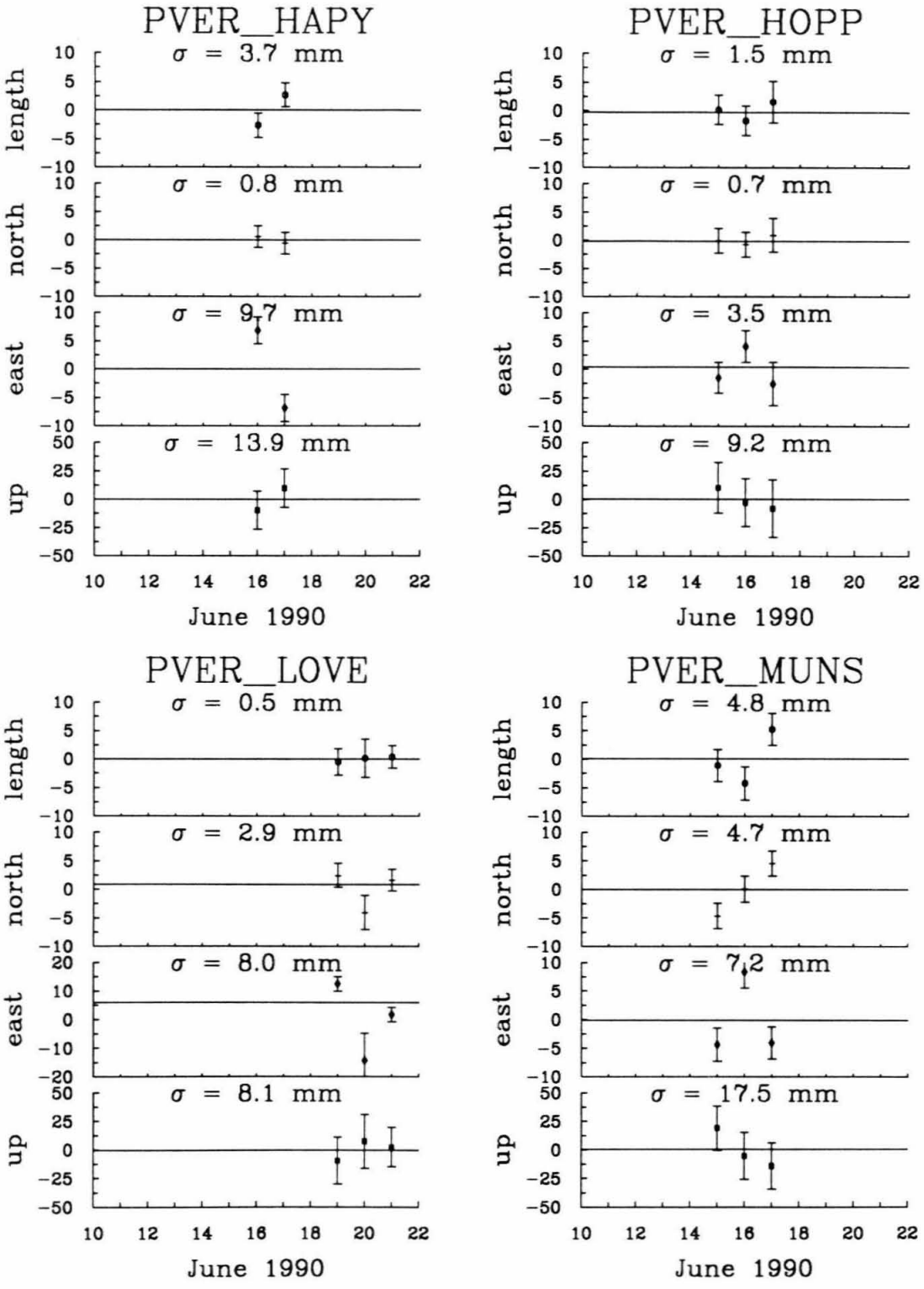
PVER_HAPY
σ = 3.7 mm
σ = 0.8 mm
σ = 9.7 mm
σ = 13.9 mm
length
north
east
up
June 1990
PVER_HOPP
σ = 1.5 mm
σ = 0.7 mm
σ = 3.5 mm
σ = 9.2 mm
length
north
east
up
June 1990
PVER_LOVE
σ = 0.5 mm
σ = 2.9 mm
σ = 8.0 mm
σ = 8.1 mm
length
north
east
up
June 1990
PVER_MUNS
σ = 4.8 mm
σ = 4.7 mm
σ = 7.2 mm
σ = 17.5 mm
length
north
east
up
June 1990

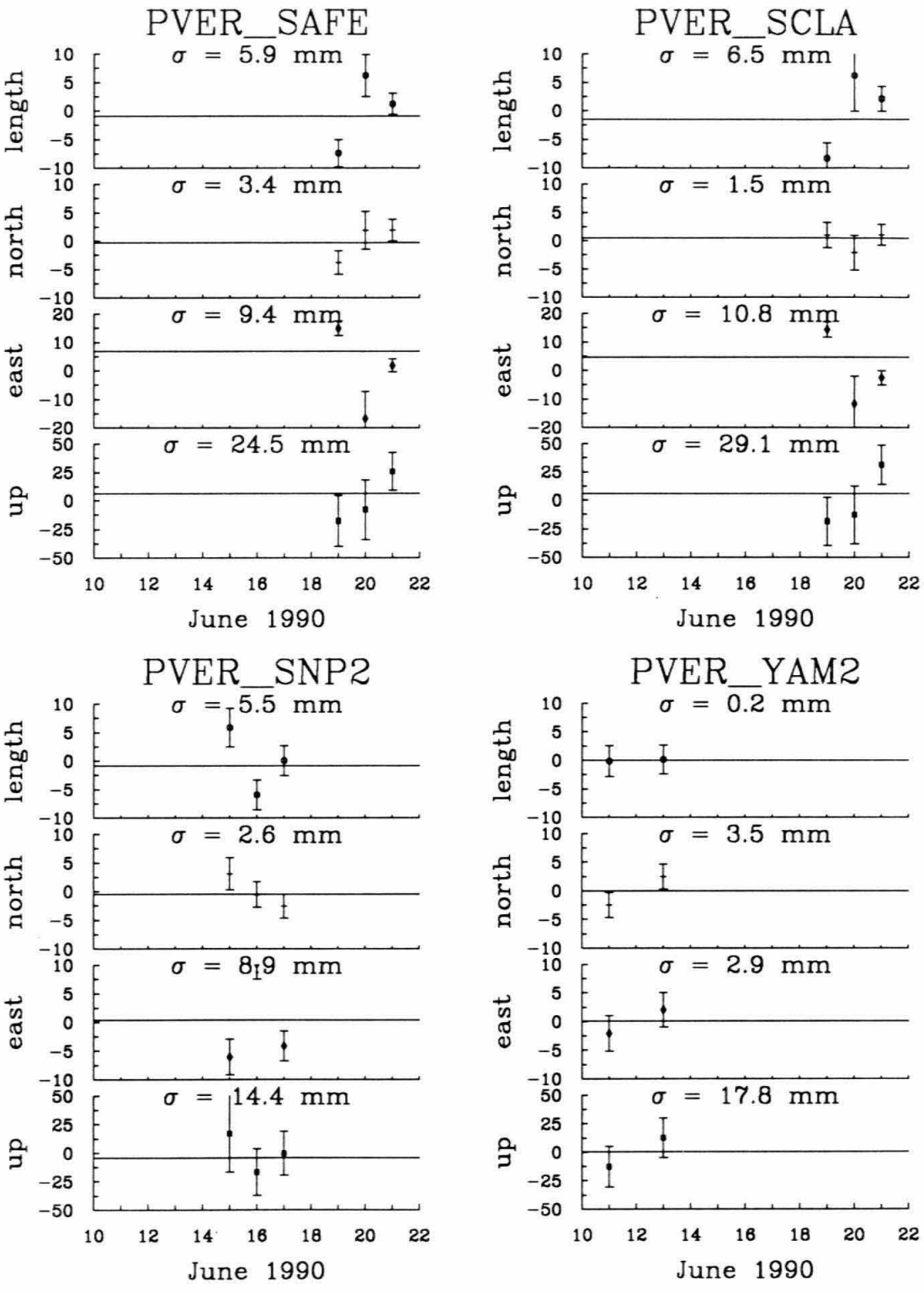
PVER_SAFE
σ = 5.9 mm
σ = 3.4 mm
σ = 9.4 mm
σ = 24.5 mm
PVER_SCLA
σ = 6.5 mm
σ = 1.5 mm
σ = 10.8 mm
σ = 29.1 mm
PVER_SNP2
σ = 5.5 mm
σ = 2.6 mm
σ = 8.9 mm
σ = 14.4 mm
PVER_YAM2
σ = 0.2 mm
σ = 3.5 mm
σ = 2.9 mm
σ = 17.8 mm
length
north
east
up
June 1990

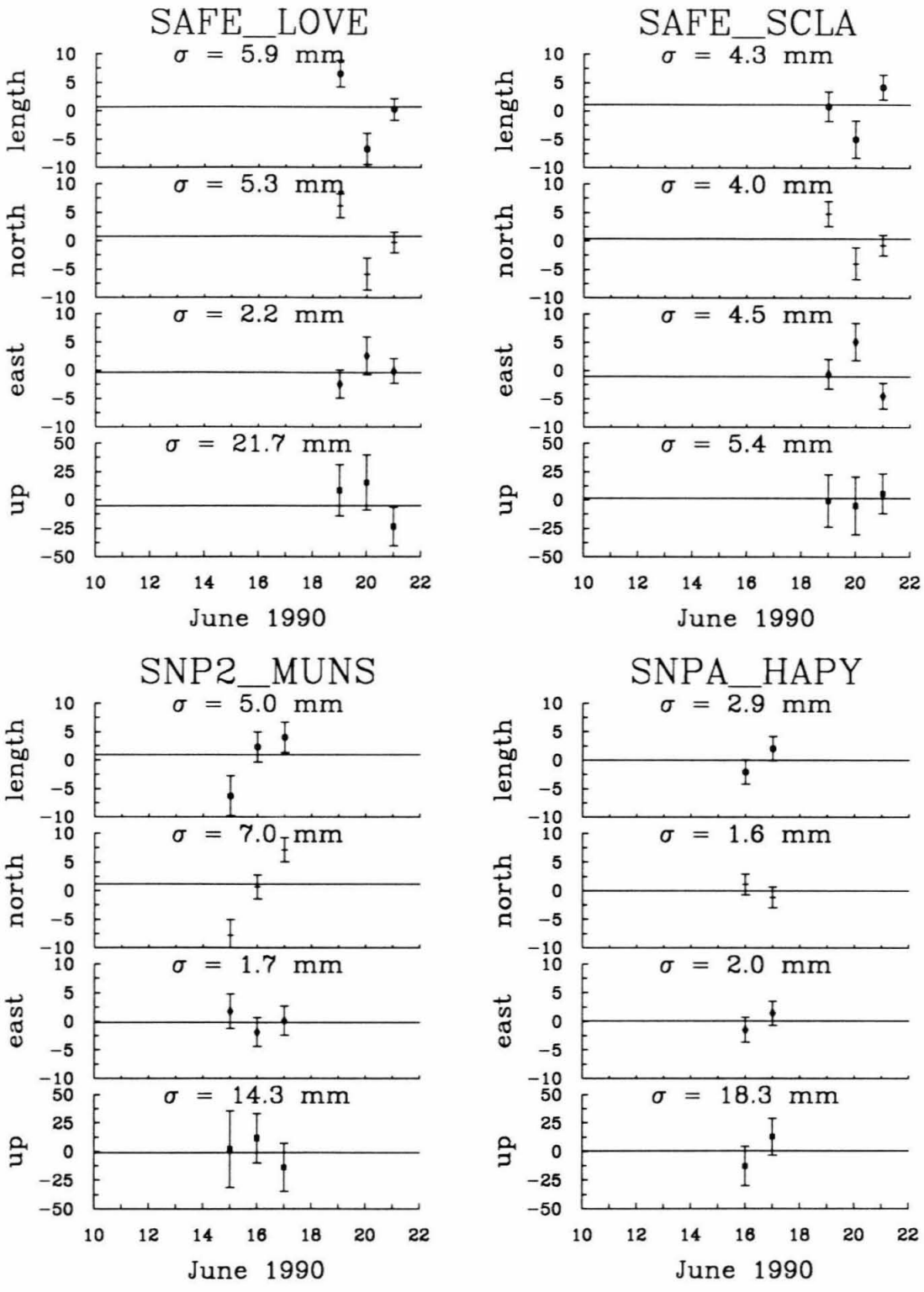
SAFE_LOVE
σ = 5.9 mm
σ = 5.3 mm
σ = 2.2 mm
σ = 21.7 mm
length
north
east
up
June 1990
SAFE_SCLA
σ = 4.3 mm
σ = 4.0 mm
σ = 4.5 mm
σ = 5.4 mm
length
north
east
up
June 1990
SNP2_MUNS
σ = 5.0 mm
σ = 7.0 mm
σ = 1.7 mm
σ = 14.3 mm
length
north
east
up
June 1990
SNPA_HAPY
σ = 2.9 mm
σ = 1.6 mm
σ = 2.0 mm
σ = 18.3 mm
length
north
east
up
June 1990

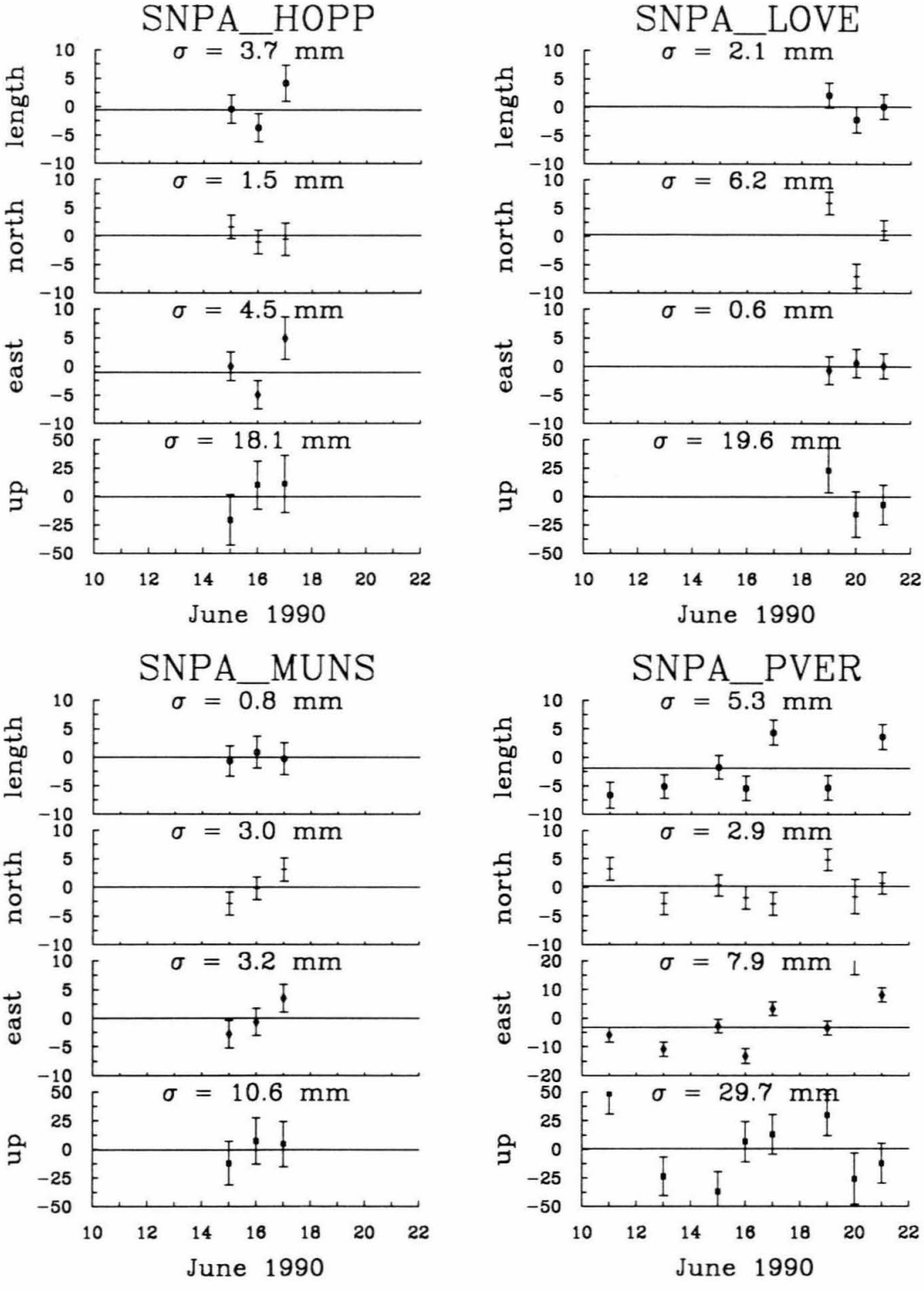
SNPA_HOPP
σ = 3.7 mm
σ = 1.5 mm
σ = 4.5 mm
σ = 18.1 mm
length
north
east
up
June 1990
SNPA_LOVE
σ = 2.1 mm
σ = 6.2 mm
σ = 0.6 mm
σ = 19.6 mm
length
north
east
up
June 1990
SNPA_MUNS
σ = 0.8 mm
σ = 3.0 mm
σ = 3.2 mm
σ = 10.6 mm
length
north
east
up
June 1990
SNPA_PVER
σ = 5.3 mm
σ = 2.9 mm
σ = 7.9 mm
σ = 29.7 mm
length
north
east
up
June 1990

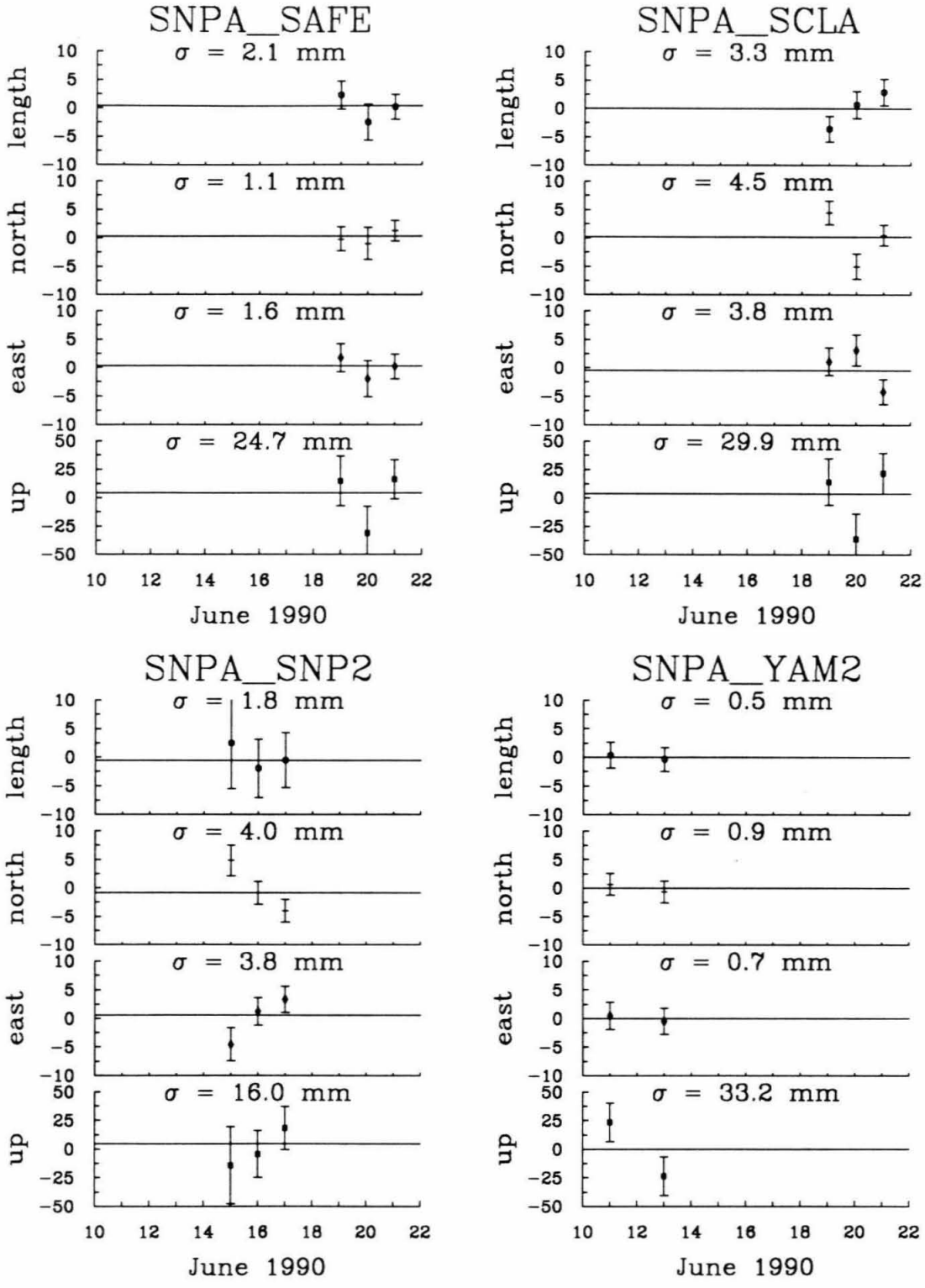
SNPA_SAFE
σ = 2.1 mm
σ = 1.1 mm
σ = 1.6 mm
σ = 24.7 mm
SNPA_SCLA
σ = 3.3 mm
σ = 4.5 mm
σ = 3.8 mm
σ = 29.9 mm
SNPA_SNP2
σ = 1.8 mm
σ = 4.0 mm
σ = 3.8 mm
σ = 16.0 mm
SNPA_YAM2
σ = 0.5 mm
σ = 0.9 mm
σ = 0.7 mm
σ = 33.2 mm
length
north
east
up
June 1990

days. Although this experiment was weak, we assume that the additional time added to the SNPA–PVER baseline measurements will improve the rate estimate between the two sites.

2.6 Error Analysis

The repeatability of baseline components shows that the north baseline components are better than the east components by about a factor of two (figure 2.5). The repeatability of the north component is generally better than 5 mm, while the east repeatability is better than 10–12 mm. There is some suggestion that the east component is better for shorter lines than for longer lines to about 90 km, at which point it levels off to about 12 mm. The shortest lines (10–40 km) show better than 5–8 mm repeatability. Apparently there is no dependence of repeatability on east or north offset (figure 2.6), suggesting that the degradation of east precision is due to line length rather than east offset. The up component shows no dependence on either line length or vertical offset. The overall repeatability of the up component is about 30 mm.

In all cases the October 1987 experiment shows the best results (solid circles, figures 2.5 and 2.6). Recall that the solutions for 1987 and 1989 are for 120 s data sampling; it appears that the less frequent sampling did not affect the 1987 experiment. The greatest source of error is probably due to a poorly understood fiducial network. The geometry of the fiducial network was different for each experiment and for the latter experiments poorly determined ties degrade the estimation of the monument position.

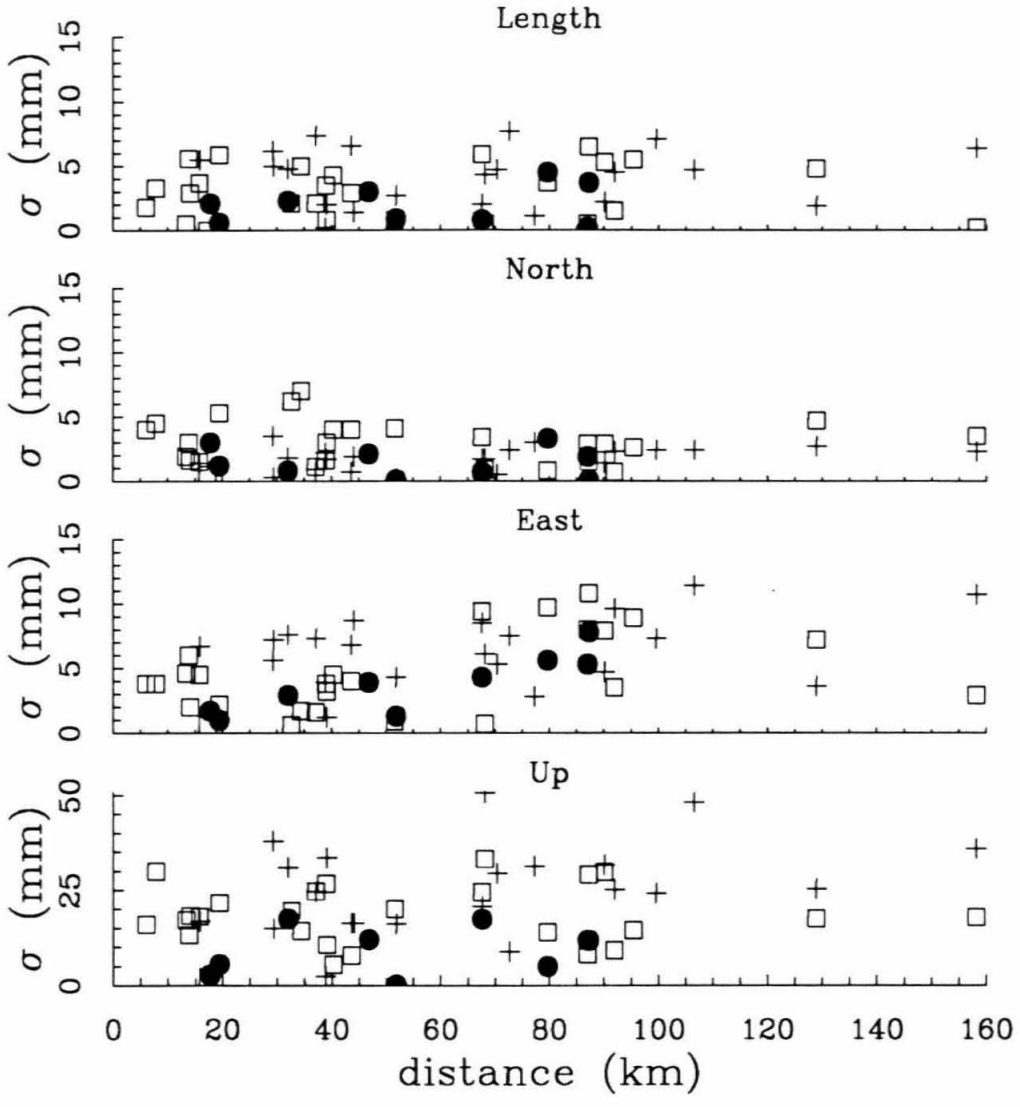

Figure 2.5: Component of repeatability by baseline length. σ is the weighted rms of the repeatability of a baseline. Filled circles refer to the 1987 experiment, open squares to the 1989 experiment and pluses to the 1990 experiment.

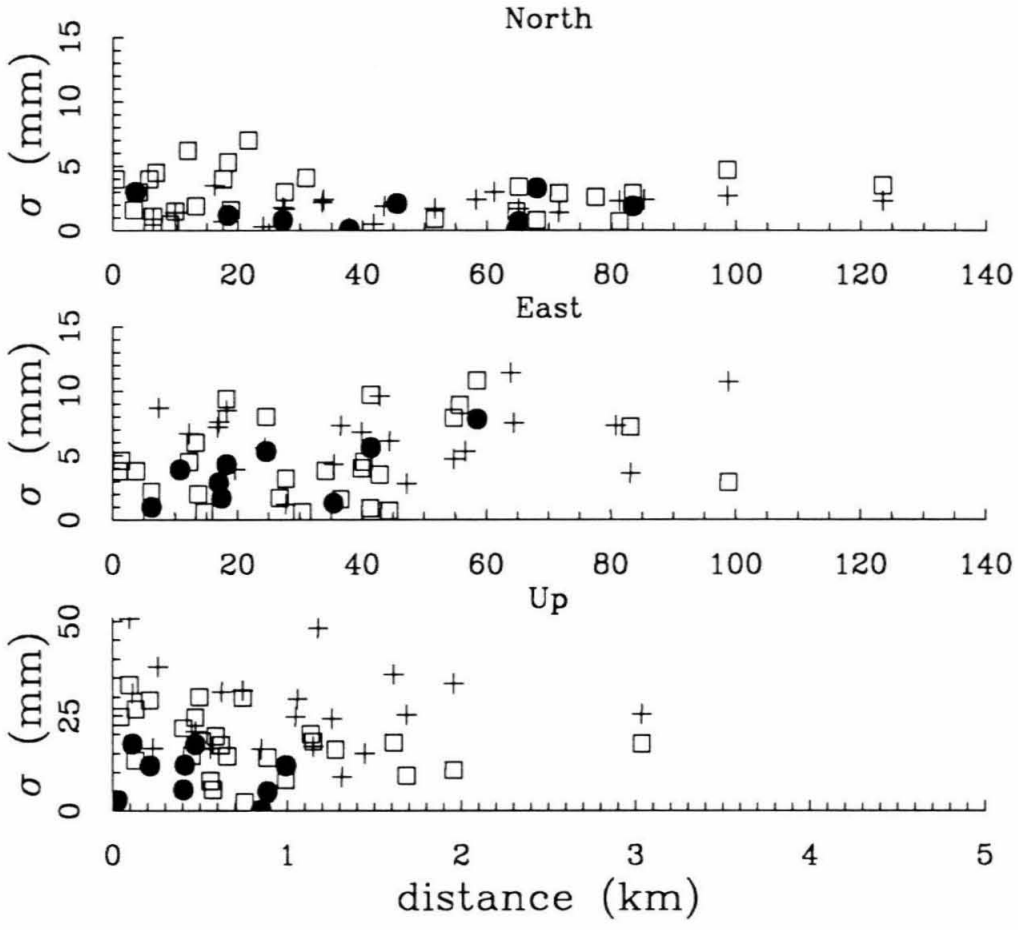

Figure 2.6: Component of repeatability by component offset. σ is the weighted rms of the repeatability. Filled circles refer to the 1987 experiment, open squares to the 1989 experiment and pluses to the 1990 experiment.

Note that the north component is the worst for the April 1989 experiment (open squares, figures 2.5 and 2.6). This is probably due to poor geometry of the fiducial network during the experiment. The sites occupied are located in Hawaii, the Mojave desert, Massachusetts, and northern Europe, forming an east-northeast line through the network. The lack of any north-south lines in the fiducial network poorly constrained the north component estimations.

Because the satellites pass in a north-south line for the most part, the satellite orbits best constrain the north component (figure A.1). Poor determination of the fiducial site positions has a greater effect, then, on the east components of the baselines. The east components show a precision of about $1 : 10^{-7}$ which could be due to an error of 3 cm in the position at Mojave, or to a greater error at the other fiducial sites.

Chapter 3

Results and Deformation

To best approximate the current deformation in the Ventura basin region we will examine repeat GPS measurements and also compare GPS to triangulation. We first look at the 2.7 years of GPS results and then compare these results to deformation estimated from comparing historical triangulation and GPS data.

3.1 GPS results

Because results from GPS are tied to a global reference frame, we can directly measure the velocities between sites by comparing results from different epochs. The velocities provide a picture of the deformation field, but it is also useful to calculate deformation parameters from the velocities. This is the most direct way of comparing GPS results with results from other geodetic techniques. Calculating the deformation parameters also yields information about rotations and the types of strain that are occurring (i.e., compression versus strike-slip).

3.1.1 Velocities

The velocities of all of the sites were estimated simultaneously using data from the four experiments. Here we present the results relevant to the Ventura basin study. Appendix B lists the results obtained during this study but not presented in the thesis.

Hopper (HOPP) and Castro (CATO) were occupied during all three experiments. Velocities relative to those two sites contain the most useful information for understanding the quality of the measured deformation of the Ventura basin. Palos Verdes (PVER) was also occupied during each GPS experiment, but its distance from the basin makes it more difficult to interpret deformation near the basin. The rate between Santa Paula (SNPA) and Palos Verdes (PVER), obtained from GPS, is useful for completing the Santa Paula footprint. We examine the baseline evolution with time to interpret the quality of the velocities for each site.

Plots of the velocities relative to both the north and south sides of the basin show the highest velocity gradients across the basin (figures 3.1 and 3.2). Tables 3.1 and 3.2 list the rates relative to Hopper and San Fernando, respectively.

Baseline component versus time plots show how well the data fit the calculated velocities (figure 3.3). In general, the baseline components versus time are linear, within the standard deviations, suggesting that the short time between the observations is adequate to assess deformation in the region of the Ventura basin. In addition to this, the rates across the basin appear high enough for the 2.7 years between observations to be adequate for resolving the displacement rates from only two measurements (i.e., figure 3.3, page 82). Although we do not make any state-

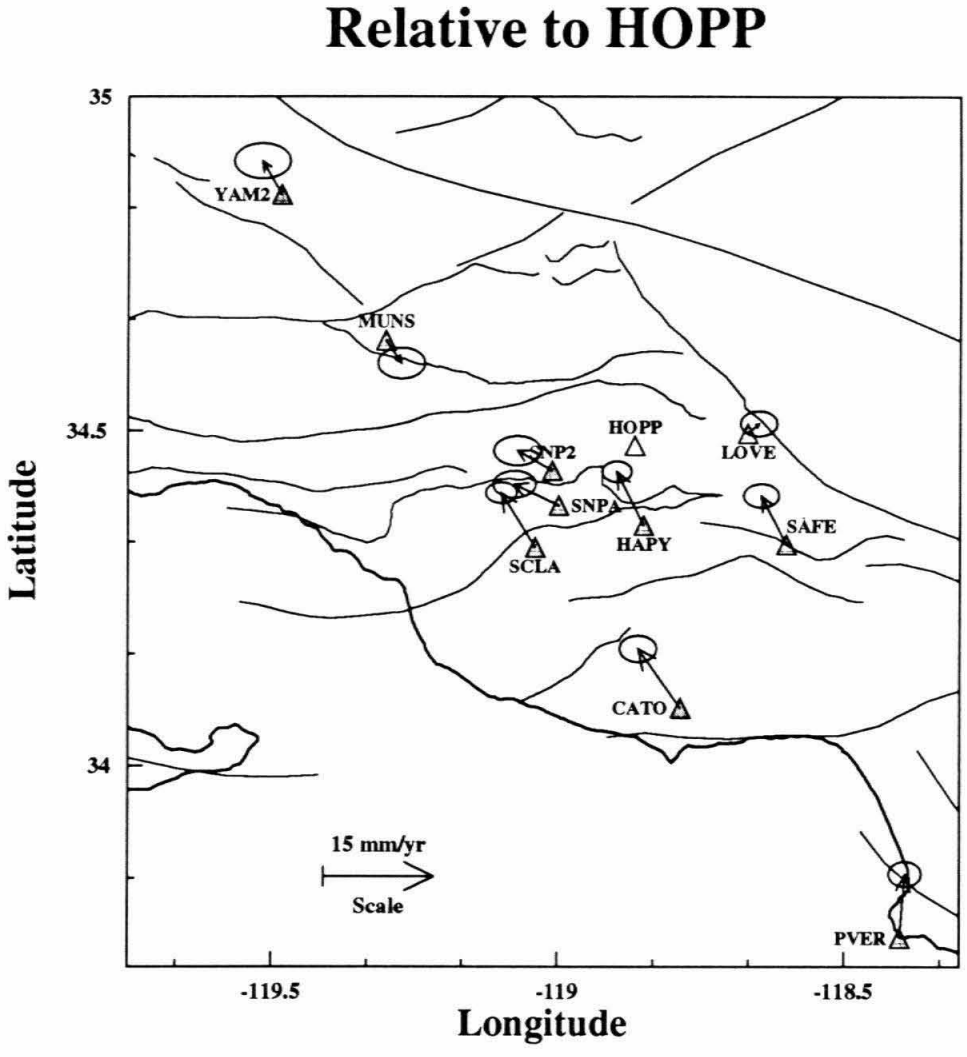

Figure 3.1: Velocities of sites relative to HOPP. Error ellipses represent one standard deviation.

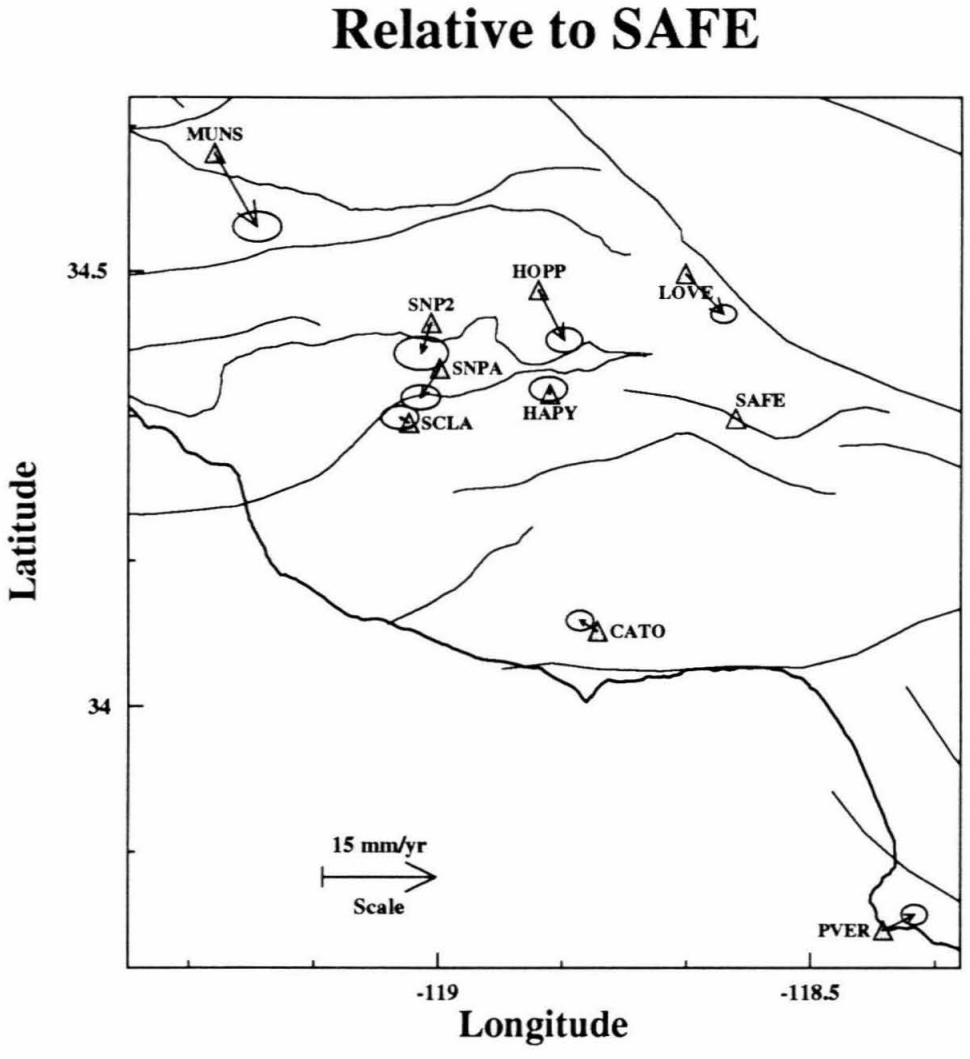

Figure 3.2: Velocities of sites relative to SAFE. Error ellipses represent one standard deviation.

Site	East	North	Length
CATO	-5.7 ± 2.5	8.0 ± 1.8	-8.8 ± 1.9
HAPY	-3.6 ± 2.0	7.3 ± 1.4	-7.0 ± 1.6
LOVE	1.5 ± 2.5	1.3 ± 1.7	2.2 ± 2.5
MUNS	2.1 ± 3.2	-3.1 ± 2.1	-3.6 ± 3.3
PVER	0.7 ± 2.2	8.7 ± 1.7	-7.4 ± 2.1
SAFE	-3.4 ± 2.4	6.6 ± 1.6	-6.6 ± 2.3
SCLA	-4.6 ± 2.1	7.4 ± 1.4	-2.2 ± 1.6
SNP2	-4.7 ± 3.2	2.7 ± 2.0	3.7 ± 2.7
SNPA	-6.0 ± 2.9	2.9 ± 1.8	0.3 ± 2.6
YAM2	-2.6 ± 3.8	4.6 ± 2.4	4.9 ± 3.7

Table 3.1: Velocities of sites relative to HOPP. Units are mm and the errors represent one formal standard deviation.

Site	East	North	Length
CATO	-2.3 ± 1.8	1.4 ± 1.3	0.0 ± 1.3
HAPY	-0.2 ± 2.5	0.7 ± 1.6	0.6 ± 2.5
HOPP	3.4 ± 2.4	-6.6 ± 1.6	-6.6 ± 2.3
LOVE	5.0 ± 1.7	-5.3 ± 1.2	-6.1 ± 1.5
MUNS	5.6 ± 3.1	-9.7 ± 2.0	-9.9 ± 3.1
PVER	4.1 ± 1.7	2.1 ± 1.3	-0.8 ± 1.4
SCLA	-1.2 ± 2.5	0.7 ± 1.5	1.2 ± 2.5
SNP2	-1.3 ± 3.6	-4.0 ± 2.2	-0.1 ± 3.7
SNPA	-2.5 ± 2.7	-3.8 ± 1.6	1.3 ± 2.7
YAM2	0.8 ± 3.7	-2.0 ± 2.3	-1.7 ± 3.5

Table 3.2: Velocities of sites relative to SAFE. Units are mm and the errors represent one formal standard deviation.

ments concerning relative vertical displacements, we present the up components to show year-to-year repeatability of that component. The vertical rates are not well-determined. This is mainly due to a poor determination of the vertical component for Munson (MUNS) and the short time period between observation epochs for that site. The rate determinations for both Yam 2 (YAM2) and Munson (MUNS) are suspect for this reason. Future measurements will result in improved velocities for those two sites. The simultaneous estimation of velocities for all stations requires closure. An improper position at one site can adversely affect velocities at other sites. A poor site position at Mojave (MOJM) might affect the results of the basin network.

The rate for the site Santa Paula (SNPA) relative to Palos Verdes (PVER) is also more poorly determined than the rates for the original eight sites (figure 3.3, page 87). As mentioned in Chapter 1, the rate obtained from VLBI between Palos Verdes (PVER) and Santa Paula (SNPA) varies greatly depending upon the number of observations used in the solution. The GPS results also vary from epoch to epoch. It appears that the north component is poorly determined in 1989 and the east component is not at all well determined in 1991. We were unable to use a bias-fixed solution for the 1991 epoch, because so few data were available then. Bias-free solutions result in poorly determined east components, but the north component is not degraded much [*Dong and Bock*, 1989]. For this reason, we consider the north component of motion to be the best determined, and the east component much more poorly determined. Because the azimuth of the SNPA to PVER baseline is approximately 45° from north, the length estimate is affected by both the questionable north

component in 1989 and the east component in 1991.

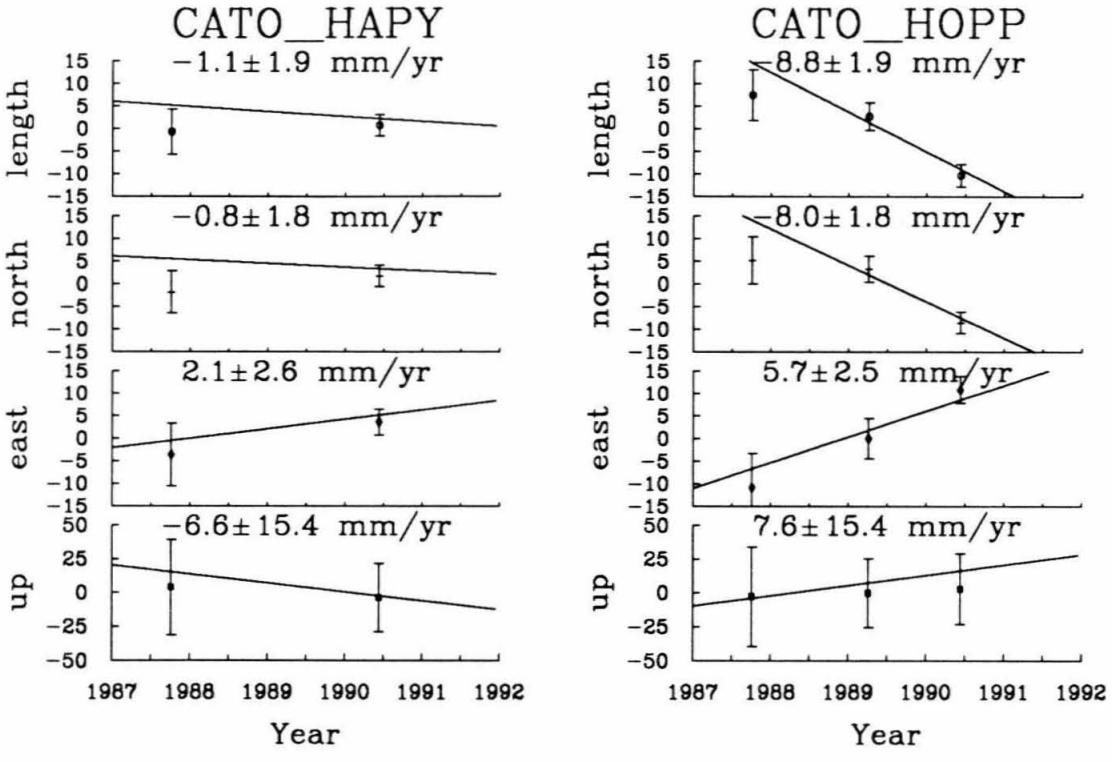

Figure 3.3: Baseline component versus time plots for all data with at least two epochs of measurements. The solid line is the calculated velocity from the Kalman filter run. Units are in millimeters.

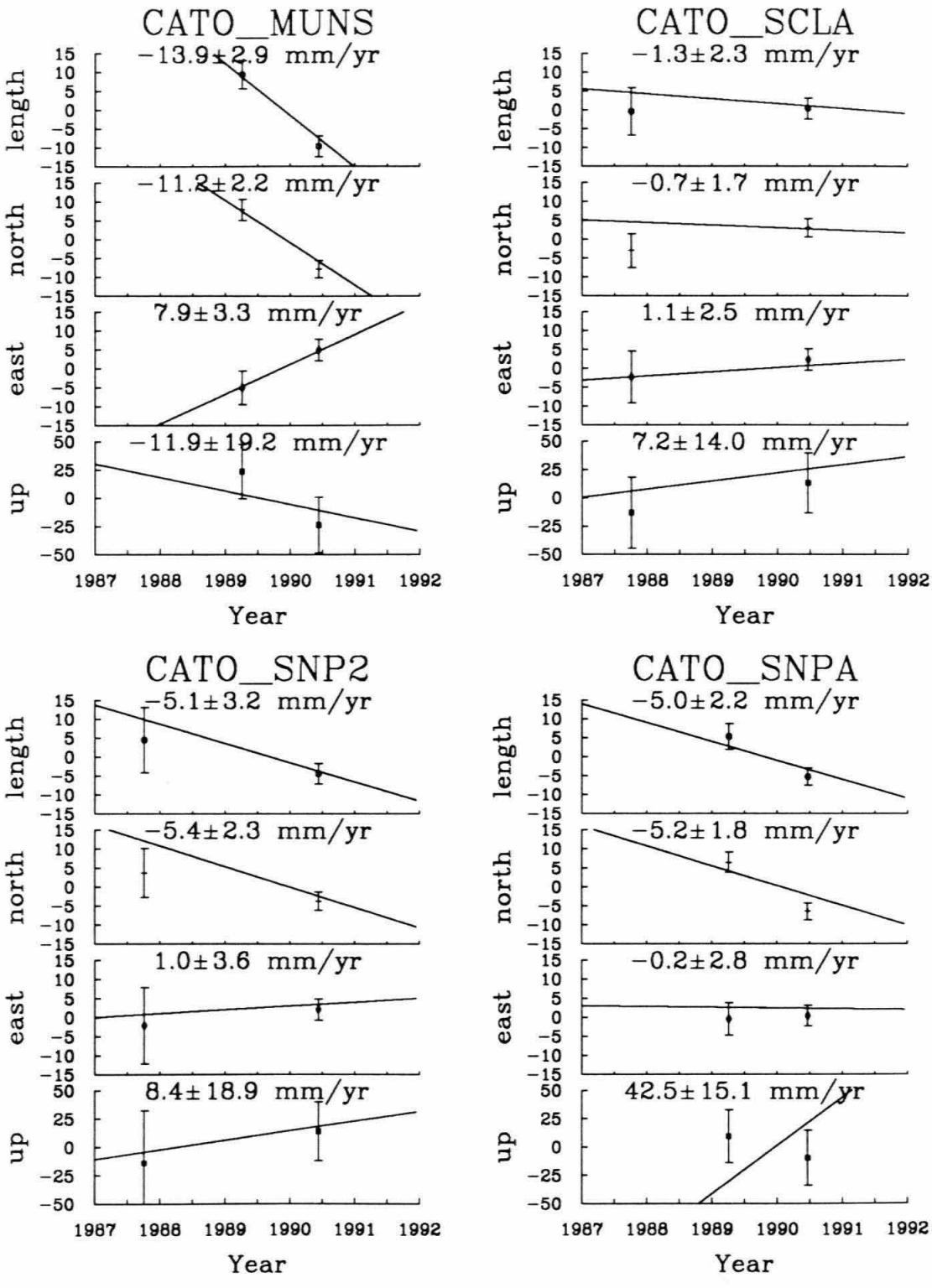
CATO_MUNS
−13.9±2.9 mm/yr
−11.2±2.2 mm/yr
7.9±3.3 mm/yr
−11.9±19.2 mm/yr
CATO_SCLA
−1.3±2.3 mm/yr
−0.7±1.7 mm/yr
1.1±2.5 mm/yr
7.2±14.0 mm/yr
CATO_SNP2
−5.1±3.2 mm/yr
−5.4±2.3 mm/yr
1.0±3.6 mm/yr
8.4±18.9 mm/yr
CATO_SNPA
−5.0±2.2 mm/yr
−5.2±1.8 mm/yr
−0.2±2.8 mm/yr
42.5±15.1 mm/yr
length
north
east
up
1987 1988 1989 1990 1991 1992
Year

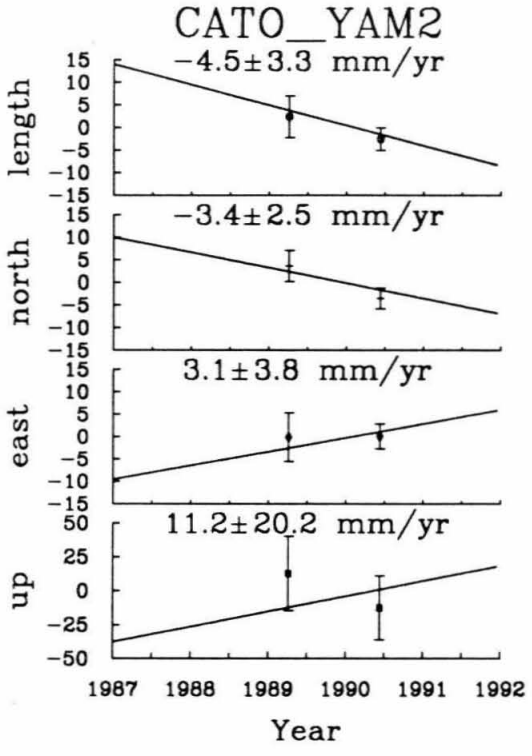
CATO_YAM2
−4.5±3.3 mm/yr
−3.4±2.5 mm/yr
3.1±3.8 mm/yr
11.2±20.2 mm/yr
length
north
east
up
Year

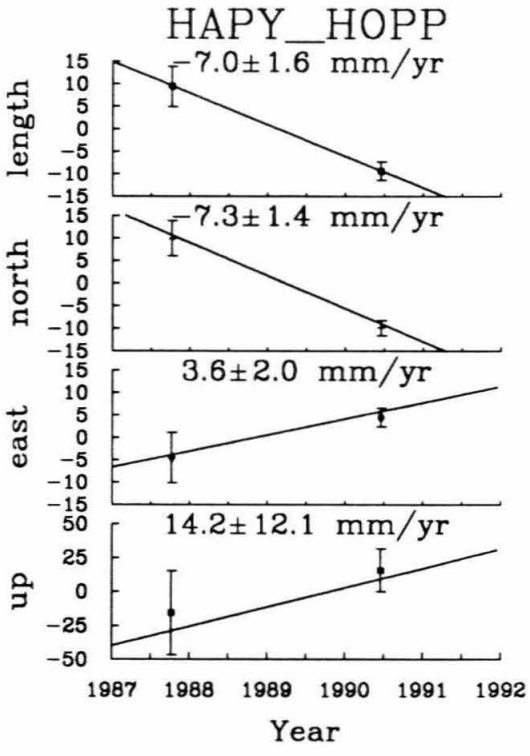
HAPY_HOPP
−7.0±1.6 mm/yr
−7.3±1.4 mm/yr
3.6±2.0 mm/yr
14.2±12.1 mm/yr
length
north
east
up
Year

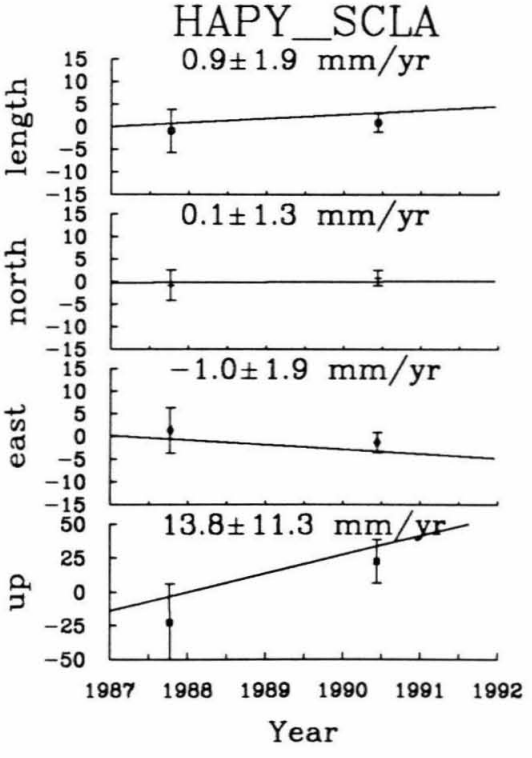
HAPY_SCLA
0.9±1.9 mm/yr
0.1±1.3 mm/yr
−1.0±1.9 mm/yr
13.8±11.3 mm/yr
length
north
east
up
Year

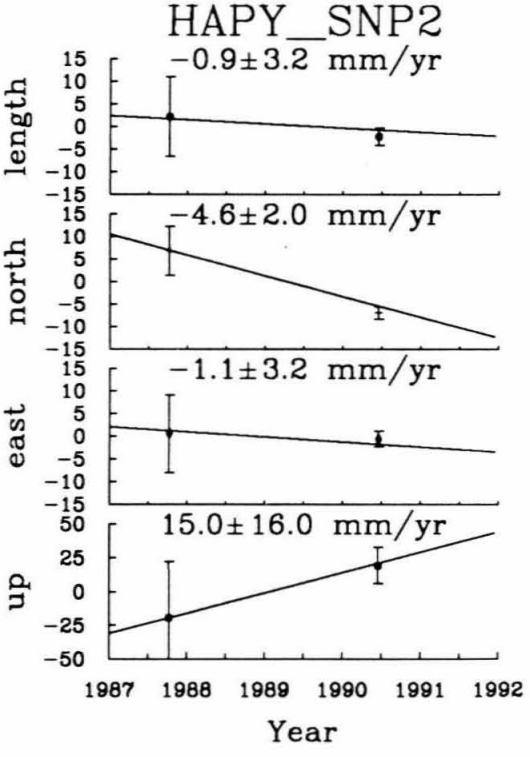
HAPY_SNP2
−0.9±3.2 mm/yr
−4.6±2.0 mm/yr
−1.1±3.2 mm/yr
15.0±16.0 mm/yr
length
north
east
up
Year

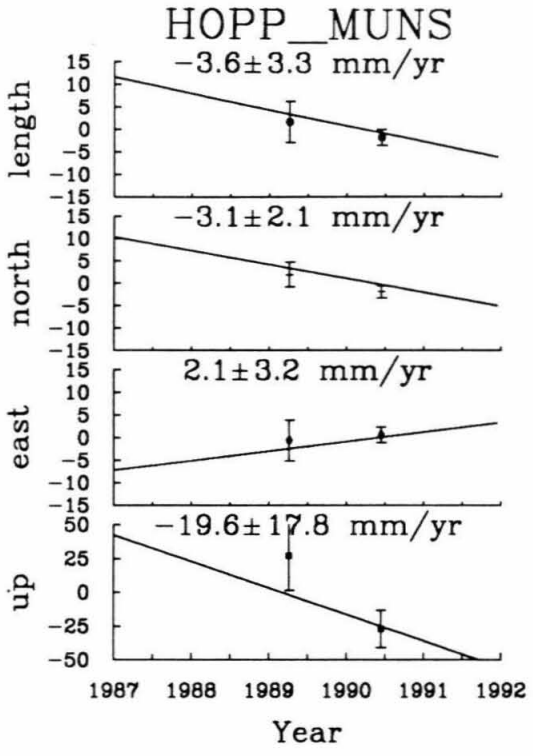
HOPP__MUNS
−3.6±3.3 mm/yr
length
−3.1±2.1 mm/yr
north
2.1±3.2 mm/yr
east
−19.6±17.8 mm/yr
up
1987 1988 1989 1990 1991 1992
Year

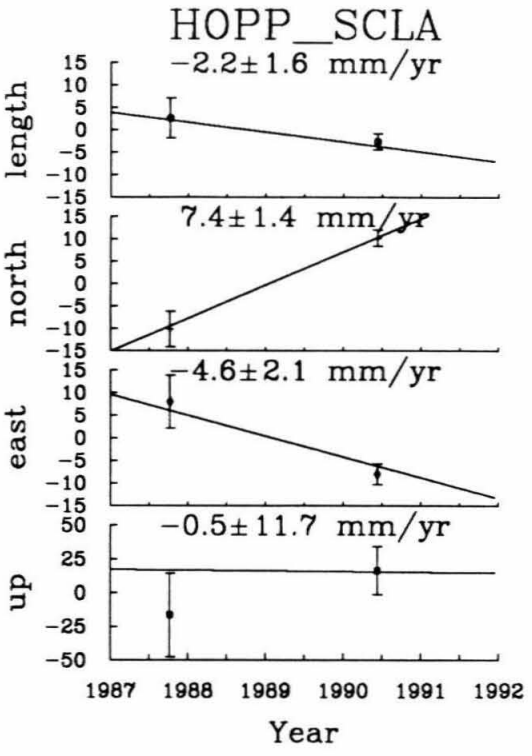
HOPP__SCLA
−2.2±1.6 mm/yr
length
7.4±1.4 mm/yr
north
−4.6±2.1 mm/yr
east
−0.5±11.7 mm/yr
up
1987 1988 1989 1990 1991 1992
Year

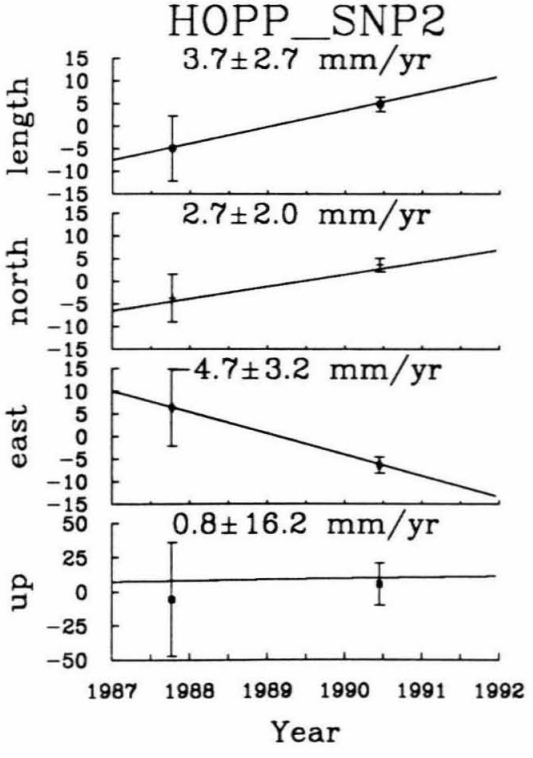
HOPP__SNP2
3.7±2.7 mm/yr
length
2.7±2.0 mm/yr
north
−4.7±3.2 mm/yr
east
0.8±16.2 mm/yr
up
1987 1988 1989 1990 1991 1992
Year

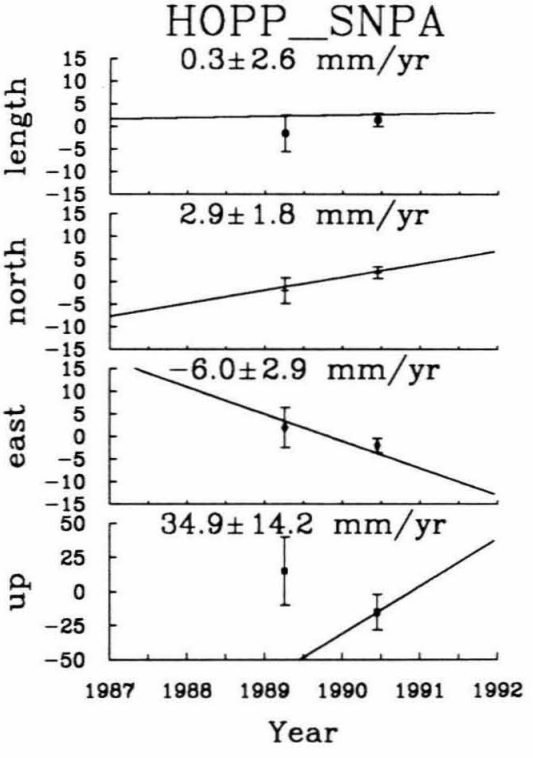
HOPP__SNPA
0.3±2.6 mm/yr
length
2.9±1.8 mm/yr
north
−6.0±2.9 mm/yr
east
34.9±14.2 mm/yr
up
1987 1988 1989 1990 1991 1992
Year

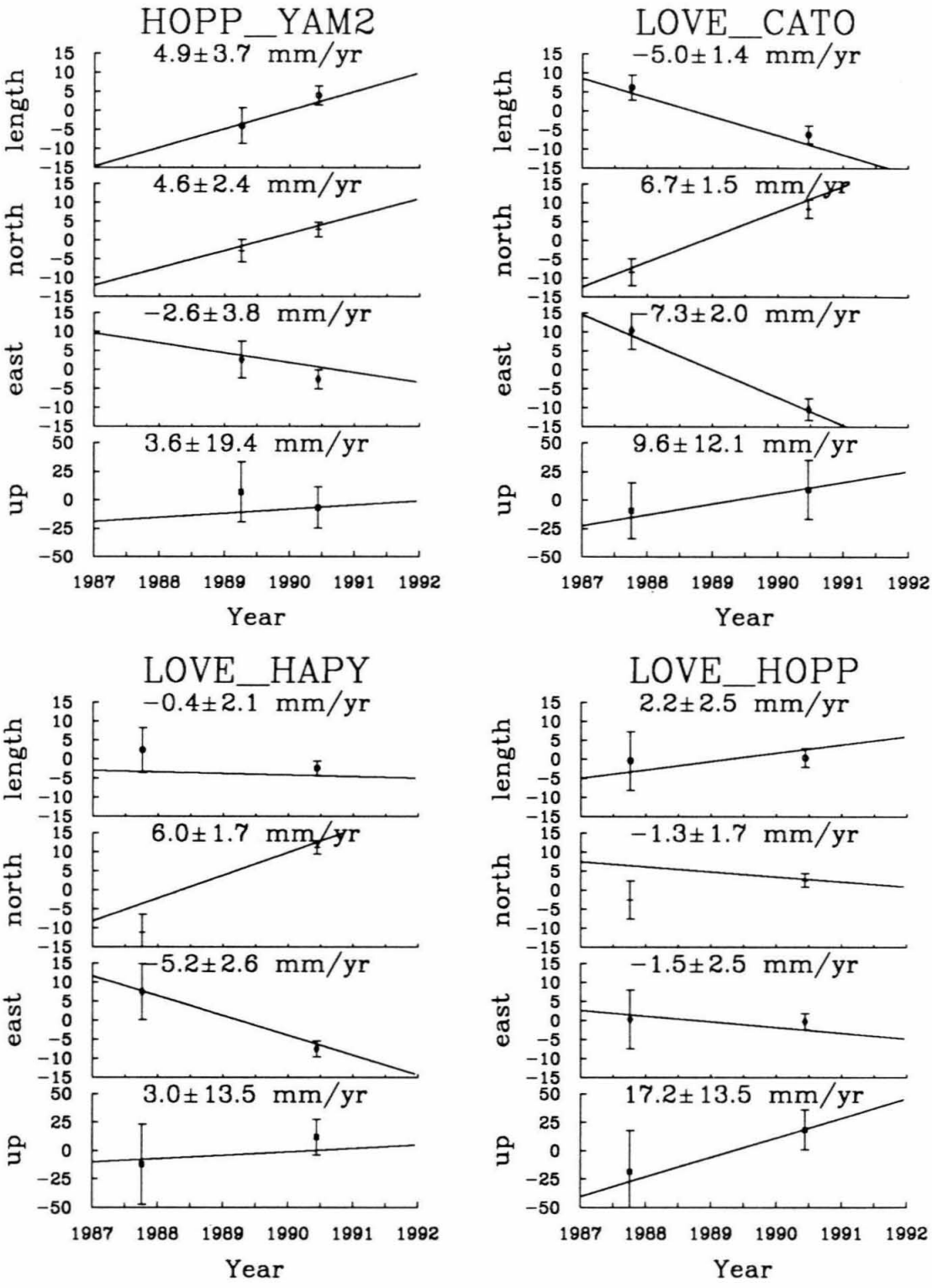
HOPP__YAM2
4.9±3.7 mm/yr
4.6±2.4 mm/yr
−2.6±3.8 mm/yr
3.6±19.4 mm/yr
LOVE__CATO
−5.0±1.4 mm/yr
6.7±1.5 mm/yr
7.3±2.0 mm/yr
9.6±12.1 mm/yr
LOVE__HAPY
−0.4±2.1 mm/yr
6.0±1.7 mm/yr
−5.2±2.6 mm/yr
3.0±13.5 mm/yr
LOVE__HOPP
2.2±2.5 mm/yr
−1.3±1.7 mm/yr
−1.5±2.5 mm/yr
17.2±13.5 mm/yr
length
north
east
up
1987 1988 1989 1990 1991 1992
Year

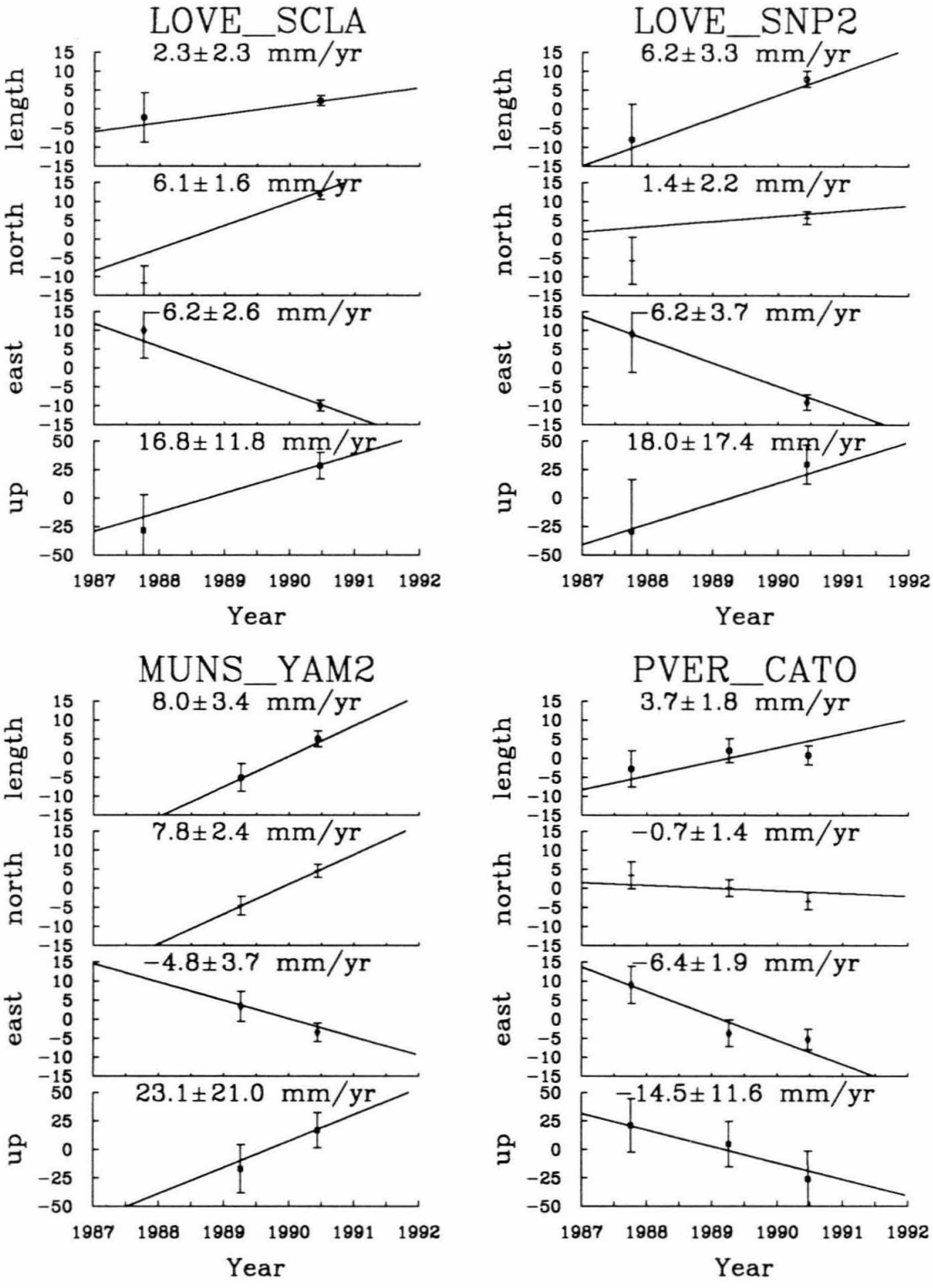
LOVE_SCLA
2.3±2.3 mm/yr
6.1±1.6 mm/yr
6.2±2.6 mm/yr
16.8±11.8 mm/yr
LOVE_SNP2
6.2±3.3 mm/yr
1.4±2.2 mm/yr
6.2±3.7 mm/yr
18.0±17.4 mm/yr
MUNS_YAM2
8.0±3.4 mm/yr
7.8±2.4 mm/yr
−4.8±3.7 mm/yr
23.1±21.0 mm/yr
PVER_CATO
3.7±1.8 mm/yr
−0.7±1.4 mm/yr
−6.4±1.9 mm/yr
−14.5±11.6 mm/yr
length
north
east
up
Year

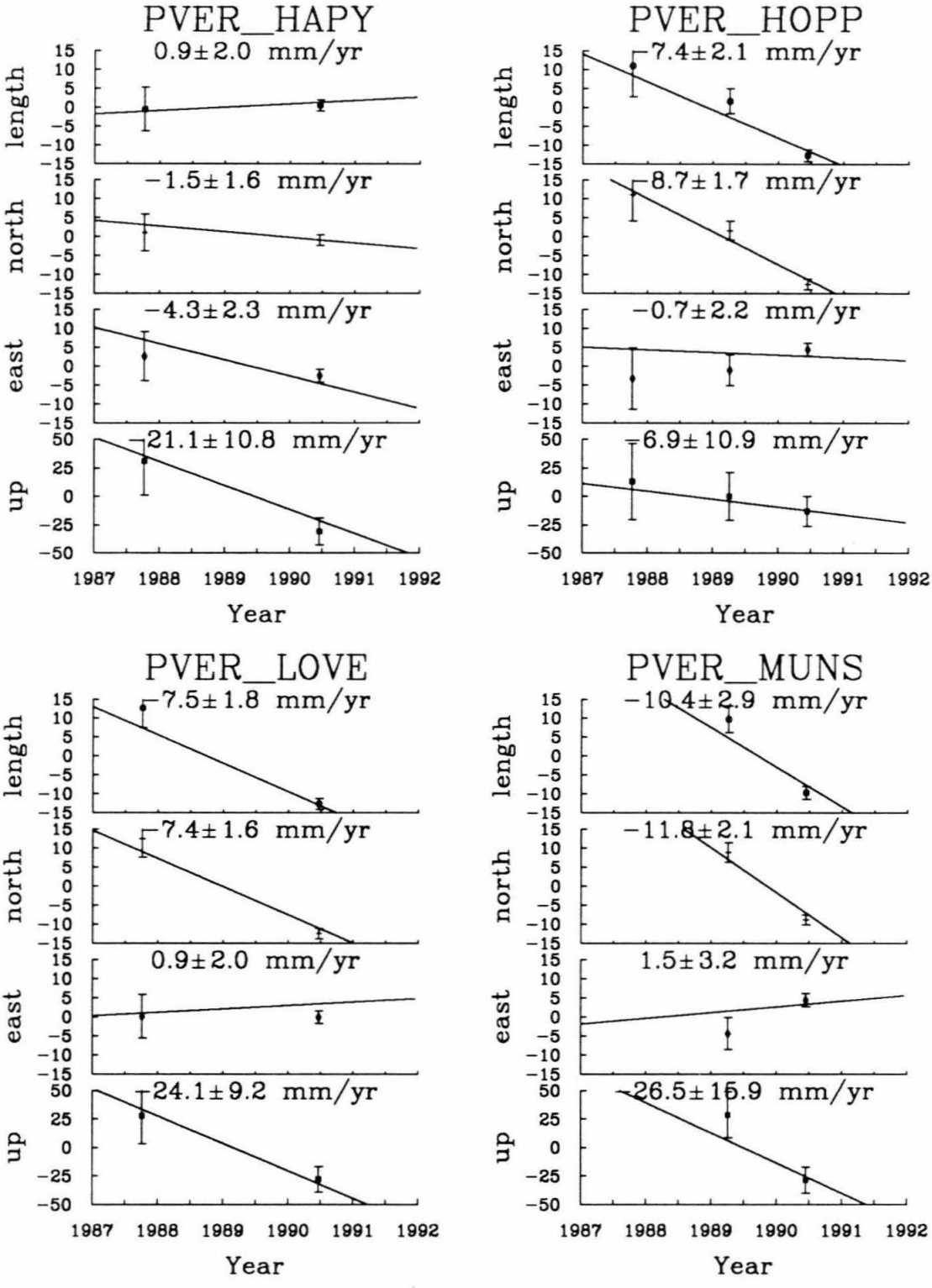
PVER_HAPY
0.9±2.0 mm/yr
−1.5±1.6 mm/yr
−4.3±2.3 mm/yr
−21.1±10.8 mm/yr
PVER_HOPP
−7.4±2.1 mm/yr
−8.7±1.7 mm/yr
−0.7±2.2 mm/yr
−6.9±10.9 mm/yr
PVER_LOVE
−7.5±1.8 mm/yr
−7.4±1.6 mm/yr
0.9±2.0 mm/yr
−24.1±9.2 mm/yr
PVER_MUNS
−10.4±2.9 mm/yr
−11.8±2.1 mm/yr
1.5±3.2 mm/yr
−26.5±15.9 mm/yr
length
north
east
up
Year
1987
1988
1989
1990
1991
1992

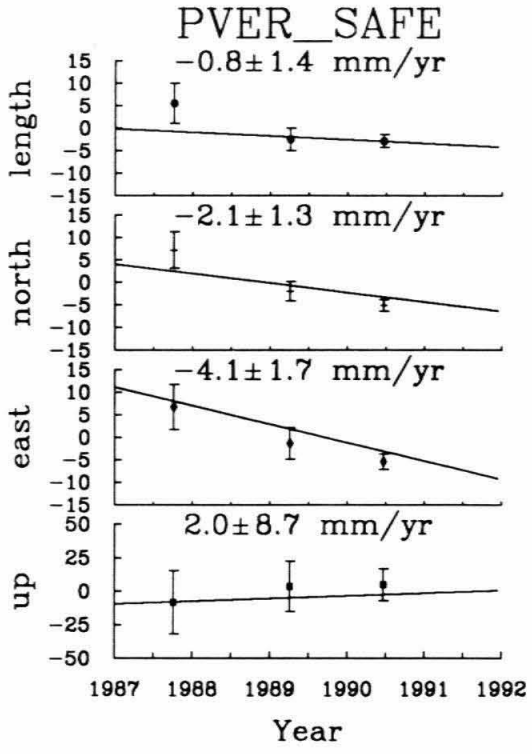
PVER_SAFE
−0.8±1.4 mm/yr
−2.1±1.3 mm/yr
−4.1±1.7 mm/yr
2.0±8.7 mm/yr
length
north
east
up
Year

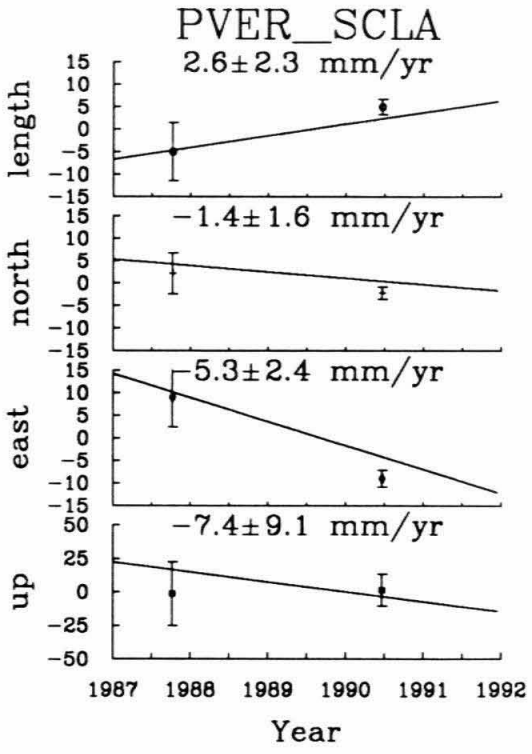
PVER_SCLA
2.6±2.3 mm/yr
−1.4±1.6 mm/yr
5.3±2.4 mm/yr
−7.4±9.1 mm/yr
length
north
east
up
Year

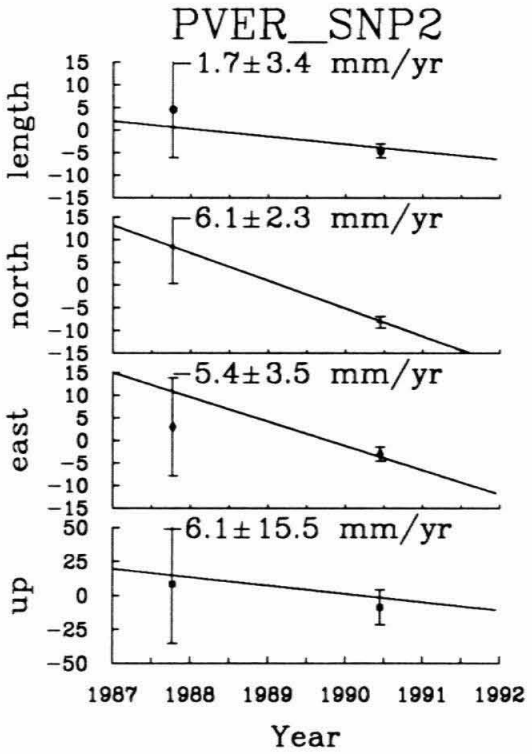
PVER_SNP2
1.7±3.4 mm/yr
6.1±2.3 mm/yr
−5.4±3.5 mm/yr
6.1±15.5 mm/yr
length
north
east
up
Year

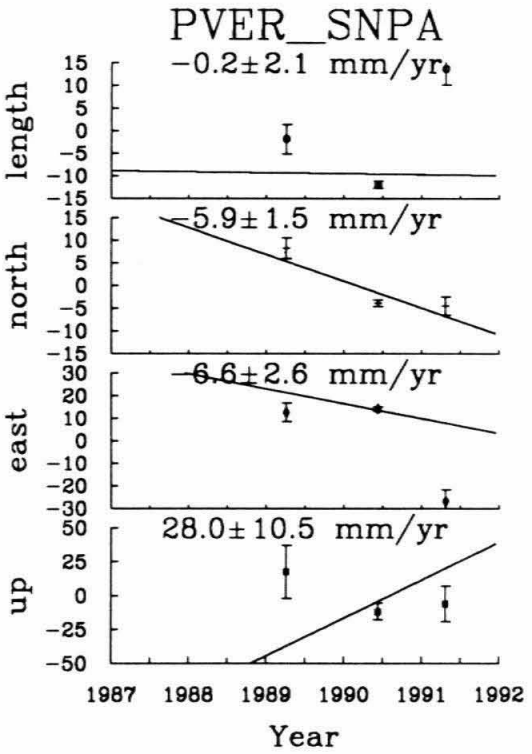
PVER_SNPA
−0.2±2.1 mm/yr
−5.9±1.5 mm/yr
6.6±2.6 mm/yr
28.0±10.5 mm/yr
length
north
east
up
Year

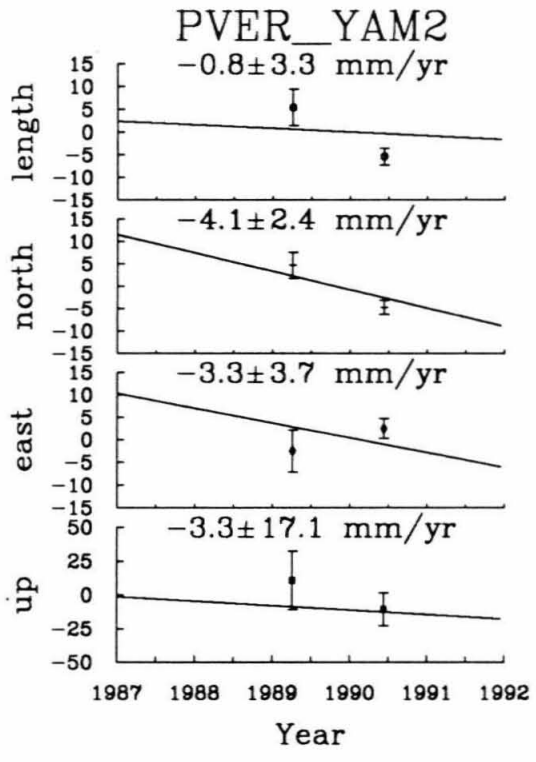
PVER_YAM2
−0.8±3.3 mm/yr
−4.1±2.4 mm/yr
−3.3±3.7 mm/yr
−3.3±17.1 mm/yr
length
north
east
up
Year

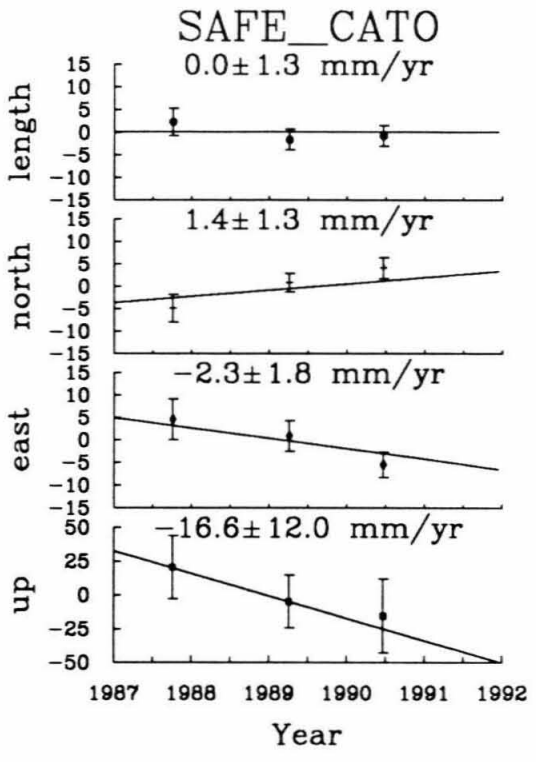
SAFE_CATO
0.0±1.3 mm/yr
1.4±1.3 mm/yr
−2.3±1.8 mm/yr
−16.6±12.0 mm/yr
length
north
east
up
Year

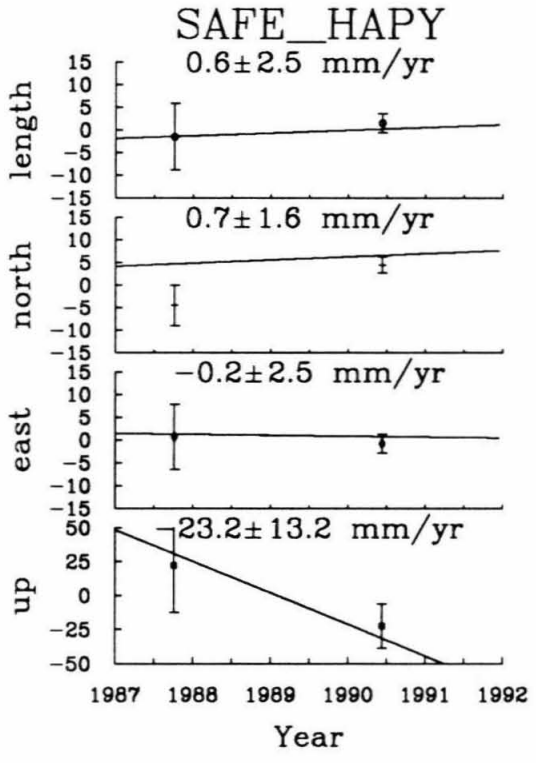
SAFE_HAPY
0.6±2.5 mm/yr
0.7±1.6 mm/yr
−0.2±2.5 mm/yr
−23.2±13.2 mm/yr
length
north
east
up
Year

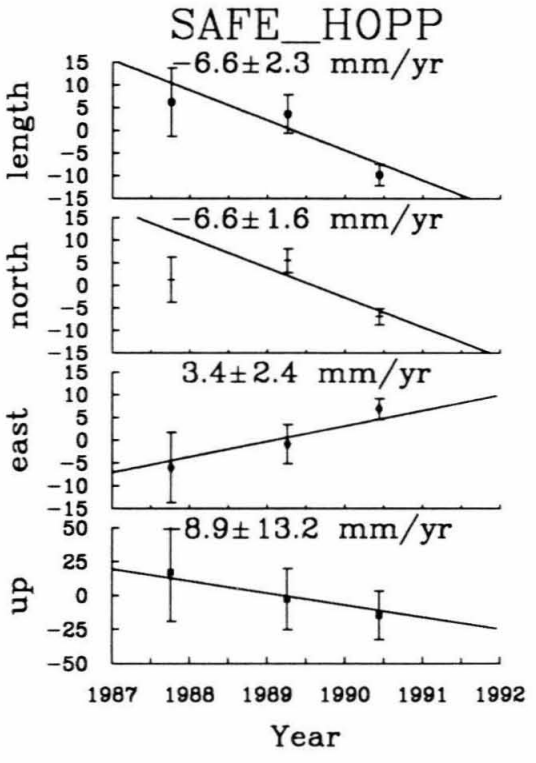
SAFE_HOPP
−6.6±2.3 mm/yr
−6.6±1.6 mm/yr
3.4±2.4 mm/yr
−8.9±13.2 mm/yr
length
north
east
up
Year

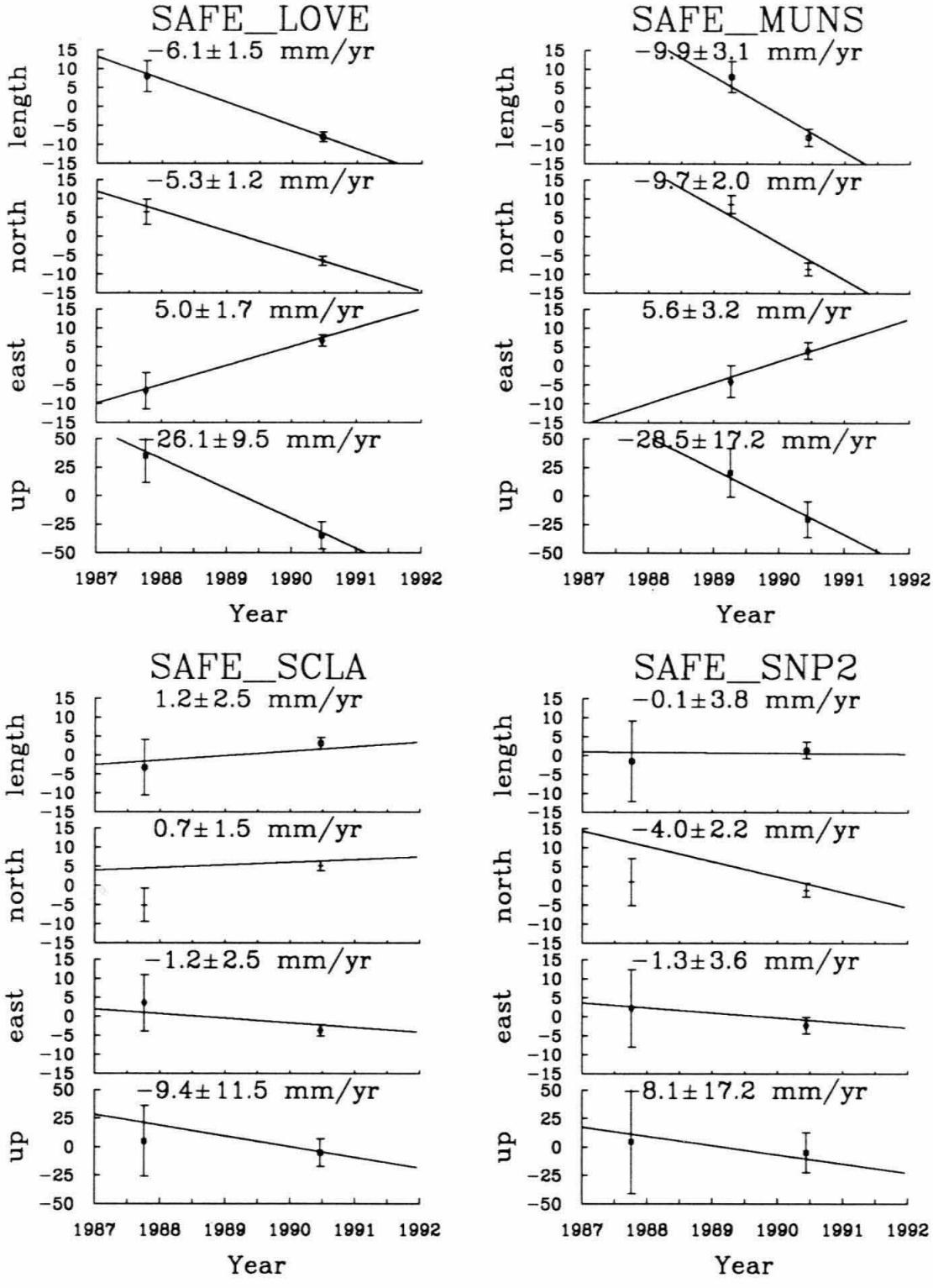
SAFE_LOVE
−6.1±1.5 mm/yr
−5.3±1.2 mm/yr
5.0±1.7 mm/yr
26.1±9.5 mm/yr
SAFE_MUNS
−9.9±3.1 mm/yr
−9.7±2.0 mm/yr
5.6±3.2 mm/yr
−28.5±17.2 mm/yr
SAFE_SCLA
1.2±2.5 mm/yr
0.7±1.5 mm/yr
−1.2±2.5 mm/yr
−9.4±11.5 mm/yr
SAFE_SNP2
−0.1±3.8 mm/yr
−4.0±2.2 mm/yr
−1.3±3.6 mm/yr
8.1±17.2 mm/yr
length
north
east
up
Year
1987
1988
1989
1990
1991
1992

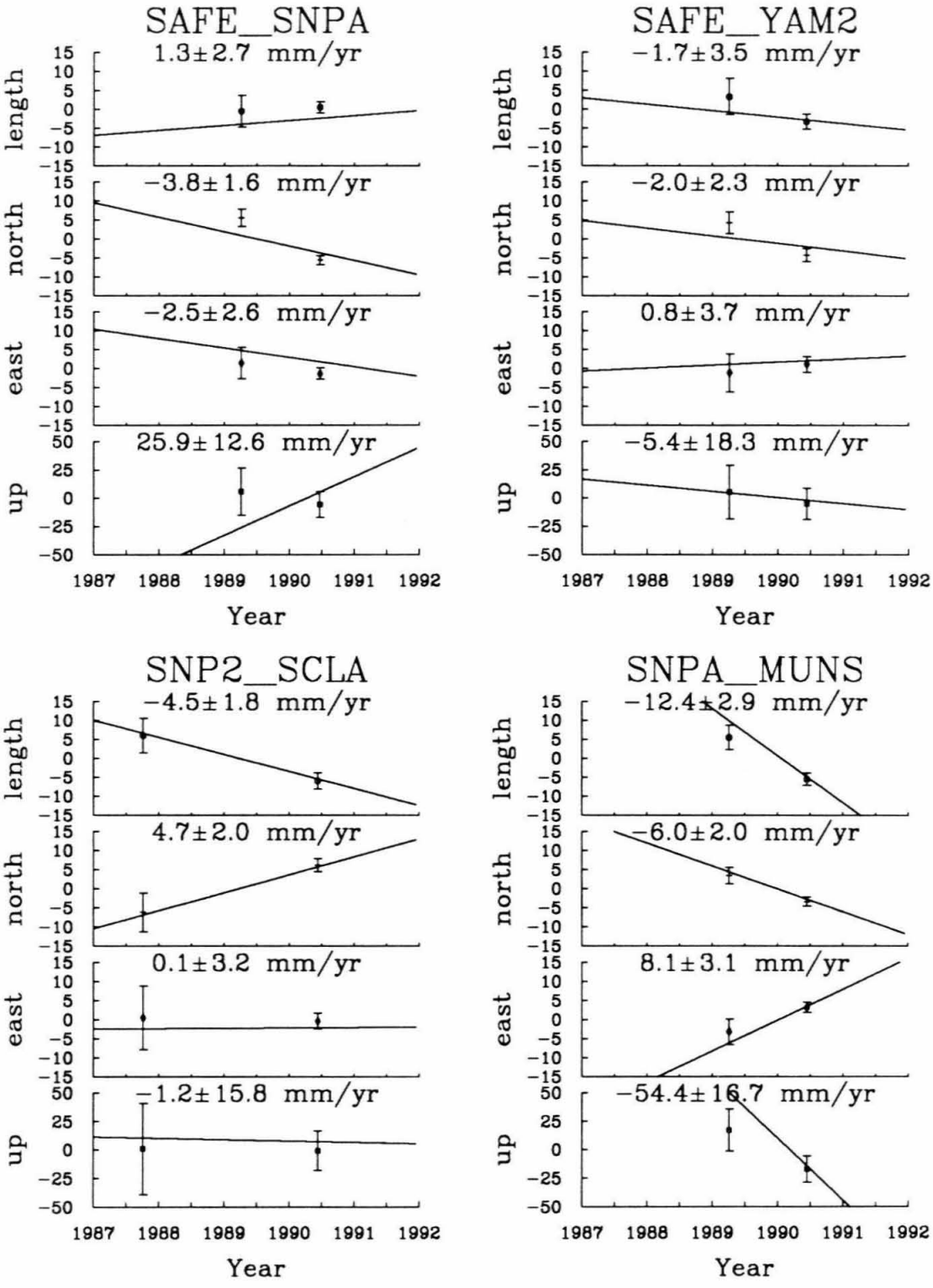
SAFE_SNPA
1.3±2.7 mm/yr
−3.8±1.6 mm/yr
−2.5±2.6 mm/yr
25.9±12.6 mm/yr
SAFE_YAM2
−1.7±3.5 mm/yr
−2.0±2.3 mm/yr
0.8±3.7 mm/yr
−5.4±18.3 mm/yr
SNP2_SCLA
−4.5±1.8 mm/yr
4.7±2.0 mm/yr
0.1±3.2 mm/yr
−1.2±15.8 mm/yr
SNPA_MUNS
−12.4±2.9 mm/yr
−6.0±2.0 mm/yr
8.1±3.1 mm/yr
−54.4±16.7 mm/yr
length
north
east
up
Year

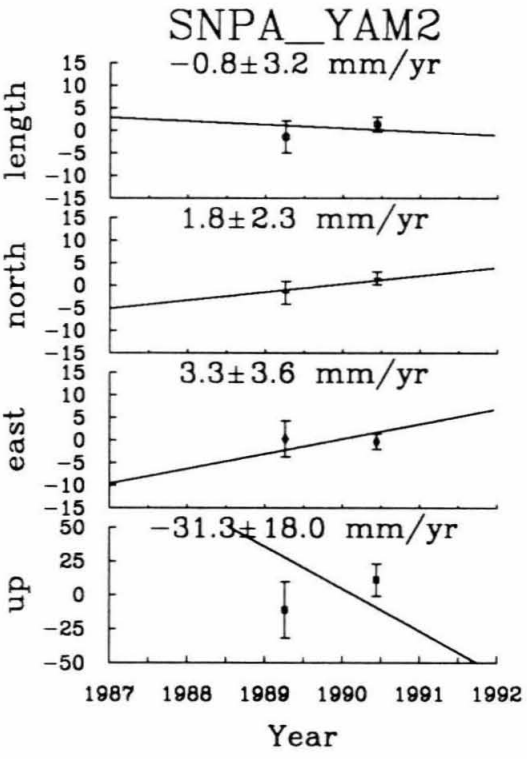
SNPA__YAM2
−0.8±3.2 mm/yr
1.8±2.3 mm/yr
3.3±3.6 mm/yr
−31.3±18.0 mm/yr
length
north
east
up
15
10
5
0
−5
−10
−15
50
25
0
−25
−50
1987
1988
1989
1990
1991
1992
Year

3.1.2 Strain Calculations

To better understand the deformation in the Ventura basin network and to compare the results obtained in this network to those observed elsewhere, we calculated deformation parameters from the velocities. We divided the network into several subnetworks to examine the distribution of strain throughout the network. Because the vertical error is larger than the horizontal error by a factor of four and because closure is poor for the vertical rates within the network, we calculate only the horizontal crustal deformation parameters.

From the velocities and positions we first solve for the velocity gradient tensor:

$$\begin{bmatrix} \frac{\partial \dot{u}_e}{\partial E} & \frac{\partial \dot{u}_e}{\partial N} \\ \frac{\partial \dot{u}_n}{\partial E} & \frac{\partial \dot{u}_n}{\partial N} \end{bmatrix} \tag{3.1}$$

where $\dot{u}$ is the velocity of a station, relative to a fixed station, and e and n refer to east and north respectively. E and N refer to the east and north baseline components respectively. Using weighted least squares we solve the following two systems of equations for the velocity gradients.

$$\partial \dot{u}_e = (\frac{\partial \dot{u}_e}{\partial E})E + (\frac{\partial \dot{u}_e}{\partial N})N \tag{3.2}$$

$$\partial \dot{u}_n = (\frac{\partial \dot{u}_n}{\partial E})E + (\frac{\partial \dot{u}_n}{\partial N})N \tag{3.3}$$

From the velocity gradient tensor we calculate the following crustal deformation parameters [*Drew and Snay*, 1989]:

$$\text{aerial dilation rate, } \dot{\Delta} = \dot{u}_{nn} + \dot{u}_{ee} \tag{3.4}$$

$$\text{clockwise rotation rate, } \dot{\omega} = (\dot{u}_{en} - \dot{u}_{ne})/2 \tag{3.5}$$

$$\text{first component of horizontal shear rate, } \dot{\gamma}_1 = \dot{u}_{ee} - \dot{u}_{nn} \tag{3.6}$$

$$\text{second component of horizontal shear rate, } \dot{\gamma}_2 = \dot{u}_{en} + \dot{u}_{ne} \tag{3.7}$$

$$\text{maximum horizontal shear rate, } \dot{\gamma} = \sqrt{(\dot{\gamma}_1^2 + \dot{\gamma}_2^2)} \tag{3.8}$$

$$\text{azimuth of maximum compression, } \theta = \frac{\arctan(\frac{\dot{\gamma}_1}{\dot{\gamma}_2})}{2} \tag{3.9}$$

We weighted the data according to the formal errors of the velocities.

To calculate the strains we divided the network into four regions (figure 3.4). The strain rate for the northern region is the most suspect, because of the short time period between observations, but we can compare our estimation of the strain with that obtained by *Eberhart-Phillips et al.* [1990]. We divided the basin into the central and eastern regions and also combined both regions to calculate the strain for the complete basin. The southern region lies to the south of the Oak Ridge. We did not include Yam 2 (YAM2) or Palos Verdes (PVER) in the calculations. The rate for Yam 2 (YAM2) is questionable and the site is possibly in a different tectonic environment. Palos Verdes (PVER) lies too far from the basin to reflect the tectonic environment of the basin.

The highest strain rates are in the regions that span the basin (tables 3.3 and 3.4). No significant deformation is occurring to the south of the basin while there is some deformation north of the basin. The deformation north of the basin that we calculate is not significantly different than that obtained by *Eberhart-Phillips et al.* [1990]. The maximum shear strain rate, $\dot{\gamma}$, that they obtain, $0.30 \pm 0.02 \times 10^{-6}$ μrad/yr, is slightly lower than the rate that we obtain, but within the error. Two factors might account for this. It is possible that some additional compression is occurring just to the north of the basin and that much less compression is taking place between

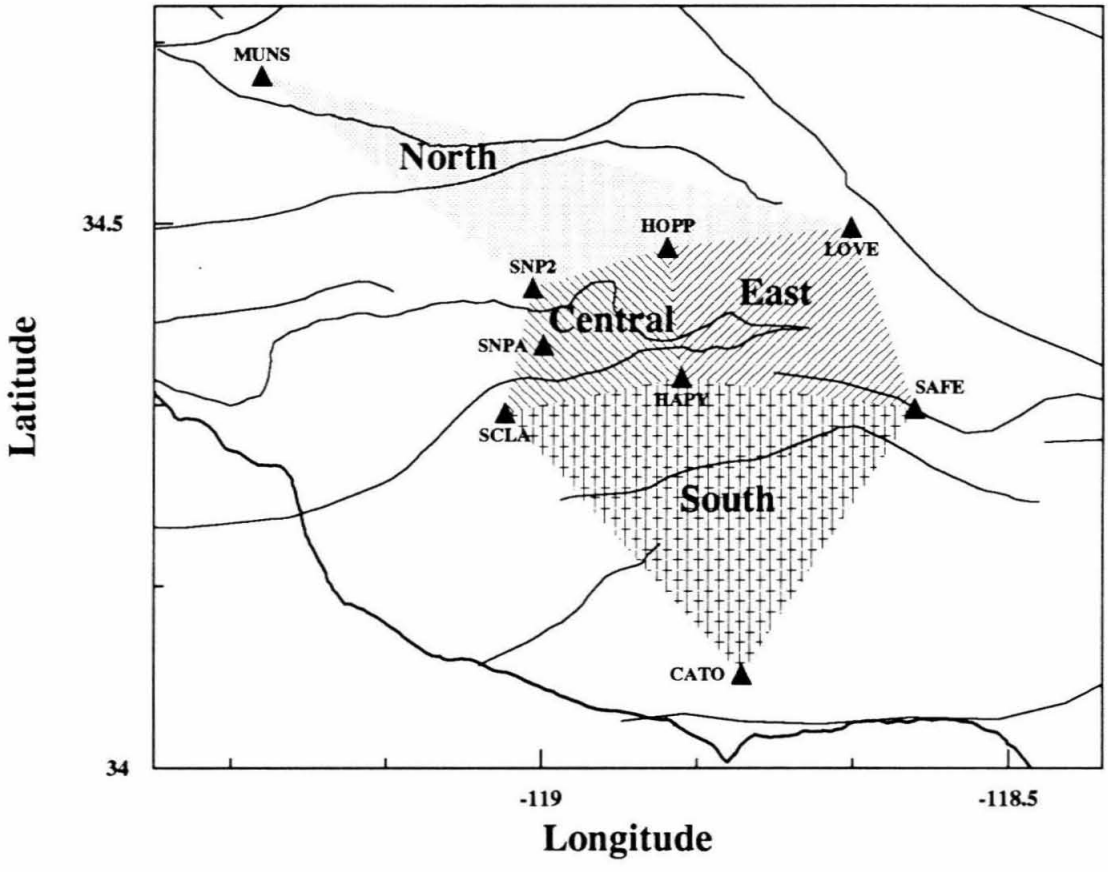

Figure 3.4: Shaded zones mark the various regions for the strain calculations. The north and east regions are combined to comprise the basin subnetwork.

Munson (MUNS) and the San Andreas fault. Because all of the strain calculations mentioned assume that strain is uniform both spatially and temporally, it might be that the *Eberhart-Phillips et al.* [1990] strain rate is an average rate for the entire Los Padres-Tehachapi network and does not adequately reflect compression occurring just north of the basin. The other possible and likely factor accounting for the difference is that the one year separating the measurements is not long enough to determine the strain rate well. A measurement error during one of the occupations would not be reflected in the formal error, but could skew the rate by a significant amount.

Further subdivision of the basin suggests that the most deformation is occurring in the east-central Ventura basin (table 3.4). In all cases the azimuth of maximum compression is oriented north-northwest. The maximum compression is oriented perpendicular to the trend of the basin in the central network. In the eastern region the compression axis is possibly oriented in a more westerly direction, although the errors on this parameter are fairly large.

The azimuth of maximum right-lateral shear (oriented 45°W of the azimuth of maximum compression) parallels the strike of the San Andreas fault in the northern region. It is oriented slightly more in the direction of the plate motion further to the south. Another interesting observation is that the strain environment changes from primarily strike-slip, north of the basin, to more compressional across the basin (figure 3.5). Approximately 5 mm/yr of compression and 2 mm/yr right-lateral shear can be accounted for across the basin. Figure 3.6 shows the estimated strains in the context of strains estimated for the surrounding region.

Parameter	(units)	north	basin	south
$\dot{u}_{ee}$	(μstrain/yr)	$.12 \pm .10$	$.09 \pm .05$	$.02 \pm .04$
$\dot{u}_{en}$	(μstrain/yr)	$.40 \pm .26$	$.30 \pm .07$	$.07 \pm .07$
$\dot{u}_{ne}$	(μstrain/yr)	$.00 \pm .06$	$.02 \pm .04$	$-.02 \pm .03$
$\dot{u}_{nn}$	(μstrain/yr)	$-.20 \pm .16$	$-.43 \pm .06$	$-.03 \pm .05$
$\dot{\Delta}$	(μstrain/yr)	$-.08 \pm .19$	$-.34 \pm .08$	$-.01 \pm .06$
$\dot{\omega}$	(°/Myr)	12 ± 8	8 ± 2	3 ± 2
$\dot{\gamma}_1$	(μrad/yr)	$.32 \pm .19$	$.52 \pm .08$	$.06 \pm .06$
$\dot{\gamma}_2$	(μrad/yr)	$.39 \pm .27$	$.33 \pm .08$	$.05 \pm .07$
$\dot{\gamma}$	(μrad/yr)	$.51 \pm .24$	$.61 \pm .08$	$.08 \pm .07$
θ	(deg)	-26 ± 27	-16 ± 8	-19 ± 43

Table 3.3: Strain calculations for the basin and subnetworks both north and south of the basin. Parameters are described in the text. Note that compression is negative.

Parameter	(units)	central	east
$\dot{u}_{ee}$	(μstrain/yr)	$.20 \pm .12$	$.05 \pm .08$
$\dot{u}_{en}$	(μstrain/yr)	$.21 \pm .12$	$.28 \pm .12$
$\dot{u}_{ne}$	(μstrain/yr)	$.05 \pm .10$	$.04 \pm .07$
$\dot{u}_{nn}$	(μstrain/yr)	$-.48 \pm .10$	$-.41 \pm .09$
$\dot{\Delta}$	(μstrain/yr)	$-.28 \pm .16$	$-.36 \pm .12$
$\dot{\omega}$	(°/Myr)	5 ± 5	7 ± 4
$\dot{\gamma}_1$	(μrad/yr)	$.68 \pm .16$	$.45 \pm .12$
$\dot{\gamma}_2$	(μrad/yr)	$.25 \pm .16$	$.32 \pm .13$
$\dot{\gamma}$	(μrad/yr)	$.72 \pm .16$	$.56 \pm .13$
θ	(deg)	-10 ± 12	-18 ± 13

Table 3.4: Strain calculations for the east and central basin subnetworks. Parameters are described in the text. Central basin actually refers to the east-central Ventura basin. Note that compression is negative.

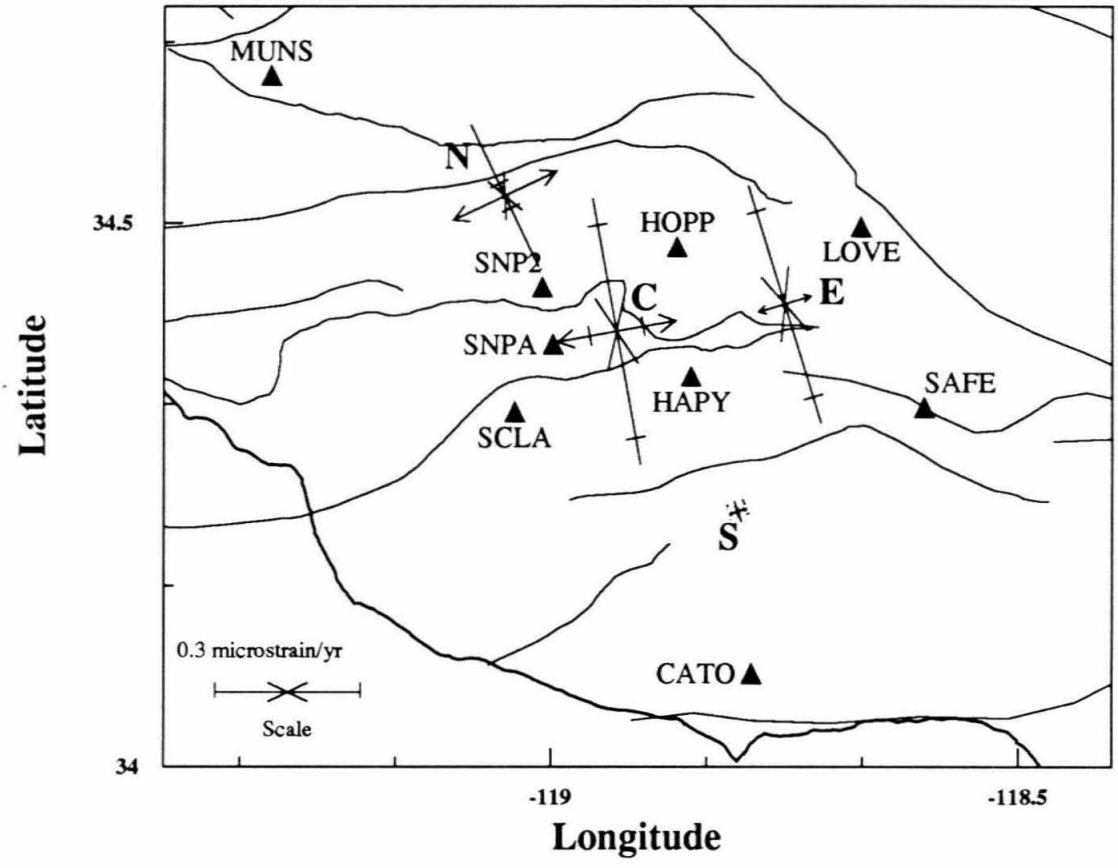

Figure 3.5: Arrows showing the principal compression and extension strain axes. The cross marks on the axes represent the standard error of the strain component. N–north region, C–central region, E–east region, S–south region.

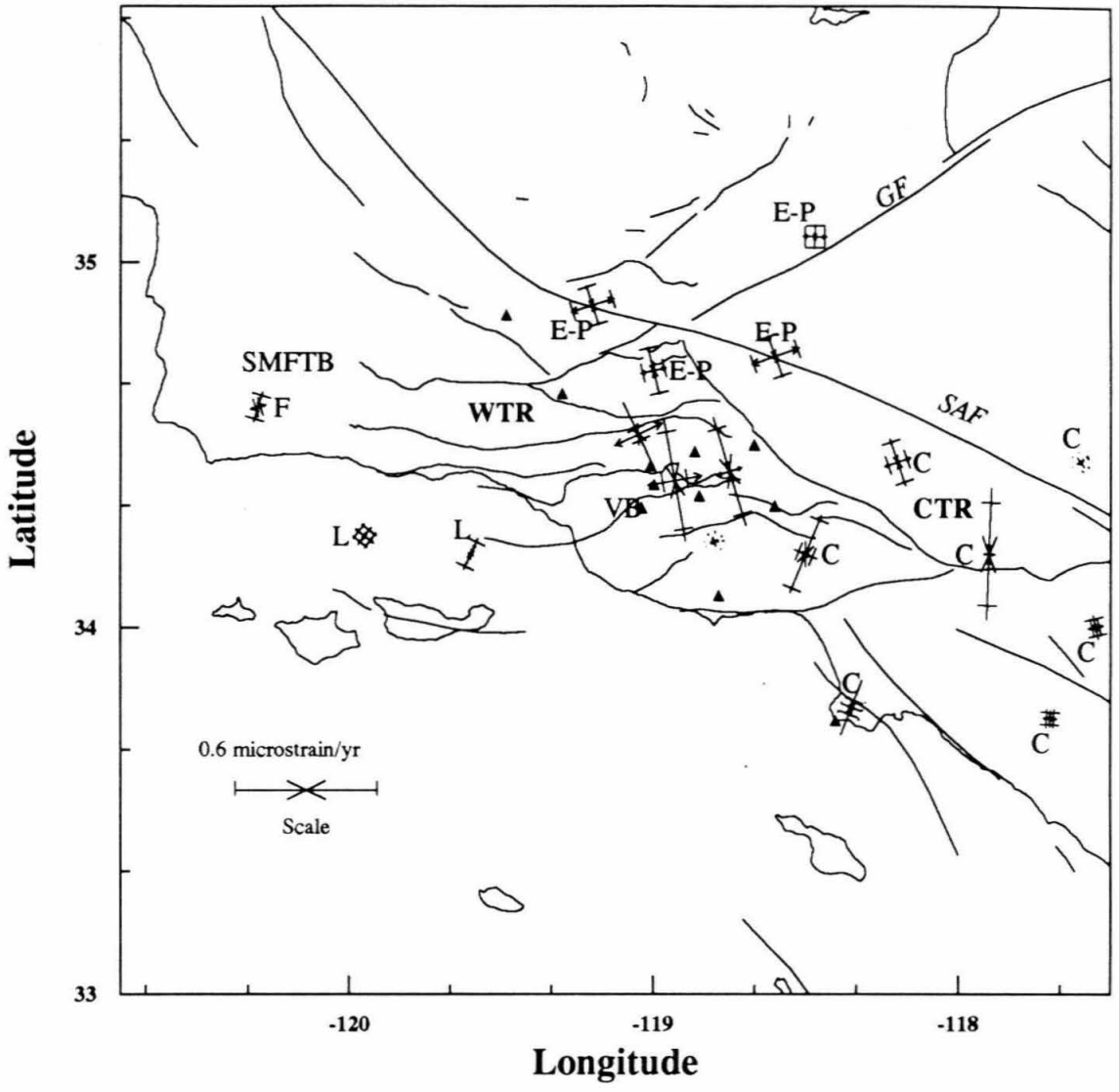

Figure 3.6: Summary of principal strains near the Ventura basin region. The cross marks on the axes represent the standard error of the strain component. *GF*–Garlock fault, *SAF*–San Andreas fault, **WTR**–western Transverse Ranges, **CTR**–central Transverse Ranges, SMFTB–Santa Maria fold and thrust belt, F–*Feigl et al.*, [1990], L–*Larsen* [1991], E-P–*Eberhart-Phillips et al.*, [1990], C–*Cline et al*, [1984]. Results from this study are not labeled.

3.2 Comparison of Triangulation and GPS

We designed the original Ventura basin network to recover historical triangulation data. To compare GPS measurements with triangulation, the GPS observations must be converted to angles projected onto a reference ellipsoid. The angles should also be corrected for the deflection of the vertical. Other factors, such as lateral refraction, may complicate the comparison.

Triangulation only yields the strain parameters $\dot{\gamma}_1$ and $\dot{\gamma}_2$ (and, hence, $\dot{\gamma}$ and the azimuths of maximum compression and shear). The angular changes provide no information regarding either dilatation or rotation. Comparing angles measured by triangulation with those determined from GPS provides a longer time baseline and a test of the GPS results. We calculate $\dot{\gamma}_1$ and $\dot{\gamma}_2$ with the method described in *Frank* [1966] and *Prescott* [1976]. For a k^{th} angle ϕ at time j and station i

$$\phi_{ijk} = t_{ij}(A^1_{ik}\dot{\gamma}_1 + A^2_{ik}\dot{\gamma}_2) + \phi^0_{ik}$$

where A^1 and A^2 are coefficients that depend on the azimuths from the station i to the first and second stations.

$$A^1_{ik} = \frac{\sin 2\theta^2_{ik} - \sin 2\theta^1_{ik}}{2}$$

$$A^2_{ik} = \frac{\cos 2\theta^2_{ik} - \cos 2\theta^1_{ik}}{2}$$

θ^1_{ik} and θ^2_{ik} are the azimuths to the first and second stations respectively. This method assumes uniform strain both spatially and temporally.

3.2.1 Reference Ellipsoids

To compare GPS and triangulation the GPS measurements must be converted into angles between stations. This is accomplished by projecting the station coordinates onto a reference ellipsoid and determining the angles between the projected vectors. For this study we are using site coordinates (latitude, longitude and elevation) in the North American Datum 1983 (NAD83). When converting site positions to angles between stations, the angles must be determined on the same reference ellipsoid as the site positions. We use *Robbin's formula* from *Bomford* [1971] to calculate the angles.

An ellipsoid has a spherical eccentricity, e, that is a function of the major and minor axes of the ellipsoid, a and b respectively.

$$e = \frac{\sqrt{a^2 - b^2}}{a}$$

The minor axis, b, can be determined from the flattening, f,

$$f = \frac{a - b}{a}$$

so

$$e = \sqrt{2f - f^2} \tag{3.10}$$

The azimuth, A_{ij}, from station i to station j can be written as

$$A_{ij} = \arctan\left[\frac{\sin \Delta\lambda}{\cos \phi_i \tan \psi_j - \sin \phi_i \cos \Delta\lambda}\right] \tag{3.11}$$

where

$$\tan \psi_j = (1 - e^2) \tan \phi_j + e^2 \frac{\nu_i \sin \phi_i}{\nu_j \cos \phi_j} \tag{3.12}$$

and

$$\Delta\lambda = \lambda_j - \lambda_i$$

λ is the latitude, north positive, and ϕ is the longitude, east positive from Greenwich. ν is the radius of curvature in the prime vertical of the station, and is a function of the major axis and the spherical eccentricity of the ellipsoid and the latitude.

$$\nu = \frac{a}{\sqrt{1 - e^2 \sin^2 \phi}} \tag{3.13}$$

It is crucial to calculate the azimuths on the same ellipsoid to which the coordinates refer, because the azimuth between stations is a function of the eccentricity of the ellipsoid and radius of curvature at each station. The more oblate the spheroid the larger the values of flattening and the greater the eccentricity. This causes a smaller radius of curvature at low latitudes, for a more oblate spheroid, and a larger radius of curvature at high latitudes. At southern California latitudes, projection of site coordinates onto a more oblate ellipsoid results in azimuths oriented more east-westerly than they actually are. In our initial comparison of GPS and triangulation, we projected our GPS results onto the more oblate NAD27 ellipsoid, which resulted in an artificially high estimation of strain [*Donnellan et al.*, 1989]. For the NAD83 reference ellipsoid the value of the flattening and the major axis of the ellipsoid are:

$$\begin{aligned} \frac{1}{f} &= 298.257222101 \\ a &= 6378137 \text{ meters} \end{aligned}$$

3.2.2 Deflection of the Vertical

To compare results from GPS to data from conventional surveys the deflection of the vertical must also be taken into account. The deflection, or deviation of the vertical,

is the angle between the tangent plane of the spheroid and the equipotential surface at the same point [*Bomford*, 1971]. Vertical is defined as normal to the geoid, not the ellipsoid, and deviation of the vertical may be due to either mass anomalies in a particular direction or to the arbitrary definition of the ellipsoid [*Bomford*, 1971]. The deflection of the vertical is recorded in terms of ξ, the north-south component of deflection, and η, the east-west component of deflection. ξ and η are considered positive when the downward vertical is deviated to the south or west respectively.

The deflection of the vertical causes the observed direction between two sites to be different than the actual direction between the sites. (The difference between two directions makes up an angle.) It is the component of the deviation, ζ, perpendicular to the line (direction), A, that must be taken into account when correcting for the deflection of the vertical.

$$\zeta = \xi \sin \mathrm{A} - \eta \cos \mathrm{A} \tag{3.14}$$

The required correction to the direction, ΔA is:

$$\begin{aligned} \Delta \mathrm{A}_{ij} &= -\zeta_{ij} \tan \beta_{ij} \\ &= -\zeta_{ij} \left(\frac{h_j - h_i}{L} \right) \end{aligned} \tag{3.15}$$

β_{ij} is the vertical angle from station i to station j, h_i and h_j are the elevations of the first and second stations respectively and L is the horizontal distance between the two stations.

If there is no elevation difference between the stations no correction needs to be applied. Figure 3.7 shows the azimuthal correction for various values of ζ and β. The correction becomes significant for values of $\beta >\sim 3°$. The typical distance between the triangulation stations is 15–30 km, so the difference in elevation between

sites must be at least 800–1500 meters for the deflection of the vertical to affect the observed angle significantly. The largest elevation angle in the Ventura basin is between the sites Santa Paula Peak (SNP2) and Santa Clara (SCLA) and has a value of 3.6°. This means that the component of deflection perpendicular to the line must be greater than 9.6″ to result in a correction greater than the error of the observed direction. Of course, two corrections must be applied to any given angle. According to *Bomford* [1971], the deflection may be on the order of 20″ in mountainous terrain.

The station pairs with the highest elevation angles are oriented north-south. The most prominent feature likely to affect the gravity field is the east-west trending western Transverse Ranges. The presence of the mountains produce a deflection of the vertical to the north. The value of ζ for the north-south station pairs would not be affected much by this northward component of deflection. The elevation angle between the two sites Hopper (HOPP) and Loma Verde (LOVE) is 1.9°, so a value of ζ greater than 20″ is necessary for the correction to be greater than the triangulation error. The only other significant elevation angle between a baseline oriented east-west is 1.1° between stations SAFE and HAPY. In this case ζ must be 37″ which is much larger than the estimate of 20″ that *Bomford* [1971] gives for the deflection due to a mountain. At least in one case (direction) the deflection should be considered.

The deflection of the vertical can be modeled by taking into account the terrain and buried mass anomalies. Buried mass anomalies can be estimated by modeling Bouguer gravity anomalies of the region. The horizontal components of gravitational attraction affect the deflection of the vertical, so local shallow anomalies influence the deflection the most. A Bouguer gravity map of the Ventura basin region [*Hanna et al.*,

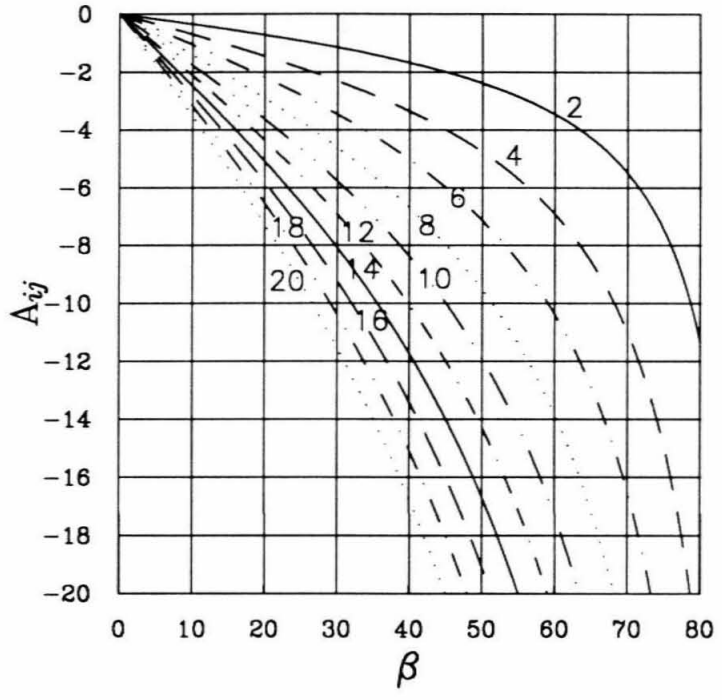

Figure 3.7: Correction, A_{ij}, for various values of the elevation angle between stations, β, and the deflection of the vertical normal to the line, ζ. The lines are for various values of ζ as marked. The units of A_{ij} are arcseconds and the elevation angle, β, is in degrees.

1974] indicates that density structures are oriented east-west south of the basin, and east-northeast, or along the trend of the basin, north of the basin. The largest Bouguer anomalies are in the Fillmore region of the basin, where there is a "bull's eye" pattern centered near Fillmore, with a maximum amplitude of -100 mgal.

To estimate the gravitational attraction due to the terrain and mass anomalies near the Ventura basin and, thus, the deflection of the vertical, we used Talwani's method to calculated the gravitational field of an infinitely long prism of arbitrary shape [*Talwani et al.*, 1959]. The prism is approximated as an $n-$sided polygon. This method lends itself well to the east-west trending Transverse Ranges and basin.

The gross Bouguer anomalies can be modeled by a simple isostatic model of the western Transverse Ranges (figures 3.8 and 3.9). The large anomalies near the basin can be modeled by a 10 km deep basin with a $-.15 g/cm^3$ density contrast to the surrounding material. The Oak Ridge is modeled as $-.1 g/cm^3$ less dense than the typical rocks of the area. The deflection of the vertical is calculated by adding the mass of the mountains at the surface to obtain the total horizontal gravitational attraction at stations north and south of the basin. The deflection on the north side of the basin is approximately $20''$N and $3 - 7''$N on the south of the basin. The orientation is $10°$ west of north. The estimates indicate that the deflection of the vertical may have a slight effect on the values of angles measured by triangulation.

The National Geodetic Survey (NGS) provides estimates of the deflection of the vertical for any given position within the United States. The NGS uses the topography, astronomic observations and the gravity field to estimate the deflection of the vertical [*NGS*, written communication, personal communication]. The accuracy

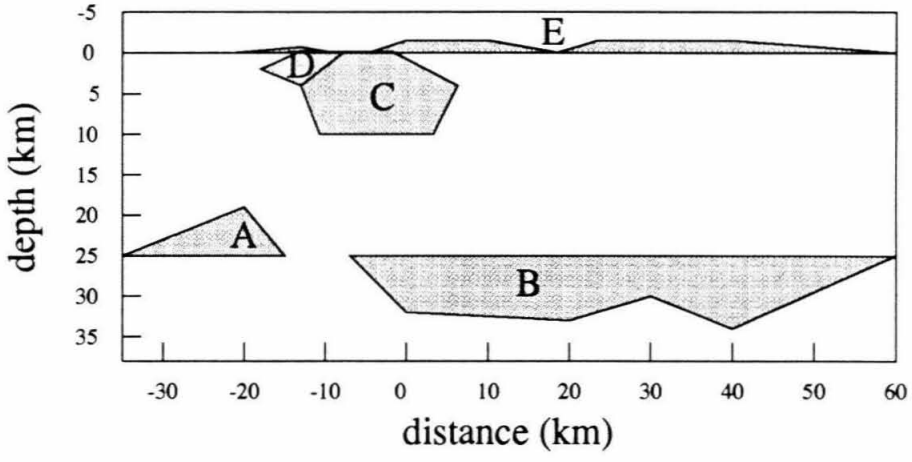

Figure 3.8: Model used to calculated the deflection of the vertical north and south of the basin. Density contrasts are as follows: A–0.56g/cm^3, B––0.56g/cm^3, C––0.15g/cm^3, D––0.1g/cm^3, E–2.32g/cm^3. Note that this model is only to approximately match the Bouguer anomalies and the topography. It is not a best model of density structures.

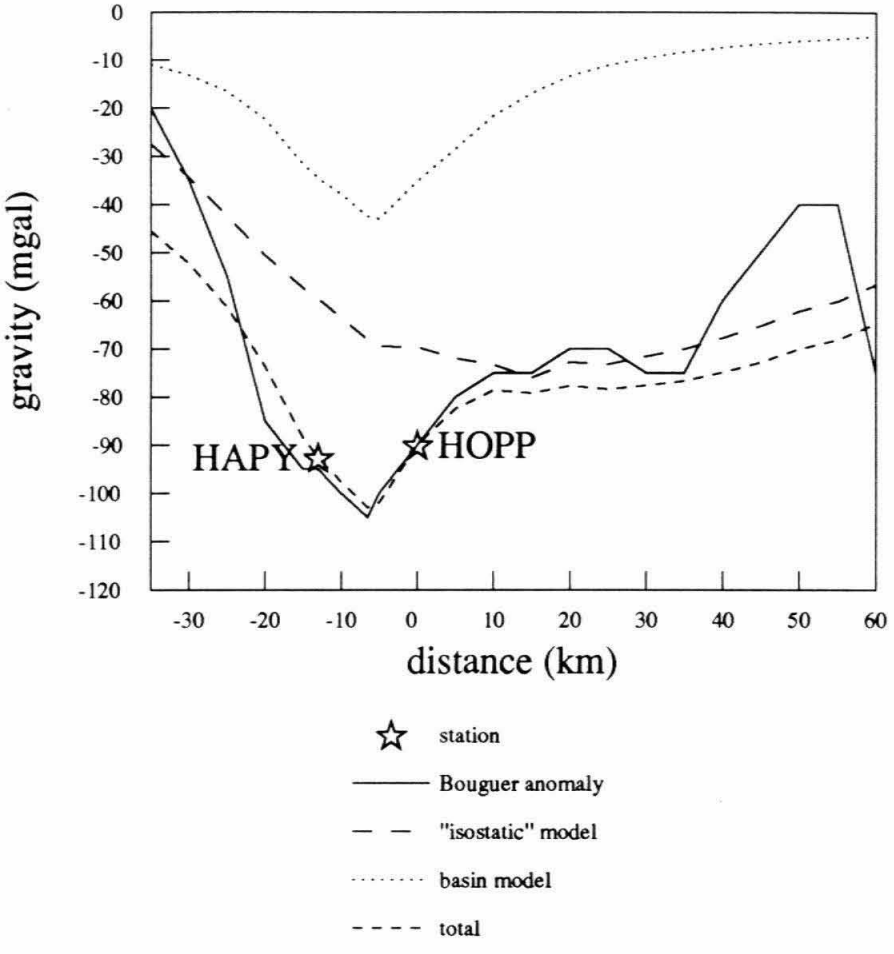

Figure 3.9: Bouguer anomalies resulting from the presence of the Ventura basin and the depression of the Moho by the Western Transverse Ranges. The actual Bouguer anomaly for a section across the basin is marked by the solid line. By isostatic model we actually mean an estimate of deep density contrasts that fit the Bouguer anomalies.

station	ξ	η	ξ_{obs}	η_{obs}
CATO			$-12.0''$	$-4.1''$
HAPY	$-5.2'' \pm 0.4''$	$-6.6'' \pm 0.4''$	$-5.1''$	$-9.4''$
HOPP	$-20.2'' \pm 0.6''$	$-1.1'' \pm 0.5''$		
LOVE	$-14.7'' \pm 0.5''$	$-1.9'' \pm 0.5''$		
SAFE	$-7.6'' \pm 0.4''$	$-2.4'' \pm 0.5''$	$-8.3''$	$-6.1''$
SCLA	$-8.7'' \pm 0.4''$	$-6.3'' \pm 0.4''$		
SNP2	$-29.2'' \pm 0.5''$	$-1.0'' \pm 0.5''$		

Table 3.5: Deflections of the vertical provided by the National Geodetic Survey for the Ventura basin sites and calculated from astronomic observations.

the estimated gravity is 5 mgals and the formal error of the deflection is listed in table 3.5. In general, the formal errors are underestimated by up to a factor of three. In rugged terrain, where the calculated deflection is compared to observation, the estimate may be off by up to $2''$. The values of deflection provided by the NGS are close to those estimated above (table 3.5). The westward component of deflection is difficult to estimate with the above method. We also calculated the deflection due to the actual topography by estimating discrete elevations as vertical prisms. To do so, we integrated over the volume of a finite prism [*Plouff*, 1976]. The components of deflection do not vary significantly from the values provided by the NGS, which include gravity observations.

The deflection of the vertical may also be calculated by measuring the astronomic

latitude and longitude and differencing these values with the actual latitude and longitude as follows [*Bomford*, 1971]:

$$\xi = \text{Astronomic latitude} - \text{geodetic latitude} \tag{3.16}$$

$$\eta = (\text{Astronomic longitude} - \text{geodetic longitude})\cos(\text{latitude}) \tag{3.17}$$

Only three astronomic positions were measured for the entire network. The observed deflections are comparable to the NGS values. Because we don't compare GPS and triangulation for the angles south of the basin, we do not need the deflection of the vertical there.

We used the NGS values of deflection to calculate the required correction for each triangulation angle in the network (table 3.6). We do not list any corrections that are under $0.3''$, because they are well within the error for triangulation. In Appendix C, we show the correction that was applied to each angle. The correction between using known values of deflection from the astronomic observation with the NGS values, does not differ by more than $0.1''$, in any case.

3.2.3 Lateral Refraction

The problem of refraction of light, out of the vertical plane, needs to be carefully examined. We are not able to determine the horizontal refraction effects, but estimate the bounds to better interpret the results. According to *Bomford* [1971] this is the worst source of error. The magnitude and direction of lateral refraction vary according to the time of day, but is smallest shortly after sunrise and in the evening [*Bomford*, 1971], presumably because the air mixes during sunrise and sunset. When all of the measurements are taken at a particular time of day systematic errors caused

angle	correction
HAPY-SNP2-HOPP	$-1.4''$
HAPY-SNP2-SCLA	$-0.6''$
HAPY-HOPP-LOVE	$-0.8''$
HAPY-HOPP-SAFE	$-0.3''$
HAPY-HOPP-SNP2	$-0.3''$
SCLA-HOPP-LOVE	$-0.3''$
SCLA-HOPP-SAFE	$0.3''$
LOVE-HOPP-SAFE	$-0.8''$
SCLA-HAPY-HOPP	$-0.4''$
HOPP-HAPY-LOVE	$-0.4''$
HAPY-LOVE-HOPP	$-0.5''$
HOPP-LOVE-SCLA	$-0.5''$
HOPP-LOVE-SAFE	$-0.4''$

Table 3.6: Corrections greater than $0.3''$ to angles within the Ventura basin triangulation network.

by lateral refraction may creep in. The amount of refraction probably varies from survey to survey depending upon the weather conditions. In order to calculate strain rates from triangulation it is desirable to have several epochs of measurements to randomize the effects of lateral refraction. According to *Vaníček and Krakiwsky* [1986], vertical refraction is about 10 orders of magnitude worse than lateral refraction and is typically $10''$. Triangulation measurements are most likely to be affected, then, by about $1''$.

During the night the lateral refraction is usually of opposite sign than during the daytime. During the day the ground is heated and the air is cooler while, during the night, the ground is cooler than the air. In southern California diurnal temperature fluctuations are large and the observations were made only during the night. *Bomford* [1971] refers measurements in India where daytime angles were wrong by $3''$ to $6''$. At night the errors were similar, but of opposite sign. In the area of the Ventura basin, where all of the triangulation measurements were taken at night, horizontal refraction may cause systematic errors that would make a comparison between GPS and triangulation difficult. The worst cases of refraction occur, however, when a line grazes a hill-slope [*Bomford*, 1971]. Fortunately the triangulation stations in the Ventura basin network are located on peaks and the lines pass a good distance from the ground, so the effects of refraction should be minimized.

From *Bomford* [1971] the lateral refraction or curvature of a ray of light is

$$16.3\frac{P}{T^2}\frac{dT}{dx}\frac{''}{\mathrm{m}}$$

where P is the pressure, taken to be constant, T is the temperature, measured in degrees Kelvin and x is the distance. Assume that the ground on which the

instrument is located is 10° warmer than the air through which the line passes. The line passes 100 m to the side of the hill. The temperature gradient is roughly 1° per 10 m. If P is 975 mbar (measured at Santa Clara (SCLA)) and T is 287°K then the lateral refraction would be $0.02''$/m. The 10° temperature difference is an extreme, estimated from the nighttime and daytime temperatures at one of the GPS stations. Along the entire line, the temperature gradient should be lower, perhaps on the order of 1° per 1000 m. For such a gradient the curvature of the ray would be $1.9 \times 10^{4''}$/m. Ventura basin lines are on the order of 15 km so the ray would be deflected about $3''$. We have no way of determining the actual refraction during any of the triangulation surveys, but the effects should be considered when interpreting strain across the basin. Assuming uniform strain with time, angles that have several epochs of measurements provide a sense of the scatter from survey to survey (figures 3.12 and 3.10). In some cases the scatter is greater than $1''$.

3.2.4 Ties between GPS and Triangulation Sites

For Castro Peak (CATO) and San Fernando (SAFE) we were unable to occupy the same benchmark that was occupied during the triangulation surveys. In order to compare the triangulation and GPS results it was necessary to make a tie between the GPS and triangulation marks.

In the case of Castro Peak, the triangulation history is sufficient to determine strain rates without including the angles from GPS. Instead we compare the results from GPS with those from triangulation without mixing data from the two types of geodesy. This avoids any error that might be introduced through an improper tie. We attempted to make a tie to the triangulation site using GPS, but the radio

frequency interference was too great and no data were collected.

San Fernando RM 3 (SAF3) is situated about 10 m away from a very large microwave transmission building. The sky to the west is obstructed. For this reason we occupy PICO L9C (SAFE) for the high precision GPS. The site is approximately 50 meters from the building and thus does not suffer from either signal multipath effects or sky obstructions. Because the two sites are so close however, one day of simultaneous GPS observations should be adequate to determine the positions of both sites. During the 1990 experiment, we occupied the San Fernando Reference Mark 3 (SAF3) and PICO L9C (SAFE) simultaneously to tie the sites together.

For the estimation of strain parameters from GPS only, we use data from PICO L9C (SAFE) and for the the triangulation comparison we use San Fernando RM 3 (SAF3), which was occupied for triangulation in 1963. The original San Fernando 1898 mark (SAF8) was paved over after 1963, but the tie between that mark and the reference mark 3 (SAF3) is well-determined. In order to recover data that included the original 1898 site we converted angles from RM 3 (SAF3) to the 1898 mark (SAF8). The azimuth from RM 3 (SAF3) to SF 1898 (SAF8), in the NAD27 reference, is 176° 19′ 12.5″ and the distance is 23.221 m. The National Geodetic Survey measured this in 1963. Because the azimuth is in the NAD27 reference frame it must be converted to the NAD83 reference frame. To do so, we assumed that the height difference between the two stations is negligible and estimated the position of SF 1898 (SAF8) in the NAD27 reference frame from the 1990 position of the RM 3 (SAF3). We then converted the position from NAD27 to the NAD83 ellipsoid. From the estimated position of San Fernando 1898 in 1990, we directly solved for

Parameter	(units)	central	east	total	south	
$\dot{\gamma}_1$	(μrad/yr)	$.48 \pm .19$	$.36 \pm .06$	$.34 \pm .05$	$.02 \pm .06$	Δ
		$.68 \pm .16$	$.45 \pm .12$	$.52 \pm .08$	$.06 \pm .06$	GPS
$\dot{\gamma}_2$	(μrad/yr)	$-.06 \pm .09$	$.12 \pm .04$	$.04 \pm .05$	$-.04 \pm .08$	Δ
		$.25 \pm .16$	$.32 \pm .13$	$.33 \pm .08$	$.05 \pm .07$	GPS
$\dot{\gamma}$	(μrad/yr)	$.48 \pm .18$	$.38 \pm .04$	$.35 \pm .05$	$.04 \pm .08$	Δ
		$.72 \pm .16$	$.56 \pm .13$	$.61 \pm .08$	$.08 \pm .07$	GPS
θ	(deg)	4 ± 10	-9 ± 7	-4 ± 7	31 ± 61	Δ
		-10 ± 12	-18 ± 13	-16 ± 8	-19 ± 43	GPS
σ_0	dimless	3.0	2.1	2.5	0.6	Δ

Table 3.7: Strain calculations from triangulation and GPS measurements for central and eastern regions of the basin and for the region south of the basin. Parameters are described in the text. GPS results listed earlier are included for comparison.

the azimuths and thus the angle between SF 1898 (SAF8) and the other stations.

3.2.5 Results

The angles used for the calculations are listed in Appendix C. We corrected the angles for the deflection of the vertical. For the calculations we divided the basin into eastern and central regions as we did for the calculations from the GPS measurements. We also calculated the strain for the region south of the basin, and the strain for the total basin. In the southern region we excluded obvious outliers from the 1956 data. The results compare favorably to the GPS strain rate calculations and are listed in

table 3.7. As shown in the plots of the residuals (figures 3.11-3.10), the triangulation measurements are fairly noisy, but they do help to confirm the GPS results. We scaled the errors by the *a posteriori* standard deviation of an observation of *a priori* weight, σ_0 [*Snay*, 1986].

$$\sigma_0 = \sqrt{\frac{\sum -i \left(\frac{o_i - c_i}{\sigma_i}\right)^2}{n}}$$

where o_i and c_i are the observed and calculated angles at station i respectively, σ_i is the standard deviation of the measured angle and n is the number of degrees of freedom. For $\sigma_0 < 1$ we did not scale the errors. We specified an error of $0.1''$ on the GPS angles. Rather than increase the error of the GPS measurements by correcting the GPS angle for the deflection of the vertical, we applied the deflection correction to the triangulation measurements.

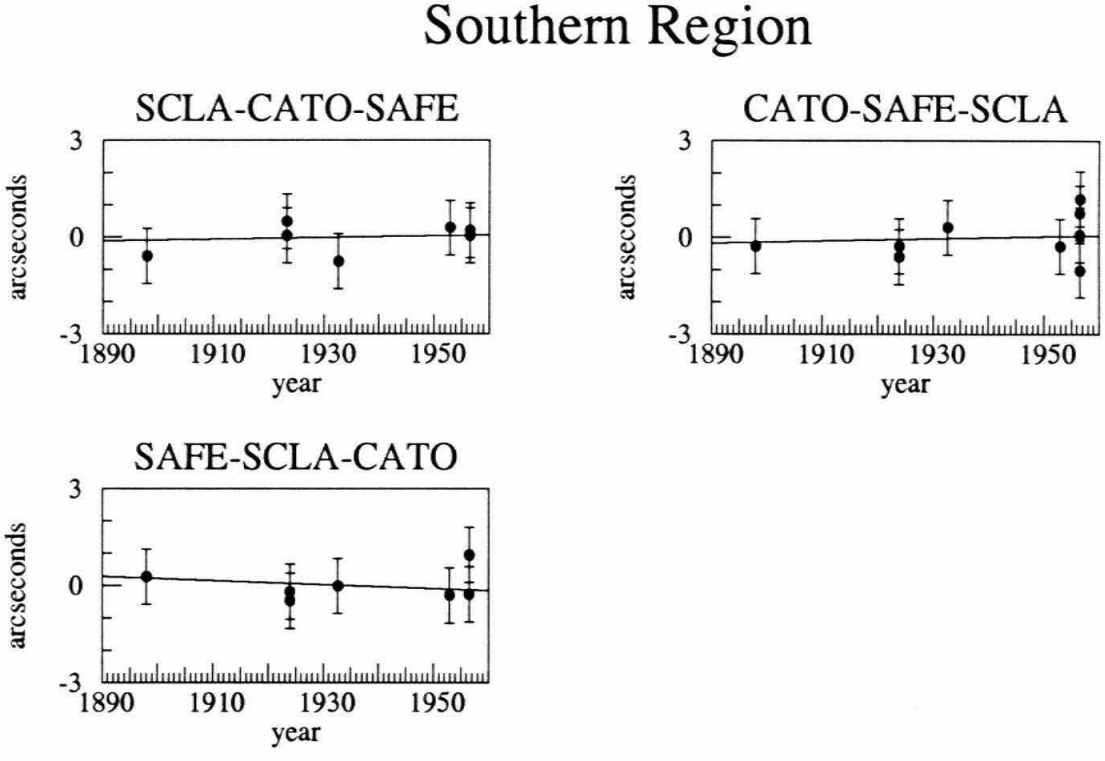

Figure 3.10: Residual plots for the region south of the Ventura basin. The line is the predicted angular change for the given angle determined from the calculated strain rate. The smaller angle between the stations is used.

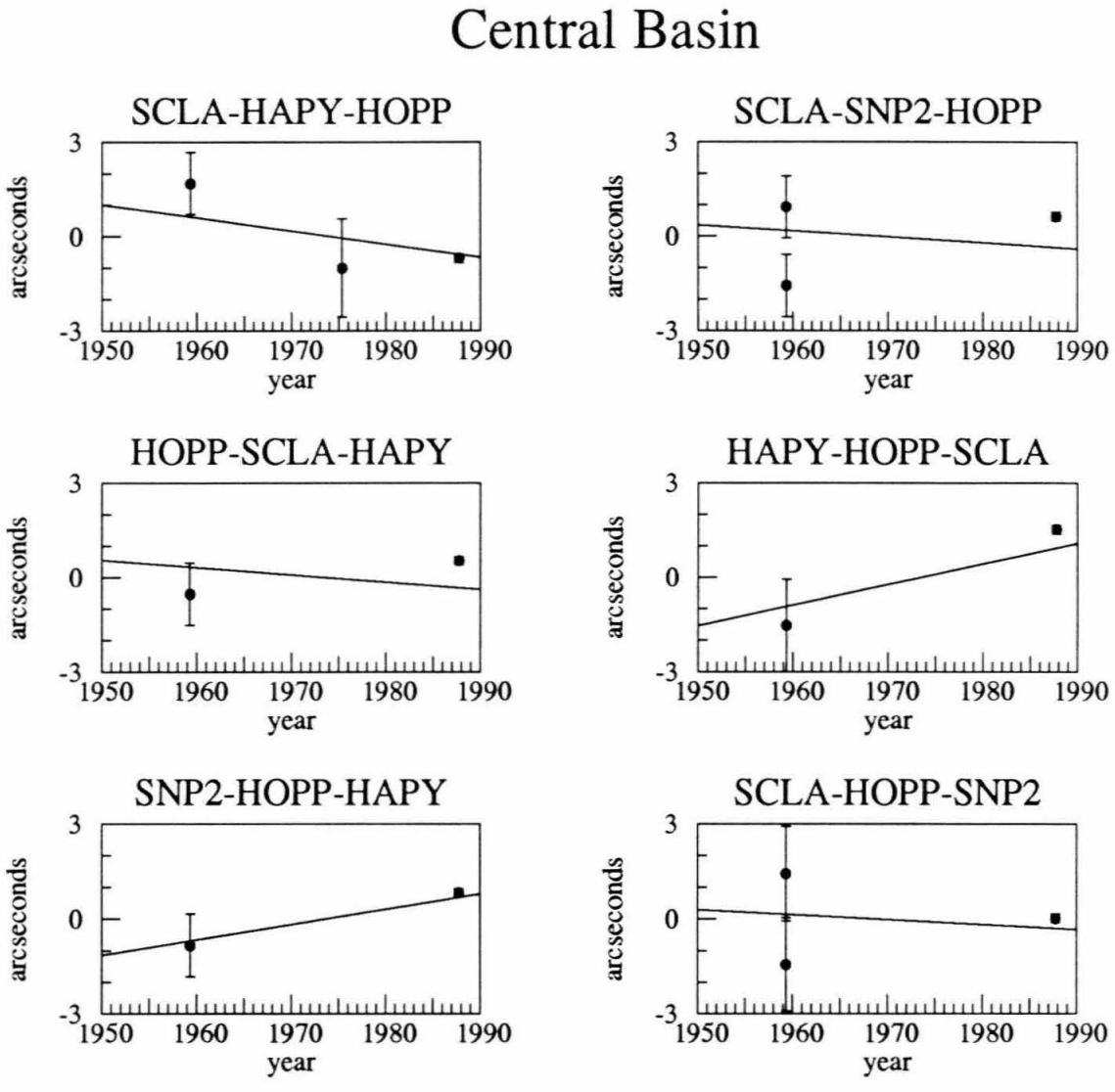

Figure 3.11: Residual plots for the east-central region of the Ventura basin. The line is the predicted angular change for the given angle determined from the calculated strain rate. The smaller angle between the stations is used.

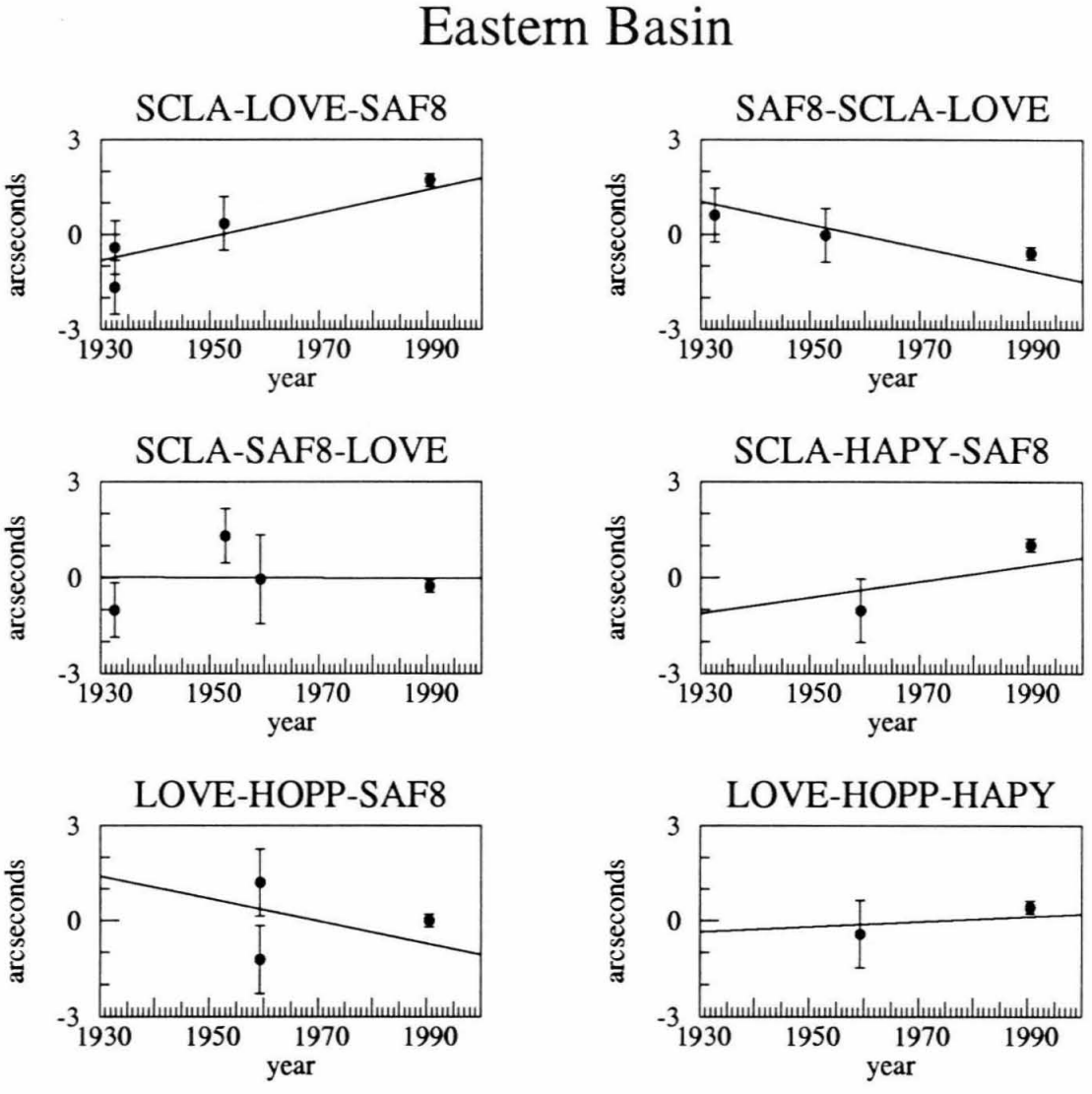

Figure 3.12: Residual plots for the eastern region of the Ventura basin. The line is the predicted angular change for the given angle determined from the calculated strain rate. The smaller angle between the stations is used. Figure continues onto next two pages.

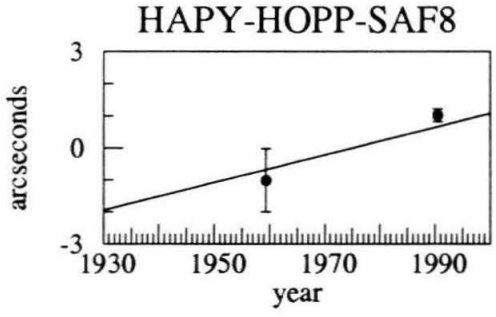
HAPY-HOPP-SAF8
arcseconds
3
0
-3
1930
1950
1970
1990
year

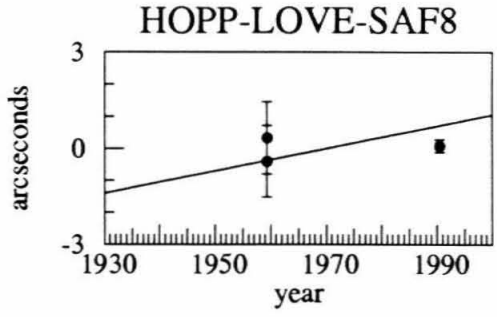
HOPP-LOVE-SAF8
arcseconds
3
0
-3
1930
1950
1970
1990
year

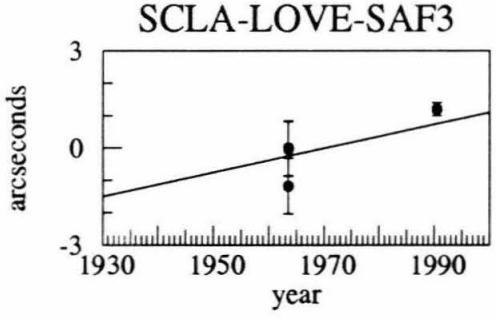
SCLA-LOVE-SAF3
arcseconds
3
0
-3
1930
1950
1970
1990
year

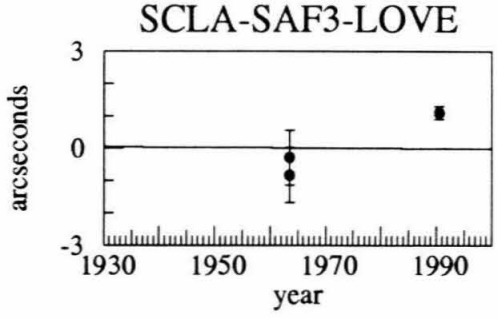
SCLA-SAF3-LOVE
arcseconds
3
0
-3
1930
1950
1970
1990
year

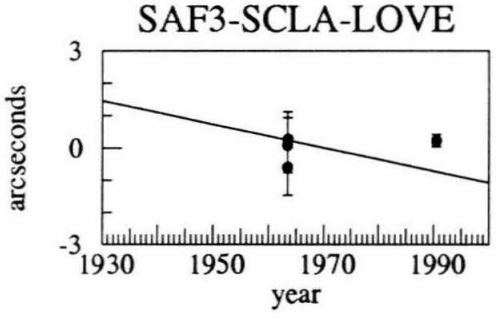
SAF3-SCLA-LOVE
arcseconds
3
0
-3
1930
1950
1970
1990
year

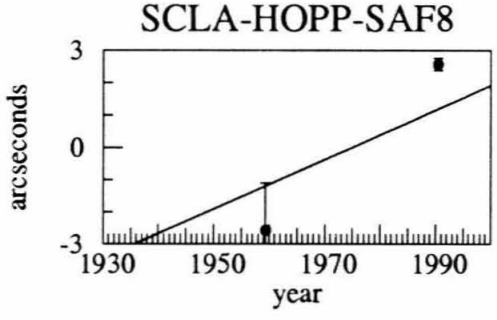
SCLA-HOPP-SAF8
arcseconds
3
0
-3
1930
1950
1970
1990
year

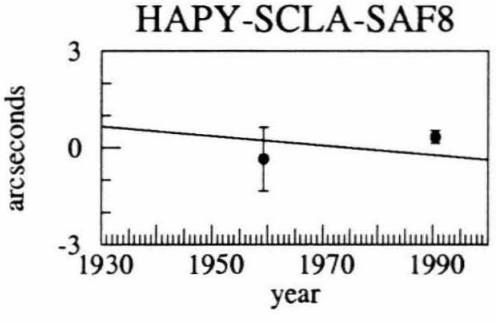
HAPY-SCLA-SAF8
arcseconds
3
0
-3
1930
1950
1970
1990
year

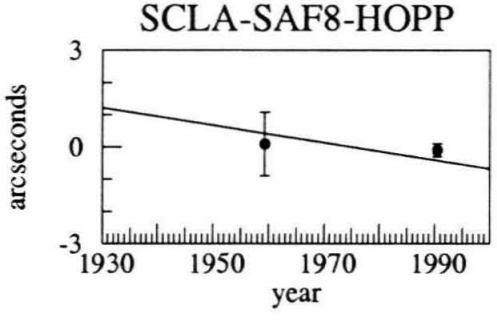
SCLA-SAF8-HOPP
arcseconds
3
0
-3
1930
1950
1970
1990
year

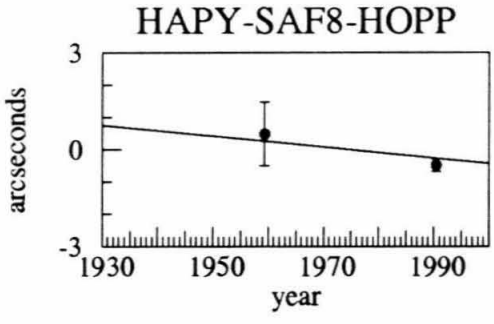
HAPY-SAF8-HOPP
arcseconds
3
0
-3
1930
1950
1970
1990
year

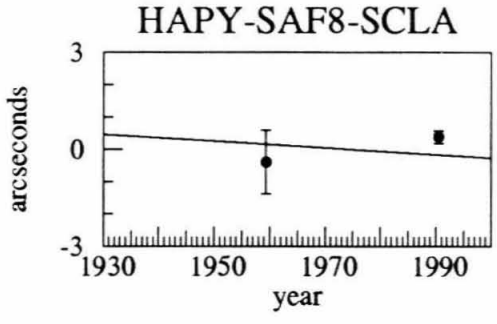
HAPY-SAF8-SCLA
arcseconds
3
0
-3
1930
1950
1970
1990
year

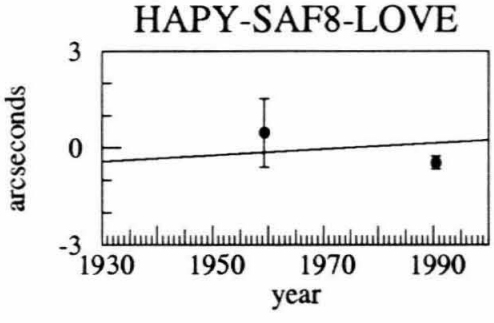
HAPY-SAF8-LOVE
arcseconds
3
0
-3
1930
1950
1970
1990
year

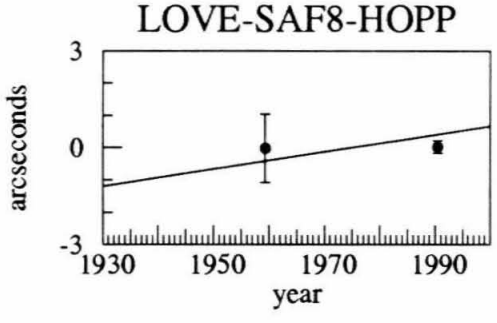
LOVE-SAF8-HOPP
arcseconds
3
0
-3
1930
1950
1970
1990
year

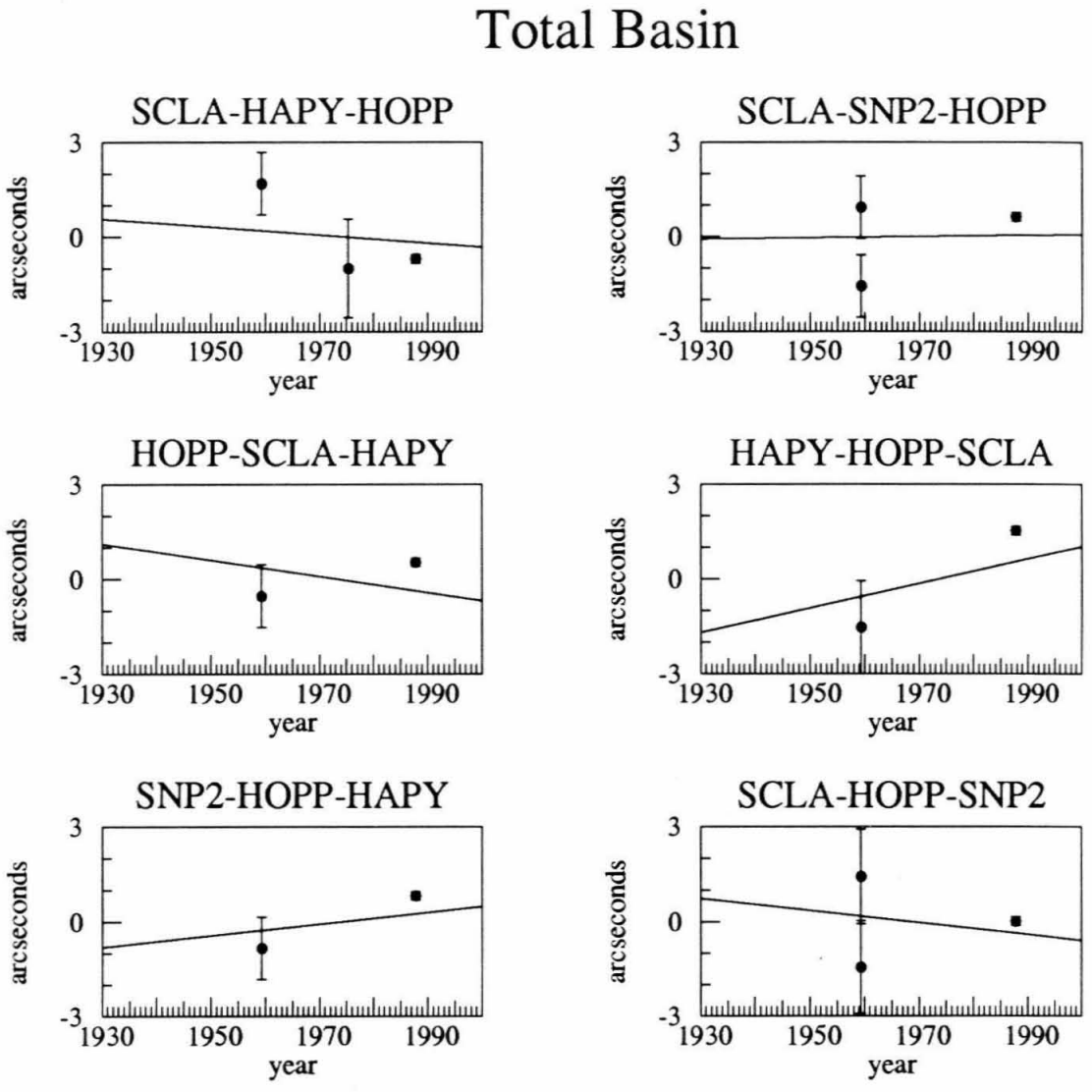

Figure 3.13: Residual plots for the total Ventura basin. The line is the predicted angular change for the given angle determined from the calculated strain rate. The smaller angle between the stations is used. Figure continues onto next three pages.

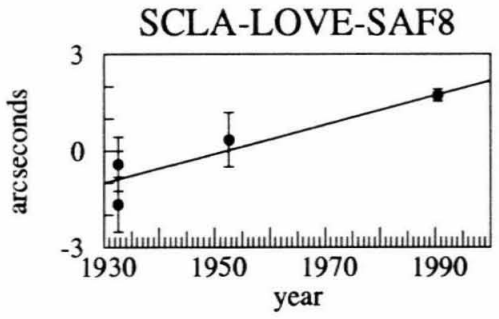
SCLA-LOVE-SAF8
arcseconds
3
0
-3
1930
1950
1970
1990
year

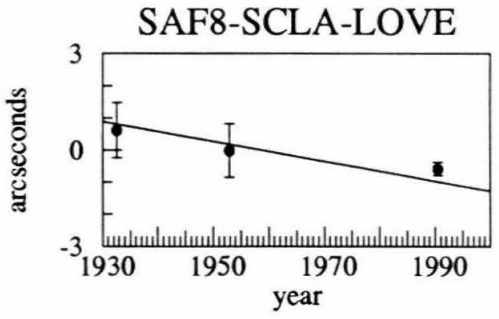
SAF8-SCLA-LOVE
arcseconds
3
0
-3
1930
1950
1970
1990
year

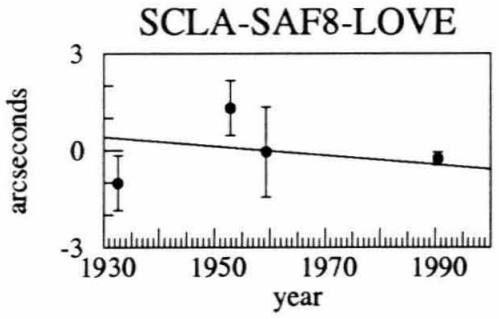
SCLA-SAF8-LOVE
arcseconds
3
0
-3
1930
1950
1970
1990
year

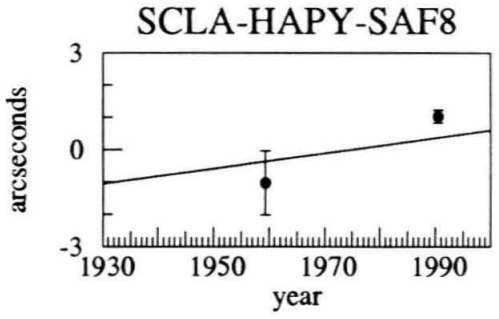
SCLA-HAPY-SAF8
arcseconds
3
0
-3
1930
1950
1970
1990
year

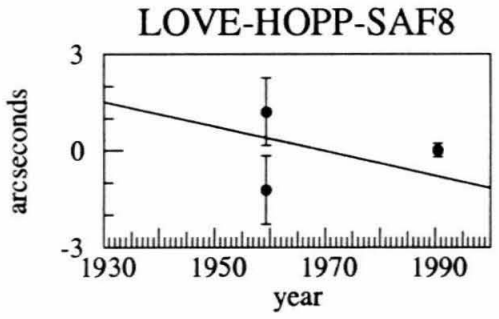
LOVE-HOPP-SAF8
arcseconds
3
0
-3
1930
1950
1970
1990
year

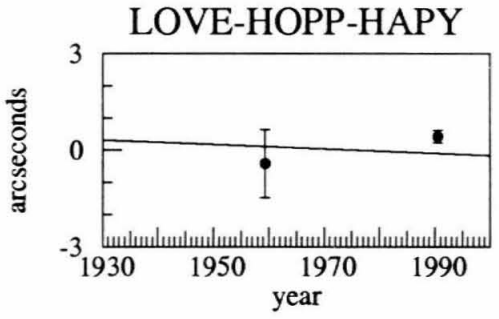
LOVE-HOPP-HAPY
arcseconds
3
0
-3
1930
1950
1970
1990
year

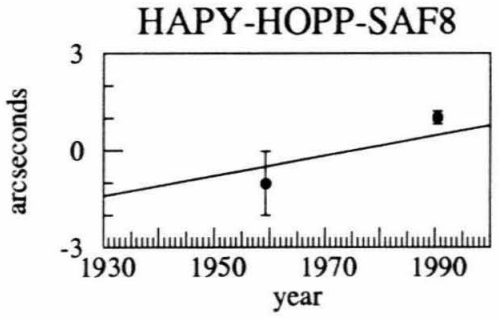
HAPY-HOPP-SAF8
arcseconds
3
0
-3
1930
1950
1970
1990
year

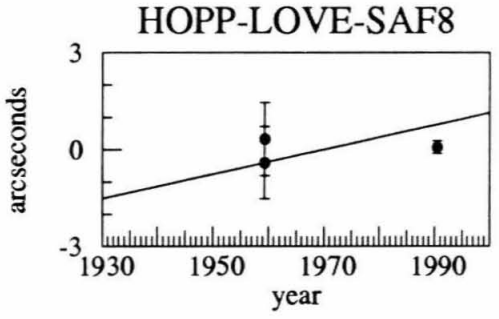
HOPP-LOVE-SAF8
arcseconds
3
0
-3
1930
1950
1970
1990
year

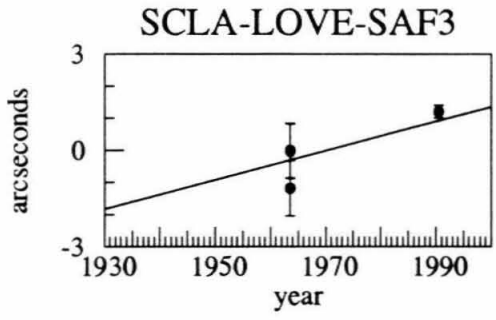
SCLA-LOVE-SAF3
arcseconds
3
0
-3
1930
1950
1970
1990
year

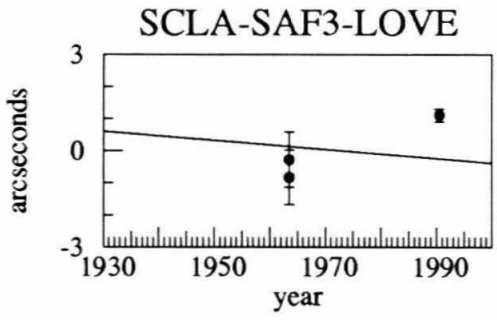
SCLA-SAF3-LOVE
arcseconds
3
0
-3
1930
1950
1970
1990
year

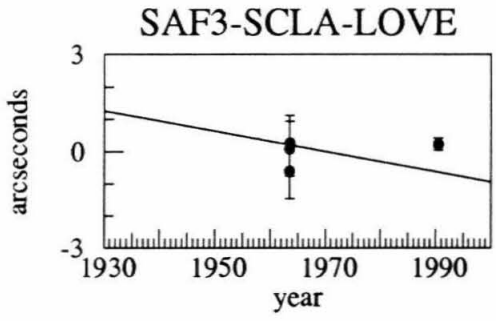
SAF3-SCLA-LOVE
arcseconds
3
0
-3
1930
1950
1970
1990
year

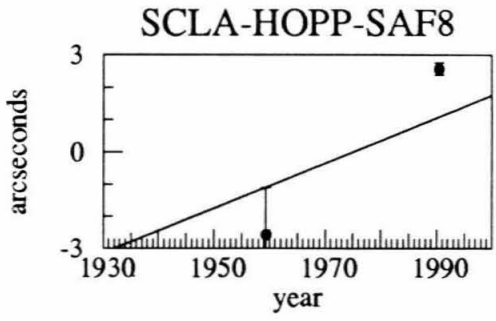
SCLA-HOPP-SAF8
arcseconds
3
0
-3
1930
1950
1970
1990
year

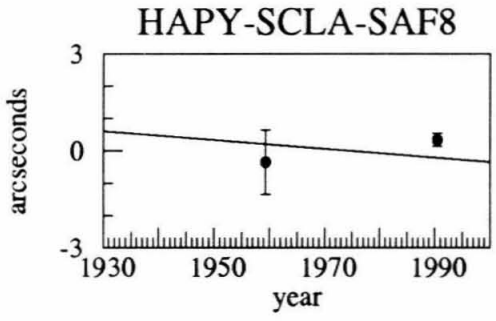
HAPY-SCLA-SAF8
arcseconds
3
0
-3
1930
1950
1970
1990
year

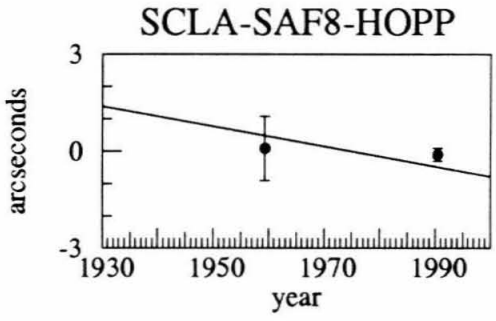
SCLA-SAF8-HOPP
arcseconds
3
0
-3
1930
1950
1970
1990
year

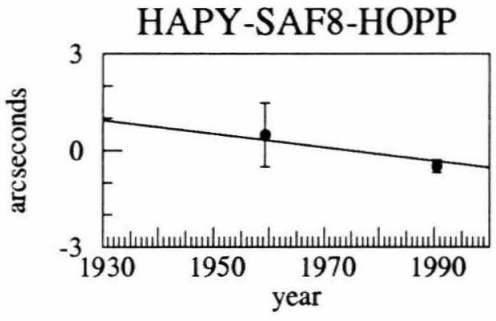
HAPY-SAF8-HOPP
arcseconds
3
0
-3
1930
1950
1970
1990
year

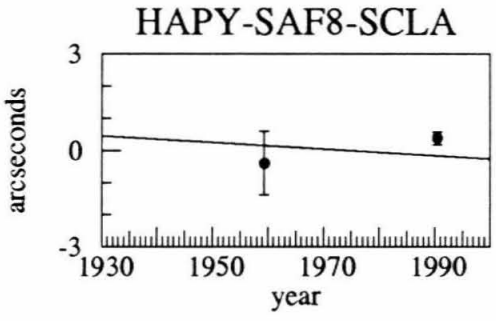
HAPY-SAF8-SCLA
arcseconds
3
0
-3
1930
1950
1970
1990
year

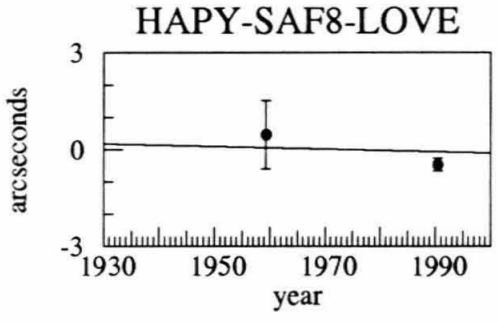
HAPY-SAF8-LOVE
3
0
-3
arcseconds
1930
1950
1970
1990
year

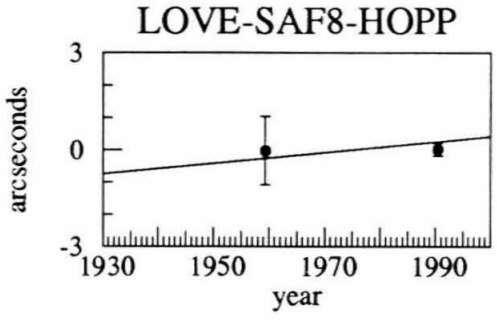
LOVE-SAF8-HOPP
3
0
-3
arcseconds
1930
1950
1970
1990
year

Chapter 4

Modeling and interpretations

We have observed deformation across the Ventura basin during a period of 2.7 years. Analysis of 30–100 years of triangulation data supports the GPS results, although in using only 2.7 years of GPS we can obtain more accurate results than in using triangulation over much longer times. In order to make tectonic interpretations of the results we must first estimate the extent to which the results reflect tectonic deformation rather than local non-tectonic motion.

4.1 Consideration of non-tectonic causes

Site instabilities or local effects induced by human activity might be causing the apparent deformation. Also grouped within this definition of "non-tectonic" are nearby earthquakes occurring within the time-span of the measurements. The earthquakes may have produced episodic motions that would corrupt the estimates of intra-earthquake rates of deformation in the Ventura basin region.

4.1.1 Site stability

The quality of the monuments makes it unlikely that any motions are due to site instabilities. All of the monuments are first order monuments, except for Yam 2 (YAM2), in the northern part of the network. The monuments are placed in bedrock. The similar results from multiple stations, both north and south of the basin, suggests that the sites are not unstable. The only questionable motion is indicated at Yam 2 (YAM2). Future observations will establish the stability of the site. Yam 2 (YAM2) is located very close to the big bend of the San Andreas fault. Other geodetic observations near the region of the big bend also show deformation unlike the surrounding region [*Eberhart-Phillips et al.*, 1990]. In light of other geodetic evidence from that region we will attempt a tectonic explanation of the motion of Yam 2 (YAM2).

As mentioned in Chapter 2, the antenna at Santa Clara (SCLA) was mounted on a 5 m tower. Although it is not likely that the site itself is unstable, the difficulty of plumbing such a distance could degrade solutions relative to the site. We used carefully calibrated optical plumbs and gravity plumb bobs to center the antenna over the mark. Tarps were wrapped around the tower to avoid motion of the plumb bob due to the wind. Different wind directions and conditions might cause mis-centering of the antenna in a different direction for each day of surveying. Our results in Chapter 2 show that the weighted rms scatter of baselines is no worse at Santa Clara (SCLA) than at any other station, suggesting that the antenna was well-centered each day. The results from the two epochs of GPS agree with the triangulation results that show little motion between Santa Clara (SCLA) and other sites on the

south side of the basin. This also indicates that mounting the tripod on the tower did not degrade the solution.

4.1.2 Oil withdrawal

Although none of the stations seem to show anomalous rates it is still possible that the results are not due to tectonic motion. A more regional, though still local, process may affect several stations in the same way. Withdrawal of oil and water from the basin could provide a mechanism by which the mountains on either side slump inward toward the center of the Ventura basin. Many prolific oil fields are distributed throughout the basin. It is important to assess whether some or all of the observed motions are a result of the withdrawal of oil from the basin. We used two methods to estimate whether oil withdrawal significantly affected our results. First, we designed our experiments in such a way that local effects from oil withdrawal should be apparent, and second, we modeled the extent to which oil withdrawal from the basin should affect our results.

The problem of oil withdrawal is of concern, because differential subsidence has been associated with both the Ventura and Rincon oil fields located north and northwest of Ventura. *Buchanan-Banks et al.* [1975] measured 277 mm of subsidence at the center of the Ventura oil field by examining leveling data spanning the period 1939–1960. Flooding of the Ventura oil field with water began in 1956 and the above workers show that there is no additional subsidence between 1960 and 1968. The Rincon oil field also subsided between 1939 and 1968, but by less than 50 mm. This lesser amount of subsidence is attributed to the smaller size of the Rincon field.

One of the reasons that we added stations both north and south of the basin

was to test for deformation on a more regional scale and compare the observations to the local basin results. If the mountains are slumping toward the basin, the baselines to the north and south should show apparent extension. Aside from Yam 2 (YAM2) there is no evidence for such extension (figure 3.1). Oil is not extracted north of the basin and the effects of extraction should be local, so it is unlikely that Munson (MUNS) would be affected in the same way as Santa Paula Peak (SNP2), Hopper (HOPP) and Loma Verde (LOVE), located much closer to the reservoirs. The Los-Padres trilateration network extends to the northern margin of the Ventura basin and the observations from trilateration indicate that compression is occurring north of the basin [*Eberhart-Phillips et al.*, 1990]. The formal errors of results from both GPS and triangulation allow for up to 1 mm/yr extension south of the basin. The 100 year history of triangulation there shows no detectable change of strain (figure 3.10), but pumping began as early as the turn of the century, so it is possible that the triangulation results reflect a component of non-tectonic motion.

An intermediate interpretation of the observed displacements would allow for tectonic strain to be accumulating uniformly over the entire GPS network. The motion of the central sites surrounding the basin may be due to a combination of oil withdrawal and strain accumulation. A century of triangulation measurements suggests that it is unlikely that significant tectonic strain is accumulating south of the basin. Oil was being pumped at one location or another during this time, but there is no resolvable variation of strain throughout the period. The geologic record also indicates that deformation should be occurring at a higher rate across the basin than in the surrounding regions. Elastic strain, however, could be accumulating on

short time-scales and not be reflected in the geologic history.

A straight line may be fit reasonably well through the data across the basin from Castro (CATO) to Munson (MUNS) (see figure 4.6). If uniform strain is actually accumulating, and the end points, Castro (CATO) and Munson (MUNS), are not affected by oil extraction, Castro (CATO) should be moving 4.9 ± 1.3 mm/yr relative to the Oak Ridge. Munson (MUNS) should be moving at a rate of 4.8 ± 1.8 mm/yr relative to the northern margin of the basin. The difference between the predicted and measured values suggests that the Oak Ridge may be slumping toward the basin at 3.6 ± 2.6 mm/yr. Possible motion due to slumping of the north side can not be resolved (0.9 ± 3.2 mm/yr). Perhaps 3.1 ± 3.3 mm/yr of closure of the basin might be attributable to oil withdrawal.

We modeled the effect of oil withdrawal to estimate the amount of motion that might be caused by extraction. It is expected that vertical subsidence should be the primary mode of deformation associated with the withdrawal of oil, but it is possible for some horizontal motion to occur as well. Anticlinal structures trap oil, and as oil is extracted, the reservoir might collapse perpendicular to the bedding, adding a horizontal component of motion. In the Ventura basin the geodetic sites are situated on the sides of such anticlines. Not much oil is being extracted near Santa Paula Peak (SNP2), Happy (HAPY) or Loma Verde (LOVE), however, and oil is being extracted from both sides of San Fernando (SAFE). Nevertheless, we will model oil withdrawal from the most productive field in the basin, which is situated near Santa Clara (SCLA).

The South Mountain oil field lies directly under Santa Clara (SCLA) and the

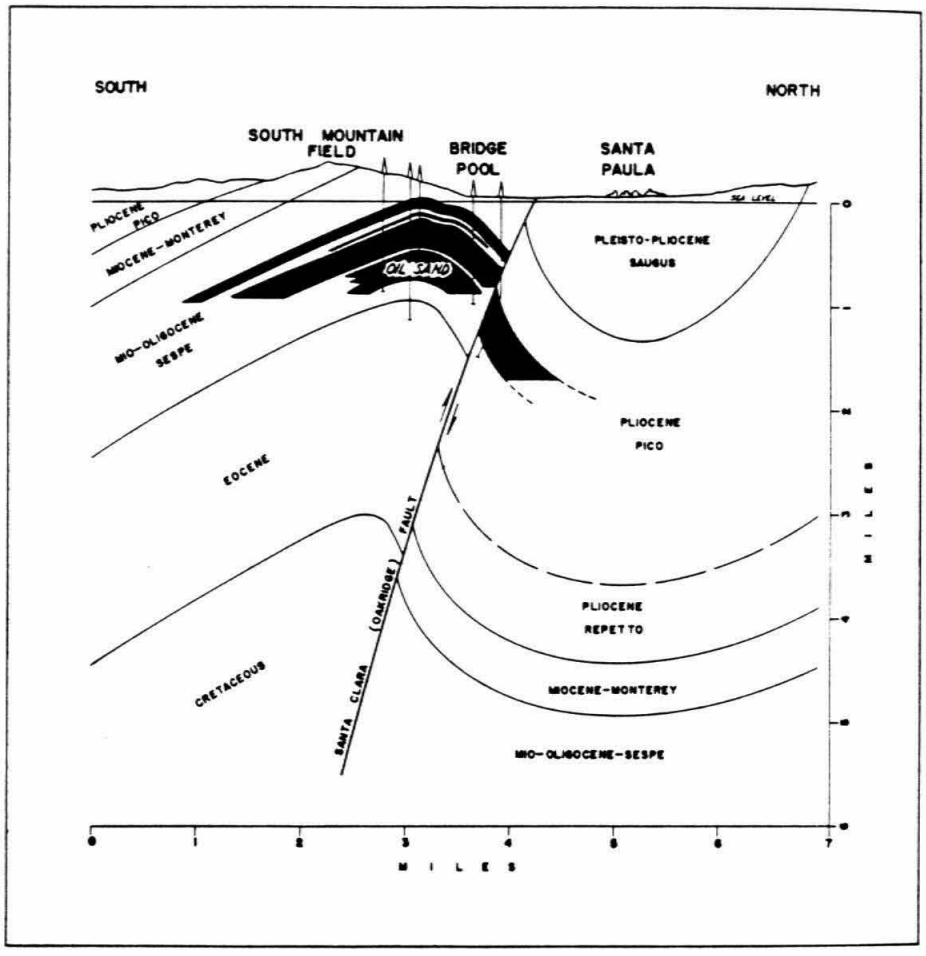

Figure 4.1: Cross-section through the south mountain oil field. The site SCLA is located on top of the highest peak under the words South Mountain Field. The black area marks the oil reservoir. The upper trap is no longer productive. Note that the axis of the anticline is situated north of the station. [From *Higgins*, 1958].

axis of the anticline is approximately 1.4 km north of the station (figure 4.1). Today the entire South Mountain field produces about 1.6 million barrels of fluid per year ($230,400 m^3/yr$) [*C. D. Cavit*, Unocal Dist. Geologist, written communication] and is the most productive field in the basin. Most of the South Mountain field lies directly under the Oak Ridge and to the east of Santa Clara (SCLA). The Bridge pool of the oil field lies along the edge of the Oak Ridge and makes up about 14% of the aerial extent of the total South Mountain field. Oil is extracted from beds below the Oak Ridge fault in a zone 380 m thick, at a depth of 2190 m. The field is 4.4 km long and 0.4 km wide. We will assume that the production of this field is 14% of the total, which is an upper bound because the producing beds of the rest of the South mountain field are much thicker. The dip of the Oak Ridge fault, which forms the trap, is 60° and we will assume that contraction is perpendicular to the fault. For any cross-section 7.3 m^2/yr of fluid should be removed. The width is 0.8 km so contraction across the section should be about 10 mm/yr. The amount of horizontal motion attributable to the withdrawal is 0.2 mm/yr. This is an upper bound because 56% of the fluid extracted from well is waste water which is injected back into water-flood wells and disposal wells [*D. C. Cavit*, Unocal, written communication, *California Div. Oil and Gas*, 1989]. To account for the 3 mm/yr of possible motion due to oil withdrawal the bridge pool must produce 4 million barrels/yr (0.6 million m^3/yr). Even if half of the motion is accommodated on the north side of the basin, 2 million barrels (3 million m^3/yr) must be produced by the Bridge pool. This is greater than the total production of the South Mountain oil field.

It is unlikely that oil withdrawal is causing any noticeable effects on the observed deformation. Although the Ventura basin was at one time extremely productive, production has dropped off considerably. Elastic models show that at the current rate of production the effects are negligible. Sites that are located near wells that are no longer producing show no differential motion with respect to other sites on the same side of the basin, suggesting that even where there are active wells the effects are negligible.

4.1.3 The effect of recent large earthquakes

Although there have been no earthquakes with a magnitude greater than 5.0 within the geodetic network, two major earthquakes occurred nearby (figures 4.2 and 4.3). The first is the Kern County earthquake of 1952. This magnitude 7.2 earthquake ruptured the White Wolf fault, which lies north of the intersection of the San Andreas and Garlock faults and about 60 km north of the basin network [*Stein and Thatcher*, 1981]. The second event is the 1971 magnitude 6.5 San Fernando earthquake. The epicenter of the earthquake was located approximately 50 km east-northeast of the center of the basin network and ruptured a 15 km long zone approximately 30 km east-southeast of the center of the network. The San Fernando earthquake occurred within one fault dimension of the Ventura basin network and between the time that data was collected for the triangulation and GPS measurements. The Kern County earthquake occurred between triangulation measurements and is located a little more than one fault dimension from the basin network. Because the earthquakes occurred between measurements, it is possible that the geodetic comparisons reflect some of the motion.

In order to model the deformation that these earthquakes may have produced, we used *Okada's* [1985] analytic solution of a dislocation in an elastic half-space. His method does not allow for a layered earth model, but it is free from singularities in places where earlier models are not.

The Kern County Earthquake

The 1952 Kern County earthquake occurred prior to any measurements across the east-central part of the Ventura basin. Angle measurements were made before and after the earthquake in the southern and eastern regions of the network. To affect the triangulation measurements the horizontal differential motion from the earthquake must be greater than about 50 mm. Considering the distance from the epicenter of the quake it is unlikely that motions would be detected from the triangulation measurements across the basin. Nevertheless, we used the three segment fault model of *Stein and Thatcher* [1981] to estimate effect of the earthquake on the Ventura basin triangulation angles. The results show negligible differential motion across, and south of, the basin (figure 4.2).

The San Fernando Earthquake

We were concerned that the 1971 San Fernando earthquake affected the results of the triangulation to GPS comparison because the earthquake occurred within the time span of the comparison. The eastern part of the Ventura Basin is located about 30 kilometers from the epicenter of this magnitude 6.5 earthquake and is within one fault dimension of the rupture zone (figure 4.3). To assure that the observed strains were not due to this earthquake, we modeled the event, both as a point source and as

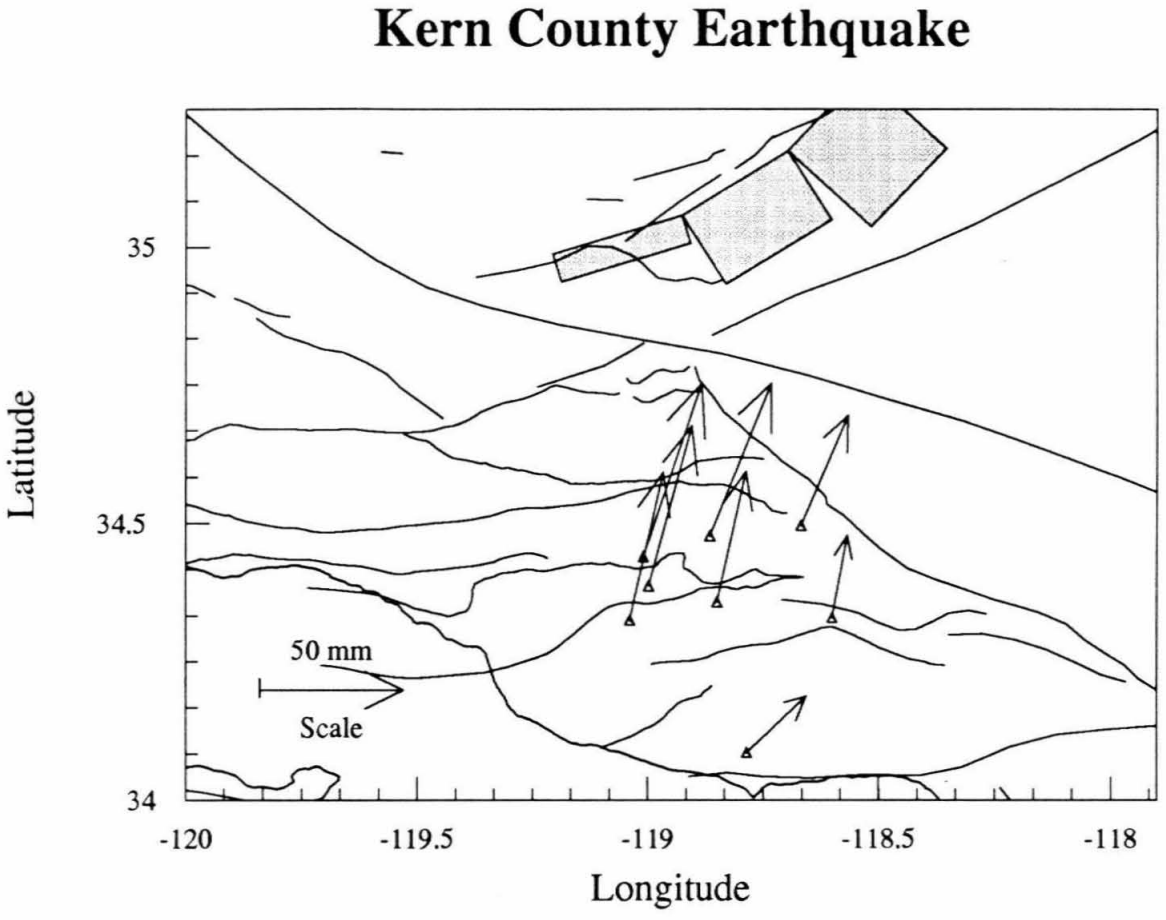

Figure 4.2: Predicted displacements of the Kern County earthquake. The shaded area marks the projection of the fault on the surface.

a finite fault that ruptured the surface, using *Heaton's* [1982] two fault model of the earthquake. The results are similar in either case and are minimal, with maximum displacements of about 50 mm occurring in the eastern part of the basin at San Fernando (SAFE). Again, typical baselines across the basin require approximately 50 mm of displacement to be detected by triangulation. We conclude from this study that the San Fernando earthquake had little impact on any observed strains in the Ventura Basin.

Viscoelastic deformation from earthquakes

Although deformation in the Ventura Basin region cannot be explained by elastic dislocation models of the San Fernando or Kern County earthquakes, it is possible that strain within the basin was associated with the earthquakes. The issue of non-uniform strain or the relation of crustal deformation to earthquake cycles has been addressed for both strike-slip and dip-slip earthquakes [*Li and Rice*, 1987, *Cohen*, 1984, *Cohen and Kramer*, 1984]. These workers find that, when an elastic crust is coupled to a Maxwellian viscoelastic asthenosphere, relaxation of the viscoelastic layer causes time-dependent deformation of the crust. *Cohen and Kramer* [1984] examined post-seismic deformation for dip-slip earthquakes using a three-layer rheological model and determined that relaxation of a standard linear solid lower lithosphere substantially increases horizontal straining. In this model the upper lithosphere is elastic, the lower lithosphere is a standard linear solid and the asthenosphere is a Maxwellian viscoelastic material. The lower lithosphere partially relaxes during the earthquake cycle, but maintains some elastic stress over longer time-scales. The vertical subsidence is most sensitive to the depth of the asthenosphere, but horizontal

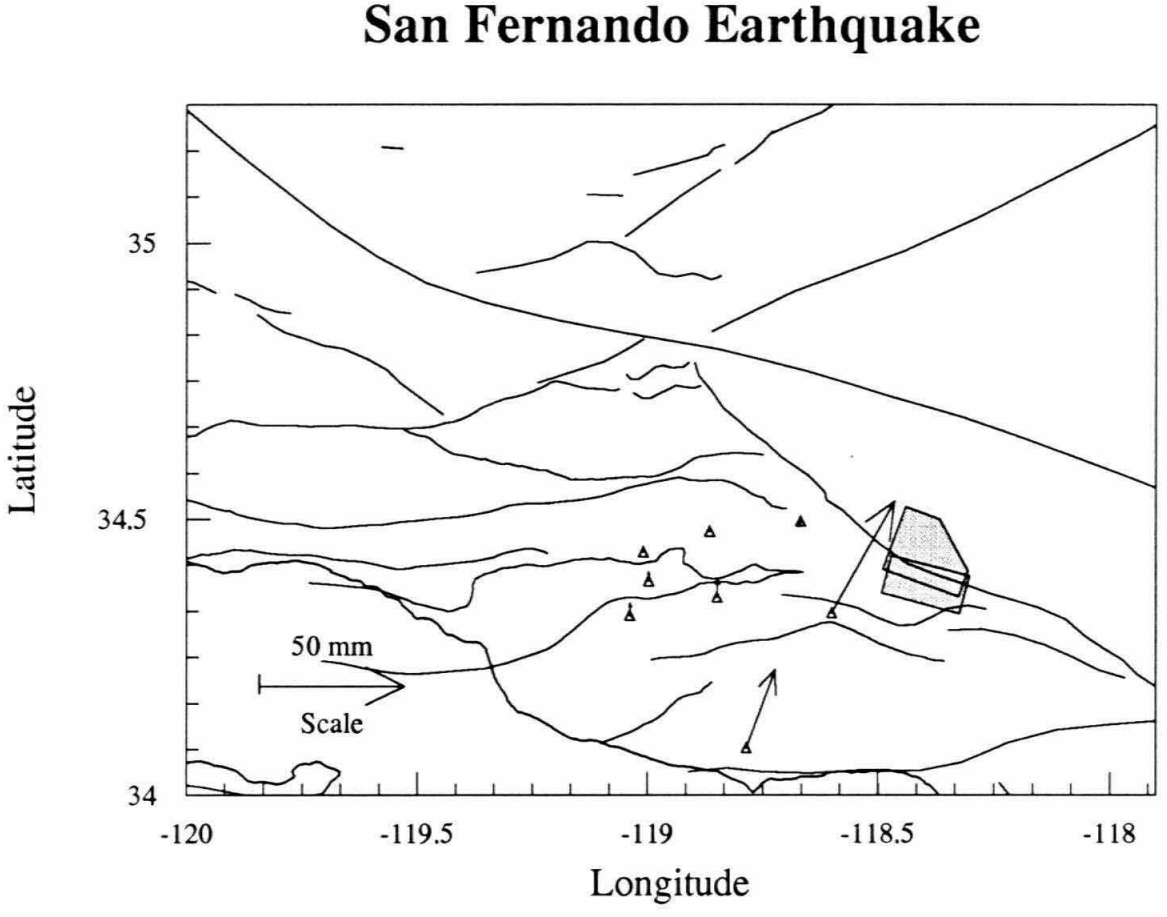

Figure 4.3: Predicted displacements of the San Fernando earthquake. The shaded areas mark the projection of the faults on the surface.

straining is dependent primarily on relaxation of the lower lithosphere.

Cohen [1984] applied this model to a fault dipping 45° and rupturing a zone from 0 to 15 kilometers depth. Displacement on the fault was 1 m. *Cohen* [1984] bases his model on the 1896 Riku-u magnitude 7.5 earthquake. The distance down dip and the displacement of the rupture zone are similar to the San Fernando earthquake. The model is plane strain, which assumes an infinite fault in the third dimension. This applies well to the Riku-u earthquake because the length of the rupture zone was 40 km [*Thatcher et al.*, 1980]. Although the San Fernando earthquake ruptured a zone only 15 km wide, parallels may still be drawn from *Cohen's* [1984] model. One of the most important aspects of the model is that a zone greater than one fault dimension is deformed both vertically and horizontally [*Cohen*, 1984]. The triangulation shows no conclusive evidence, however, that the deformation was any different before the earthquake than after the earthquake. We conclude that both the Kern County and San Fernando earthquakes had little effect on the geodetic results within the network.

4.2 Current Tectonics of the Ventura Basin

The results presented in Chapter 3 indicate that the highest velocity gradients in the geodetic network occur across the Ventura basin in a narrow compressive zone about 15 km wide and 40 km long. We have found no evidence of significant deformation between the southern margin of the basin and the coast. These rates have been sustained for approximately 30–50 years across the basin and for about 90 years south of the basin. The east-central Ventura basin may exhibit a slightly higher

strain rate than the eastern part of the basin. Deformation north of the basin is poorly determined, but appears to be occurring at a lower rate than across the basin. The results suggest that the deformation is spatially non-uniform. Within this network the geodetic results cannot be fit by the broad simple shear zone that *Ward* [1988] applies to California. More complex processes must account for the pattern of deformation. We will first examine possible fault models of the basin region. Then we will discuss the Ventura basin in a more regional setting.

4.2.1 Fault models

Southern California has been modeled as a megashear zone [*Ward*, 1988], and geodetic results near the big bend of the San Andreas fault can be modeled by creep at depth on the San Andreas, Garlock, and Big Pine faults [*Eberhart-Phillips et al.*, 1990]. We will start by taking into account existing models and test how well the data fit those models. Then we will attempt to fit any discrepancies with more detailed models of the basin region.

Because the *Eberhart-Phillips* [1990] model is the most detailed of the region, we used it to model the displacements in the Ventura basin network due to the San Andreas, Garlock, and Big Pine faults. We modeled the displacements with an elastic dislocation model [*Okada*, 1985]. Motion on the three faults has little effect on the Ventura basin network (compare figures 3.1 and 4.4). The largest, though still minor, effects are at Munson (MUNS) and Yam 2 (YAM2), which are nearest to the San Andreas and Big Pine faults. The difference in motion is not outside the standard deviation of the observed motion, however. It appears that the velocities estimated near the Ventura basin are unrelated to the San Andreas fault system.

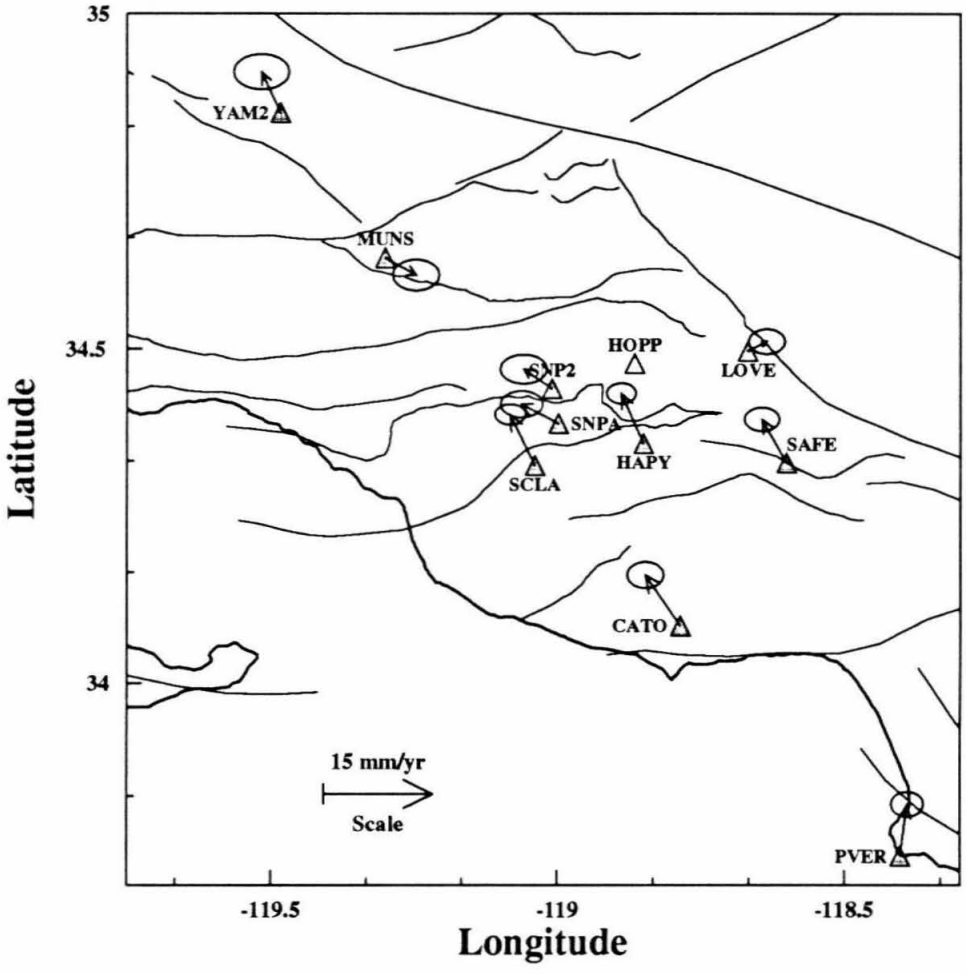

Figure 4.4: Velocities of the stations minus the predicted motion from the San Andreas, Garlock, and Big Pine faults.

Although simple elastic dislocations do not provide a complete picture of crustal deformation, much can still be learned from such models. An elastic dislocation is a good approximation for modeling surface deformation within the Ventura Basin, provided that faults are creeping. We use *Okada's* method [1985] as discussed above to model the north-south cross-section, A–A', across the east-central Ventura Basin (figure 4.5). This section extends perpendicular to the trend of the east-central Ventura Basin. We projected the data shown in the following models onto the line A–A'. All of the displacements calculated are relative to Hopper (HOPP).

To constrain an initial model we used geologic cross-sections and estimates of displacement rates on faults bounding the basin. We constructed the model from an eastward extrapolation of a cross-section throughout the western Transverse Ranges [*Namson and Davis*, 1988], and a cross-section through the east-central basin [*Suppe and Medwedeff*, 1990] (figure 4.6). For this model, we assumed that any faults on the south side of the basin are locked, because man-made structures crossing the ridge show no evidence of deformation [*Yeats*, 1988]. We also keep the San Cayetano fault on the north side of the basin locked. Evidence of scarps along the fault and no tilting or warping of deposits indicates that this fault is locked between earthquakes [*Rockwell*, 1988]. We extend the locked faults on either side of the basin to mid-crustal detachments. The northern detachment fault represents an arbitrary horizontal fault that is creeping at a rate of 15 mm/yr. We estimated the depth of the fault from the depth of earthquakes north of the basin [*Yerkes and Lee*, 1979]. The southern detachment fault represents the South Mountain thrust [*Namson and Davis*, 1988; *Suppe and Medwedeff*, 1990] with 12 mm/yr of creep imposed on it. We

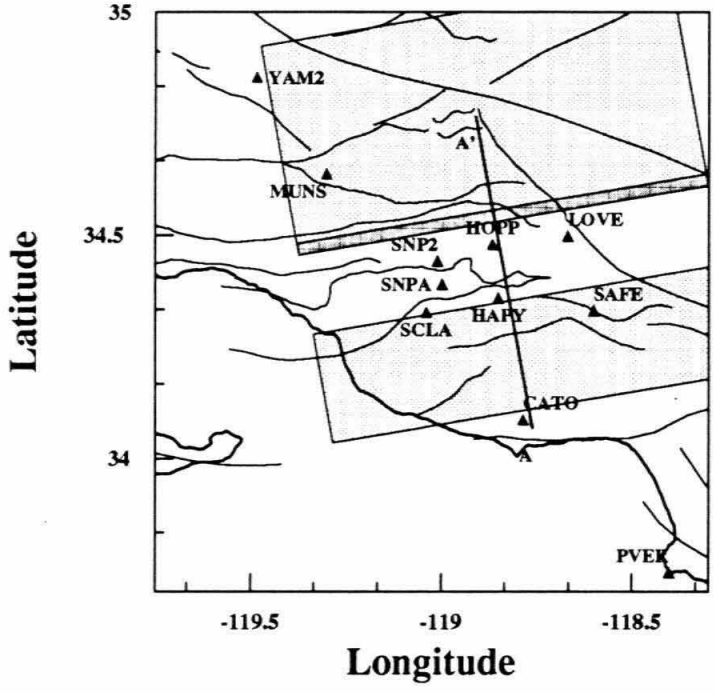

Figure 4.5: Map showing cross-section A–A' used for the dislocation calculations. The fault projections are marked by the shaded areas. Displacements of each of the stations are projected onto the section A–A'.

based the creep rates of the faults on the rate of deformation across the Oak Ridge and the total rate across the western Transverse Ranges [*Yeats*, 1988; *Namson and Davis*, 1988]. Both faults extend 50 kilometers on either side of section A–A'. The northern fault extends 50 km northward, which is physically too large because it is unlikely that the detachment crosses the San Andreas [*Eberhart-Phillips*, personal communication] and faults north of the San Andreas thrust towards the north. The 50 km width of the fault allows for a compressive regime to exist throughout the western Transverse Ranges, however. The southern fault extends 29.2 km down dip to a depth of 15.5 km. This is the extent of the fault shown by *Namson and Davis* [1988]. At the bottom, the fault possibly joins with a reverse-dipping fault that is situated underneath the South Mountain Thrust [*Namson and Davis*, 1988]. On this fault the upper block moves south over the lower block. (We modeled only the faults near the surface.)

The calculated versus observed displacements for this model match to well within the errors of the data, except for Santa Paula Peak (SNP2) (figure 4.6). If Loma Verde (LOVE) rather than Hopper (HOPP) is the representative site on the north side of the basin, the model curve is shifted up slightly and the model fits the data better. The data show evidence of block motion south of the basin from Castro (CATO) to the Oak Ridge, on which lie Santa Clara (SCLA), San Fernando (SAFE) and Happy (HAPY). The block motion can be satisfied by creep on the South Mountain Thrust, which terminates under the Oak Ridge. Motion on this fault accounts for about 3.5 mm/yr of displacement across the basin with the sharpest velocity gradient occurring along the northern margin of the Oak Ridge. We also extended

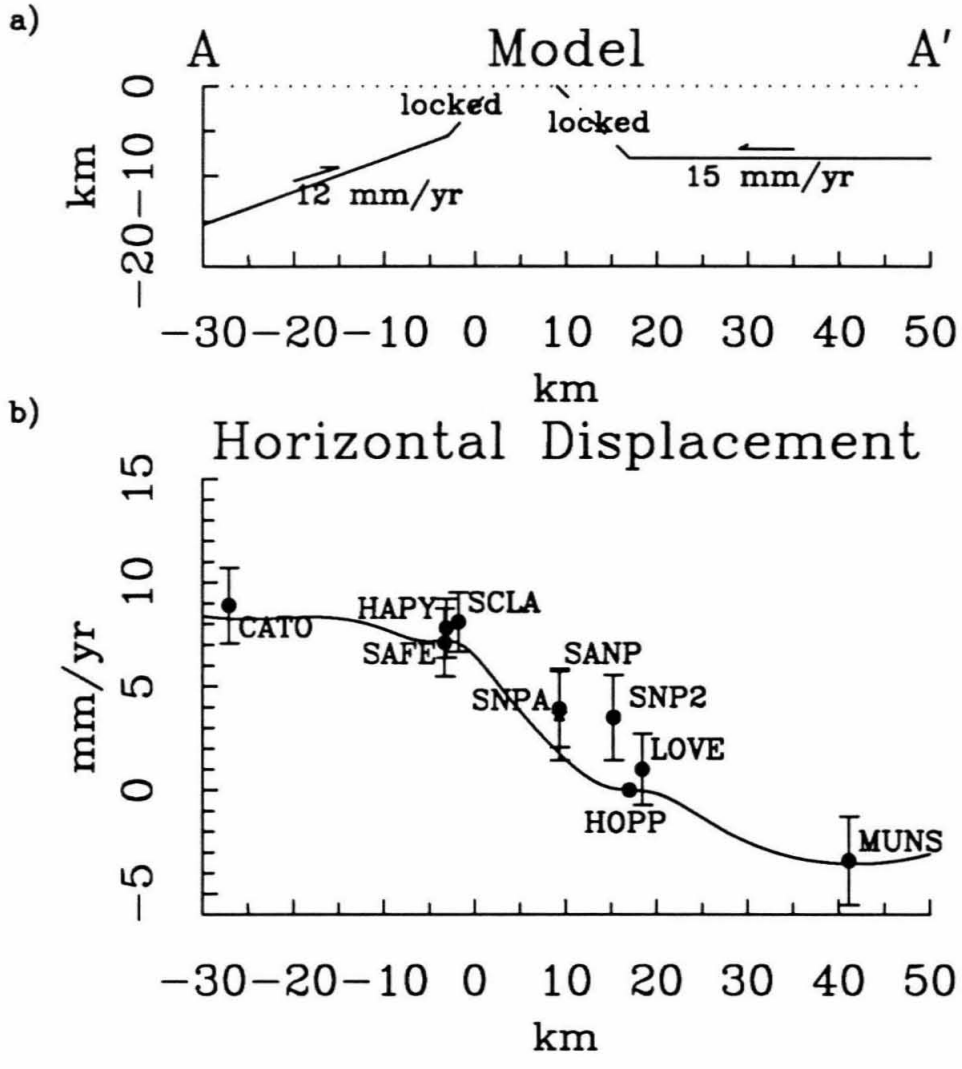

Figure 4.6: a) Fault model used for the dislocation calculations. The map view of the section is marked on the previous figure. b) Observed and modeled horizontal displacements relative to HOPP. The observed displacements and coordinates of the sites have been projected onto the cross-section A–A'. SANP is marked by an asterisk and is the rate at Santa Paula (SNPA) determined from VLBI.

the fault, at its southern terminus, into a horizontal detachment fault. This model is not significantly different, but results in a slight gradient south of the basin. The data from the Oak Ridge northward can be nearly fit by a sloping, straight line. The deeper detachment fault on the north side of the basin is responsible for a more uniform velocity gradient across the section. The fault is responsible for about 5 mm/yr of displacement across the basin and 3 mm/yr of convergence north of the basin. Shortening the northward extent of the detachment fault so that it lies only south of the San Andreas fault, has little effect on the surface profile. The position of the stations relative to the model is constrained by the geology to about ± 2 km.

Suppe and Medwedeff [1990] propose that the Oak Ridge anticline is a fault-propagation fold. In such a fold, faulting and folding are coincident. The fold forms at the tip of a propagating thrust fault. In some cases the fold may cease to form and the fault will break through the structure [*Suppe and Medwedeff*, 1990]. It is not known whether this process occurs episodically or uniformly with time, but our model is consistent with a fault-propagation fold that forms by creep on a structure similar to that predicted by *Suppe and Medwedeff* [1990]. *Sheffels and McNutt* [1986] propose that the Ventura basin, within the western Transverse Ranges, marks a plate boundary in which the southern plate is subducting under the northern plate. *Sheffels and McNutt* [1986] estimate that the elastic thickness of the southern plate is only 5 km, while the elastic thickness of the northern plate is greater than 40 km. If the southern plate is indeed so thin, it is possible that the location of a creeping detachment fault may be shallow.

The displacements on the north side of the basin do not match the model quite

so well. The data in the center of the basin at Santa Paula (SNPA) indicate that the velocity gradient is higher on the north side of the basin than the model predicts. The depth to the detachment fault is the shallowest depth likely for such a fault based on the seismicity of the region. An alternative model that allows for creep of 5 mm/yr below 5 km on the San Cayetano fault fits the data better than the first model (figure 4.7).

The models are non-unique and also approximate the Ventura basin as a two-dimensional structure. The San Cayetano fault makes a sharp jog between the stations Santa Paula Peak (SNP2) and Hopper (HOPP) (figure 4.5). Three-dimensional effects are likely to account for the difference in velocity between Santa Paula Peak (SNP2) and the other stations on the north side of the basin.

To understand the slope of the velocity gradients and the total displacement across the basin, we carried out simple models that are not related to the basin structures. In the first and second models we varied the dip of a single thrust fault that extends up to 1 and 5 km respectively (figures 4.8 and 4.9), and we varied the depth of a horizontal detachment in the third model (figure 4.10). The slope of the velocity gradient at the tip of the propagating fault is controlled by the depth of the fault. The shallower the fault, the steeper the gradient. The deeper the fault, the more constant the velocity gradient across the profile. Shallower faults take up more of the total slip in a narrower area. The complexity of the curvature behind the tip of the propagating thrust is controlled by the dip of the fault. This is because the steeper the dip, to more vertical motion there is and the horizontal displacements fan away from the uplifted area. Variation of dip has little effect on the slope of

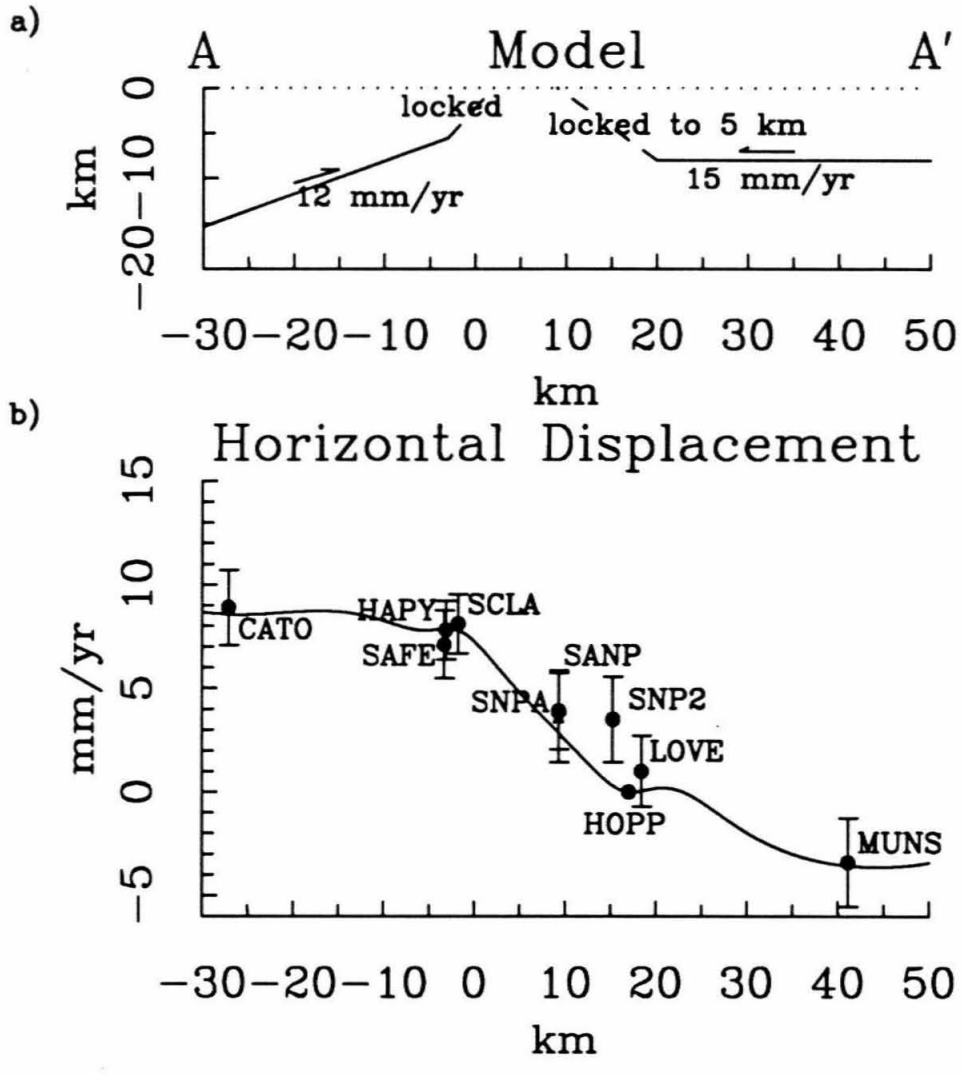

Figure 4.7: a) Fault model used for the dislocation calculations. The northern fault is locked to 5 km and creeps at a rate of 5 mm/yr from 5 to 8 km. b) Observed and modeled horizontal displacements relative to HOPP. The observed displacements and coordinates of the sites have been projected onto the cross-section A–A'. SANP is marked by an asterisk and is the rate at Santa Paula (SNPA) determined from VLBI.

the gradient, which is steepest near the fault tip, but does affect the total observed displacement. The more horizontal the dip of the fault, the more block-like the displacements at the surface on the forward propagating side of the fault (to the left in figure 4.8). Intermediate dipping faults show the most block-like motion behind the fault (to the right in figures 4.8 or 4.9). The displacements are more complicated directly above the fault.

The limiting cases shown above suggest that a combination of horizontal and dipping faults is most likely controlling the deformation of the Ventura basin. The geodetic observations agree with the geological observations that no faults should be creeping at the surface. The velocity gradient is steep across the basin, but can best be accounted for by intermediate depth faults. The sharp corners in the velocity profile can be explained by creep on dipping faults at the edges of the basin.

Our model is greatly simplified from the real earth case and limitations apply. The model assumes a linear, elastic isotropic medium in a half-space. The real earth is layered and the elastic upper crust most likely overlies a ductile lower crust [e.g., *McNutt et al.*, 1988]. In an area of such complexity as the Ventura basin it is unlikely that the medium is isotropic. The basin itself is filled to great depths with sediments which may be more loosely consolidated and less rigid than the surrounding bedrock. The basin may not deform elastically, at least in the upper part. Within the basin, earthquakes have only been observed at depths greater than 20 km (figures 4.11–4.13).

The model assumes that the deformation is uniform through time. The evidence of brittle failure on the San Cayetano fault suggests that the deformation is time-

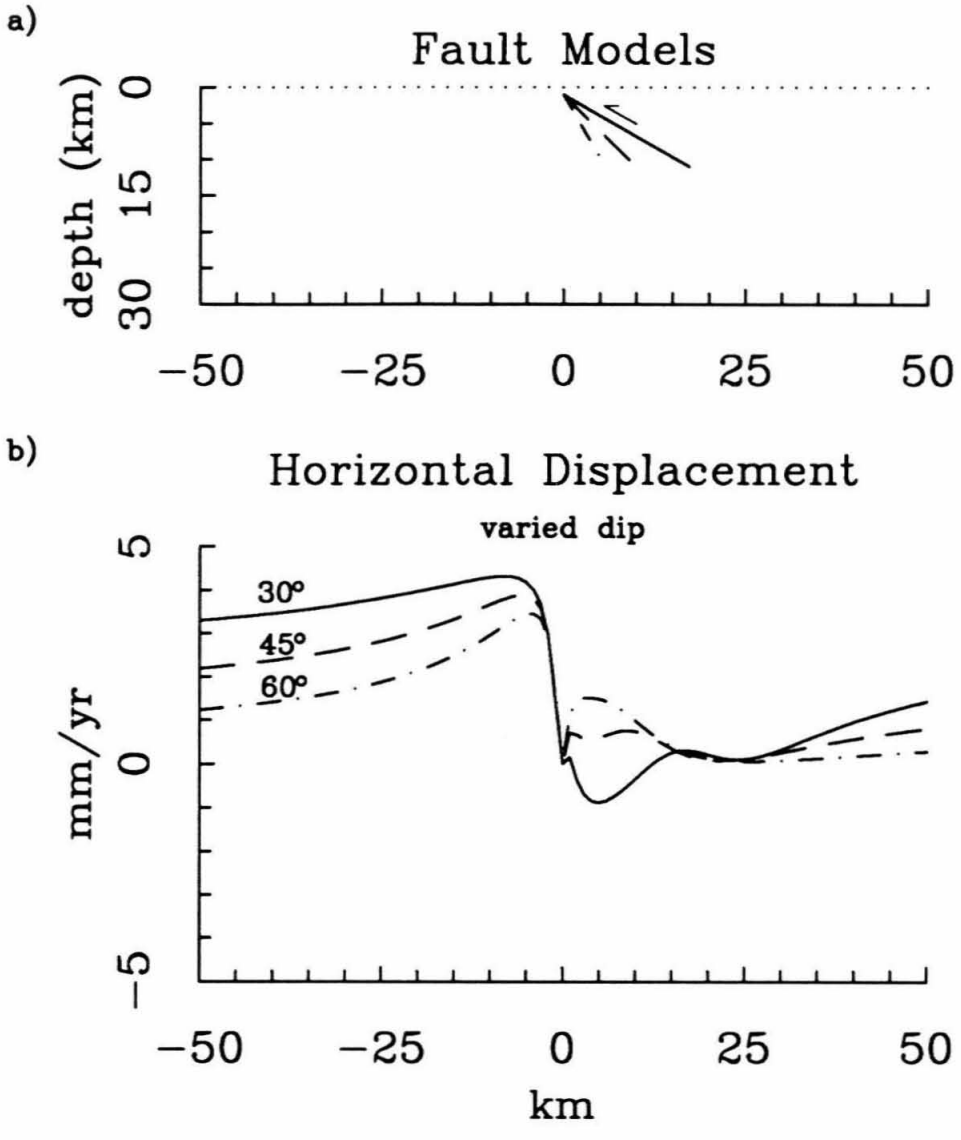

Figure 4.8: Effect on the velocity profile from varying dips on a fault that extends to 1 km from the surface. The sample fault extends from 1–11 km depth, in each case, with a slip of 10 mm/yr up dip.

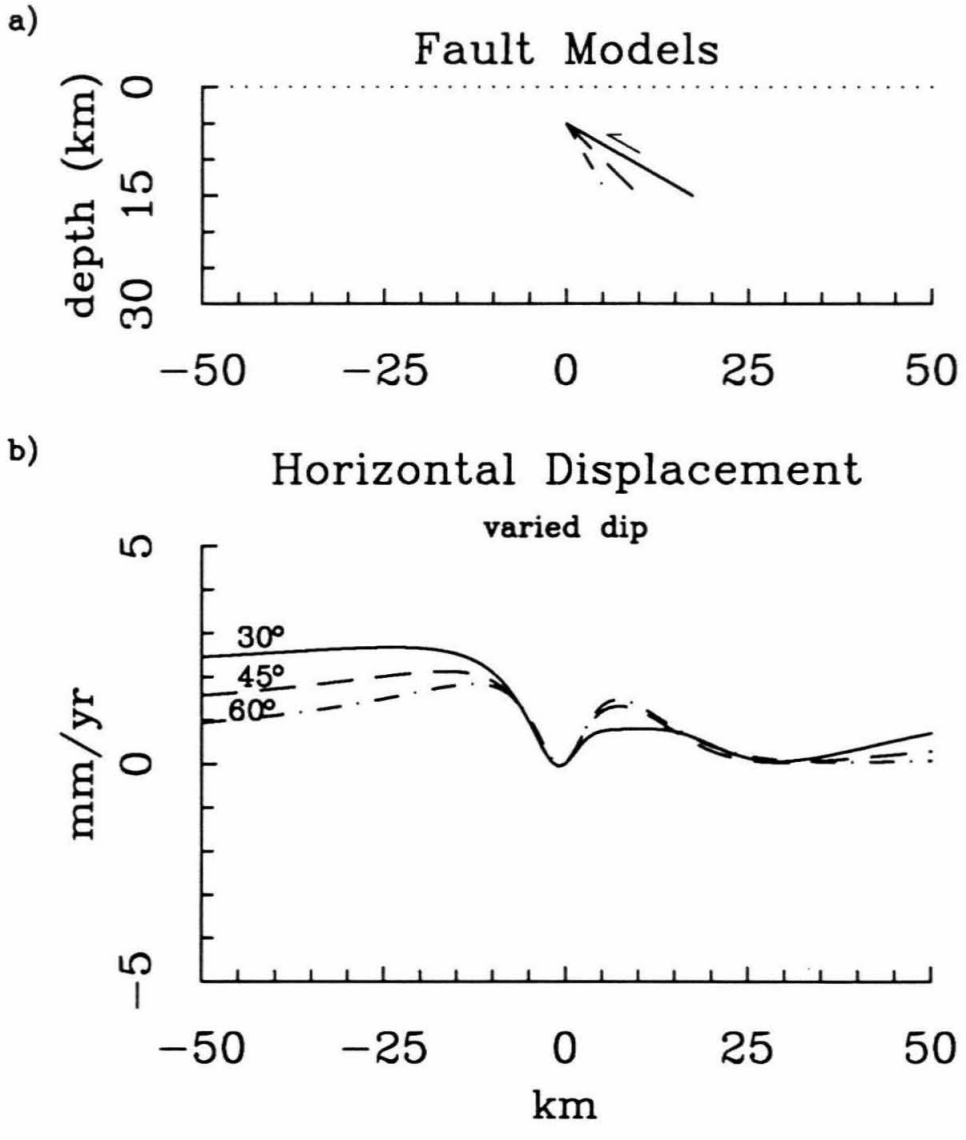

Figure 4.9: Effect on the velocity profile from varying dips on a fault that extends to 5 km from the surface. The sample fault extends from 5–16 km depth, in each case, with a slip of 10 mm/yr up dip.

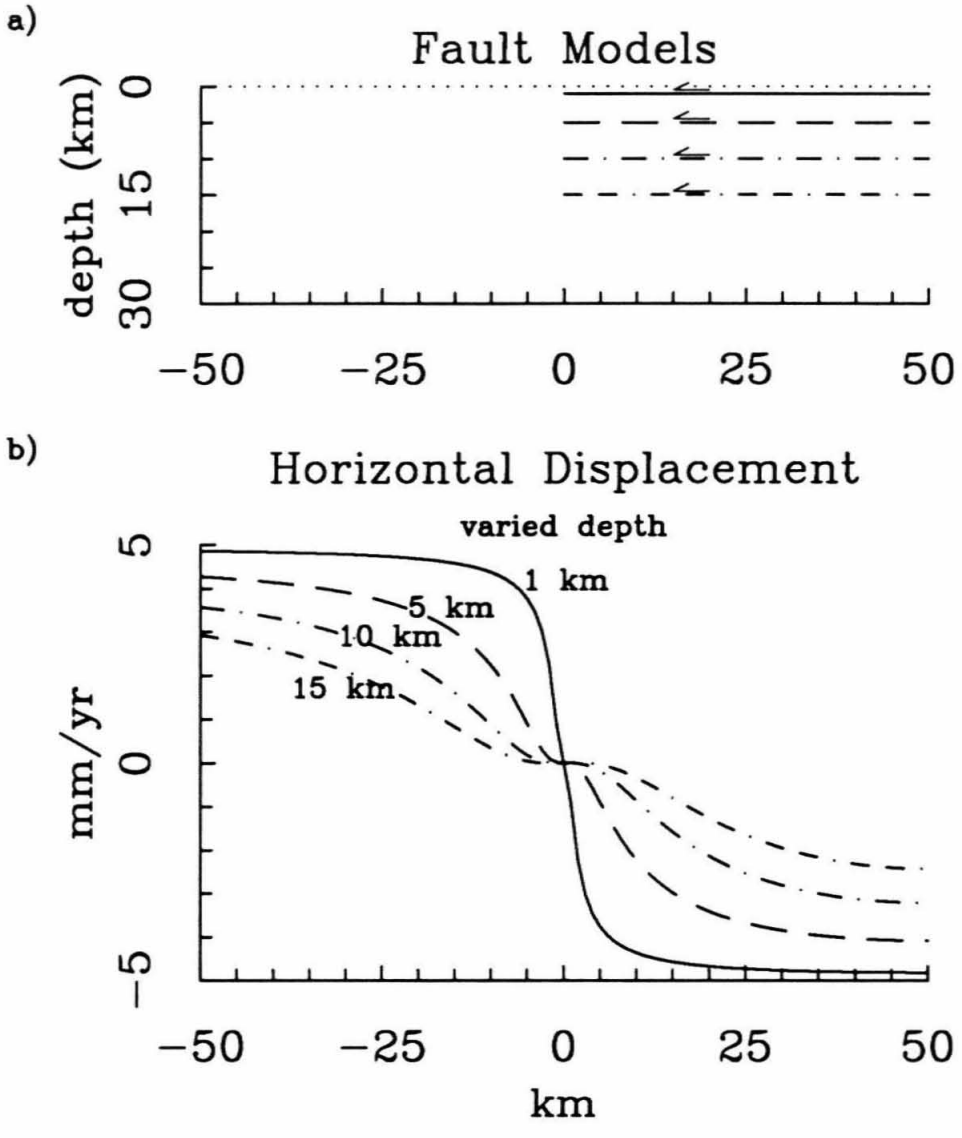

Figure 4.10: Effect on the velocity profile from varying depths. The sample fault is a horizontal detachment starting at 0 km and ending at 100 km (off the figure). The slip on each fault is 10 mm/yr with the top layer moving toward the left over the bottom layer.

dependent. This is perhaps the greatest limitation of our model. Viscoelastic models by *Cohen* [1984b] and *Li and Rice* [1987] show that surface deformation is non-uniform throughout the earthquake cycle. Geodetic data associated with the Kern County and Loma Prieta earthquakes also indicate that deformation varies with time. Prior to the Kern County earthquake, the strain rate near the fault zone was twice as high as the ambient strain rate of the region [*Stein and Thatcher*, 1981]. An increase of strain by about a factor of two preceded the 1989 Loma Prieta earthquake beginning about one year prior to the earthquake [*Lisowski et al.*, 1990]. The change in deformation was not necessarily a precursor, but the observations demonstrate that crustal deformation is not necessarily uniform in time. Our model may still reflect the short-term pattern of displacement on faults near the Ventura basin, however, assuming that the fault motion we described occurs near the elastic upper crust.

The deep seismicity within the Ventura basin itself seems inconsistent with the above model. We consider, however, that the basin seismicity might be due to the high rates of convergence, as the result of sediment loading. As anticlines are rapidly forming both north and south of the basin, sediments are being shed off into the Santa Clarita River Valley (the central axis of the Ventura basin). Landslides, along the margins of the basin, have been occurring for thousands of years [*Hacker*, 1969, *Truex*, 1977]. Depressed heat flow values in the Basin and a concave-down temperature profile are indicative of cold sediments subsiding within the basin [*DeRito et al.*, 1989]. These colder sediments, when compacted, are presumably brittle to a greater depth than the surrounding region. In addition to this, we still maintain that a north-south compressive stress regime exists at depths below the detachment faults.

The fault model shown above is an incomplete model across the Ventura Basin but is adequate for modeling the surface deformation. It is believed that a downgoing flow lies underneath the western Transverse Ranges [*Humphreys and Hager*, 1990]. Although it is questionable whether the downgoing flow is of a slab-like nature, we will sometimes refer to it here as a slab for the sake of simplicity. *Namson and Davis* [1988] incorporate this concept into their cross-section of the western Transverse Ranges that passes through the western edge of the Ventura basin. The thrust faults at the surface are coupled with faults that connect with the region of downgoing flow. The surface is effectively being scraped off the colliding plates.

In Chapter 1, we mentioned the presence of north-south striking normal events deep within the basin near the town of Fillmore. The orientation of the focal mechanisms indicate east-west extension. The depths of the hypocenters are about 28 km [*Bryant and Jones*, personal communication]. All earthquakes mentioned were relocated by *Bryant and Jones* [1991] with an improved velocity model. We maintain that the earthquake was still a result of a north-south tectonic compressive regime. Near the surface the principal events show north-south thrusting [*Yerkes and Lee*, 1979]. We will examine the principle stresses of the region. For the sake of simplicity we assume that the tectonic stress regime is entirely compressive in the north-south direction. Focal mechanisms indicate that the dominant stress regime of the region is north-south compressive. If east-west is taken as the *1*-axis, north-south the *2*-axis and vertical the *3*-axis then stress tensor for a confined basin, neglecting pore-fluid

pressure and assuming a uniform tectonic stress with depth, is as follows:

$$\sigma_{ij} = \begin{bmatrix} \frac{\nu}{(1-\nu)}\rho g h + \sigma_{T_E} & 0 & 0 \\ 0 & \frac{\nu}{(1-\nu)}\rho g h + \sigma_{T_N} & 0 \\ 0 & 0 & \rho g h \end{bmatrix}$$

where σ_{T_E} and σ_{T_N} are the east and north tectonic stresses, respectively, ν is Poisson's ratio, ρ is the density, g is the gravitational acceleration, h is depth and compressive stress is positive. From the stress tensor above, the deviatoric stress is:

$$\sigma'_{ij} = \begin{bmatrix} \frac{\frac{-(1-2\nu)}{(1-\nu)}\rho g h + 2\sigma_{T_E} - \sigma_{T_N}}{3} & 0 & 0 \\ 0 & \frac{\frac{-(1-2\nu)}{(1-\nu)}\rho g h - \sigma_{T_E} + 2\sigma_{T_N}}{3} & 0 \\ 0 & 0 & \frac{\frac{2(1-2\nu)}{(1-\nu)}\rho g h - \sigma_{T_E} - \sigma_{T_N}}{3} \end{bmatrix}$$

In this case, the dominant tectonic regime is north-south compressive, so $\sigma_{T_N} > \sigma_{T_E}$ and $\sigma'_{NN} > \sigma'_{EE}$. At shallow depths, while $h < \frac{(1-\nu)\sigma_{T_E}}{(1-2\nu)\rho g}$, $\sigma'_{NN} > \sigma'_{EE} > \sigma'_{UU}$. This explains the north-south thrust regime, because the maximum principal stress is oriented north-south and the minimum principal stress is vertical. Deeper, while $h < \frac{(1-\nu)\sigma_{T_E}}{(1-2\nu)\rho g} < h < \frac{(1-\nu)\sigma_{T_N}}{(1-2\nu)\rho g}$, $\sigma'_{NN} > \sigma'_{UU} > \sigma'_{EE}$. At these depths strike-slip mechanisms should prevail. This agrees reasonably well with observation; at intermediate depths strike-slip mechanisms are common (figures 4.11–4.13). Very deep, when $h > \frac{(1-\nu)\sigma_{T_N}}{(1-2\nu)\rho g}$, $\sigma'_{UU} > \sigma'_{NN} > \sigma'_{EE}$. Normal events should occur at these greatest depths because the principal deviatoric stresses change orientation so that the maximum compressive stress is vertical and the minimum stress is east-west extensional. Such events are observed deep within the basin at about 28 km.

The normal events occur in the deepest parts of the basin and Santa Barbara Channel at a depth of about 28 km. Assuming an average density of 2.8 g/cm^3,

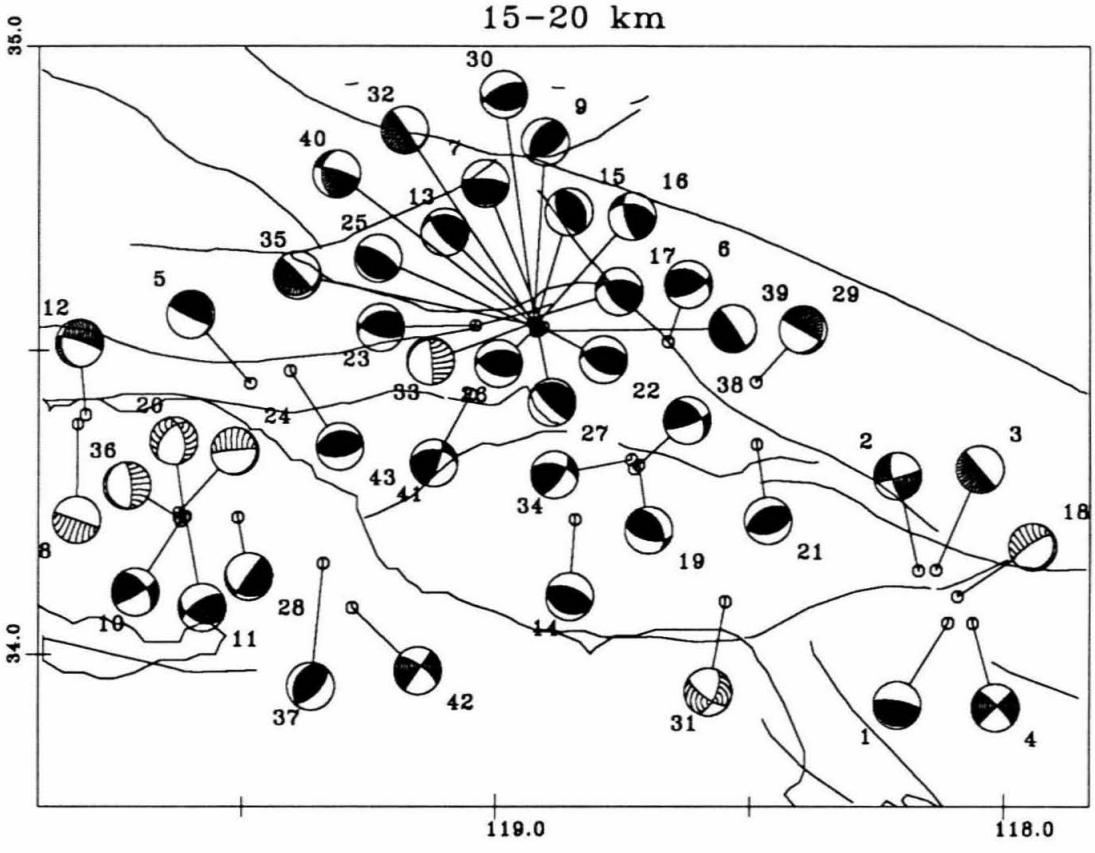

Figure 4.11: Focal mechanisms for events from 15-20 km near the Ventura basin. Thrust events are identified by shaded focal mechanisms, strike-slip events by intermediate spaced hash marks, and normal events by widely spaced hash marks (preferred solution). Events are for 1981–1989 inclusive. The events are sorted by depth with smaller numbers referring to the lowest depth cutoff. Offshore events are not reliably located, resulting in unreliable mechanisms [all events relocated with an improved velocity model by *Bryant and Jones*, 1991].

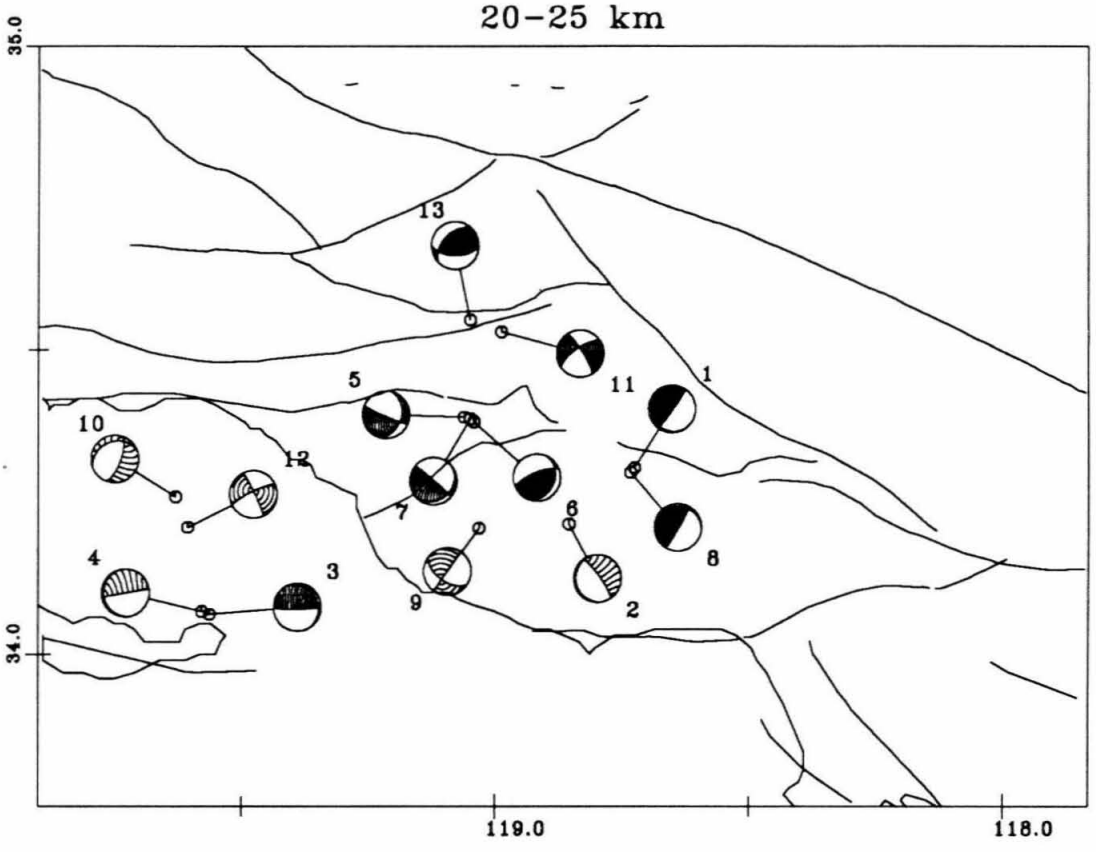

Figure 4.12: Focal mechanisms for events from 20-25 km near the Ventura basin. Thrust events are identified by shaded focal mechanisms, strike-slip events by intermediate spaced hash marks, and normal events by widely spaced hash marks (preferred solution). Events are for 1981-1989 inclusive. The events are sorted by depth with smaller numbers referring to the lowest depth cutoff. Offshore events are not reliably located, resulting in unreliable mechanisms [courtesy of *Bryant*, 1991].

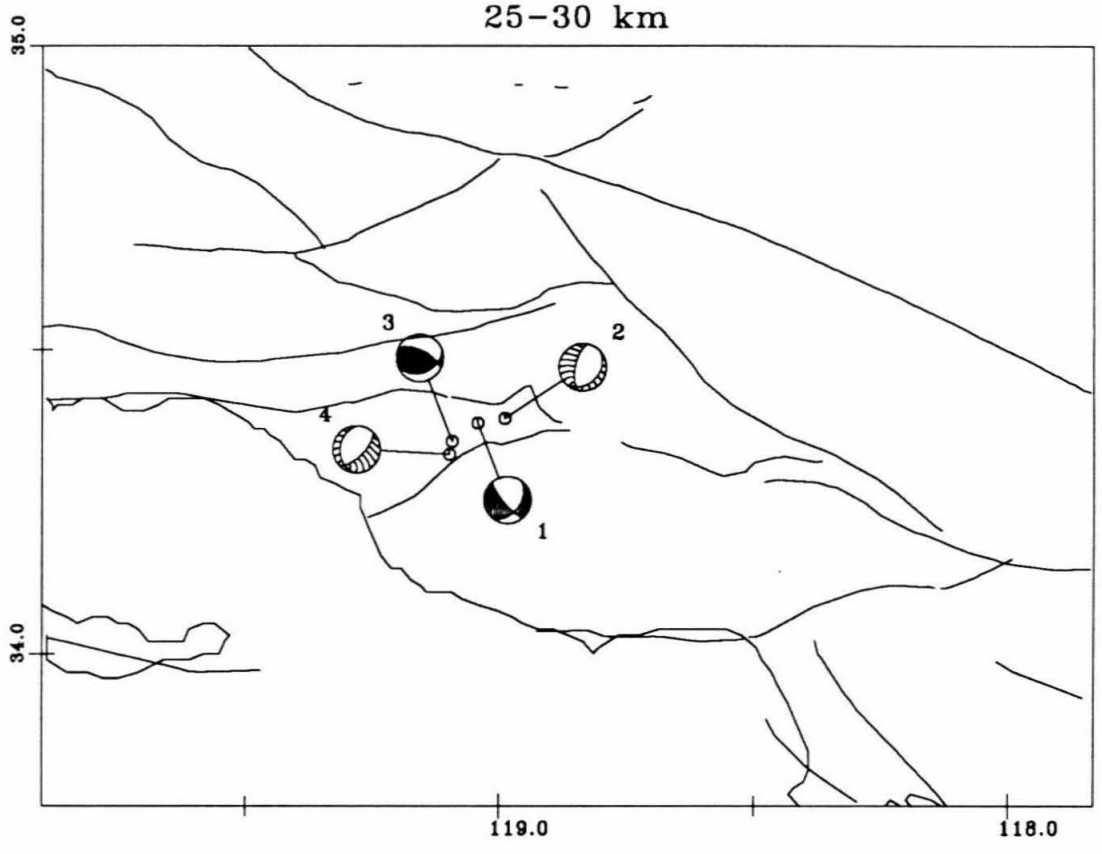

Figure 4.13: Focal mechanisms for events from 25-30 km near the Ventura basin. Thrust events are identified by shaded focal mechanisms, strike-slip events by intermediate spaced hash marks, and normal events by widely spaced hash marks (preferred solution). Events are for 1981-1989 inclusive. The events are sorted by depth with smaller numbers referring to the lowest depth cutoff [courtesy of *Bryant*, 1991].

Poisson's ratio of 0.25, and that the earthquakes occur at the depth transition from north-south compression to east-west extension, the north-south tectonic stress is 5.1 Kbar. This neglects any pore-fluid pressure effects and assumes that σ_{T_E} and σ_{T_N} are not functions of depth. Pore-fluid pressure would effectively decrease the lithostatic pressure and lower the estimate of σ_{T_N}.

4.3 Implications

The geodetic study of the Ventura basin implies that this section of the Transverse Ranges is dominated by almost pure compression. It appears that the basin itself is a boundary between two separate tectonic blocks that are converging on one another. The rate of convergence is rapid compared with elsewhere in southern California and the zone of convergence is very narrow.

4.3.1 Seismic hazard assessment

The fault models described above, in combination with other observations, can place bounds on the potential seismic activity of the Ventura basin. As noted in Chapter 1, the Ventura basin has not yielded a large earthquake in 200 years of record keeping [*Yeats*, 1988], yet the Ventura basin should have one of the highest frequencies of damaging earthquakes in southern California [*Wesnousky*, 1986]. There is evidence of previous earthquakes on the San Cayetano fault [*Rockwell*, 1988], but none have occurred in historical time. Evidence of earthquakes on the Oak Ridge fault is not as clear, but the hazard on the south side of the basin must still be considered. Perhaps the most important implication of the fault modeling above is that any faults near the basin might be locked at the surface. Release of strain across any of these locked

faults could occur by rupture during an earthquake.

Our model can be satisfied by creep on faults both north and south of the basin. We will assume that the northern and southern faults are unrelated and first consider the northern fault. The San Cayetano fault may be locked to a depth of 5–8 km and the fault dips about 45°, so the rupture could extend for up to 7–11 km. The geologic rate of displacement on the fault is highest between the sites Hopper (HOPP) and Santa Paula Peak (SNP2) and the geodetic rate is highest near Hopper (HOPP). The area is characterized by little seismicity, except for deep seismicity at one location, so we expect the Hopper region to be the most likely place of a future earthquake. The surface trace of the fault dies out just east of Hopper. It is possible that a large earthquake could rupture a zone 15 km wide. This is similar to the width of the surface rupture of the San Fernando earthquake. The moment release, M_0, of an earthquake is related to the rigidity of the rocks, μ, the surface area of the rupture, ΔS, and the average slip on the fault, $\overline{u}$:

$$M_0 = \mu \Delta S \overline{u}$$

The moment release for a slip of 1.4–2.2 m (7–11 mm/yr for 200 years) over a 15×7 km area ranging to a 15×11 km area would be $2.9\text{–}7.3 \times 10^{25}$ dyne cm. This corresponds to a moment magnitude, **M**, of 6.3–6.5 where

$$\mathbf{M} = \frac{2}{3} \log M_0 - 10.7$$

[*Hanks and Kanamori*, 1979]. The average slip rate we impose on the fault is less than the slip rate on the decollement. We assume that the additional compression is taken up by folding as the many folds of the basin suggest. The magnitude that we

estimate is based on a recurrence interval of 200 years. A longer time interval between earthquakes would increase the average slip per event and hence the magnitude of a potential earthquake. The smallest event likely for a fault that breaks the surface is probably a magnitude 6.0 for a 7×7 km rupture zone and an average slip of 1.4 m. The largest event might rupture a 11×30 km zone with an average slip of 3.0 m resulting in a magnitude 6.8 earthquake.

The earthquake hazard of the south side of the basin is probably much lower than the potential hazard of the north side. Our fault model shows that the Santa Susana thrust fault is likely to be creeping to a depth of 5.5 km. Evidence points to minor reactivation of the Oak Ridge fault [*Suppe and Medwedeff*, 1990]. The largest earthquake possible, assuming that the Oak Ridge fault slips 2.5 m over a 6×10 km zone, would be $\mathbf{M} = 6.2$. The large folds indicate that much of the deformation is accommodated through folding rather than by slip on faults. Our model does not account for slip on the upper part of the buried South Mountain thrust from a depth of 5.5 to 3 km. An event on this part of the thrust might produce a magnitude 5.5–5.8 earthquake.

A study of geodetic data before and after the Kern County earthquake suggests that near the rupture zone the strain rate was twice as high for approximately 15 years prior to the earthquake than it was after the earthquake [*Stein and Thatcher*, 1981]. Both leveling data and triangulation data support their observation. Following the earthquake, the strain rate near the rupture zone matched the typical strain rates for the region surrounding the fault. Stress is greatest at the tip of a propagating dislocation, so the strain in that region should also be greater. Following the release

of the accumulated stress it is likely that the strain rate would drop back to the ambient levels of the area.

Although we cannot determine the time of a future earthquake in the Ventura basin, it is possible that a magnitude 6.0–6.8 earthquake will occur on the San Cayetano fault within the next 200 years. The south side of the basin poses a lower threat, but could still produce a moderate $\mathbf{M} = 5.5-6.2$ earthquake. The high strain rate across the basin, which is about twice the ambient strain rate of the region, is characteristic of the strain rate near the rupture zone of the Kern County earthquake prior to the event [*Stein and Thatcher*, 1981]. The Loma Prieta earthquake was also preceded by increased strain [*Lisowski et al.*, 1990]. Unfortunately, the geodetic history surrounding earthquakes is so limited that it is not possible to assess whether these strain anomalies were precursors. We will only be able to interpret the high strain rate in terms of earthquake hazard after recording a more complete history of strain across the basin, and by making measurements both before and after an earthquake near the Ventura basin.

4.3.2 Santa Paula VLBI Footprint

Before we make any tectonic interpretations of the Santa Paula mark we will first compare our GPS results with those obtained from VLBI measurements. We occupied two VLBI sites in our study, Santa Paula (SNPA) and Palos Verdes (PVER), so we can compare our results directly with VLBI results. The VLBI results include data through 1990 (figures 4.14 and 4.15) and are the most recent solution for baseline component changes of Santa Paula (SANP) and Palos Verdes (PVER) relative to Mojave. All of the VLBI results were obtained from the VLBI group at

	East	North	Up
VLBI	-0.3 ± 1.1	-5.0 ± 1.5	13.3 ± 10.9
GPS	-6.6 ± 2.6	-5.9 ± 1.5	28.0 ± 10.5

Table 4.1: Comparison of results from VLBI and GPS. The given rates are of Santa Paula relative to Palos Verdes.

Goddard Space Flight Center and refer to Goddard solution glb721a [*Chopo Ma*, NASA/GSFC, written communication].

The comparison suggests that the north rate is the best determined component of the GPS solution (table 4.1) which is also shown by the formal uncertainties discussed in Chapter 2. We expected this because we were forced to use a bias-free solution from 1991 which weakens the east component. The longer time span obtained by adding the 1991 measurement probably improved the north component, because this component is not affected as strongly by unresolved ambiguities. The GPS solution matches the VLBI solution of *Ward* [1990] indicating that the rates estimated from any method or data set are not as well-determined as the formal errors suggest. Perhaps the site is locally unstable from fluctuations of the ground water table. It is interesting to note that both methods show Santa Paula rising relative to Palos Verdes. Displacement on the faults we modeled previously should cause uplift of Santa Paula, so it is probable that Santa Paula is indeed rising, rather than Palos Verdes subsiding. Note that if Santa Paula is indeed rising, oil withdrawal appears not to be causing subsidence of the basin.

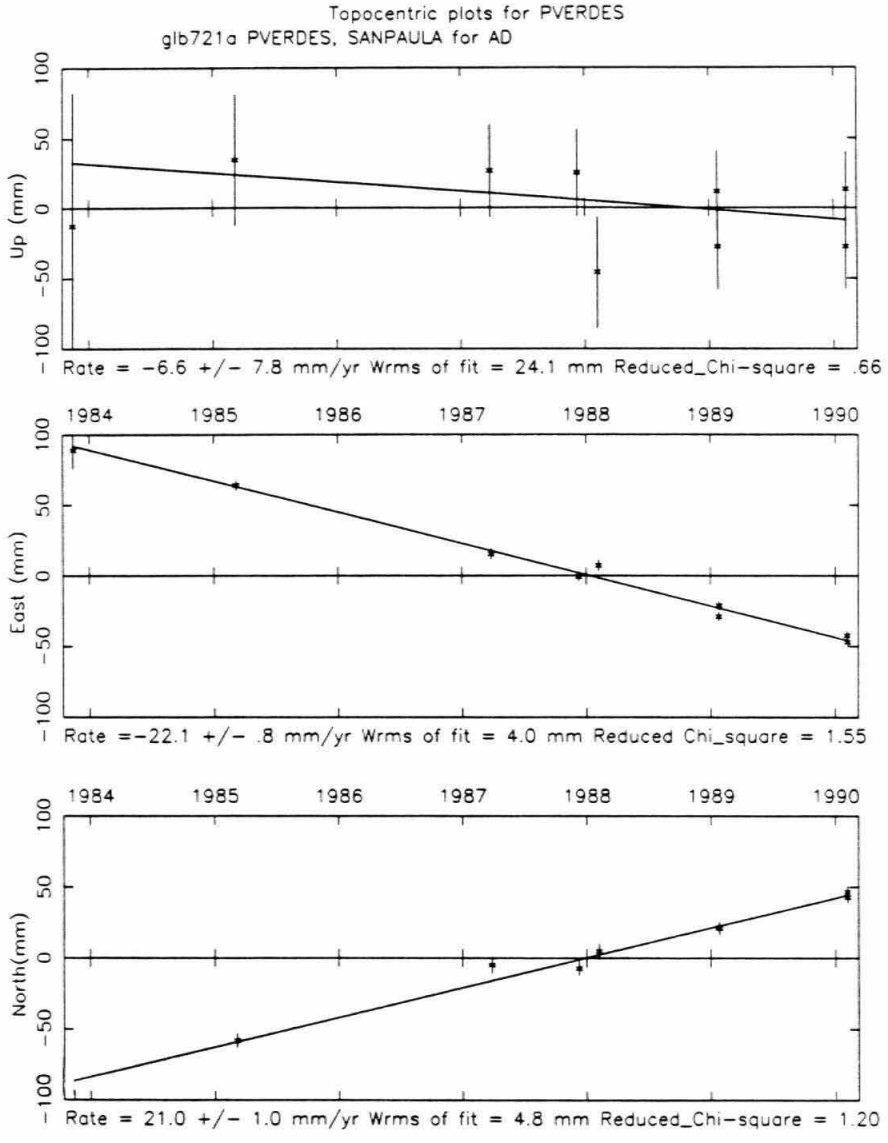

Figure 4.14: Plots showing baseline component changes with time of Palos Verdes relative to Mojave [courtesy of *Chopo Ma*, NASA/GSFC, 1991].

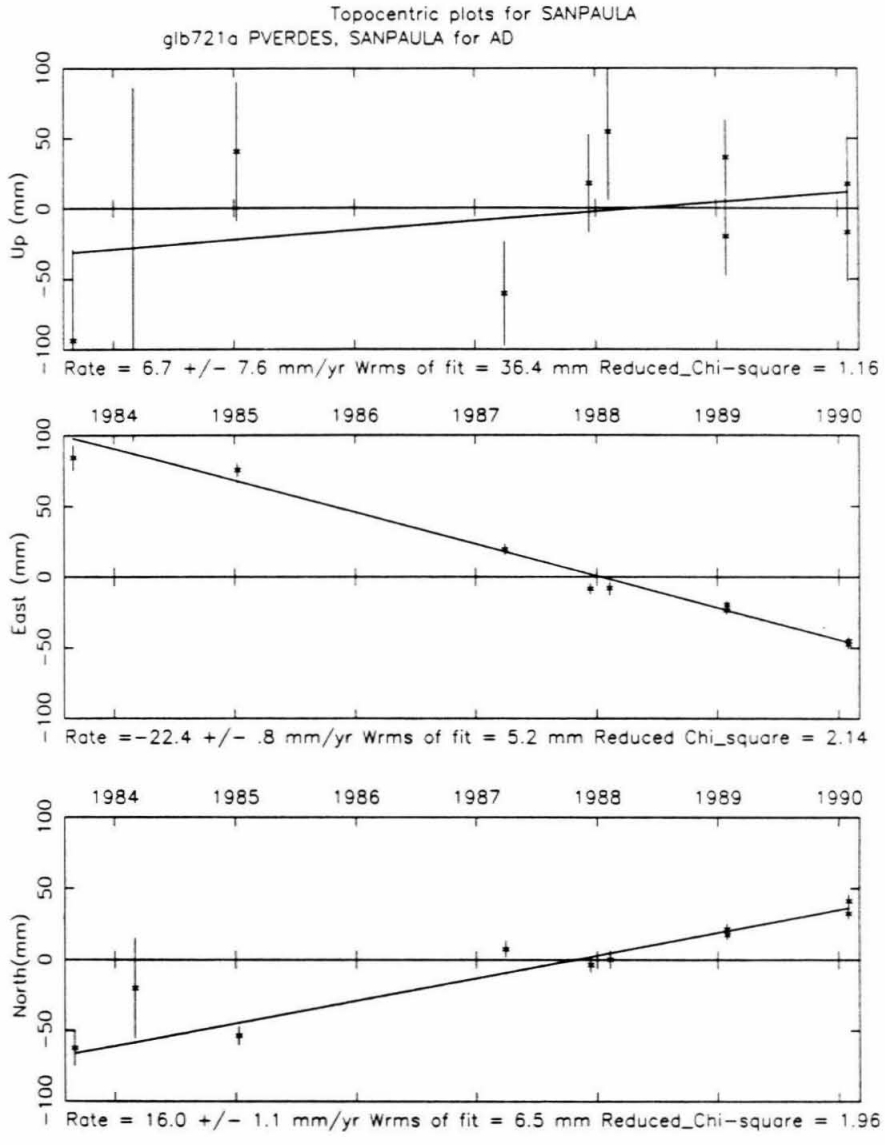

Figure 4.15: Plots showing baseline component changes with time of Palos Verdes relative to Mojave [courtesy of *Chopo Ma*, NASA/GSFC, 1991].

In this discussion, we have placed greater weight on the VLBI results because of the longer time history of the VLBI measurements. The results agree fairly well, but our task is to discuss Santa Paula in terms of its tectonic setting. GPS errors are baseline length dependent implying that our short baselines are more reliable.

From our results, and the morphology of the area, Santa Paula lies within the middle of a north-south compressional zone. This is not reflected in VLBI results from other stations. Thus, the compressional regime in which Santa Paula is situated must be fairly local, smaller than the surrounding region of VLBI stations. Santa Paula does not fit into the simple shear zone that can describe most of California. The compressional zone surrounding the station is narrow from north to south and is possibly only 15–30 km wide. The zone is not likely to extend far in the west direction either. Results from other GPS studies [*Murray*, 1991] indicate that La Cumbre Peak (LACU), near Santa Barbara, is moving slowly relative to Palos Verdes (PVER). Motion of the sites can be explained by shearing of the Pacific and North American plates. We have also not discussed, in detail, our results that show Yam 2 (YAM2), near the big bend of the San Andreas, not moving significantly relative to Palos Verdes (PVER). It seems that the zone of compression extends only from the San Andreas fault to the Oak Ridge just south of the basin. Future rate determinations of all of the stations in the 1990 network will serve to better define the tectonic setting of Santa Paula. In our last section, we will more completely discuss the kinematics of the Ventura basin region.

This work has also served to identify potentially active faults of the region. One of these, the San Cayetano fault, is exposed very near the Santa Paula (SNPA)

monument. Should this fault rupture we will be better able to understand the motion of Santa Paula (SNPA) related to fault movement, making it possible to understand motions of the site relative to other VLBI sites.

4.3.3 Relation to other observations

Our observations, when coupled with fault models, reflect what has been inferred from the geologic record. One goal of this study was to compare the geologic and geodetic rates, and patterns, of deformation. If the short-term and geologic rates are comparable, it is likely that faults are creeping up to the surface and that folds are forming anelastically. If the two do not match, the surface is probably elastically deforming. The geologic record reflects the average rate of deformation over many earthquake cycles, or cycles of elastic strain accumulation and release. Broad zones of deformation suggest that strain is accumulating elastically. The integrated strain over a large enough region should reflect the geologic rate on a fault or set of faults.

Our observations indicate that horizontal deformation is occurring over a fairly broad zone, with slightly higher rates in a localized zone across the basin. On geologic time scales, the western Transverse Ranges are a north-south convergent zone, and the Ventura basin, at the front of the ranges, is the most actively deforming part of the zone. *Namson and Davis* [1988] have inferred that 17–26 mm/yr of convergence has occurred across the western Transverse Ranges during the last 2–3 myr. We obtain a rate of convergence of 9–13 mm/yr across the southern half of the Ranges during a period of nearly three years. Combining our results with those of *Eberhart-Phillips et al.* [1990], which show approximately 7 mm/yr of convergence between the San Andreas fault and the Ventura basin, suggests that the present short-term

rate of convergence across the Ranges matches the lower bound on the geologic rate. Although we model approximately 25 mm/yr of horizontal shortening at depth, the total horizontal deformation at the surface is about 15 mm/yr, for the southern half of the western Transverse Ranges.

Geologic rates across the Ventura basin are difficult to measure precisely, because many of the faults are bedding plane faults, but 12–58 mm/yr of north-south convergence have been estimated [*Yeats*, 1983]. Our geodetic results show 6–9 mm/yr of closure across the basin, but the results of our dislocation models suggest an average rate up to approximately 18 mm/yr, over the earthquake cycle. This assumes that motion observed north of the basin at Munson (MUNS) is due to elastic strain accumulation that will be released on one or more faults bounding the basin. Based on our fault displacement model and the presence of active faults bounding the basin it is likely that such an event will eventually occur. Our detachment model accounts for up to 25 mm/yr of shortening across the southern half of the western Transverse Ranges.

Considering that we have measured such a rapid rate of deformation across the Ventura basin, the seismicity is quite low. The types of mechanisms and the depths at which they occur can be explained by a north-south compressive regime coupled with lithostatic loading. This is consistent with the observations from GPS. In addition to this, the pattern of seismicity suggests faults that are consistent with our fault model, which satisfies both the geodetic observations and geology.

The rapid rate of deformation implies high uplift rates and rapid rates of sedimentation. Gravity anomalies indicate that the Ventura basin is filled with sediments

to depths up to 14 km [*Luyendyk and Hornafius*, 1987]. Sedimentation causes subsidence which should depress the temperature profile. Within the basin the heat flow values are 48 mW/m^2, considerably lower than the 70 mW/m^2 found elsewhere in southern California [*DeRito et al.*, 1988]. The low heat flow indicates that the basin is colder, and presumably more brittle, to greater depths than the surrounding region, which explains why earthquakes occur deeper there than elsewhere. The unusual normal events are found in the Ventura basin because the brittle ductile transition is deeper than the depth transition to east-west extensional regime.

Paleomagnetic results show that block rotations have occurred near the basin at rates on the order of 5°/m.y. [*Hornafius*, 1985; *Kamerling and Luyendyk*, 1985]. We calculate rotations of a similar amount both north of and within the basin (tables 3.3 and 3.4). We can not delineate discrete blocks from our results, just as we can not delineate faults that are creeping at the surface. These diffuse blocks probably become more discrete as time passes and earthquakes along faults relieve elastic strain.

4.4 Regional setting of the Ventura basin

To this point we have discussed the Ventura basin without bringing it into the larger southern California tectonic picture. Some of the results in our network seem inconsistent with the compressive regime we have described so far. For example, Yam 2 (YAM2), in the Cuyama Valley, shows extension relative to other stations on the north side of the basin. The short time between measurements at this station weakens the solution, but we will give a possible tectonic explanation for the apparent

anomaly. We also consistently observe north-northwest compression across the basin while some workers prefer northeast-southwest compression [e.g., *Jackson and Molnar*, 1990]. When viewed on a larger scale these observations seem less anomalous.

During each experiment we occupied Palos Verdes (PVER), which is situated about 90 km southeast of the center of our basin network. This site was also occupied as part of the southern California GPS network so it provides a common reference for examining the Ventura basin in a regional framework. In figure 4.16 we combine results from the Ventura basin study with velocities estimated west of the network [*Murray*, 1991]. The error ellipses are smaller in the other study due to the longer time duration between measurements and increased number of measurements.

We calculated the expected displacements relative to Palos Verdes from the *Eberhart-Phillips et al.* [1990] model to test the extent to which the model satisfies the GPS data (figures 4.17 and 4.18). Comparison between the data and model suggests that a second buried right-lateral fault must be creeping, parallel to the main trend of the San Andreas, west of La Cumbre (LACU). The shear zone must pass south and west of La Cumbre (LACU) near Santa Barbara and north and east of Santa Cruz Island. The comparison of GPS and trilateration across the Santa Barbara Channel by *Larsen* [1991] also indicates right-lateral shear through this part of the channel. In general, the *Eberhart-Phillips et al.* [1990] model does not match the GPS results south of the big bend of the San Andreas, although the north component of sites south of the basin is fairly consistent with the model.

Several identifiable tectonic blocks appear to be present in the western Transverse Ranges. It appears that a right-lateral strike-slip structure must run parallel to the

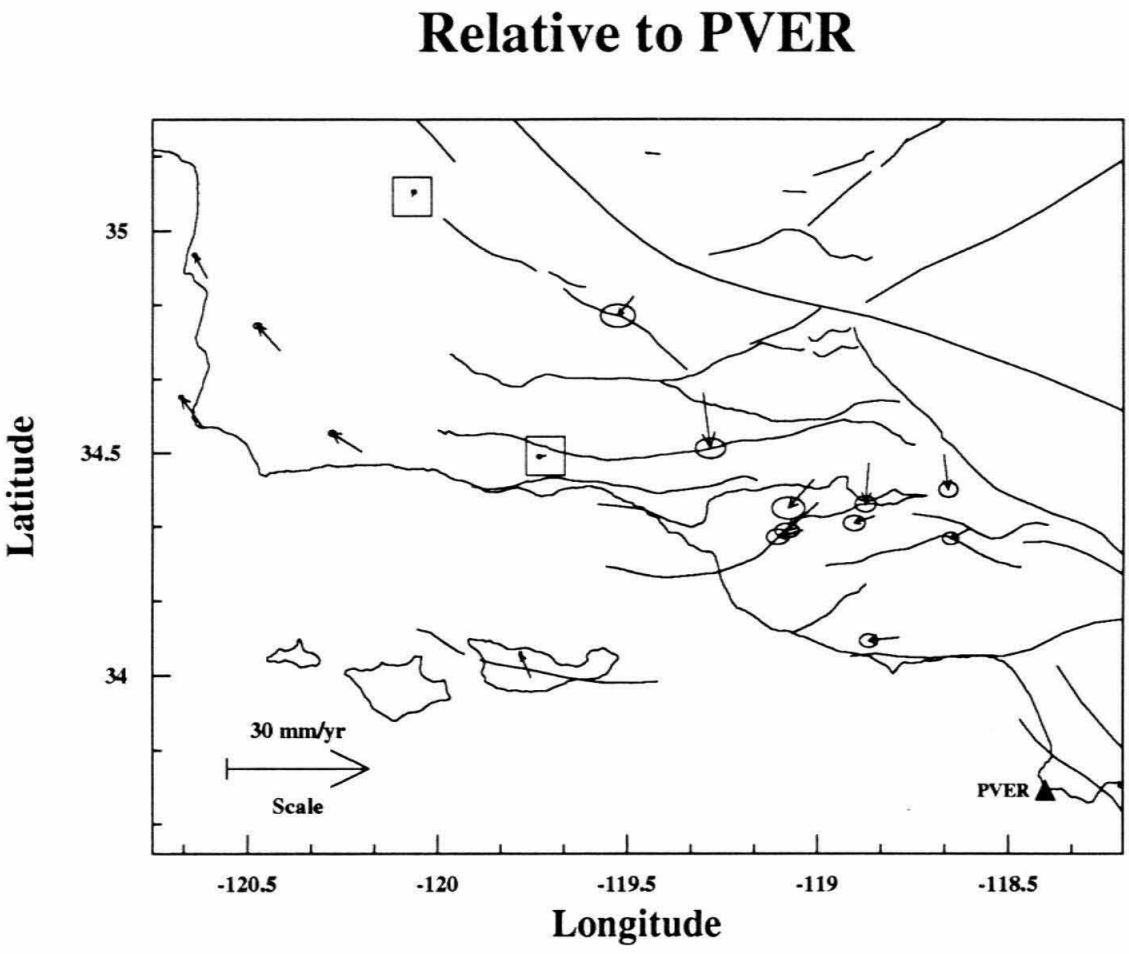

Figure 4.16: Velocities of sites in the western Transverse Ranges. The error ellipses represent one formal error. The open boxes mark stations that show little motion relative to Palos Verdes (PVER). Results from stations not in the Ventura network from *Murray* [1991].

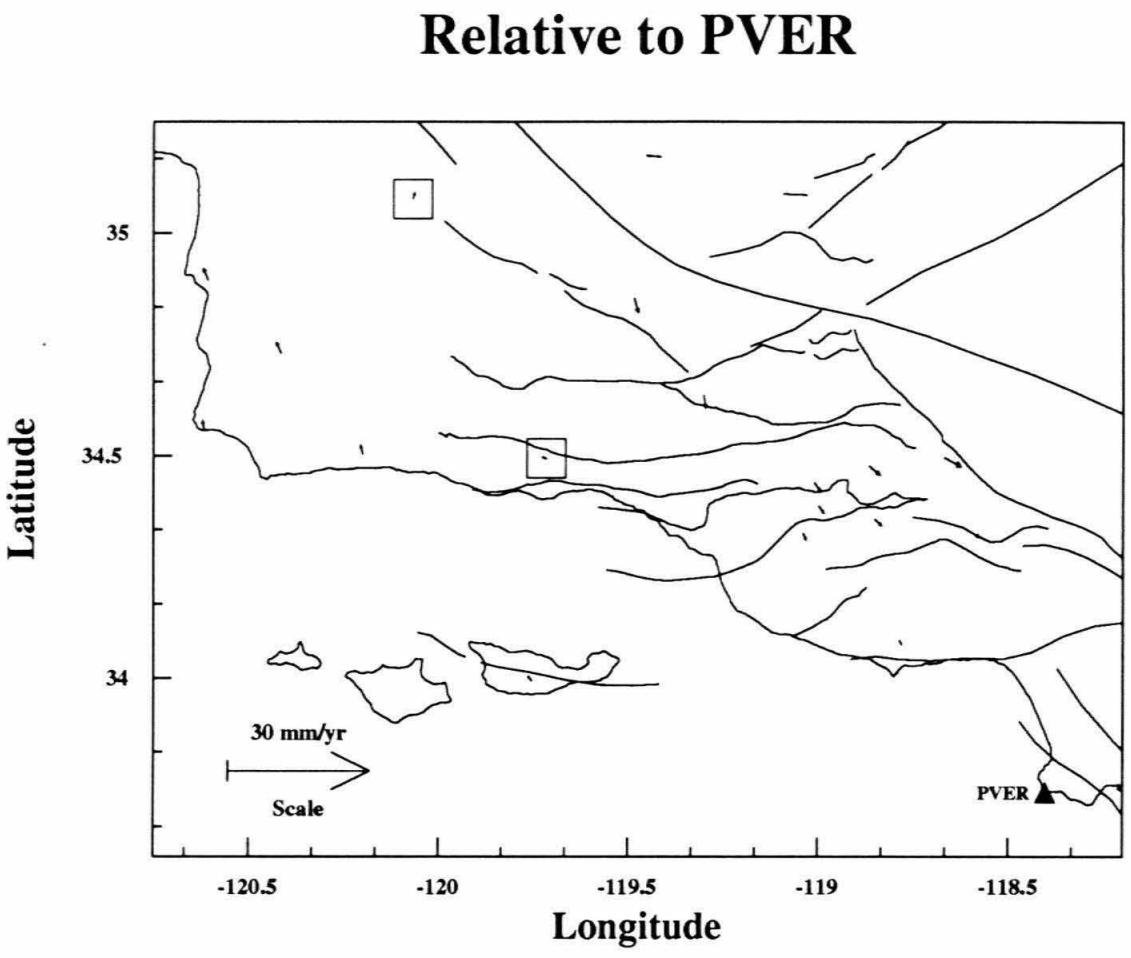

Figure 4.17: Velocities of sites in the western Transverse Ranges calculated from the *Eberhart-Phillips et al.* [1990] model of creep at depth on the San Andreas, Garlock and Big Pine faults.

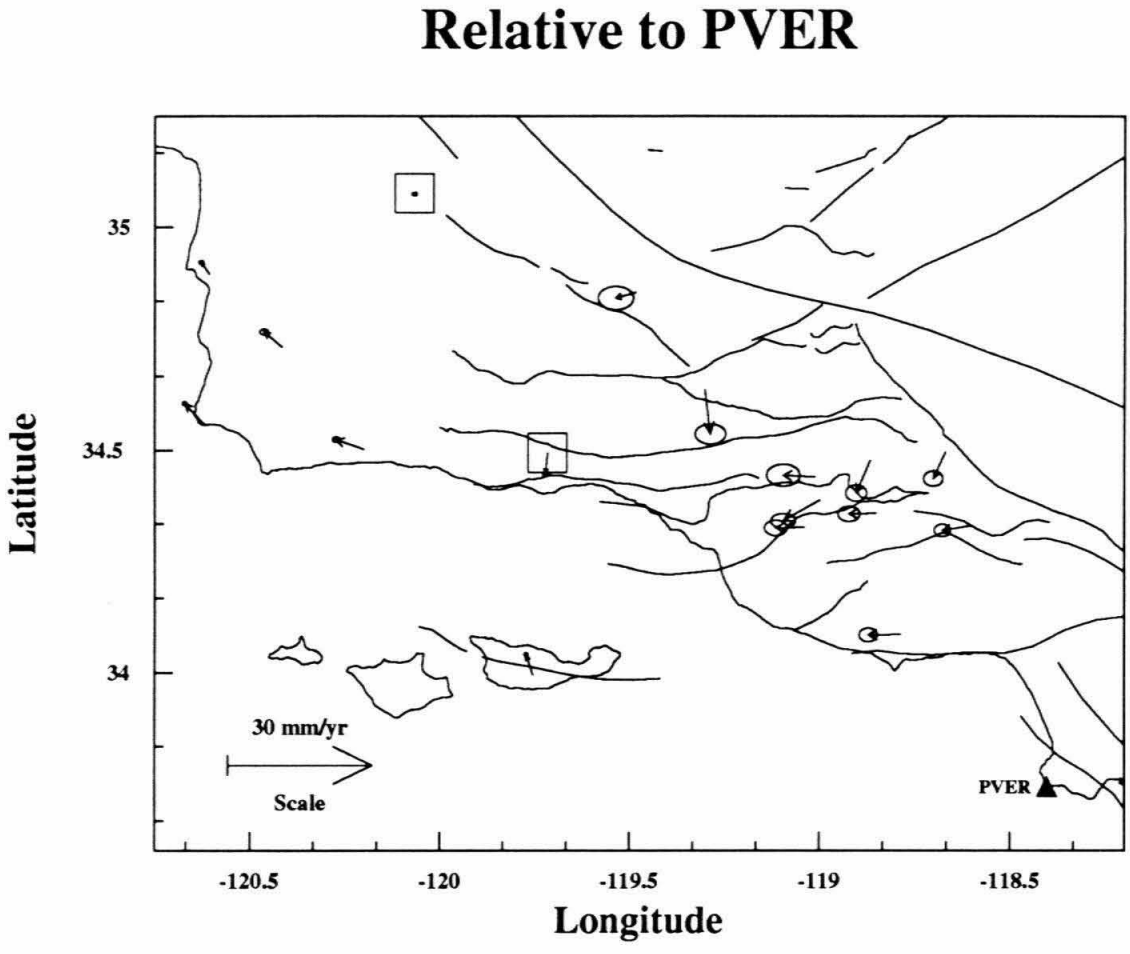

Figure 4.18: Residual velocities in the western Transverse Ranges of the difference between the observed velocities and the *Eberhart-Phillips et al.* [1990] model.

main trend of the San Andreas fault between the offshore islands and Palos Verdes (PVER). The boundaries of the "blocks" to which we refer are diffuse. Any creep of faults that we mention refers to creep at depth, thus producing a fairly broad zone of deformation. The structure divides the western portion of the western Transverse Ranges and the central portion of the western Transverse Ranges. A second strip or block includes Palos Verdes (PVER) and the boxed sites in figure 4.16. This strip moves parallel to the San Andreas fault at a lower velocity than the western strip. Rather than being described by discrete blocks, bounded by right-lateral motion, this area might be described the by the simple shear zone of *Ward* [1990]. Just southeast of the big bend, a change occurs from the strike-slip regime to a compressive regime. Apparently the change in strike of the San Andreas fault fosters this compressive regime and Palos Verdes (PVER) lies outside the area affected by the presence of the big bend.

The tectonics within this area, south of the big bend are complex (figure 4.19). *Eberhart-Phillips et al.* [1990] reduced line length residuals by modeling the Big Pine fault as actively creeping at depth with a left-lateral offset. The velocities of the two sites in the northern part of the Ventura basin network seem to reflect this trend, but not to greater than one-standard deviation. Evidence of left-lateral motion along the Big Pine fault is suggested from the difference in the velocities between Yam 2 (YAM2), near the big bend, and MADC, the northernmost boxed site in figure 4.16, but the extent of left-lateral differential motion observed with GPS is greater than the *Eberhart-Phillips et al.* [1990] model predicts. It appears that MADC is the pivot point of a block that is rotating clockwise and is bounded by the left-lateral Big Pine

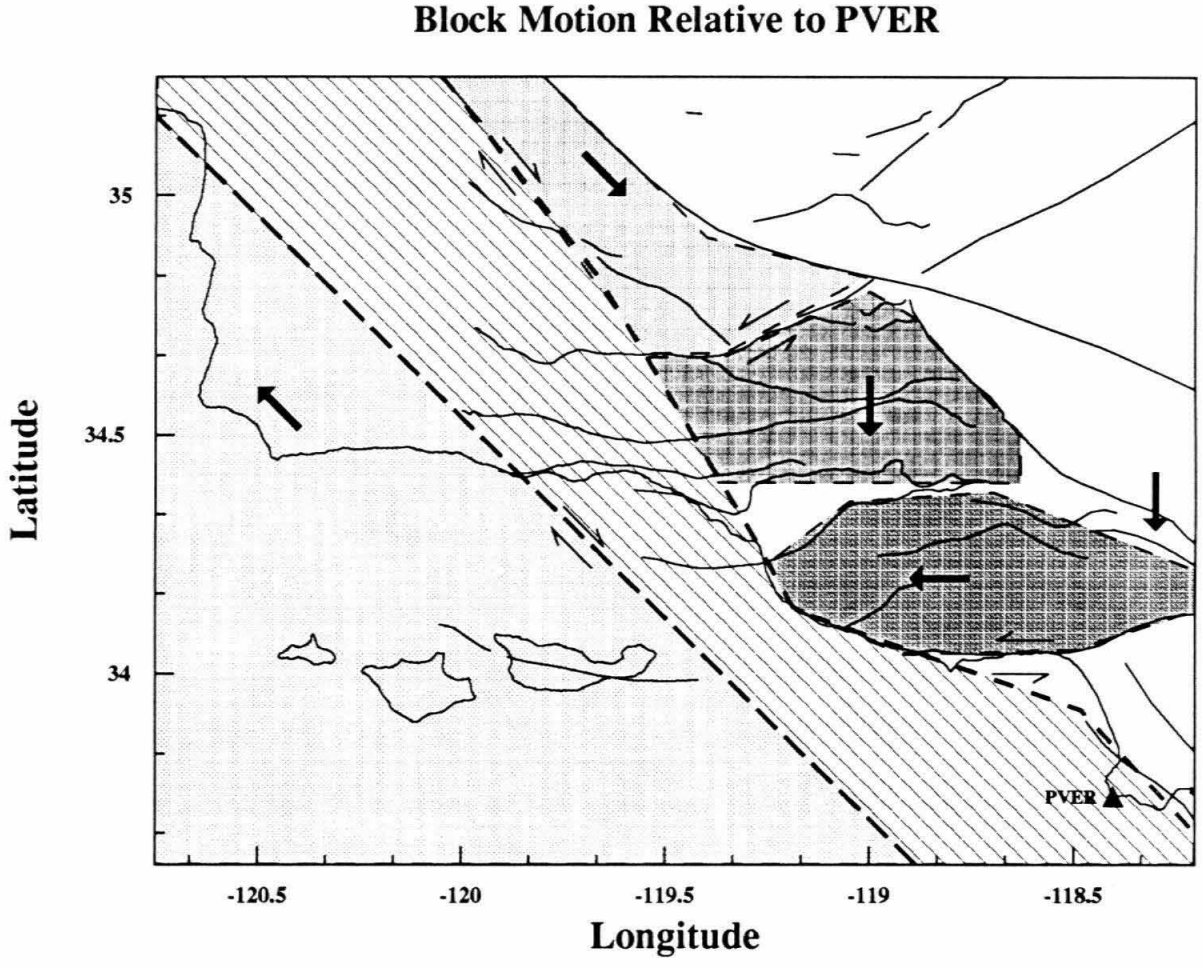

Figure 4.19: Cartoon of block motions relative to Palos Verdes (PVER) south of the San Andreas fault. The arrows indicate the sense of motion of each block, the amount of motion is not reflected by the arrows. The boundaries of the blocks are not as well defined as the cartoon suggests.

fault. Clockwise rotation of the block coupled with right lateral shear would result in apparent extension between Yam 2 (YAM2) north of the Big Pine fault and Munson (MUNS) south of the fault. Results from trilateration also show that stations near the big bend of the San Andreas fault cannot be placed in the same tectonic regime as sites just east of the big bend and south of the San Andreas [*Eberhart-Phillips et al.*, 1990]. The apparent extension can not be explained by crustal extension because geologic features indicate compression in the big bend region [e.g., *Namson and Davis*, 1988; *Davis et al.*, 1986].

A compressive regime, that seems to be elastically deforming, lies to the south of the Big Pine fault. Combining our results with those of *Eberhart-Phillips et al.* [1990] suggests that the compression is fairly uniform across a block bounded on the north by the Big Pine and San Andreas faults and by the Ventura basin on the south. This block also shows clockwise rotation. Santa Paula Peak (SNP2), the westernmost site bounding the north side of the basin shows a larger west component of velocity than the other sites within this block.

The velocities of the three sites at the west end of the basin network, Santa Paula Peak (SNP2), Santa Paula (SNPA), and Santa Clara (SCLA), suggest that the axis of maximum compression may be oriented more in a northeast-southwest direction, although we did not calculate strains for this subregion. These results are slightly more speculative, however. Recall that the VLBI results do not show that Santa Paula VLBI (SANP) moving west as strongly as the GPS results. Future measurements will better constrain deformation in this part of the network.

A rigid block is situated just south of the Ventura basin. This block, which has

shown no deformation during the last century, is bounded on the south by the Malibu Coast fault system. The Malibu fault, or a similar structure south of it, shows a left-lateral sense of motion. The rigid block south of the basin is escaping westward, probably due to compression across the Los Angeles basin. A significant component of compression has been documented across the Los Angeles basin by *Cline et al.* [1984]. The westward motion of the southern block explains why convergence across the basin is north-northwest, rather than north-northeast as it is farther west in the western Transverse Ranges and also in the eastern Santa Barbara Channel. The westward motion of the southern block, coupled with north-south convergence of the basin, causes oblique convergence across the basin. It appears that the Ventura Basin is less rigid than the surrounding region, making it more deformable than the surrounding region. Geodetic results show that compression across the eastern Santa Barbara Channel is oriented northeast-southwest. If the western limit of the block is marked by the coast, western motion of the block should rotate the axis of compression, within the Channel, clockwise from the regional trend of north-south compression.

Within the western Transverse Ranges, several tectonic blocks can be identified. Except for the block north of the Ventura basin, these blocks are fairly rigid. The block north of the basin, unlike the southern block, seems to be elastically deforming over about a 40 km region. This may imply strain accumulation due to motion on a detachment fault. In time, this elastic strain accumulation could be released in a moderate earthquake along the northern Ventura basin. The south side of the Ventura basin appears to be weaker than the surrounding region. Deformation may

be occurring anelastically and aseismically in the form of a creeping fault-propagation fold. The propagating fault must have a slightly oblique component of slip as the block overriding it is pushed westward into the Santa Barbara Channel. Motions, due to the big bend of the San Andreas fault, north-south regional compression from a downgoing flow under the Transverse Ranges, and northwest shear between the Pacific and North American plates, are competing to produce this complex pattern of deformation in the Ventura basin region.

Bibliography

Allen, C. R., San Andreas fault zone in San Gorgonio Pass, southern California, *Geol. Soc. Am. Bull.* **68**, 315-350, 1957.

Anderson, D. L., The San Andreas fault, *Sci. Am.*, **225**, 52-68, 1971.

Bell, L., R. Allenby, M. Bryant, and V. Nelson, The CDP site stability project: Geodetic footprinting of CDP VLBI/SLR observing sites using GPS, *written communication*, 1991.

Bird, P., R. W. Rosenstock, Kinematics of present crust and mantle flow in southern California, *Geol. Soc. Am. Bull.* **95**, 946-957, 1984.

Bryant, A. A., and L. M. Jones, Anomalously Deep Crustal Earthquakes in the Ventura Basin, Southern California *J. Geophys. Res*, **submitted**, 1991.

Bomford G., *Geodesy, third edition*, Oxford University Press, 731 pp., 1971.

Buchanan–Banks, J. M., R. O. Castle, and J. I. Ziony, Elevation changes in the central Transverse Ranges near Ventura, California, *Tectonophys.*, **29**, 113-125, 1975.

California Dept. of Conservation, Div. Oil and Gas, 75^{th} annual report of the state oil and gas supervisor, 1989.

Çemen, I., Near-Surface Expression of the Eastern Part of the San Cayetano Fault: A Potentially Active Thrust Fault in the California Transverse Ranges, *J. Geophys. Res.*, **94**, 9665-9677, 1989.

Cline, M. W., R. A. Snay, and E. L. Timmerman, Regional deformation of the earth model for the Los Angeles region, California, *Tectonophys.* **107**, 279-314, 1984.

Cohen, S. C., Postseismic deformation due to subcrustal viscoelastic relaxation following dip-slip earthquakes, *J. Geophys. Res.*, **89**, 4538-4544, 1984.

Cohen, S. C., and M. J. Kramer, Crustal deformation, the earthquake cycle, and models of viscoelastic flow in the asthenosphere, *Geophys. J. R. Astro. Soc.* **78**, 735-750, 1984.

Corbett, E. J., and C. E. Johnson, The Santa Barbara, California earthquake of 13 August, 1978, *Bull. Seismol. Soc. Am.*, **72**, 2201-2236, 1982.

Crowell, J. C., Late Cenozoic basins of onshore southern California: complexity is the hallmark of their tectonic history, in *Cenozoic Basin Development of Coastal California*, **Rubey Vol. 6**, 207-241, 1987

Davis, T. L., T. W. Dibblee Jr., M. L. Lagne, J. S. Namson, Geologic transect across the western Transverse Ranges, in *Geologic Transect Across the Western Transverse Ranges, guidebook*, Ďavis, T. L, and J. S. Namson ed., 41-74, 1986.

DeMets, C., R. G. Gorden, S. Stein, and D. F. Argus, A revised estimate of Pacific-North America motion and implications for Western North America plate boundary zone tectonics, *Geophys. Res. Letters*, **14**, 911-914, 1987.

DeRito, R. F., A. H. Lachenbruch, T.H. Moses and R. J. Munroe, Heat flow and thermotectonic problems of the central Ventura basin, southern California, *J. Geophys. Res.*, **94**, 681-699, 1989.

Dixon, T., G. Blewitt, K. Larson, D. Agnew, B. Hager, P. Kroger, L. Krumega, and W. Strange, GPS measurements of regional deformation in southern California, *Eos, Trans. Am. Geophys. Union*, **71**, 1051-1056, 1990.

Dixon, T. H., An Introduction to the Global Positioning System and some geologic applications, *Rev. Geophys.*, **29**, 249-276, 1991.

Dong, D. N., Y. Bock, Global Positioning System network analysis with phase ambiguity resolution applied to crustal deformation studies in California, *J. Geophys. Res.*, **94**, 3949-3966, 1989.

Donnellan, A., B. H. Hager, S. Larsen, Determination of convergence rates across the Ventura basin, southern California, using GPS and historical triangulation, *EOS, Trans. Am. Geophys. Union*, **69**, 326, 1989.

Drew, A. R., R. A. Snay, DYNAP–software for estimating crustal deformation from geodetic data, *Tectonophys.*, **162**, 331-343, 1989.

Eberhart-Phillips, D., M. Lisowski, and M. D. Zoback, Crustal strain near the big bend of the San Andreas fault: Analysis of the Los Padres–Tehachapi trilateration networks, California, *J. Geophys. Res.*, **95**, 1139-1153, 1990.

Feigl, K. L., R. W. King, and T. H. Jordan, Geodetic measurement of tectonic deformation in the Santa Maria Fold and Thrust Belt, California, *J. Geophys. Res.*, **95**, 2679-2699, 1990.

Feigl, K. L., *Geodetic Measurement of Tectonic Deformation in Central California*, PhD Thesis, Mass. Inst. of Tech., 222 pp., 1991.

Frank, F. C., Deduction of earth strains from survey data, *Bull. Seism. Soc. Am.*, **56**, 35-42, 1966.

Gosset, F. R., *Manual of geodetic triangulation*, U. S. Dept. Comm. Coast and Geod. Survey, **spec. pub. 247**, 344 pp., 1959.

Hacker, R. N., *Geology and oilfields of coastal areas, Ventura and Los Angeles basins, California*, AAPG, SEG, SEPM Guidebook, 61 pp., 1969.

Hadley, D. and H. Kanamori, Seismic structure of the Transverse Ranges, California, *Bull. Seism. Soc. Am.*, **68**, 1449-1457, 1978.

Hager, B. H., R. W. King, and M. H. Murray, Measurement of crustal deformation using the Global Positioning System, *Ann. Rev. of Geophys.*, **19**, 351-382, 1991.

Hanks, T. C., and H. Kanamori, A moment magnitude scale, *J. Geophys. Res.*, **84**, 2348-2350, 1979.

Hanna, W. F., J. D. Rietman, S. Biehler, Bouguer gravity map of California, Los Angeles sheet, *Cal. Div. Of Mines and Geology*, 1974.

Hayford, J. F., A. L. Baldwin, The earth movements in the California earthquake of 1906, *U. S. Coast and Geod. Surv. Rep. for 1907, App. 3* reprinted, 1973, in *Reports on Geodetic Measurement of Crustal Movement 1906-1971*, 1971.

Heaton, T. H., The 1971 San Fernando Earthquake: A double event?, *Bull. Seismol. Soc. Am.*, **72**, 2037-2062, 1982.

Herring, T., J. Davis, I. Shapiro, Geodesy by radio interferometry: The application of Kalman filtering to the analysis of very long baseline interferometry data, *J. Geophys. Res.*, **95**, 12561-12581, 1990.

Higgins, J. W., *A guide to the geology and oil fields of the Los Angeles and Ventura Regions*, Pac. Sec., A.A.P.G., 204 pp., 1958.

Hill, M. L., Anomalous trends of the San Andreas fault in the Transverse Ranges, California, *Geology and Mineral Wealth of the California Transverse Ranges: Hill volume*, ed. D. L. Fife and J. A. Minch, *South Coast Geol. Soc., Annu. Symp. Guideb.* **10**, 367-369, 1982.

Hill, M. L., and T. W. Dibblee, Jr., San Andreas, Garlock and Big Pine faults, California – A study of the character, history and tectonic significancs of their displacement, *Geol. Soc. Am. Bull.*, **64**, 443-458, 1953.

Hornafius, S. J., Neogene tectonic rotation of the Santa Ynez Range, western Transverse Ranges, California, suggested by paleomagnetic investigation of the Monterey Formation, *J. Geophys. Res.*, **90**, 12,503-12522, 1985.

Humphreys, E. D., and B. H. Hager, A kinematic model for the late Cenozoic development of southern California crust and upper mantle, *J. Geophys. Res.*, **95**, 19747-19762, 1990.

Jackson, J., and P. Molnar, Active Faulting and Block Rotations In The Western Transverse Ranges, California, *J. Geophys. Res.*, **95**, 22,073-22,087, 1990.

Kamerling, M. J., and B. P. Luyendyk, Paleomagnetism and Neogene tectonics of the northern Channel Islands, California, *J. Geophys. Res.*, **90**, 12,485-12,502, 1985.

King, R. W., E. G. Masters, C. Rizos, A. Stolz, and J. Collins, *Surveying with GPS, Monogr. Ser.,*, **9**, School of Surveying, University of New South Wales, New South Wales, Australia, 128 pp., 1985.

Larsen, S. C., *Geodetic Measurement of Deformation in Southern California*, PhD thesis, California Institute of Technology, 351 pp., 1991.

Larson, K. M., *Precision, Accuracy, and Tectonics from the Global Positioning System*, PhD thesis, Univ. California, San Diego, 255 pp., 1990.

Li, V. C., and J. R. Rice, Crustal deformation in great California earthquake cycles, *J. Geophys. Res.*, **92**, 11,533-11,551, 1987.

Lisowski, M., W. H. Prescott, J. C. Savage, and J. L. Svarc, A possible geodetic anomaly observed prior to the Loma Prieta, California, earthquake, *Geophys. Res. Lett.*, **17**, 1990.

Lung, R., and R. J. Weick, Exploratory trenching of the Santa Susana fault in Los Angeles and Ventura Counties, *U. S. Geol. Surv. Prof. Pap.* **1339**, 65-70, 1987.

Luyendyk, B. P. and J. S. Hornafius, Neogene crustal rotations, fault slip, and basin development in southern California, *Cenozoic Basin Development of Coastal California*, **Rubey vol 6**, R. V. Ingersoll, W. G. Ernst, eds., 259-283, 1987.

McNutt, M. K., M. Diament, and M. G. Kogan, Variations of elastic plate thickness at continental thrust belts, *J. Geophys. Res.*, **83**, 8825-8838, 1988.

Mitchell, H. C., *First and Second Order Triangulation in California (1927 Datum)*, U. S. Dept. Comm. Coast and Geod. Survey, **spec. pub. 202**, 548 pp., 1936.

Murray, M. H., *Global Positioning System Measurement of Crustal Deformation in Central California*, PhD Thesis, Mass. Inst. of Tech., 1991.

Namson, J., and T. Davis, Structural transect of the western Transverse Ranges, California: Implications for lithospheric kinematics and seismic risk evaluation, *Geology*, **16**, 675-679, 1988.

Norris, R. M., and R. W. Webb, *Geology of California, second edition*, John Wiley & Sons, Inc., New York, 541 pp., 1990.

Okada, Y., Surface deformation due to shear and tensile faults in a half-space, *Bull. Seism. Soc. Am.*, **75**, 1135-1154, 1985.

Plouff, D., Gravity and magnetic fields of polygonal prisms and application to magnetic terrain corrections, *Geophys.*, **41**, 727-741, 1976.

Prescott, W. H., An extension of Frank's method for obtaining crustal shear strains from survey data, *Bull Seism. Soc. Am.*, **66**, 1847-1853, 1976.

Reed, R. D., and J. S. Hollister, *Structural Evolution of Southern California*, published by Am. Assoc. Petrol. Geol., 157 pp., 1936.

Roberts, C. W., R. C. Jachens, and H. W. Oliver, Preliminary isostatic residual gravity map of California, *U. S. Geol. Surv. Open-File Rep.*, **OFR-81-573**, 1981.

Rockwell, T. K., E. A. Keller, M. N. Clark, and D. L. Johnson, Chronology and rates of faulting of Ventura River terraces, California, *Geol. Soc. of Am. Bull.*, **95**, 1466-1474, 1984.

Rockwell, T., Neotectonics of the San Cayetano fault, Transverse Ranges, California, *Geol. Soc. of Am. Bull.*, **100**, 500-513, 1988.

Rockwell, T. K., E. A. Keller, and G. R. Dembroff, Quaternary rate of folding of the Ventura Avenue anticline, western Transverse Ranges, southern California, *Geol. Soc. of Am. Bull.*, **100**, 850-858, 1988.

Sarna-Wojcicki, A. M., K. R. Lajoie, S. W. Robinson, and R. F. Yerkes, Recurrent Holocene displacement on the Javon Canyon fault, rates of faulting and regional uplift, Western Transverse Ranges, California, *Geol. Soc. Am Abs. with Prog.*, **11**, 125, 1979.

Sheffels, B., and M. McNutt, Role of subsurface loads and regional compensation in the isostatic balance of the Transverse Ranges, California: Evidence for intracontinental subduction, *J. Geophys. Res.*, **91**, 6419-6431, 1986.

Snay, R. A., Horizontal deformation in New York and Connecticut: examining contradictory results from the geodetic evidence, *J. Geophys. Res.*, **91**, 12,695-12,702, 1986.

Stein, R. S., and W. Thatcher, Seismic and aseismic deformation associated with the 1952 Kern County, California earthquake and relationship to the Quaternary history of the White Wolf fault, *J. Geophys. Res.*, **86**, 4913-4928, 1981.

Suppe, J., Reactivated normal faults in the western Taiwan fold-and-thrust belt, *Mem. Geol. Soc. China*, **7**, 187-200, 1986.

Suppe, J., and D. A. Medwedeff, Geometry and kinematics of fault-propagation folding, *Eclogae, Geol. Helv.*, **83**, 409-454, 1990.

Talwani, M., J. L. Worzel, and M. Landisman, Rapid gravity computations for two-dimensional bodies with application to the Mendocino submarine fracture zone, *J. Geophys. Res.*, **64**, 49-59, 1959.

Thatcher, W., T. Matsuda, T. Kato, and J. B. Rundle, Lithosphere loading by the 1986 Riku-u earthquake, northern Japan: Implications for plate flexure and asthenosphere rheology, *J. Geophys. Res.*, **85**, 6429-6435, 1980.

Truex, J. N., *San Cayetano Fault, Field Trip*, Pac. Sec. AAPG guidebook, 35 pp., 1977.

Vaníček, P., E. J. Krakiwsky, *Geodesy: The Concepts*, Elsevier Science Publishers B.V., 697 pp., 1986.

Ward, S. N., North America-Pacific plate boundary, and elastic megashear, evidence from very long baseline interferometry. *J. Geophys. Res.*, **93**, 7716-7728, 1988.

Ward, S. N., Pacific-North America plate motions: new results from very long baseline interferomtry, *J. Geophys. Res.*, **95**, 21,965-21,981, 1990.

Webb, F. H., *Geodetic Measurement of Deformation in the Offshore of Southern California*, PhD thesis, California Institute of Technology, 211 pp., 1991.

Webb, T. H., and H. Kanamori, Earthquake focal mechanisms in the eastern Transverse Ranges and San Emigdio Mountains, southern California and evidence for a regional decollement, *Bull. Seism. Soc. Am.*, **75**, 737-757, 1985.

Weldon, R. J., *The late Cenozoic Geology of Cajon Pass; Implications for Tectonics and Sedimentation Along the San Andreas Fault*, PhD thesis, California Institute of Technology, 382 pp., 1985

Weldon, R. and E. Humphreys, A kinematic model of southern California, *Tectonics*, **5**, 33-48, 1986.

Wells, D., *Guide to GPS Positioning*, Canadian GPS Associates, Fredericton, New Brunswick, 1987.

Wesnousky, S. G., Earthquakes, Quaternary faults, and seismic hazard in California, *J. Geophys. Res.*, **91**, 1986.

Yeats, R. S., Large-scale Quaternary detachments in Ventura basin, southern California, *J. Geophys. Res.*, **88**, 569-583, 1983.

Yeats, R. S., W. H. K Lee, and R. F. Yerkes, Geology and seismicity of the eastern Red Mountain fault, Ventura County, *U. S. Geol. Surv. Prof. Pap.*, **1339**, 161-167, 1987.

Yeats, R. S., Late Cenozoic structure of the Santa Susana fault zone, *U. S. Geol. Surv. Prof. Pap.*, **1339**, 137-160, 1987.

Yeats, R. S., Late Quaternary slip rate on the Oak Ridge fault, Transverse Ranges, California: Implications for seismic risk, *J. Geophys. Res.*, **93**, 12,137-12,149, 1988.

Yeats, R. S., Huftile, F. B. Grigsby, Oak Ridge fault, Ventura fold belt, and the Sisar decollement, Ventura basin, California, *Geology*, **16**, 1112-1116, 1988.

Yerkes, R. F., and W. H. K. Lee, Faults, fault activity, epicenters, focal depths, focal mechanisms, 1970-1975 earthquakes, western Transverse Ranges, Calif., *U. S. Geol. Surv. Misc. Field Stud. Map, MF-1032*, 2 sheets, 1979.

Yerkes, R. F. and W. H. K. Lee, Late Quaternary deformation in the Western Transverse Ranges, *U. S. Geol. Surv. Prof. Pap.*, **1339**, 71-82, 1987.

Yerkes, R. F., A. M. Sarna-Wojcicki, and K. R. Lajoie, Geology and Quaternary deformation of the Ventura area, *U. S. Geol. Surv. Prof. Pap.*, **1339**, 169-178, 1987.

Appendix A

Method of Processing the GPS Data

GPS data from the Ventura Basin exist for three experiments called Trex9, Trex16 and Trex19. Data were collected during other experiments for stations that we added during Trex19. Table A.1 lists all of the data near the Ventura basin and the days of the observations. We also used data from Palos Verdes (PVER) and Santa Paula (SNPA) from 1991 data collected by Caltrans.

We used the same general method to process each set of data. Using the global tracking data and the site coordinates estimated from VLBI, we solved for multi-day orbits using the MIT GPS processing software, GAMIT. We loosely constrained the orbits, and constrained the global stations to perform bias-fixed single-day solutions on the Ventura Basin data. Palos Verdes was occupied for every Ventura Basin experiment, so all of the results use Palos Verdes as the reference station. For none of the calculations did we include any meteorologic data. It has been shown that inclusion of the weather data in the solution does not significantly affect the results [*King*, MIT, personal communication]. The data were combined to solve for the

Site	Dec 86	Dec 86	Jan 87	Jan 87	Oct 87	Apr 89	Jun 90
CATO					278-279	094-097	170-172
COTR		363-002					162-164
HAPY					280-281		166-168
HOPP					280-281	094-097	166-168
LACU		364-002	003-007				162-164
LOVE					278-279		170-172
MPNS							164,170
MUNS						094-097	166-168
PVER	350-354		003-007	020-023	275-282	094-097	162-172†
SAFE					278-279	094-097	170-172
SCLA					280-281		170-172
SNP2					281		166-168
SNPA	352-354			022-023		094-097	162-172†
SOLI			004-007				162-164
WHIT							166-168
YAM2						094-097	162-164

Days of site occupations.

†Not occupied days 165 or 169

Table A.1: GPS site occupation history for the Ventura Basin.

ID	Name	Latitude	Longitude	Radius
MOJA	Mojave	35 9 0.77137	W116 53 17.34413	6371929.5370
WSFD	Westford	42 25 17.84192	W71 29 36.01412	6368465.3430
YKNF	Westford	62 19 7.82173	W114 28 8.01775	6361532.7420

Table A.2: Coordinates used for the Trex9 orbit improvement.

site velocities from all of the experiments using the program GLOBK written by T. A. Herring at the Massachusetts Institute of Technology. Following is a detailed description of the methods used to process each subset of the data.

A.1 TREX9: October 5-7, 1987

Trex9 was a small eight station experiment that took place over four days. Only Palos Verdes was occupied for the entire four days. All of the other stations were occupied for at most two days as listed in table A.1. Two sites, Hopper (HOPP) and Santa Paula Peak (SNP2), have only one day of usable data. SNP2 was only occupied for one day and the data are bad for Hopper on day 280. Only three global sites were occupied during the time span of this experiment. These are Westford, Yellowknife and Mojave. For the bias-fixed solutions we constrained the ionosphere to one part per million. We did not apply an atmospheric constraint, but adjusted the atmospheric parameter at one site. Table A.2 shows the SV4 coordinates used in the solution. Constraints of 20 mm were applied to the north, east, and up components of each fiducial site. Palos Verdes (PVER) was constrained to 200 mm.

All biases were reliably fixed for day 278. On day 279 all of the wide-lane biases were correctly fixed, but four of the 19 narrow-lane integer biases were not fixed. The rest were reliably fixed. During day 280 six of the nine narrow-lane biases were fixed. Some of the wide-lane biases were not fixed. During day 281 one bias was not fixed. The rest were reliably fixed. The normalized rms for the solutions of days 278-281 are 0.29, 0.28, 0.30, and 0.27 respectively.

A.2 TREX16: April 4-7, 1989

During Trex16 we collected four days of data. In processing this experiment we calculated the orbits separately from the local data and then used the constrained orbits to perform a bias-fixed solution on the local data. Table A.3 shows which data were used for the determination of the orbits. The site coordinates that we used are listed in table A.4. We constrained all of the global sites to 20 mm in latitude, longitude and radius. Palos Verdes (PVER) was constrained to 200 mm.

This experiment took place near a solar maximum so we loosely constrained the ionosphere to 5 ppm for the bias-fixed solution. We applied atmospheric constraints for the local solution and applied no atmospheric constraints to the orbit determination and instead adjusted the atmospheric parameter at one site.

All biases were fixed for day 094, three biases were not fixed for day 095, five for day 096 and two were not fixed on day 097. The normalized rms for each day is 0.38, 0.35, 0.32, and 0.33 respectively.

	094	095	096	097
KOKE	X	X	X	X
MOJF		X	X	X
MOJM	X	X	X	X
ONSA	X	X	X	X
WETT	X	X	X	X
WSFM	X	X	X	X

Table A.3: Fiducial data used for orbit determination during Trex16.

ID	Name	Latitude	Longitude	Radius
KOKE	Kokee FRPA	21 59 34.09290	W159 39 53.61456	6376291.9354
MOJF	Mojave FRPA	35 9 0.77108	W116 53 17.34581	6371929.5538
MOJM	Mojave Minimac	35 9 0.60908	W116 53 17.34338	6371929.3727
ONSA	Onsala	57 13 13.29726	E11 55 31.85005	6363045.5734
WETT	Wettzell	48 57 15.00109	E12 52 43.10270	6366610.8036
WSFM	Westford	42 25 17.95907	W71 29 35.96656	6368464.4776

Table A.4: Coordinates used for the Trex16 orbit determination.

A.3 TREX19: June 11-21, 1990

Because of its size, Trex19 was broken down into three sub-experiments called experiments A, B and C. For consistency and to test for repeatability PVER and SNPA were occupied during each sub-experiment. We observed for three consecutive days during each sub-experiment and processed each sub-experiment individually. Problems we encountered are discussed below.

We used Trimble 4000 SST dual frequency receivers to collect data for Trex19. These receivers support two modes of data sampling. The first mode, referred to as "standard data format" by Trimble, does not record data at precise time intervals but varies the sampling time. The second mode called "compact data format" samples at precise, even GPS seconds. By even we mean, for example, that the data are sampled at 15.000 seconds not at 15.080 seconds. During experiments A and B of Trex19 the data were sampled asynchronously because half of the receivers were set to record data in standard format and half were set for compact format. During Experiment C all of the data were sampled in compact format at precise GPS seconds. Table A.5 shows which data were sampled under standard format and which were sampled under compact format. Partially due to this problem no Block II satellites were used in the analysis of Trex19. During Trex19, Selective Availability (S/A) of the Block II satellites was turned on. Three of the global stations we used were occupied by TI4100 receivers which also do not sample at even GPS seconds, so we did not solve for orbits of the Block II satellites. No block II satellites were observed during any of the previous experiments so our solutions are no worse off during Trex19 for the lack of Block II satellites.

	Experiment A		Experiment B		Experiment C
	standard	compact	standard	compact	compact
CATO					X
COTR	X*				
HAPY			X		
HOPP			X*		
LACU	X*				
LOVE					X*
MPNS	X				X
MUNS			X*		
PVER		X		X	X
SAFE					X*
SCLA					X*
SNP2			X*		
SNPA	X		X		X
SOLI		X			
WHIT				X	
YAM2		X			

Table A.5: Summary of which stations were sampled under compact format and which were sampled under Trimble standard format. The asterisks indicate that PRN 6 was not tracked at that station. During experiment C PRN 6 was tracked on day 172 at all stations.

Table A.5 points out another problem encountered during Trex19. Three of the receivers were set to ignore and not track PRN 6 until day 172 which was the last day of the experiment. Fortunately this satellite has a track that is fairly redundant with other block I satellites. Figure A.1 is a sky plot that shows the tracks of the satellites during the observations. Note that the tracks of the block II satellites are short and, in most cases, low on the horizon.

A.3.1 Orbits

As mentioned, we calculated orbits using the global fiducial data. For the first three-day sub-experiment we calculated a five-day orbit and used a five-day arc in the GLOBK solution. Four-day orbits were used for the other sub-experiments. Table A.6 lists which stations were used for the orbit calculations, and table A.7 lists the full names and coordinates of the stations. The coordinates (for all experiments) are in the SV5 coordinate system [*Murray*, 1991]. For the calculations we constrained all of the fiducial stations to 20 mm in latitude, longitude and radius except for Tsukba, which we constrained to one meter in each dimension.

For the TI4100 receivers (YKNA, ONSA and KOKE) we modeled the clocks with a polynomial fit. Mini-Mac clocks were not modeled.

The ionosphere-free combination of L1 and L2 (LC) was used for the orbit calculations. We applied no atmospheric constraint and we adjusted the atmospheric parameter at one site on each day of the calculation. We used 30 second data for the calculations.

We did not use data from day 163 in the final velocity solution. The results from this day were very different from the other days. We have not yet determined

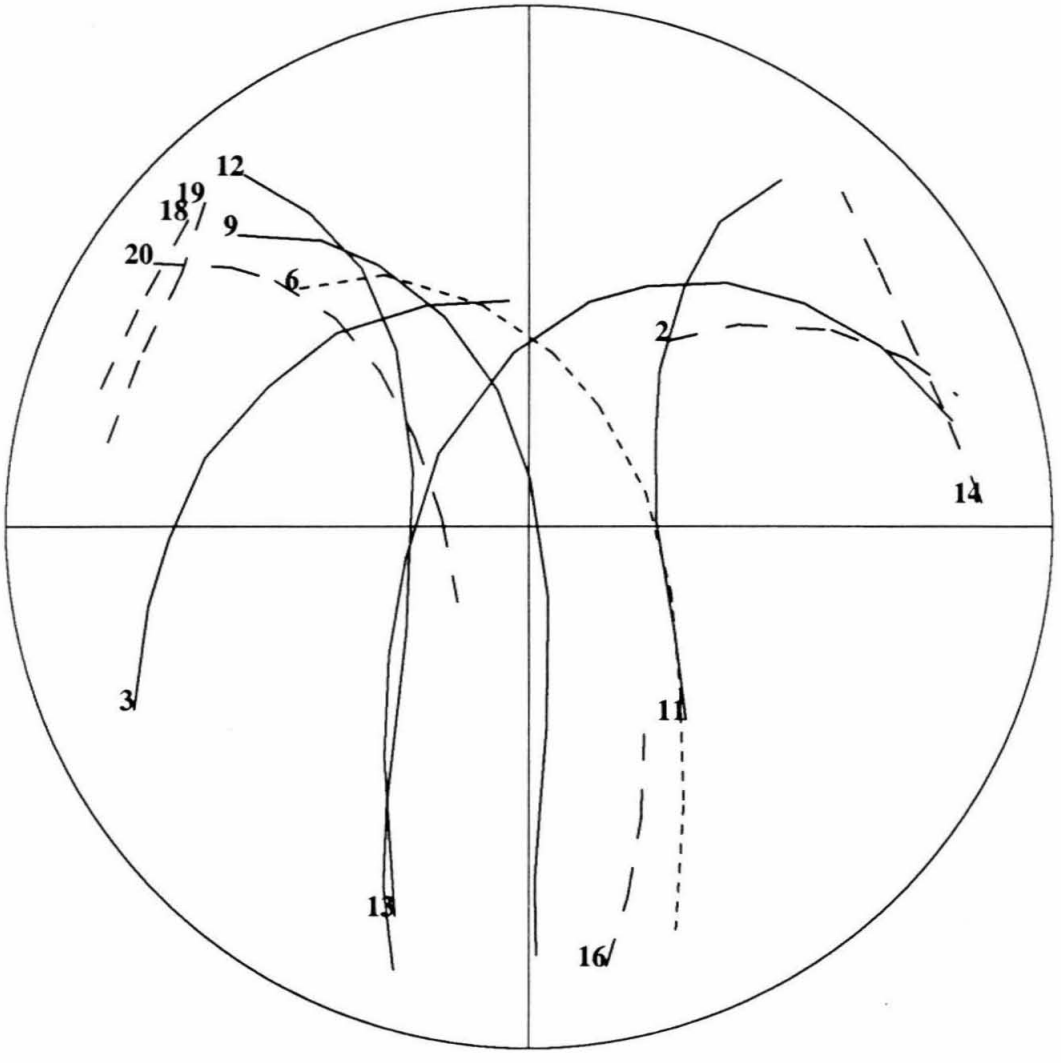

Figure A.1: Sky plot of the satellite tracks during June 11-12, 1990 from 19:18 to 3:02 UTC. The solid lines indicate block I satellites that were tracked at all stations during the entire experiment. The dotted line shows the track of PRN 6 and the dashed lines show the tracks of the Block II satellites.

	Experiment A					Experiment B				
	161	162	163	164	165	165	166	167	168	169
KOKE	X	X	X	X						
MOJM	X	X	X	X	X	X	X	X	X	X
ONSA		X		X	X		X			
RICM	X	X	X	X	X	X	X	X	X	X
TSUK	X	X	X	X	X	X	X	X	X	X
WSFM		X		X	X	X	X	X	X	X
YKNA	X	X	X	X	X	X	X	X	X	X

	Experiment C				
	169	170	171	172	173
KOKE		X		X	
MOJM	X	X	X	X	
ONSA				X	
RICM	X	X	X	X	
TSUK	X	X	X	X	
WSFM	X	X	X	X	
YKNA	X	X	X	X	

Table A.6: Days of the fiducial data used for calculating the orbits for Trex19. The X indicates that data were used for the listed day. A blank indicates that no data were used.

ID	Name	Latitude	Longitude	Radius
KOKE	Kokee FRPA	N21 59 34.09029	W159 39 53.61679	6376291.9354
MOJM	Mojave	N35 9 0.60888	W116 53 17.34406	6371929.3710
ONSA	Onsala	N57 13 13.29782	E 11 55 31.85093	6363045.5739
RICM	Richmond	N25 27 50.81107	W 80 23 3.05379	6374151.2486
TSUK	Tsukba	N35 55 22.27366	E140 5 15.10506	6370823.9855
WSFM	Westford	N42 25 17.95922	W 71 29 35.96736	6368464.4777
YKNA	Yellowknife	N62 19 22.43402	W114 28 50.50668	6361529.0052

Table A.7: Geocentric (spherical) coordinates used to constrain the orbits of the satellites during Trex19. KOKE, ONSA and YKNA were occupied by TI4100 receivers, all other stations were occupied by Minimac receivers.

the cause of this difference. During this day, the data from Westford (WSFM) were unusable, so we did not include that station on day 163. It is likely that a poor tie at either this station or one of the other fiducial stations skewed the results. The position of Mojave (MOJM) may be wrong from an improper tie [*Murray*, MIT, personal communication]. If this is so, the deletion of Westford (WSFM) during day 163 probably weakened the solution by adding greater weight to Mojave (MOJM). The global stations were constrained to 20 mm in each component and Palos Verdes (PVER) was constrained to 200 mm.

A.4 Caltrans Survey: April 23-25, 1991

For the Caltrans survey the only local sites occupied were Palos Verdes (PVER) and Santa Paula (SNPA) (table A.8). The same constraints were applied to the global stations of 20 mm. Both Santa Paula (SNPA) and Palos Verdes (PVER) were constrained to 1 m. The bias-fixed solutions were not reliable so we used bias-free solutions.

A.5 GLOBK solution

For the velocity estimation we used bias-fixed solutions for all but the April 1991 experiment. Table A.10 lists the constraints applied to the stations for the velocity calculations. Table A.11 lists the stochastic Markov parameters that were applied to the satellites. High Markov's were place on eclipsing satellites.

	113	114	115
KOKE	X	X	X
MOJ1	X	X	X
PVER	X	X	
RIC1	X	X	X
SNPA		X	X
WES1	X	X	X
WTZ1	X	X	X

Table A.8: Sites used in the 1991 solution.

ID	Name	Latitude	Longitude	Radius
KOKE	Kokee	21 59 34.09142	W159 39 53.61913	6376291.6909
MOJ1	Mojave	35 9 0.60866	W116 53 17.34479	6371929.3692
RIC1	Richmond	25 27 50.81107	W80 23 3.05426	6374151.2488
WES1	Westford	42 25 17.95937	W71 29 35.96820	6368464.4777
WTZ1	Wettzell	48 57 14.63333	E12 52 43.03608	6366606.9943

Table A.9: Coordinates used for the Caltrans orbit improvement.

Site	X	Y	Z	$\dot{X}$	$\dot{Y}$	$\dot{Z}$
KOKE	0.02	0.03	0.02	F	F	F
MOJA	0.01	F	0.01	F	F	F
MOJ1	0.01	F	0.01	F	F	F
ONSA	0.02	0.04	0.04	F	F	F
RICH	0.02	0.03	0.03	F	F	F
RIC1	0.02	0.02	0.02	F	F	F
WETT	0.02	0.04	0.05	F	F	F
WSFD	0.02	0.03	0.02	F	F	F
WES1	0.02	0.04	0.03	F	F	F
WTZ1	0.02	0.04	0.02	F	F	F
YKNA	0.02	0.02	0.02	0	0	0
YKNF	0.10	0.17	0.17	0	0	0
MUNS	1.0	1.0	1.0	0.10	0.10	0.10
others	1.0	1.0	1.0	0.05	0.05	0.05

Table A.10: Constraints applied to the stations.

PRN	X, Y, Z	$\dot{X}$, $\dot{Y}$, $\dot{Z}$	Rad, Ybias, Zbias
	m^2/yr	$(mm/s)^2/yr$	$(dimless)^2/yr$
2	3.65×10^4	3.65×10^2	3.65×10^2
3	3.65×10^4	3.65×10^2	3.65×10^2
11	3.65×10^4	3.65×10^2	3.65×10^2
16	3.65×10^4	3.65×10^2	3.65×10^2
others	3.65×10^2	3.65×10^{-2}	3.65×10^{-2}

Table A.11: Stochastic orbit specifications.

Appendix B

Results from Data Collected Only in 1990

Five of the stations occupied in 1990 were not occupied during the other experiments, so velocities were not estimated for these sites. We present plots of the quality of the results here (figure B.1).

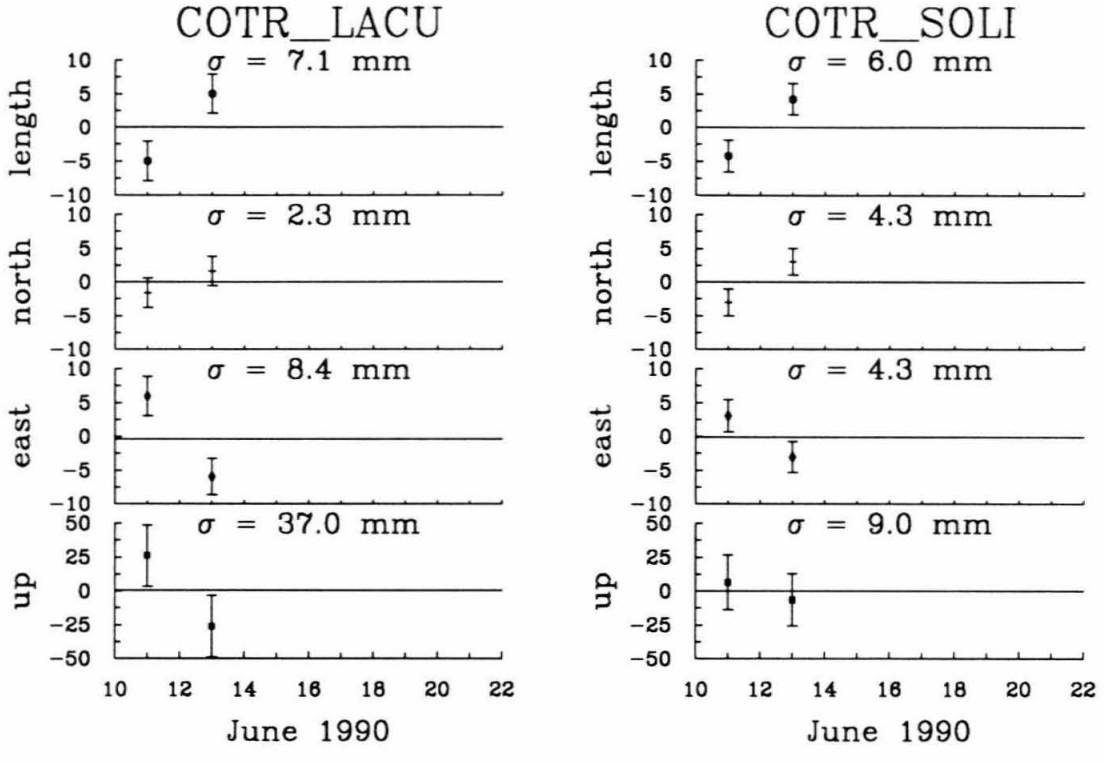

Figure B.1: Repeatability plots of stations not shown in Chapter 2 for the 1990 experiment. Zero is the average value of the points. The horizontal line near zero is the weighted mean of the points. The components are the coordinate of the second site minus the first site, with the average subtracted out. σ is the wrms scatter for the data. The figure continues for six pages.

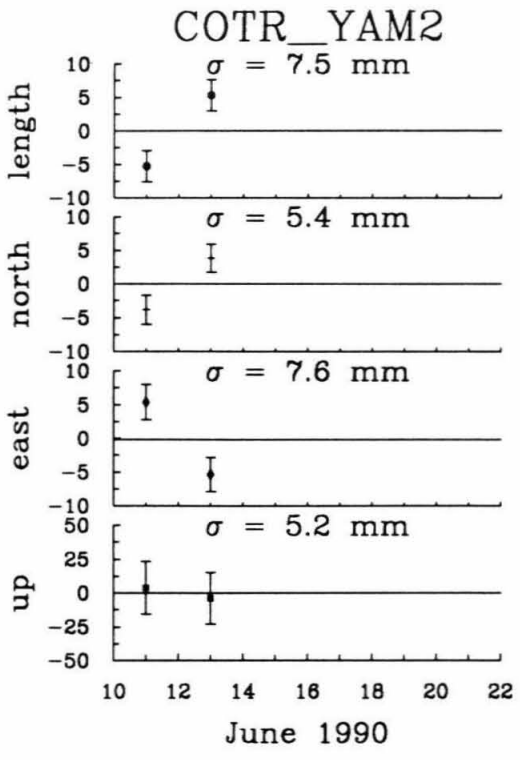
COTR_YAM2
σ = 7.5 mm
σ = 5.4 mm
σ = 7.6 mm
σ = 5.2 mm
length
north
east
up
June 1990

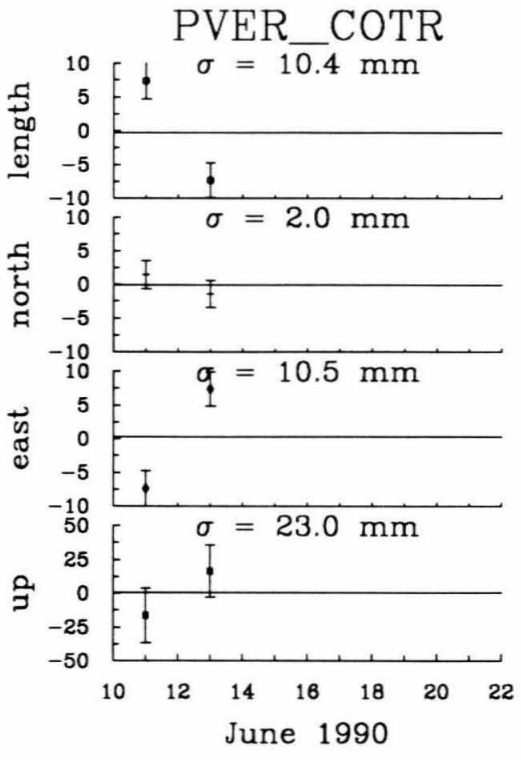
PVER_COTR
σ = 10.4 mm
σ = 2.0 mm
σ = 10.5 mm
σ = 23.0 mm
length
north
east
up
June 1990

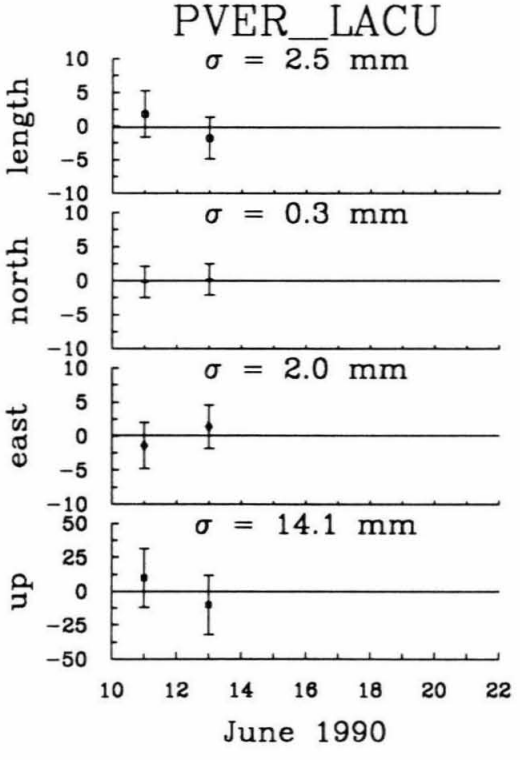
PVER_LACU
σ = 2.5 mm
σ = 0.3 mm
σ = 2.0 mm
σ = 14.1 mm
length
north
east
up
June 1990

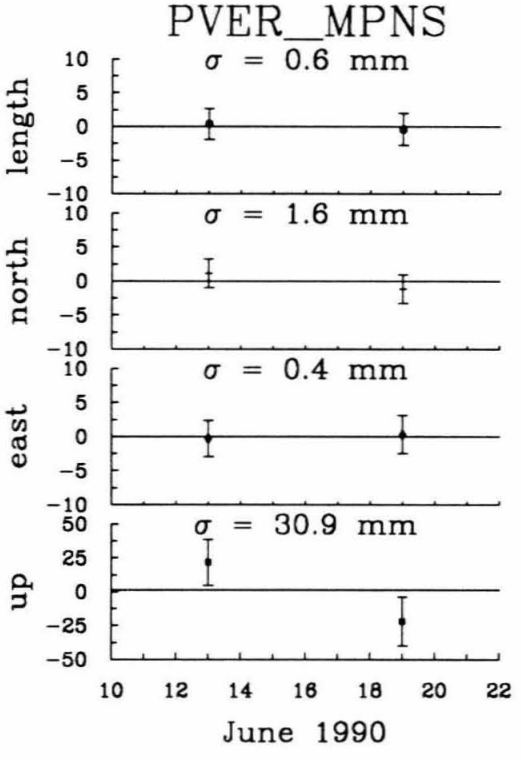
PVER_MPNS
σ = 0.6 mm
σ = 1.6 mm
σ = 0.4 mm
σ = 30.9 mm
length
north
east
up
June 1990

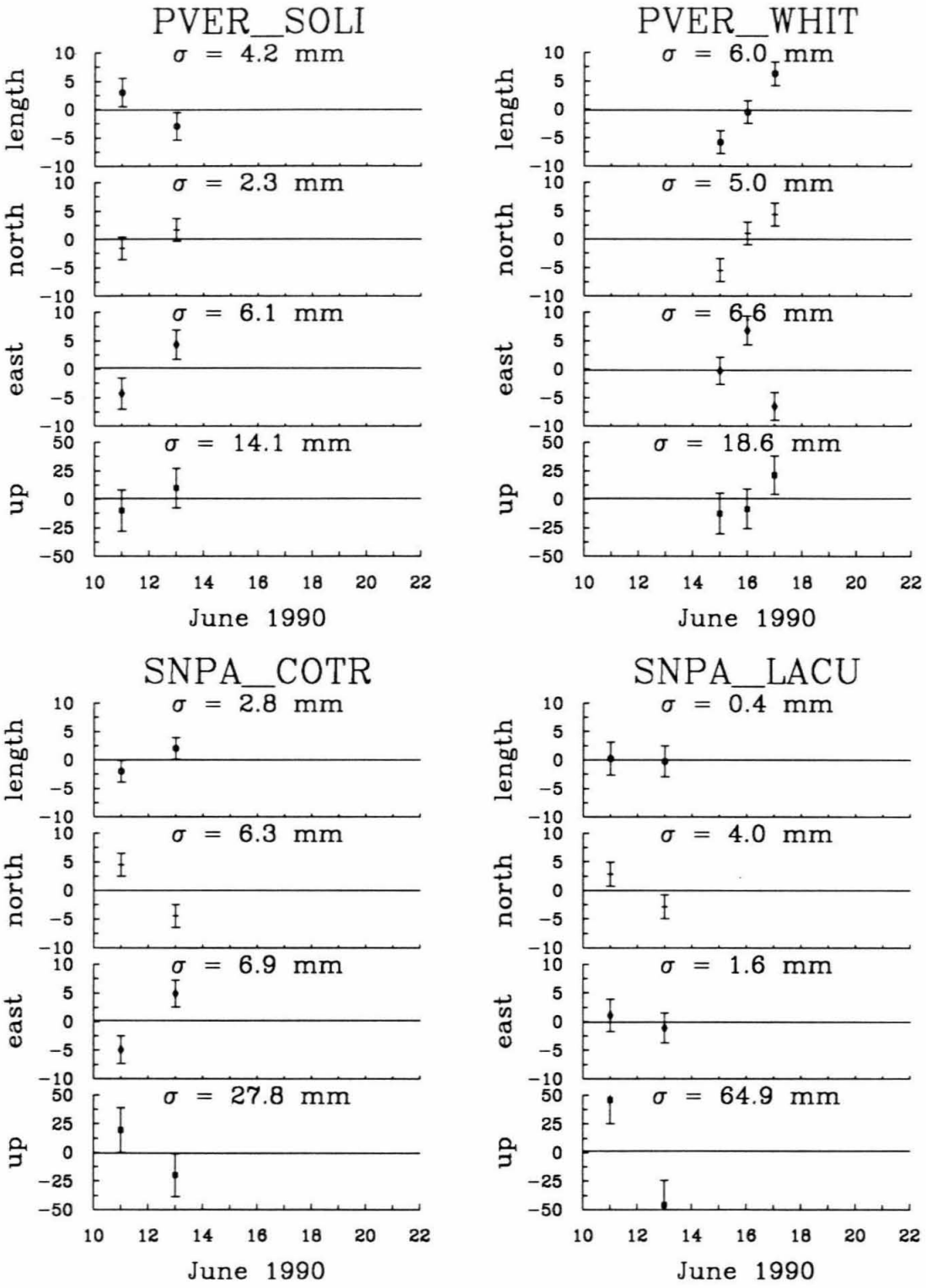
PVER_SOLI
σ = 4.2 mm
σ = 2.3 mm
σ = 6.1 mm
σ = 14.1 mm
PVER_WHIT
σ = 6.0 mm
σ = 5.0 mm
σ = 6.6 mm
σ = 18.6 mm
SNPA_COTR
σ = 2.8 mm
σ = 6.3 mm
σ = 6.9 mm
σ = 27.8 mm
SNPA_LACU
σ = 0.4 mm
σ = 4.0 mm
σ = 1.6 mm
σ = 64.9 mm
length
north
east
up
June 1990

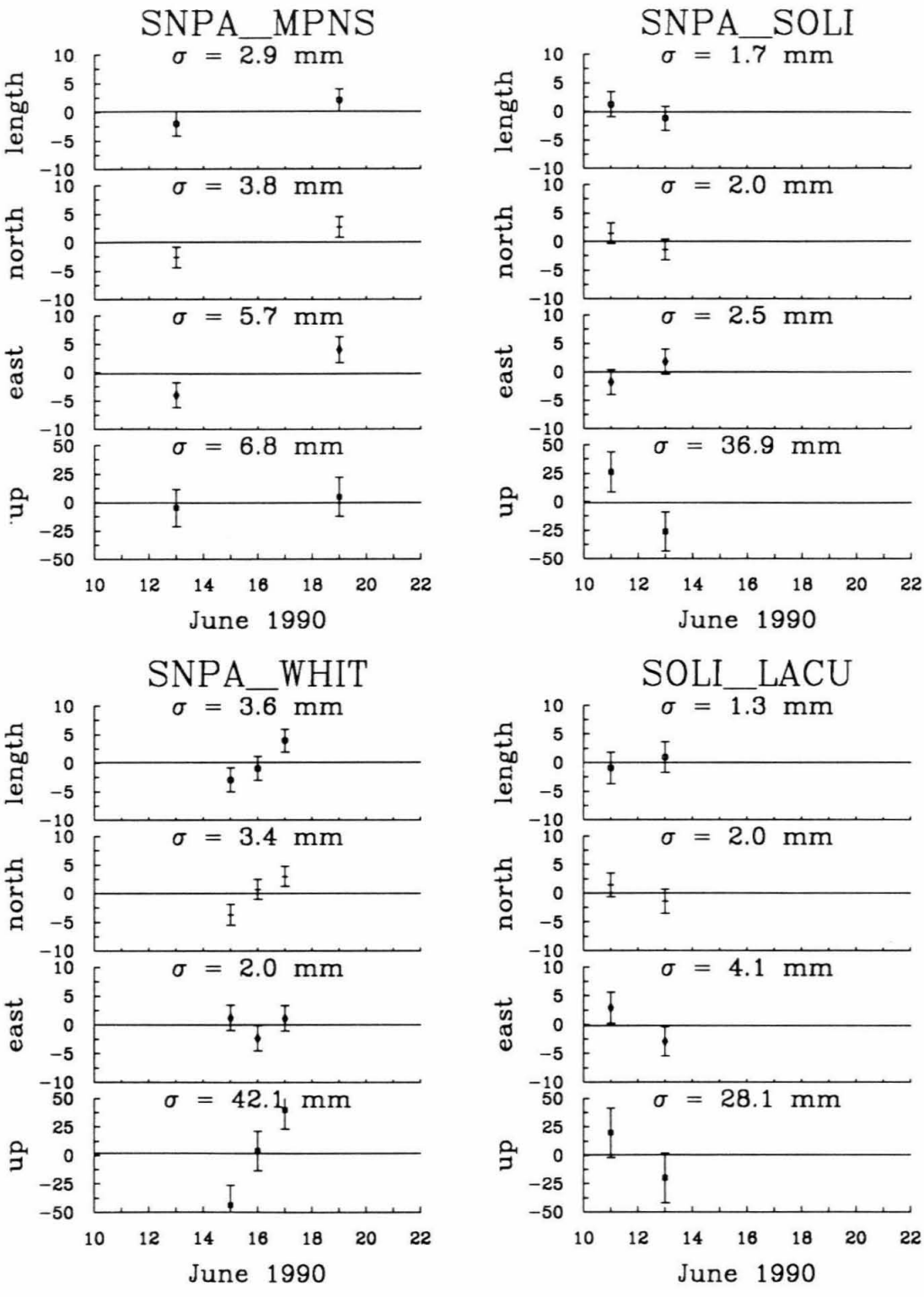
SNPA_MPNS
σ = 2.9 mm
σ = 3.8 mm
σ = 5.7 mm
σ = 6.8 mm
length
north
east
up
June 1990
SNPA_SOLI
σ = 1.7 mm
σ = 2.0 mm
σ = 2.5 mm
σ = 36.9 mm
length
north
east
up
June 1990
SNPA_WHIT
σ = 3.6 mm
σ = 3.4 mm
σ = 2.0 mm
σ = 42.1 mm
length
north
east
up
June 1990
SOLI_LACU
σ = 1.3 mm
σ = 2.0 mm
σ = 4.1 mm
σ = 28.1 mm
length
north
east
up
June 1990

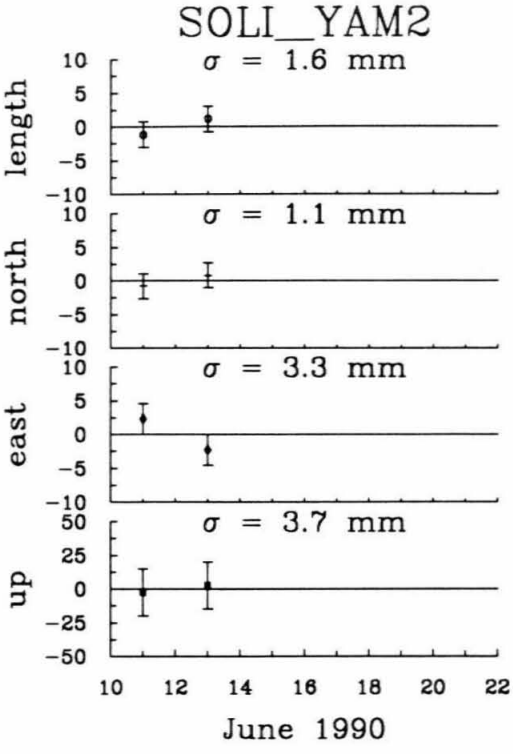
SOLI_YAM2
σ = 1.6 mm
σ = 1.1 mm
σ = 3.3 mm
σ = 3.7 mm
length
north
east
up
June 1990

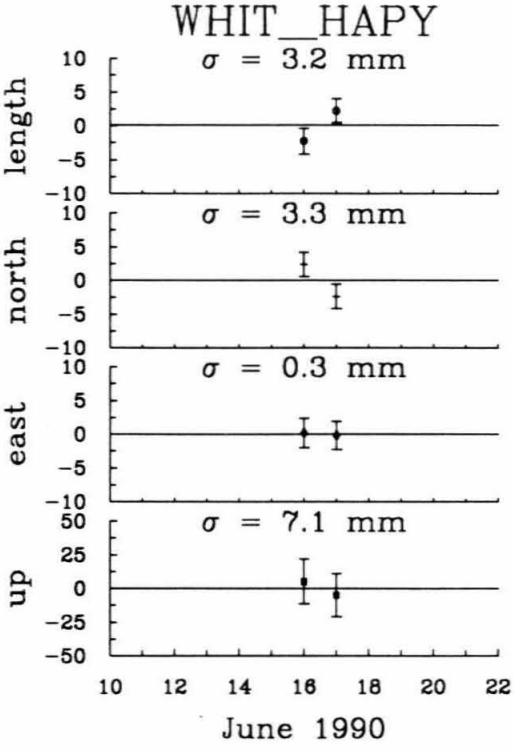
WHIT_HAPY
σ = 3.2 mm
σ = 3.3 mm
σ = 0.3 mm
σ = 7.1 mm
length
north
east
up
June 1990

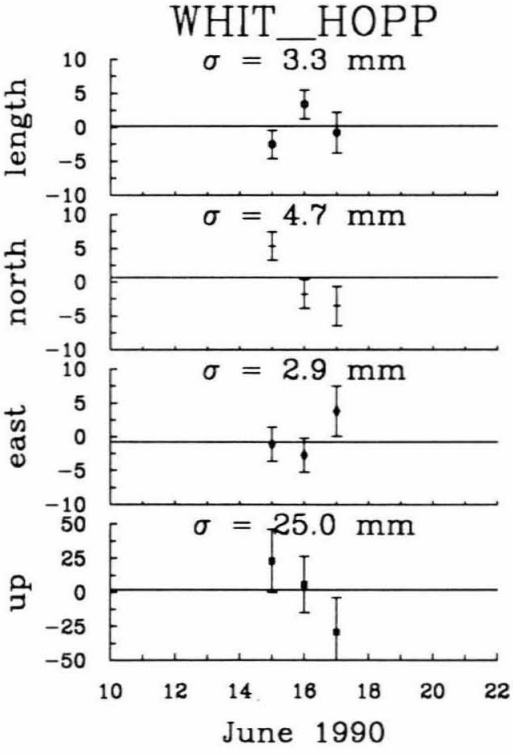
WHIT_HOPP
σ = 3.3 mm
σ = 4.7 mm
σ = 2.9 mm
σ = 25.0 mm
length
north
east
up
June 1990

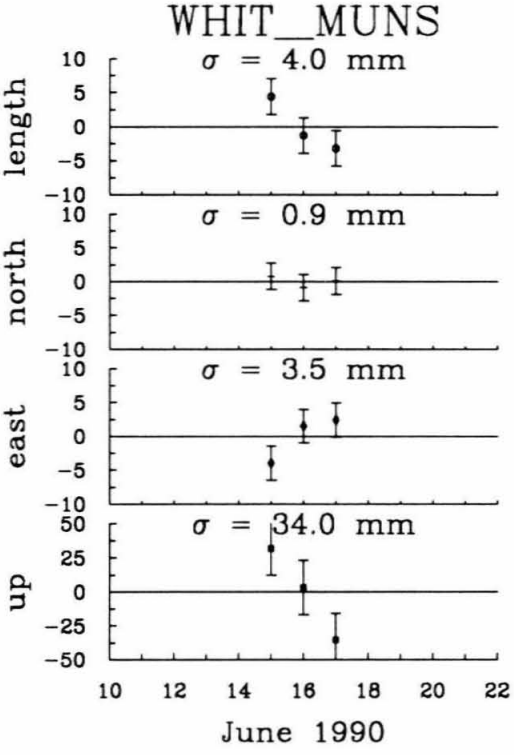
WHIT_MUNS
σ = 4.0 mm
σ = 0.9 mm
σ = 3.5 mm
σ = 34.0 mm
length
north
east
up
June 1990

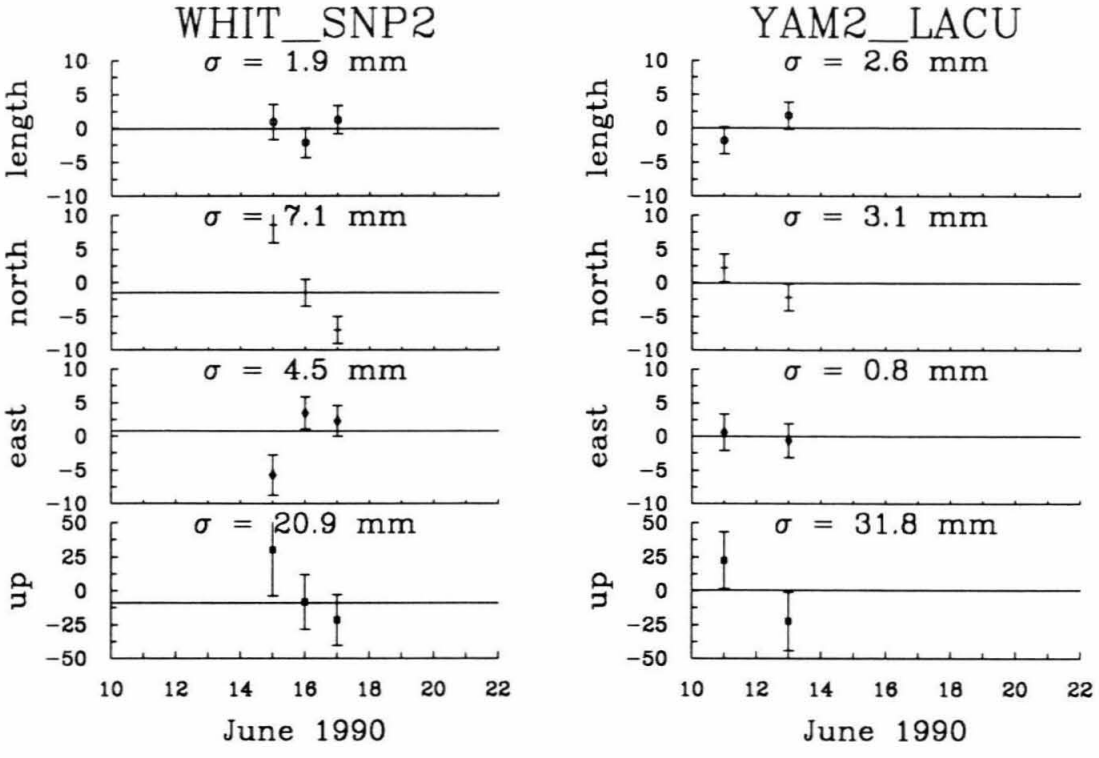
WHIT_SNP2
σ = 1.9 mm
σ = 7.1 mm
σ = 4.5 mm
σ = 20.9 mm
length
north
east
up
June 1990
YAM2_LACU
σ = 2.6 mm
σ = 3.1 mm
σ = 0.8 mm
σ = 31.8 mm
length
north
east
up
June 1990

Appendix C

Triangulation Data Used for Strain Calculations

The following data were used for the comparisons between GPS and triangulation. The listed directions are not corrected for deflection of the vertical. Table C.5 lists the corrections of deflection of the vertical applied to each direction for the strain calculations.

from	to	date	direction			error
HAPY	SCLA	04/28/1959	51°	22′	33.28″	0.7″
	HOPP		146°	52′	48.23″	0.7″
SNP2	HOPP	04/29/1959	0°	0′	0.00″	0.8″
	SCLA		119°	29′	51.09″	0.7″
SNP2	HOPP	05/03/1959	0°	0′	0.00″	0.7″
	SCLA		119°	29′	48.60″	0.7″
SCLA	HOPP	04/28/1959	218°	52′	1.14″	0.7″
	HAPY		253°	47′	42.66″	0.7″
HOPP	HAPY	05/04/1959	90°	28′	29.62″	0.7″
	SCLA		140°	2′	31.82″	1.3″
	SNP2		169°	12′	58.78″	0.7″
HOPP	SCLA	05/05/1959	140°	2′	33.43″	0.7″
	SNP2		169°	12′	57.52″	0.7″
HAPY	HOPP	05/08/1975	0°	0′	0.00″	1.0″
	SCLA		264°	29′	47.74″	1.2″

Table C.1: History of triangulation for the east-central part of the Ventura basin, near Fillmore, and the observed directions. Convention for the date is month/day/year.

from	to	date	direction			error
LOVE	SAF8	07/20/1932	137°	8′	40.64″	0.6″
	SCLA		216°	49′	15.67″	0.6″
LOVE	SAF8	07/21/1932	0°	0′	0.00″	0.6″
	SCLA		79°	40′	36.29″	0.6″
SCLA	LOVE	07/19/1932	0°	0′	0.00″	0.6″
	SAF8		28°	23′	31.18″	0.6″
SAF8	SCLA	07/19/1932	57°	15′	59.86″	0.6″
	LOVE		129°	11′	52.55″	0.6″
LOVE	SAF8	11/18/1952	137°	8′	38.39″	0.6″
	SCLA		216°	49′	15.44″	0.6″
SAF8	SCLA	11/16/1952	57°	15′	59.28″	0.6″
	LOVE		129°	11′	54.29″	0.6″
SCLA	LOVE	11/17/1952	0°	0′	0.00″	0.6″
	SAF8		28°	23′	30.54″	0.6″
SCLA	HAPY	04/28/1959	253°	47′	42.66″	0.6″
	SAF8		264°	42′	45.22″	0.6″

Table C.2: History of triangulation for the eastern Ventura basin and the observed directions. Convention for the date is month/day/year. *Continued on next page.*

from	to	date	direction			error
HAPY	SAF8	04/29/1959	0°	0′	0″	0.7″
	SCLA		160°	43′	20.56″	0.7″
HOPP	LOVE	05/04/1959	0°	0′	0″	0.8″
	SAF8		40°	29′	35.08″	0.7″
	HAPY		90°	28′	29.62″	0.7″
HOPP	LOVE	05/05/1959	0°	0′	0″	0.8″
	SAF8		40°	29′	32.65″	0.7″
LOVE	HOPP	04/29/1959	102°	10′	47.41″	0.8″
	SAF8		0°	0′	0.00″	0.8″
SAF8	SCLA	05/04/1959	23°	48′	39.37″	0.7″
	HAPY		32°	10′	12.97″	0.7″
	HOPP		58°	24′	53.30″	0.7″
	LOVE		95°	44′	33.03″	0.8″
LOVE	HOPP	04/29/1959	0°	0′	0.00″	0.8″
	SAF8		257°	49′	13.32″	0.8″
LOVE	SAF3	07/01/1963	137°	7′	34.02″	0.6″
	SCLA		216°	49′	13.36″	0.6″
LOVE	SAF3	07/01/1963	137°	7′	33.52″	0.6″
	SCLA		216°	49′	14.01″	0.6″
LOVE	SAF3	07/02/1963	137°	7′	33.00″	0.6″
	SCLA		216°	49′	13.52″	0.6″

Table C.2: *Continued.*

from	to	date	direction			error
SAF3	SCLA	06/27/1963	188°	23′	00.36″	0.6″
	LOVE		260°	19′	47.74″	0.6″
SAF3	SCLA	06/27/1963	188°	22′	59.68″	0.6″
	LOVE		260°	19′	46.51″	0.6″
SCLA	LOVE	06/28/1963	0°	0′	0.00″	0.6″
	SAF3		28°	21′	30.59″	0.6″
	SAF3		28°	21′	31.28″	0.6″
SCLA	LOVE	07/17/1963	0°	0′	0.00″	0.6″
	SAF3		28°	21′	31.46″	0.6″

Table C.2: *Continued.*

from	to	date	direction			error
CAT8	SCLA	11/17/1952	0°	0′	0.00″	0.6″
	SAF8		73°	18′	21.84″	0.6″
CAT8	SCLA	xx/xx/1898	0°	0′	0.00″	0.6″
	SAF8		73°	18′	20.96″	0.6″
CAT8	SAF8	03/01/1923	0°	0′	0.00″	0.6″
	SCLA		286°	41′	38.41″	0.6″
CAT8	SAF8	03/02/1923	0°	0′	0.00″	0.6″
	SCLA		286°	41′	37.96″	0.6″

Table C.3: History of triangulation directly south of the Ventura basin and the observed directions. Convention for the date is month/day/year. *Continued on next page.*

from	to	date	direction			error
CAT8	SCLA	06/05/1956	43°	6′	20.20″	0.6″
	SAF8		116°	24′	41.97″	0.6″
CAT8	SCLA	06/06/1956	43°	6′	19.29″	0.6″
	SAF8		116°	24′	41.03″	0.6″
CAT8	SCLA	06/07/1956	43°	6′	20.87″	0.6″
	SAF8		116°	24′	42.48″	0.6″
CAT8	SCLA	07/18/1932	0°	0′	0.00″	0.6″
	SAF8		73°	18′	20.79″	0.6″
SAF8	CAT8	11/16/1952	0°	0′	0.00″	0.6″
	SCLA		57°	15′	59.28″	0.6″
SAF8	CAT8	xx/xx/1898	0°	0′	0.00″	0.6″
	SCLA		57°	15′	59.27″	0.6″
SAF8	CAT8	11/0x/1923	109°	02′	17.28″	0.6″
	SCLA		166°	18′	16.19″	0.6″
SAF8	CAT8	11/0x/1923	109°	02′	17.16″	0.6″
	SCLA		166°	18′	16.45″	0.6″

Table C.3: *Continued.*

from	to	date	direction			error
SAF8	CAT8	06/05/1956	109°	02′	18.95″	0.6″
	SCLA		166°	18′	18.59″	0.6″
SAF8	CAT8	06/05/1956	109°	02′	25.02″	0.6″
	SCLA		166°	18′	17.48″	0.6″
SAF8	CAT8	06/06/1956	109°	02′	18.44″	0.6″
	SCLA		166°	18′	18.76″	0.6″
SAF8	CAT8	06/07/1956	109°	02′	18.83″	0.6″
	SCLA		166°	18′	17.37″	0.6″
SAF8	CAT8	06/07/1956	109°	02′	23.19″	0.6″
	SCLA		166°	18′	16.29″	0.6″
SAF8	CAT8	06/28/1956	52°	59′	27.95″	0.6″
	SCLA		110°	15′	28.70″	0.6″
SAF8	CAT8	07/19/1932	0°	0′	0.00″	0.6″
	SCLA		57°	15′	59.86″	0.6″
SCLA	SAF8	11/17/1952	28°	23′	0.54″	0.6″
	CAT8		77°	49′	12.66″	0.6″
SCLA	SAF8	xx/xx/1898	263°	35′	32.53″	0.6″
	CAT8		313°	1′	15.26″	0.6″

Table C.3: *Continued.*

from	to	date	direction			error
SCLA	SAF8	11/07/1923	0°	0′	0.00″	0.6″
	CAT8		49°	25′	42.24″	0.6″
SCLA	SAF8	11/08/1923	0°	0′	0.00″	0.6″
	CAT8		49°	25′	41.96″	0.6″
SCLA	CAT8	06/04/1956	0°	0′	0.00″	0.6″
	SAF8		310°	34′	17.89″	0.6″
SCLA	SAF8	06/05/1956	0°	0′	0.00″	0.6″
	CAT8		49°	25′	43.37″	0.6″
SCLA	SAF8	06/05/1956	0°	0′	0.00″	0.6″
	CAT8		49°	25′	45.27″	0.6″
SCLA	SAF8	06/07/1956	0°	0′	0.00″	0.6″
	CAT8		49°	25′	39.93″	0.6″
SCLA	HAPY	04/28/1959	253°	47′	42.66″	0.7″
	SAF8		264°	42′	45.22″	0.7″

Table C.3: *Continued.*

from	to	date	direction		
HOPP	SCLA	10/05/1987	−136°	31′	9.78″
	HAPY		173°	54′	44.40″
	SNP2		−107°	20′	44.80″
	LOVE		83°	26′	13.59″
SCLA	HOPP	10/05/1987	43°	22′	57.01″
	HAPY		78°	18′	39.58″
HAPY	HOPP	10/05/1987	−6°	4′	44.26″
	SCLA		−101°	34′	56.47″
SNP2	HOPP	10/05/1987	72°	34′	21.85″
	SCLA		−167°	55′	46.60″
HOPP	SAF8	06/20/1990	123°	55′	48.01″
	HAPY		173°	54′	44.57″
	SCLA		−136°	31′	9.57″

Table C.4: Directions calculated from the GPS observations. Convention for the date is month/day/year. *Continued on next page.*

from	to	date	direction		
SCLA	SAF8	06/20/1990	89°	13′	42.91″
	HAPY		78°	18′	39.59″
	SAF3		89°	11′	44.36″
	LOVE		60°	50′	12.85″
HAPY	SAF8	06/20/1990	97°	41′	40.96″
	SCLA		−101°	34′	56.46″
LOVE	SAF3	06/20/1990	161°	21′	5.09″
	SAF8		161°	22′	8.38″
	SCLA		−118°	57′	13.29″
	HOPP		−96°	27′	5.07″
SAF8	LOVE	06/20/1990	−18°	35′	33.94″
	HOPP		−55°	55′	13.86″
	SCLA		−90°	31′	27.46″
	HAPY		−82°	9′	53.01″
SAF3	LOVE	06/20/1990	−18°	36′	37.26″
	SCLA		−90°	33′	26.04″

Table C.4: *Continued.*

from	to	$\tan\beta$	ζ	correction
HAPY	HOPP	0.05	$7.10''$	$-0.36''$
HAPY†	HOPP	0.05	$9.88''$	$-0.51''$
HAPY	LOVE	0.00	$0.45''$	$0.00''$
HAPY†	LOVE	0.00	$2.38''$	$-0.01''$
HAPY	SAFE	0.02	$-6.12''$	$0.12''$
HAPY†	SAFE	0.02	$-6.41''$	$0.12''$
HAPY	SCLA	0.00	$3.92''$	$0.00''$
HAPY†	SCLA	0.00	$3.32''$	$0.00''$
HAPY	SNP2	0.05	$7.91''$	$-0.37''$
HAPY†	SNP2	0.05	$9.31''$	$-0.43''$
HOPP	HAPY	-0.05	$-3.17''$	$-0.16''$
HOPP	LOVE	-0.03	$20.00''$	$-0.68''$

Table C.5: Deflection of the vertical applied to each direction for the strain calculations. † refers to deflections calculated from astronomic observations. *Continued on next page.*

from	to	$\tan\beta$	ζ	correction
HOPP	SAFE	-0.01	17.33″	−0.14″
HOPP	SCLA	-0.03	13.38″	0.40″
HOPP	SNP2	0.01	19.04″	−0.17″
LOVE	HAPY	0.00	9.76″	0.02″
LOVE	HOPP	0.03	14.45″	−0.49″
LOVE	SAFE	0.02	−6.21″	0.12″
LOVE	SCLA	0.00	12.23″	0.02″
SCLA	HAPY	0.00	−7.43″	0.01″
SCLA	HOPP	0.03	−1.63″	0.05″
SCLA	LOVE	0.00	−4.58″	0.01″
SCLA	SAFE	0.01	−8.80″	0.10″
SAFE	HAPY	-0.02	7.87″	0.15″
SAFE†	HAPY	-0.02	9.10″	0.17″

Table C.5: *Continued.*

from	to	$\tan\beta$	ζ	correction
SAFE	HOPP	0.01	$7.64''$	$-0.06''$
SAFE†	HOPP	0.01	$10.29''$	$-0.09''$
SAFE	LOVE	-0.02	$4.57''$	$0.09''$
SAFE†	LOVE	-0.02	$8.31''$	$0.16''$
SAFE	SCLA	-0.01	$7.63''$	$0.08''$
SAFE†	SCLA	-0.01	$8.37''$	$0.09''$
SAFE	SNP2	0.01	$7.96''$	$-0.08''$
SAFE†	SNP2	0.01	$9.88''$	$-0.09''$
SNP2	HAPY	-0.05	$-24.20''$	$-1.13''$
SNP2	HOPP	-0.01	$-28.27''$	$-0.27''$
SNP2	SCLA	-0.06	$8.00''$	$0.50''$

Table C.5: *Continued.*